Studies of lead-free halide perovskite photocatalysts



Zhiyang Zhong

St Catherine's College

University of Oxford

Supervisor: Angus I. Kirkland

Co-Supervisor: S. C. Edman Tsang

A thesis submitted for the degree of

Doctor of Philosophy

Trinity 2026

Dedication

In memory of Prof Edman Tsang

To my beloved grandmother

And to my mum and dad

Statement of authorship

I hereby declare that this thesis is my own original work. Any work that is the result of collaboration is clearly indicated and acknowledged. All sources and previous work by others are properly cited. Permission was granted for all images used in this thesis from other sources. This thesis has not been submitted, either in whole or in part, for a degree or diploma at any other institution.

Acknowledgements

As my DPhil journey is coming to an end, I feel immense gratitude for those who helped me reach this point. I would like to acknowledge them here, though I know that not everyone who made a difference can be named individually.

I am deeply grateful to my supervisor Prof Angus Kirkland, who gave me the opportunity to work on this project, and offered wise mentorship as well as encouragement along the way. His wide-ranging knowledge and tireless dedication made him a remarkable role model and gave me unparalleled insight throughout my research.

I am equally thankful to my secondary supervisor, Prof Edman Tsang, whose passion and profound expertise in the field of catalysis have inspired not one but multiple generations of scientists. I was devastated upon hearing the news of his passing. May he rest in peace in heaven.

My heartfelt gratitude goes towards my mum and dad. Their support has been fundamental. Getting through Covid lockdown was very tough; I could feel they were behind me when I was on edge, even though we were physically separated then.

Special thanks are due to Dr Judy Kim and Prof Neil Young, for being my DPhil assessors and gave me important feedback during Transfer and Confirmation of Status. I would also like to thank the staff at DCCEM for their help on the microscopes, as well as Dr Ali Mostaed on training me to use the advanced microscope ARM, and Dr Ryan Clark at Chemistry Teaching Laboratory to show me how to use the instruments available in the teaching lab.

I feel privileged to have met my friends and informal mentors, Prof Yanjie Wang and Dr Zhiyuan Ding, who offered me invaluable advice on technical aspects of my project, and navigating life when I was struggling with my research.

I would like to thank my colleagues from the Tsang group, particularly Amy Radford for allowing me to use her Schlenk line from time to time, and Dr Yiyang Li for guidance in experiments and research in general. The stimulating technical discussions within the group enriched my research, and casual chats whilst being in the lift together travelling between basement and 2M simply made the day a little more enjoyable. The pub trips and barbecues also created some fond memories during this journey.

To my colleagues in the EM groups based in the Holder offices 30.15 & 30.16, my trustworthy source of help for anything EM-related. The casual chats and group outings also added joy and connection to the experience. Your presence made me believe that there is always a way forward.

My sincere appreciation extends to Yuka Kodama Ballet Group and Oxford University Touch Rugby Club. The activities they provided often helped me regroup myself and try once more after a series of failed experiments. They also provided a sense of belonging when I was feeling lost.

Finally, I feel fortunate to be able to work on this project, where I could do synthesis, run photocatalytic tests, and perform most of the characterisation techniques myself. Access to advanced electron microscopes was a gift. The images have been delivering wonder since I first got my hands on a TEM, and even now, the results from my samples continue to amaze me.

Abstract

Hydrogen is a source of clean energy. It can be used as a replacement for fossil fuels, reducing the amount of greenhouse gas produced. However, a very large proportion of hydrogen produced these days still relies on fossil fuels. In this way, more environmentally friendly methods to generate hydrogen are needed. In this thesis, two routes to hydrogen production were investigated: methanol photo-oxidation and photocatalytic water splitting. Methanol is a high-density hydrogen carrier, as it contains four hydrogen atoms per molecule. Compared to traditional thermocatalytic processes, photocatalysis can achieve hydrogen extraction from methanol at significantly lower temperature and pressure. Formaldehyde can also be produced in this process as a valuable byproduct, which otherwise also requires high temperate reactions to obtain commercially. Halide perovskites are promising photocatalysts in multiple fields, but the most effective ones contain lead, which is detrimental to both human health and the environment. In this thesis, lead-free halide perovskite $Cs_2AgBiBr_6$ (CABB) was studied as a potential photocatalyst for methanol photo-oxidation, which had not been reported before. The objectives were to find out how the material performed and whether the activity could be further improved, how different morphology of the sample would affect the reaction rate, and how the material would change during the photoreaction. A plausible reaction mechanism was also proposed. Different synthesis routes were tested, yielding CABB in bulk, nanocube and nanosheet forms. CABB nanocubes washed with ethanol were found to show the highest activity, reaching a peak hydrogen generation rate of 229 $\mu mol\ g^{-1}\ h^{-1}$ in the photocatalytic reaction with methanol vapour. The stability of the catalyst was also tested, and it could produce hydrogen consistently for at least 10 hours. Electron microscopy (EM) was used to study CABB specimens to investigate any changes in the structure as the reaction progressed, linking these observations to the rates of reaction. Additional characterisation

techniques including in-situ X-ray photoelectron spectroscopy were also used, revealing that Ag^{+} and Bi^{3+} played a major role in the photocatalytic reaction. For the photocatalytic water splitting reaction, both CABB and tin-based PEA_2SnBr_4 (PSB) were tested as catalysts. CABB was found to react with water and form a BiOBr layer. The hydrogen production rate was around 3 μmol g^{-1} h^{-1}. However, when PSB was mixed with 15 wt% MoS_2 to form a PSB/MoS_2 heterojunction, it achieved the highest hydrogen generation rate of 605 μmol g^{-1} h^{-1} in water with 10 vol% TEOA and 3 wt% Pt. However, PSB was calculated to have a critical fluence of only eight electrons per square Angstrom, so limited EM data were obtained.

Table of Contents

Chapter 1 Introduction 1

1.1. Photocatalytic water splitting reactions 1
1.2. Methanol photo-oxidation and production of formaldehyde 3
1.3. Halide perovskites 4
1.3.1. Overview 4
1.3.2. PEA_2SnBr_4 as a photocatalyst 7
1.3.3. $Cs_2AgBiBr_6$ as a photocatalyst 12
1.4. Aims and objectives 13

Chapter 2 Background on $Cs_2AgBiBr_6$ 14

2.1. Introduction 15
2.2. Morphology and synthesis of CABB 16
2.2.1. HBr mixing and heating for bulk CABB 16
2.2.2. Dissolution and precipitating methods 17
2.2.3. Hot injection methods 19
2.2.4. Microwave-assisted solvothermal methods 22
2.3. Using CABB as a photocatalyst 23
2.3.1. Hydrogen generation 23
2.3.2. CO_2 reduction 26
2.3.3. Dye degradation 31
2.3.4. Other applications 33
2.4. Strategies to improve activity 36
2.4.1. Washing and surface ligand control 36
2.4.2. Heterojunctions 38
2.4.3. Elemental doping/substitution 44
2.4.4. Introducing defects into the structure 44
2.4.5. Adjusting light intensity 47
2.5. Methods to improve stability 48
2.5.1. Dynamic equilibrium 48
2.5.2. Attachment to the surface of larger structures 48
2.5.3. Deposition within porous materials 50

2.6. Research progress of other photocatalysts 52
2.6.1. Hydrogen generation 53
2.6.2. CO_2 reduction 53
2.6.3. Pollutant degradation 54
2.7. Evaluating output via turnover frequency 54
2.8. Conclusions 55

Chapter 3 Experimental methods 56

3.1. Synthesis of PEA_2SnBr_4 and MoS_2 heterojunctions 57
3.2. Synthesis of $Cs_2AgBiBr_6$ 57
3.2.1. Synthesis of bulk samples 57
3.2.2. Synthesis of nanocubes via hot injection 58
3.2.3. Synthesis of nanosheets via hot injection 58
3.2.4. Synthesis of bulk and nano CABB at room temperature 59
3.3. Photocatalytic reactions 60
3.3.1. The photocatalytic water splitting reaction 60
3.3.2. Reactions in liquid methanol 61
3.3.3. Reactions with methanol vapour 62
3.4. X-ray diffraction (XRD) 62
3.5. UV-visible spectroscopy (UV-vis) 64
3.5.1. Theory 64
3.5.2. Bandgap calculations using powder UV-vis 66
3.5.3. Formaldehyde quantification using liquid UV-vis 66
3.6. Fourier transform infrared spectroscopy (FTIR) 68
3.7. X-ray photoelectron spectroscopy (XPS) 70
3.8. Gas chromatography (GC) and quantification of hydrogen 74
3.8.1. Principles of gas chromatography 74
3.8.2. Hydrogen quantification process 77
3.8.3. Turnover frequency calculations 78
3.9. Zeta potential and surface charge 79
3.10. (Time-resolved) photoluminescence 81
3.11. Electron microscopy and sample preparations 83
3.11.1. (Scanning) transmission electron microscopy 83
3.11.2. Electron fluence calculations 91

3.11.3. Lattice measurements 93
3.11.4. Scanning electron microscopy 95
3.11.5. TEM sample preparations 97
3.11.6. SEM sample preparations 98
3.11.7. EDX data analysis 98

Chapter 4 $Cs_2AgBiBr_6$ as a photocatalyst in methanol oxidation .. 99

4.1. Introduction 99
4.2. Results and discussion 101
4.2.1. Characterisation of as-synthesised bulk CABB and nanocubes 101
4.2.2. Photocatalytic performance in liquid methanol with NaBr 105
4.2.3. Photocatalytic performance with methanol vapour 107
4.2.4. Fast Fourier Transform and nanoparticle surface study 120
4.2.5. Formaldehyde detection 124
4.2.6. Mechanistic analysis 125
4.3. Conclusions 133

Chapter 5 Degradation studies on lead-free halide perovskites in photocatalytic water splitting 134

5.1. Introduction 134
5.2. Results and discussion 135
5.2.1. Synthesis and characterisation of PEA_2SnBr_4 and its heterojunctions 135
5.2.2. Reactions of bulk CABB in water 140
5.2.3. CABB nanocubes in water 146
5.2.4. CABB nanosheets in water 150
5.3. Conclusions 154

Chapter 6 Conclusions and future work 155

6.1. Conclusions 155
6.2. Future work 156

Appendix Additional experimental results 158

A1. Characterisation of CABB-HBr and CABB-NC 158
A2. Photoreactions with methanol vapour 162
A3. STEM-EDX analysis of CABB-NC and CABB-NC-EtOH after photoreactions 165
A4. CABB nanosheets 170
A5. Zeta potential and heterojunctions 174
A6. FFT analysis of CABB-NC-EtOH, 2D-CABB and CABB-NC 176
A7. Surface analysis of CABB nanoparticles 180
A8. CABB-DMSO photoreactions and characterisation 181

References 183

Chapter 1 Introduction

Contents

1.1. Photocatalytic water splitting reactions 1
1.2. Methanol photo-oxidation and production of formaldehyde 3
1.3. Halide perovskites 4
1.3.1. Overview 4
1.3.2. PEA_2SnBr_4 as a photocatalyst 7
1.3.3. $Cs_2AgBiBr_6$ as a photocatalyst 12
1.4. Aims and objectives 13

1.1. Photocatalytic water splitting reactions

Hydrogen is a type of clean energy that is promising as a replacement for fossil fuels in the future, helping to solve environmental problems such as climate change[1]. It does not create greenhouse gas, and the only reaction product with oxygen is water when combusted. Feasible methods to produce hydrogen have been a research topic for decades[2–4], but an economical and sustainable way to produce large quantities of hydrogen has not been found. Obtaining hydrogen from fossil fuels currently remains the cheapest and the most common method[5]. An alternative pathway is to harvest solar energy directly to perform water splitting, storing the energy in hydrogen bonds[6]. The Sun provides virtually unlimited energy to the Earth and on average its surface power density is 1336.1 W m^{-2} at the top of the Earth's atmosphere[7]. Solar energy is also free, clean and renewable, which is worth harvesting and can be used as the energy source for water splitting reactions.

To convert one molecule of H_2O into H_2 and O_2, the photocatalyst needs to absorb at least 1.23 eV of energy from a photon to initiate the reaction. The process can be described

using two half-equations, the hydrogen evolution reaction (HER) and the oxygen evolution reaction (OER), where hydrogen and oxygen are produced separately. When combined, these two half-equations form the overall water splitting reaction[6];

$$H_2O + 2\ h^+ \rightarrow ½\ O_2 + 2\ H^+ \quad \text{(OER)}$$

$$2\ H^+ + 2\ e^- \rightarrow H_2 \quad \text{(HER)}$$

$$H_2O \rightarrow ½\ O_2 + H_2 \quad \text{(Overall reaction)}$$

Hence to achieve this water splitting reaction, the semiconductor catalyst should possess a bandgap larger than 1.23 eV. Its conduction band needs to be more negative than the reduction potential of H^+/H_2, which is itself negative with respect to the normal hydrogen electrode (NHE). The valence band of the semiconductor is also required to be more positive than the oxidation potential of O_2/H_2O at 1.23 eV with respect to the NHE[8].

The photocatalysis process can be described in four steps: (1) the photons carrying energy greater than the bandgap of the catalyst are absorbed; (2) the photoexcited electrons and holes are generated from the material after receiving energy from photons; (3) the electrons are excited to conduction band, leaving holes in the valence band; (4) the water splitting redox reaction takes place, where electrons in the conduction band (CB) get involved in reduction of H^+, and holes in valence band (VB) take part in oxidation of water[9]. The overall photocatalytic process is illustrated in Figure 1.1.

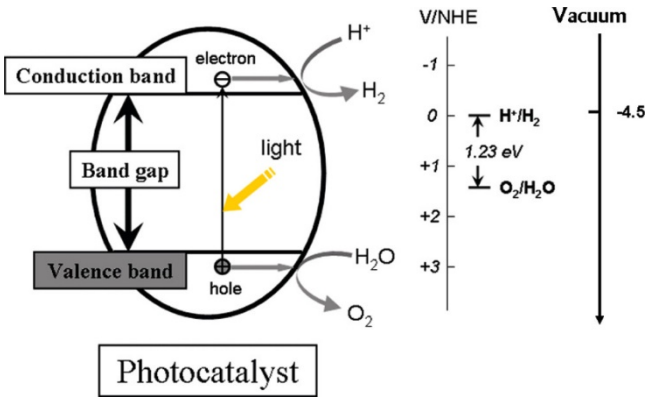

Figure 1.1. Schematic diagram showing the mechanism of photocatalytic water splitting. Reproduced with permission from reference[10]. Copyright 2010 American Chemical Society.

Achieving photocatalytic water splitting is not a simple task, and some of the hurdles are discussed here. Firstly, the Gibbs energy required is +237 kJ mol^{-1} for the overall reaction[11]. The positive Gibbs energy means the reverse reaction is favourable, and adequate energy needs to be introduced to overcome the reverse reaction[12]. Secondly, the charge carriers need to travel to the surface of the catalyst before the water splitting reaction can take place. Charge recombination can occur easily during this step, anywhere from within the material to its surface, which causes generation of unwanted heat[12]. Moreover, the OER requires four electron-hole pairs, which could be a rate limiting step compared to the HER. To solve these problems, lots of ongoing research focusses on developing new catalysts or modifying currently available ones[8]. The catalysts studied in this thesis are the lead-free halide perovskites PEA_2SnBr_4 (PSB) and $Cs_2AgBiBr_6$ (CABB), which are introduced in Sections 1.3.2 and 1.3.3 respectively.

1.2. Methanol photo-oxidation and production of formaldehyde

Methanol has been intertwined with humans since ancient Egyptian times, where it was made as a byproduct of charcoal fabrication from wood, and used for preserving mummies[13]. The breakthrough in industrial production of methanol took place in 1923, by the German company BASF[14]. As a valuable raw material for multiple industrial processes, methanol is converted to other chemicals including acetic acid and the fuel additive methyl tertiary butyl ether (MTBE)[13]. However, formaldehyde synthesis is the main source of methanol consumption, taking up approximately 35% of the total methanol produced[14]. Formaldehyde also has important industrial values. For example, wooden furniture normally requires resins made with formaldehyde for binding, and production of some plastics use formaldehyde as a precursor[13].

Methanol is an excellent hydrogen storage vessel, as one litre of liquid methanol contains more hydrogen than a litre of cryogenically stored hydrogen[15]. In addition, hydrogen is in gaseous form at atmospheric pressure and room temperature, so storage and transport of hydrogen require high pressure and cryogenic temperature for compression. Methanol is easier to store and to transport, as it is naturally in liquid form. There are four main processes to extract hydrogen from methanol thermochemically: steam reforming, partial oxidation, autothermal reforming and methanol decomposition[16]. However, these methods require high temperature and sometimes high pressure, and the main products are H_2, CO_2 and/or CO[16]. Alternatively, under milder reaction conditions, at around room temperature and close to ambient pressure, methanol can be oxidised to formaldehyde via photocatalytic reactions[17]. Commercially, two main methods are used to produce formaldehyde from methanol: the silver contact process which requires a working temperature in the range of 600 °C to 720 °C, and the iron-molybdenum oxide method (Formox process) that operates between 250 °C and 400 °C[18,19]. Lowering the temperature required to around room temperature for formaldehyde synthesis can lead to less energy consumption. In turn, this can cut down costs and leave a smaller carbon footprint. Hence, methanol photo-oxidation at around room temperature was studied in this thesis.

1.3. Halide perovskites

1.3.1. Overview

Halide perovskites refer to a set of materials with a similar crystal structure to calcium titanate, $CaTiO_3$. Their general chemical formula can be written as ABX_3, where A and B are different cations, and X is an anion[20]. Ideally A should have a larger ionic radius than B cation[21]. Typically A = Cs^+, Rb^+, methylammonium (MA), formamidinium (FA), B = Pb^{2+} or Sn^{2+}, X = Br or I, for organic-inorganic and all-inorganic metal halide perovskites[20,21].

The Goldschmidt tolerance factor, *t*, is an established estimation to evaluate the stability of the 3D perovskite structure as;

$$t = \frac{r_A + r_X}{\sqrt{2} \times (r_B + r_x)} \quad (1.1)$$

where r_A, r_B, and r_X are the ionic radii of the ions in the ABX_3 perovskite structure[22]. It is commonly considered that when *t* is between 0.813 and 1.107, the perovskite structure formed is stable[23]. The approximate radii of common ions that can be found in halide perovskites are listed in Table 1.1.

Table 1.1. Estimated radii of common ions that can form perovskite structures[24,25].

Ion type	**Radius (Å)**	**Ion type**	**Radius (Å)**
Cs^+	1.67	Ag^+	1.15
Rb^+	1.52	In^{3+}	0.80
MA^+	2.17	Eu^{3+}	0.95
FA^+	2.53	Sb^{3+}	0.76
DMA^+	2.72	Bi^{3+}	1.03
PEA^+	3.80	Ti^{4+}	0.61
Pb^{2+}	1.19	Mn^{2+}	0.70
Sn^{2+}	1.18	I^-	2.20
Ge^{2+}	0.73	Br^-	1.96
Sn^{4+}	0.69	Cl^-	1.84

Lead-based perovskites were the first type of halide perovskites studied. An article published in 1958 showed that crystals with chemical formula of $CsPbX_3$ (X = Cl or Br) have perovskite structures and are photoconductive[26]. $CsPbBr_3$ has a Goldschmidt tolerance factor of 0.815 and the value for $CsPbCl_3$ is 0.819, suggesting that their perovskite structures are stable. Lead-based perovskites have been extensively studied since then[27].

Halide perovskites have proved their worth in solar cells. The best performing lead-based halide perovskite solar cell achieved an efficiency of 27.0%[28], which is better than a commercial silicon-based solar cell[29]. The superiority of halide perovskites in light absorption may also be utilised in photocatalysis.

A lot of catalysts have been studied apart from halide perovskites. Pt is the benchmark catalyst for HER, and IrO_2 and RuO_2 are the standard for OER[30,31]. However, their high costs restrict their widespread deployment. TiO_2 generally performs well in photocatalysis, but its wide bandgap (3.2 eV) means it can only absorb UV light[32]. ZnO also suffers similar wide bandgap issues[33]. Given the limitations of these materials, making use of the advantages that halide perovskites possess could lead to potent photocatalysts.

Some important properties of lead-based perovskites include high optical absorption coefficients, good charge carrier mobility, small effective charge carrier mass, high defect tolerance, and high electronic dimensionality[34]. The electron configuration of Pb contributes to these properties, due to the filled 6p orbital and the 6s lone-pair state[34]. However, imperfections in the crystal lattice and the existence of impurities create defects in the material, which may affect the performance of the device[35]. Halide perovskites such as $CsPbBr_3$ were found to be able to retain acceptable electronic properties while defects are present[36]. They are hence considered to be defect tolerant.

However, due to the toxic nature of lead, lead-based perovskites as photocatalysts can be problematic in terms of being widely applicable. Lead can form substances that are water-soluble[27]. It can also accumulate in the food chain, and cause organ damage to humans[21]. Alternative options to lead-based halide perovskites should hence be explored.

1.3.2. PEA_2SnBr_4 as a photocatalyst

1.3.2.1. Choosing Sn as the replacement

To replace lead-based halide perovskites, an option is to find a replacement for Pb^{2+} that is normally in a 2+ oxidation state. Filip et al.[37] proposed a set of criteria which limit the range of suitable elements: with an oxidation state of 2+; the scalar relativistic bandgap calculated by density functional theory (DFT) is lower than 3.5 eV; the perovskite geometry is preserved after being shaken and relaxed; the fully relativistic bandgap is lower than 2.0 eV. In this way, the number of candidates is cut down substantially, as shown in Figure 1.2, and the possible 248 initial metal-halide combinations is reduced to 25. Considering other factors such as toxicity, relative stability and photovoltaic properties, Sn^{2+} is the most appropriate substitute[38].

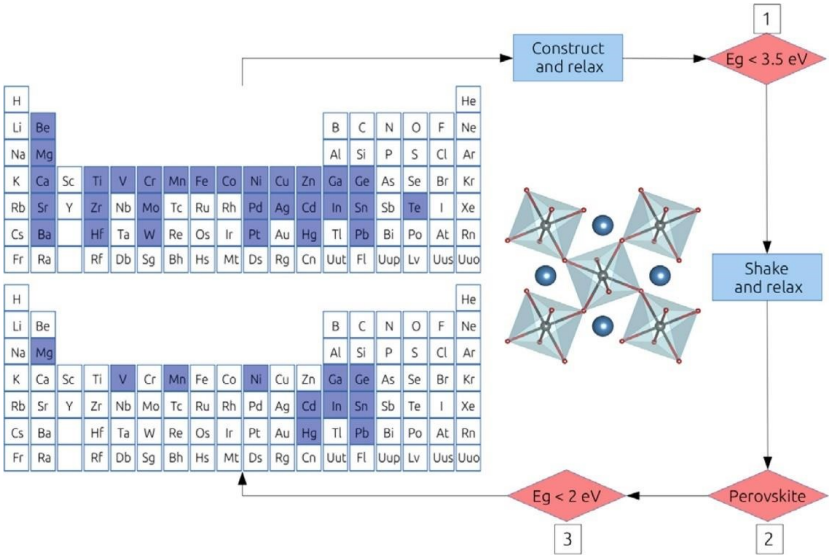

Figure 1.2. Illustration of the screening process to find an element that can replace lead. Reproduced with permission from reference[37]. Copyright 2016 American Chemical Society.

An important reason why Sn is a potential candidate is that it has a lone pair of electrons in the 5s orbital. This is similar to the configuration of lead, where the lone pair of electrons are in the 6s orbital[34]. In some respects, tin-based halide perovskites have advantages over the lead-based halide perovskites. For example, tin-based halide perovskites generally have bandgaps around 1.2-1.4 eV, which are around 0.2 eV lower than lead-based systems[23,39]. Tin-based halide perovskites also possess high electron and hole

mobility, as well as high optical absorption coefficients[23]. However, there is a significant drawback that makes studying Sn-based halide perovskites difficult: higher elements in Group 14 have more unstable 2+ oxidation states[40]. For instance, the Sn^{2+} ion can be easily oxidised to the Sn^{4+} state, even in an anaerobic environment with only trace amounts of oxygen, such as a glovebox[40]. This needs to be overcome before it can supersede lead-based perovskites. However, even if Sn^{2+} is oxidised and forms SnO_2, it is still environmentally friendly[41].

1.3.2.2. Improving stability for halide perovskites

There are currently few methods available to enhance the stability of tin-based halide perovskites. The perovskites can be immersed in a halogen acid-saturated solution while performing photocatalysis; low-polarity solvents can also be used to diminish the contact between the catalyst and the undesirable high-polarity environment; the perovskite can be encapsulated for protection from the polar solvent; the addition of metallic tin to reduce Sn^{4+} back to Sn^{2+} can be used; the intrinsic stability of the perovskite can be improved, by replacing the organic cation with an inorganic cation and adopting perovskites with lower dimensions, to achieve long-term photoreactions[42–44]. From the above approaches, trying to increase the inherent stability of the catalyst was the main strategy explored in this research project.

A 2D lead iodide-based perovskite has been reported which exhibited improved stability when in contact with moisture[44]. Lin et al.[45] proved that low-dimensional perovskites inhibit ion migration, unlike 3D perovskites. This also applies to Sn-based perovskites, and Liao et al.[46] showed that low-dimensional Sn perovskites have enhanced stability in air. Furthermore, lower dimensional structures may provide a larger area for active sites compared to their 3D counterparts, therefore enhancing reaction rates.

A 2D perovskite structure can be regarded as a section of 3D perovskite that has been cut along a specific plane[27]. At present, two main types of 2D halide perovskites are being studied; the first type is a Ruddlesden-Popper (RP) phase, where two mono-cationic spacers are present per formula unit; the second group is a Dion-Jacobson (DJ) phase where there is only one di-cation spacer molecule per formula unit[47]. As illustrated in Figure 1.3, RP and DJ phases have general chemical formulae of $A'_2A_{n-1}B_nX_{3n+1}$ and $A''A_{n-1}B_nX_{3n+1}$ respectively[27,47], where A' is the monovalent organic cation and A'' is the bivalent organic spacer. In addition, n is an integer that specifies the number of metal halide octahedral layers stacked together; when n = 1, the structure is entirely 2D; when n = ∞, it corresponds to a 3D structure; any other finite value in between represents a quasi-2D structure[27,47]. The 1+ cations in the RP phases allow more possibilities in layer stacking, while the 2+ cations in DJ phases are more rigid and difficult to modify[26]. Hence RP-phase halide perovskites were studied in this project because of the flexibility they offer.

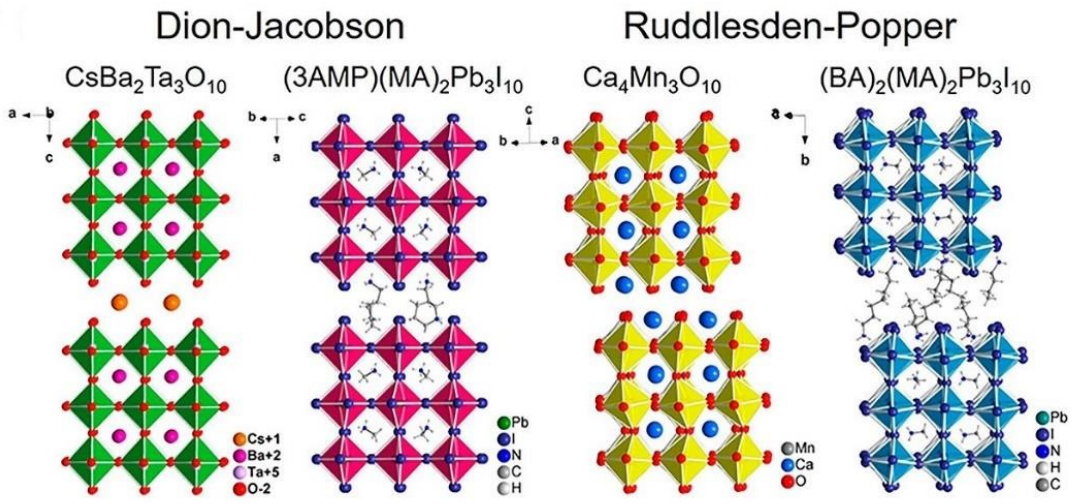

Figure 1.3. Structures of Dion-Jacobson and Ruddlesden-Popper phases. Reproduced with permission from reference[48]. Copyright 2018 American Chemical Society.

1.3.2.3. Synthesis of PEA_2SnBr_4

It has been reported that phenethylammonium (PEA), a type of hydrophobic organic cation, makes perovskites more resistant to moisture[49]. In the research reported by Cheng et al.[49], $MAGeI_3$ and $(PEA)_2GeI_4$ were synthesised and then tested in a humid environment to determine their resistance to moisture. It was observed that after two days, XRD peaks linked to MAI and GeI_4 from the $MAGeI_3$ sample could be detected, indicating the disintegration and oxidation of the sample; while XRD peaks for the $(PEA)_2GeI_4$ sample remain unchanged. They hypothesised that the long PEA chain protected the perovskite from direct contact with water, resulting in better moisture resistance and hence oxidation defence. Moreover, in a separate report, bromide perovskites were noted to be more stable than iodide ones[50], as PEA_2SnBr_4 was found to be more stable in air than PEA_2SnI_4[51]. In this way, the combination of PEA, Sn and bromide can enhance the stability of tin-based halide perovskites, making PEA_2SnBr_4 a sensible choice.

The next step is to aim for a 2D, or at least a layered structure. Solvent selection is critically important as it can greatly influence the synthesis[52]. Taking the synthesis of lead-based halide perovskites as an example, some solvents have weak interaction with the Pb^{2+} centre, allowing the lead halide precursors to form halide perovskite single crystals; other solvents that interact strongly with the Pb^{2+} centre would block halide precursors from approaching, stalling perovskite crystallisation[52]. N,N-dimethylformamide (DMF) is a common polar solvent, and may be able to act as a Lewis base to break down the three-dimensional structure of a halide perovskite into a layered framework[53]. Zhu et al.[54] produced nanosheets with the chemical formula PEA_2PbX_4 (X = Cl, Br or I), using DMF. Both transmission electron microscopy (TEM) and atomic force microscopy (AFM) images validated that the structure of PEA_2PbI_4 was sheet-like, and the thickness was in the range of 4.0 nm to 8.6 nm. Images from this work are shown in Figure 1.4.

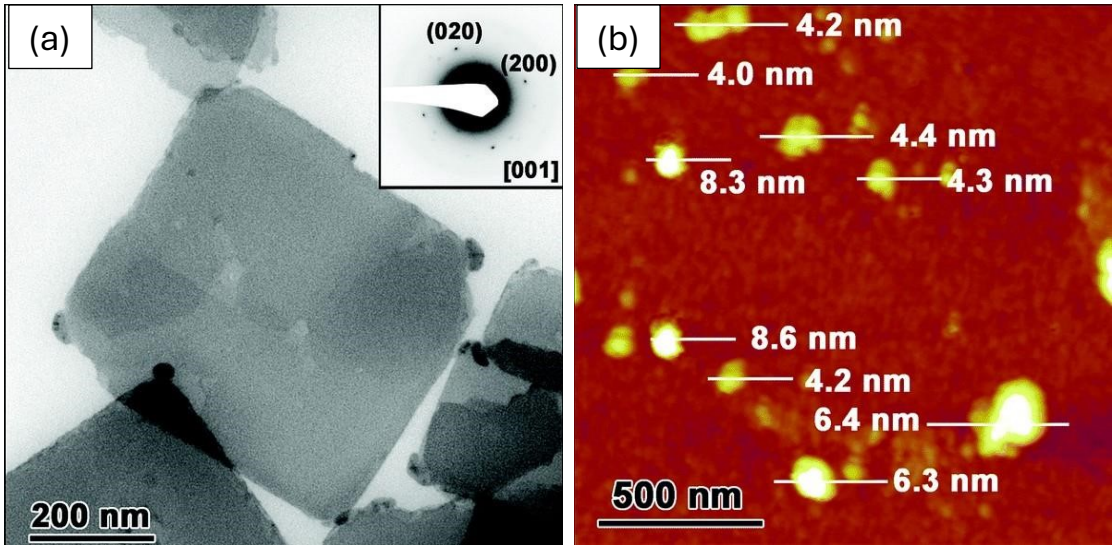

Figure 1.4. (a) TEM and (b) AFM images of PEA_2PbI_4 nanosheets. Reproduced with permission from reference[54]. Copyright 2018 Royal Society of Chemistry.

Since PEA_2SnBr_4 and PEA_2PbI_4 are both organic-inorganic metal halide perovskites, it may be possible to adapt the method used for synthesis of PEA_2PbI_4 nanosheets to create two-dimensional PEA_2SnBr_4. Romani et al.[55] claimed that they have successfully synthesised two-dimensional PEA_2SnBr_4, but lack clear proof, albeit this system exhibited enhanced catalytic performance.

Incorporating different materials and forming heterojunctions in the photocatalytic system have several benefits. Forming heterojunctions impedes charge recombination, which contributes to more effective charge transfer during the photocatalytic reaction[56]. There are additional benefits in using heterojunctions: they allow a broader absorption of wavelengths; they can act as charge acceptors or donors in the reaction process; the overall surface area can be increased, so more active sites are available for reactions[56]. In addition, PEA_2SnBr_4 has a CB of -1.7 eV and VB of 1.0 eV[55]. Since its VB is inadequate for OER (1.23 eV)[57], as explained in Section 1.1, a heterojunction must be formed to achieve overall water splitting. The project in Chapter 5 further investigated the properties and photocatalytic performance of PEA_2SnBr_4.

1.3.3. $Cs_2AgBiBr_6$ as a photocatalyst

Alternatively, the 2+ ions in the perovskite structure can be replaced by 1+ and 3+ ions arranged in an alternate fashion. $Cs_2AgBiBr_6$ (CABB) is a promising type of lead-free double halide perovskite based on this arrangement, mainly because of its suitable bandgap for photocatalytic reactions, ambient stability, long carrier lifetimes, small carrier effective masses and resistance to heat[58–60]. CABB has a bandgap of around 1.95 eV, but it is indirect[61]. Theoretically, it is structurally stable, with a tolerance factor, t = 0.89, that falls within the acceptable range[62]. CABB has been reported to be useful in multiple applications, such as photodetectors, solar cells and photocatalysts[63]. Figure 1.5 (a) illustrates the structure of CABB, and Figure 1.5 (b) shows the band structure of CABB from calculations. The synthesis, applications and methods to improve photoreaction activity for CABB are further discussed in Chapter 2.

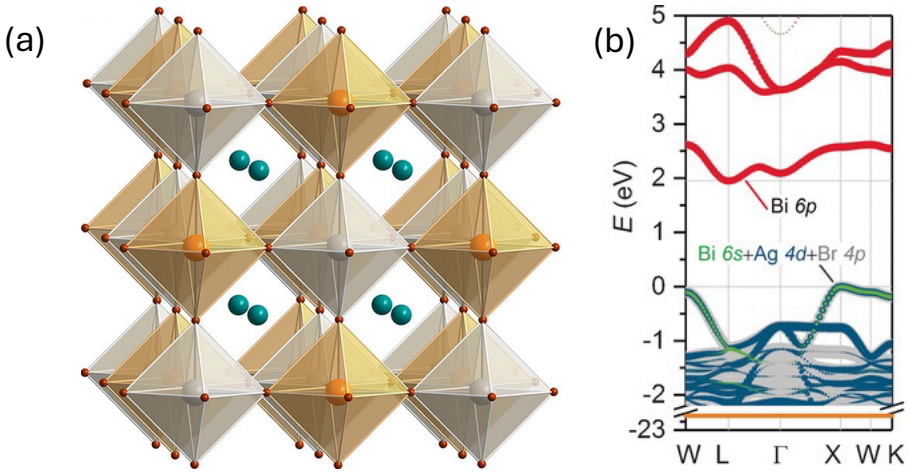

Figure 1.5. (a) Illustrative structure of CABB. The green spheres represent Cs, red spheres represent Br, silver spheres represent Ag, and orange spheres represent Bi. Reproduced with permission from reference[64]. Copyright 2016 American Chemical Society. (b) Calculated band structure of CABB. Reproduced with permission from reference[65]. Copyright 2017 Wiley-VCH.

1.4. Aim and objectives

The aim of this thesis is to assess the structures and performance of two lead-free halide perovskites, $Cs_2AgBiBr_6$ and PEA_2SnBr_4, in photocatalytic hydrogen generation reactions. The objectives of this thesis are (i) to design experiments that can run photocatalytic reactions and analyse the products; (ii) to find out approaches that can improve the activity of the catalysts; (iii) to use electron microscopes which probe the structure before and after reaction, to find out how the structure is related to the performance; (iv) to investigate the photoreaction mechanism.

In this thesis, Chapter 2 provides a literature review of reports related to the lead-free double halide perovskite, $Cs_2AgBiBr_6$ (CABB), the main material studied in this research. This literature review encompasses its various synthesis methods and applications as a photocatalyst, as well as strategies to improve its activity and stability in photocatalytic reactions. Non-halide perovskite photocatalysts are also briefly addressed for insights into some of the best performing catalysts. Chapter 3 covers all the methodology and practical steps in the experiments carried out. This chapter includes the synthesis methods used, the photocatalytic tests, and descriptions of the characterisation techniques. Chapter 4 reports the synthesis, photocatalytic tests and characterisation of CABB. Three different forms of CABB were synthesised, tested and characterised: bulk, nanocubes and nanosheets. The photoreaction studied in this chapter is methanol photo-oxidation to hydrogen and formaldehyde, using CABB as the photocatalyst. Finally, Chapter 5 investigates the performance PEA_2SnBr_4 (PSB), as well as CABB, in photocatalytic water splitting. To increase the reaction rate, the reaction systems involving the catalysts were added with different sacrificial agents and co-catalysts. Their structural degradations were also studied using techniques including electron microscopy (EM).

Chapter 2 Background on $Cs_2AgBiBr_6$

Contents

2.1. Introduction 15
2.2. Morphology and synthesis of CABB 16
2.2.1. HBr mixing and heating for bulk CABB 16
2.2.2. Dissolution and precipitating methods 17
2.2.3. Hot injection methods 19
2.2.4. Microwave-assisted solvothermal methods 22
2.3. Using CABB as a photocatalyst 23
2.3.1. Hydrogen generation 23
2.3.2. CO_2 reduction 26
2.3.3. Dye degradation 31
2.3.4. Other applications 33
2.4. Strategies to improve activity 36
2.4.1. Washing and surface ligand control 36
2.4.2. Heterojunctions 38
2.4.3. Elemental doping/substitution 44
2.4.4. Introducing defects into the structure 44
2.4.5. Adjusting light intensity 47
2.5. Methods to improve stability 48
2.5.1. Dynamic equilibrium 48
2.5.2. Attachment to the surface of larger structures 48
2.5.3. Deposition within porous materials 50
2.6. Research progress of other photocatalysts 52
2.6.1. Hydrogen generation 53
2.6.2. CO_2 reduction 53
2.6.3. Pollutant degradation 54
2.7. Evaluating output via turnover frequency 54
2.8. Conclusions 55

2.1. Introduction

The concept of hydrogen economy was proposed in 1972 and has been developing since[66]. Hydrogen has a specific energy of 33.31 kW h kg^{-1}, which is better than petrol (12.89 kW h kg^{-1}) and lithium-ion batteries (around 0.2 kW h kg^{-1})[67]. Hydrogen can potentially replace all types of fuel, such as petrol that powers a vehicle. Environmental evaluations show that energy systems based on hydrogen are likely to release less greenhouse gas than energy systems based on fossil fuels[68]. However, approximately 96% of hydrogen produced come from natural gas and coal[69], showing a huge potential for hydrogen generated from sustainable routes.

Electrocatalysis of water for hydrogen production is an established sustainable method, especially when electricity from renewable sources is used[70]. Though the electricity can be generated from renewable solar power, a lot of energy is lost in this two-step conversion, from solar energy to electricity and then from electricity to hydrogen. It could be more efficient if the energy from light can be directly used in hydrogen production. This thesis hence focusses on photocatalysis that harvest energy from light to initiate the hydrogen generation reaction.

$Cs_2AgBiBr_6$ is a versatile catalyst that can be used in photocatalytic hydrogen generation as well as other fields. Several review articles have discussed various aspects of CABB, especially its uses in photovoltaics[61,63]. This chapter discusses published reports on CABB as used in photocatalysis. The contents include synthesis methods and consequent product morphology, different types of applicable photocatalytic reactions, and methods to improve reaction rate and stability. Some non-halide perovskite photocatalysts are also discussed to compare how CABB perform against some of the best in the field.

2.2. Morphology and synthesis of CABB

There are multiple methods reported for the synthesis of CABB, and the product is formed of various shapes and sizes. As examples, Slavney et al.[64] synthesised CABB red single crystals a few millimetres in size, McClure et al.[71] prepared polycrystalline CABB as an orange powder, Wu et al.[72] produced CABB films for solar cells, and Creutz et al.[73] synthesised CABB nanocubes around 10 nm in size. The sizes and synthesis methods of CABB photocatalyst are discussed in this section.

2.2.1. HBr mixing and heating for bulk CABB

A method based on HBr mixing and 110 °C heating method is the most used, as it was one of the earliest reported[64]. This is a simple and straightforward process, which involves mixing CsBr, AgBr and $BiBr_3$ in a molar ratio of 2:1:1 in HBr, followed by heating at 110 °C for two hours. Larger single crystals can be obtained by controlling the cooling rate at the end of heating[64], but for catalysis a powder product is adequate, so cooling naturally is satisfactory. Sample particles synthesised this way are typically around 3 μm in size, and Figure 2.1 shows an image of CABB particles obtained from a scanning electron microscope (SEM). This method is referred to as 'HBr method' and sample synthesised this way is referred to as 'CABB-HBr' for the remainder of this thesis.

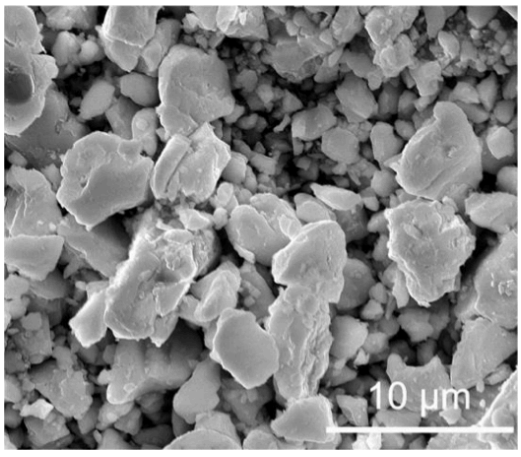

Figure 2.1. SEM image of CABB-HBr. Reproduced with permission from reference[74]. Copyright 2020 Wiley-VCH.

2.2.2. Dissolution and precipitating methods

2.2.2.1. DMSO method for bulk and nano CABB

A second method to synthesise CABB involves dissolving precursor materials such as CsBr, AgBr and $BiBr_3$ in dimethyl sulfoxide (DMSO), and then precipitating in isopropanol. Since the chemicals are dissolved in DMSO, the solution is often used for spray coating to create a thin film[75,76]. Bulk and nano sample powders can also be obtained this way, and in previous reports the nano form was used more[77]. This simple synthesis process does not require heating, and the nanoparticles formed are generally spherical as displayed in Figure 2.2. This process is referred to as 'DMSO method' for the remainder of this thesis.

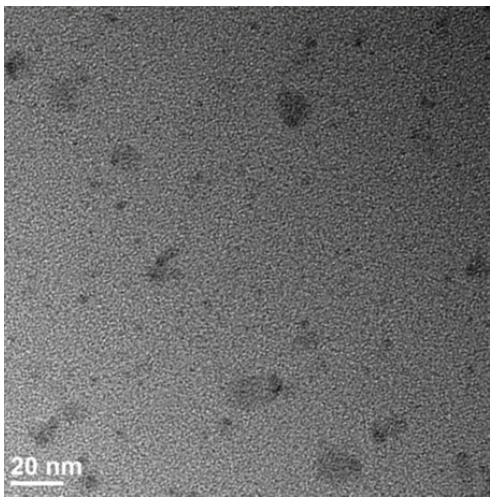

Figure 2.2. TEM image of CABB nanoparticles obtained from the DMSO method. Reproduced with permission from reference[77]. Copyright 2023 Wiley-VCH.

2.2.2.2. Other options for solvents and anti-solvents

There have been alternative options of solvents and anti-solvents (liquids that reduce the solubility of the solute) reported. Chen et al.[78] dissolved halide salts in ethanol and poured the mixture into a vessel containing DMF and n-octylamine, followed by precipitation. This process yields CABB in thin slices as shown in Figure 2.3 (a). Sena et al.[79] synthesised CABB samples using a ligand assisted reprecipitation (LARP) method, where the halide salts were dissolved in DMF with 10 vol% oleic acid, while heating at 80 °C. After the mixture was cooled down, the solution was poured into ethyl acetate for precipitation. In this process

the oleic acid ligands restrict the size of CABB particles[79]. TEM images of CABB particles synthesised using this technique are shown in Figure 2.3 (b).

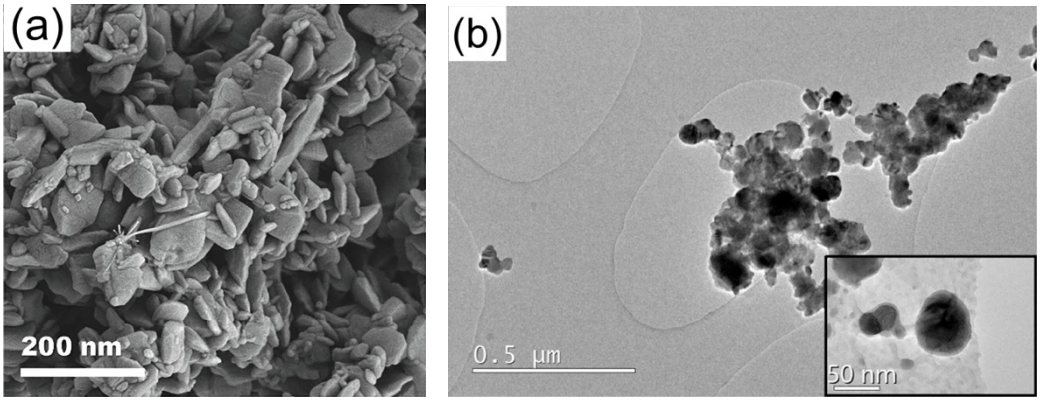

Figure 2.3. (a) SEM image of thin-slice CABB. Reproduced with permission from reference[78]. Copyright 2022 Elsevier B.V. (b) TEM images of CABB synthesised using the LARP method. Reproduced under a Creative Commons licence from reference[79]. Copyright 2023 American Chemical Society.

There are also reports synthesising CABB using the HBr method first, followed by dissolving the CABB in DMSO and reprecipitating in dichloromethane (DCM), in order to moderate particle size[80,81]. Using this process, the size of the CABB particles was reduced to around 100 nm, as shown in Figure 2.4.

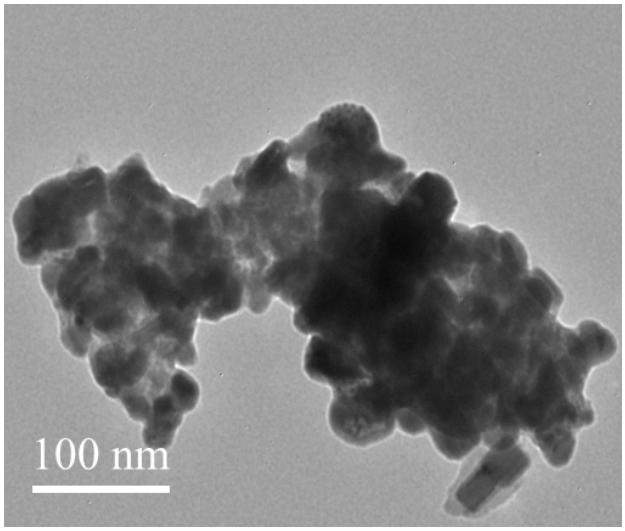

Figure 2.4. TEM image of CABB particles with a reduced size. Reproduced with permission from reference[81]. Copyright 2022 Elsevier B.V.

2.2.3. Hot injection methods

The hot injection methods were used in the synthesis of halide perovskites such as $CH_3NH_3PbBr_3$ and $CsPbBr_3$ before CABB[82,83]. The methods were adapted for CABB to produce nanocubes (CABB-NC) and nanosheets (CABB-NS). Two similar approaches for the synthesis of CABB nanocubes were reported at around the same time, with one method requiring separate preparation of Cs-oleate[84], while the other method, one-pot process, needing the injection of trimethylsilyl bromide (TMSBr)[73]. These two processes are discussed in detail below.

2.2.3.1. Cs-oleate hot injection for CABB nanocubes

This synthesis process is summarised in Figure 2.5 (a). Cs-oleate is first prepared by dissolving Cs_2CO_3 in heated octadecene and oleic acid under a N_2 or Ar atmosphere. This solution is denoted as solution A. Separately, $BiBr_3$ and AgBr (or $AgNO_3$) were mixed and heated in a flask with octadecene, oleic acid and oleylamine under a N_2 or Ar atmosphere. Zhou et al.[84] noted that for this step, addition of HBr was important to prevent an AgBr impurity from developing. However, CABB products from other experiments that excluded HBr did not show obvious AgBr impurities[85,86]. Subsequently, a small portion of solution A was injected into the flask containing Bi^{3+} and Ag^{+}, and the flask was then cooled in a water bath. To collect the sample, washing and centrifuging is required. Nanocubes synthesised using this method are around 10 nm in size, as shown in Figure 2.5 (b). The size distribution of the nanocubes can be tuned by adjusting the ratio of oleic acid to oleylamine[85]. This method is referred to as ‘Cs-oleate hot injection’ method for the remainder of this thesis.

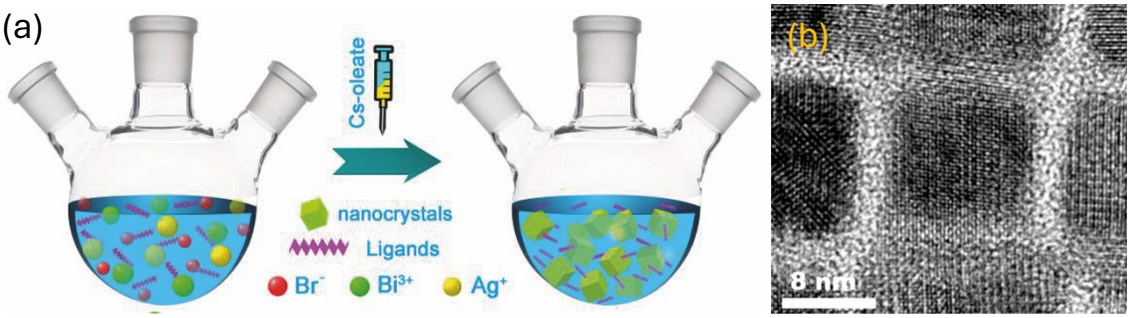

Figure 2.5. (a) Illustration showing the synthesis process of CABB nanocubes. Reproduced with permission from reference[84]. Copyright 2018 Wiley-VCH. (b) TEM image of the CABB nanocubes. Reproduced with permission from reference[86]. Copyright 2018 American Chemical Society.

2.2.3.2. TMSBr hot injection for CABB nanocubes

This is a one-pot synthesis method which also produces CABB nanocubes[73]. In summary, caesium acetate, silver acetate and bismuth acetate are dissolved in octadecene, oleic acid and oleylamine. This mixture is then heated in vacuum at 110 °C, before increasing the temperature to 140 °C, and injecting TMSBr. The mixture is then rapidly cooled by plunging into a water bath, followed by washing and centrifuging. Figure 2.6 (a) shows a TEM image of the nanocubes produced from this method, and Figure 2.6 (b) presents the size distribution of the nanocubes. This method is referred to as 'TMSBr hot injection method' for the remainder of this thesis.

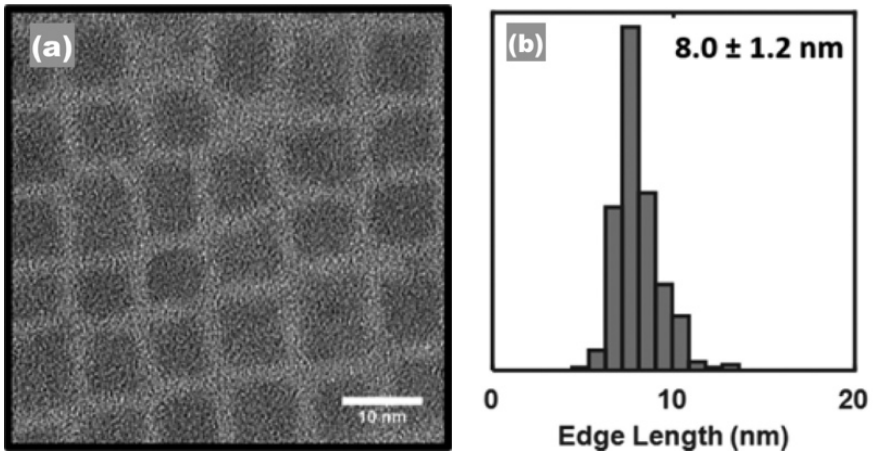

Figure 2.6. (a) TEM image of CABB nanocubes synthesised using the TMSBr method. (b) Particle size distribution of the CABB nanocubes. Reproduced with permission from reference[73]. Copyright 2018 American Chemical Society.

2.2.3.3. Cs-oleate hot injection for CABB nanosheets

This method is similar to the Cs-oleate hot injection method for nanocubes, with a few modifications. As shown in Figure 2.7, Liu et al.[87] prepared Cs-oleate as previously described in Section 2.2.3.1. In a separate flask, $BiBr_3$, $AgNO_3$, octadecene, HBr, oleic acid and oleylamine were mixed and heated to 120 °C under vacuum. This was further heated to 200 °C under nitrogen flow and held for 10 minutes, before being cooled naturally to room temperature, when a portion of room-temperature Cs-oleate solution was injected into the flask. The mixture was then stirred at room temperature for 10 minutes, before raising the temperature to 230 °C. Finally, the mixture was plunged into a water bath, washed and centrifuged. This method is referred to as 'Cs-oleate hot injection for nanosheets' method for the remainder of this thesis.

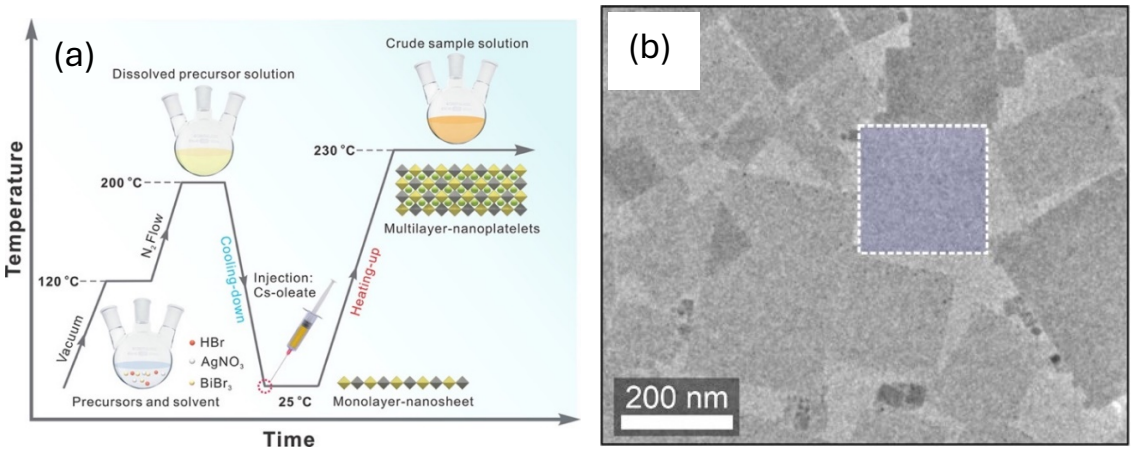

Figure 2.7. (a) Diagram outlining the synthesis process of CABB monolayer nanosheets and few-layer nanosheets. (b) TEM image of the platelets produced. Reproduced with permission from reference[87]. Copyright 2021 American Chemical Society.

Huang et al.[88] proposed a similar method to produce CABB nanosheets, and morphology control from nanosheets to nanocubes was also achieved. To synthesise nanosheets, Cs-oleate was prepared first. Subsequently, AgBr, $BiBr_3$, oleic acid, oleylamine, octanoic acid, octylamine and octadecene were mixed and heated to 100 °C under vacuum. The

temperature was then raised to 150 °C under nitrogen, where 1 mL Cs-oleate was injected. After five minutes, the flask was cooled in a water bath, and the contents were washed and centrifuged. The authors found that changing the amount of AgBr and $BiBr_3$ led to a change in morphology of the product. Specifically, 0.03 mmol AgBr and 0.06 mmol $BiBr_3$ led to formation of nanocubes; 0.04 mmol AgBr and 0.08 mmol $BiBr_3$ yielded a mixture of nanocubes and nanosheets; 0.06 mmol AgBr and 0.12 mmol $BiBr_3$ produced nanosheets.

2.2.4. Microwave-assisted solvothermal methods

In addition to the common approaches to synthesise CABB as previously described, Low et al.[89] proposed a rapid microwave-assisted solvothermal method. In this approach CsBr, AgBr and $BiBr_3$ were mixed with isopropanol, followed by addition of HBr, oleic acid and oleylamine. The vial was then put into a microwave for 2 minutes at 160°C under 600 rpm stirring. It was finally washed and centrifuged with ethanol to collect the product. Sample particles made this way had an average size of 72 nm, as shown in Figure 2.8. The sample had a long carrier lifetime of 921 ns. The particle size is larger than the ones synthesised by hot injection, but it takes a short time.

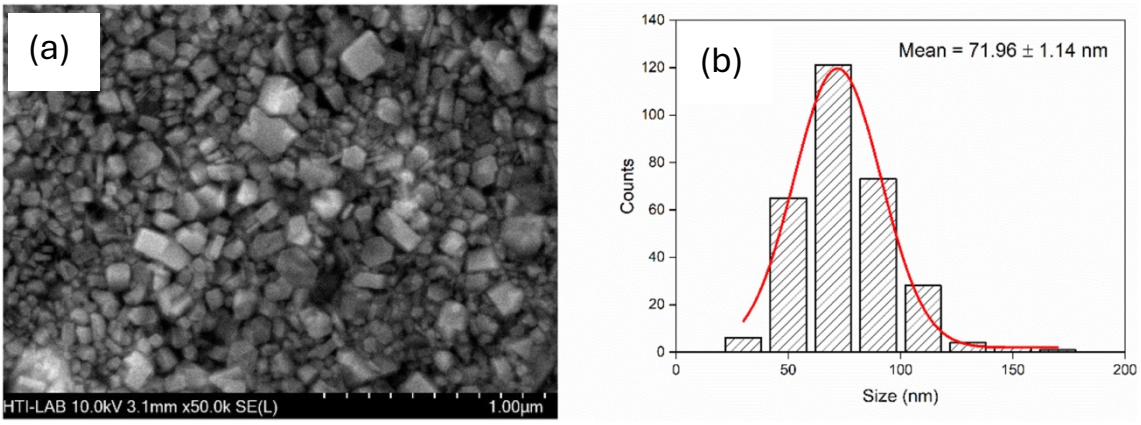

Figure 2.8. (a) SEM image of CABB synthesised via solvothermal method, and (b) size distribution of the CABB particles produced using this method. Reproduced with permission from reference[89]. Copyright 2023 Elsevier Ltd.

2.3. Using CABB as a photocatalyst

CABB is commonly used as a photocatalyst for hydrogen evolution[74], CO_2 reduction[84], dye[58] and organic pollutant degradation[78]. Additional uses, such as NO degradation[90], toluene oxidation[91] and benzyl alcohol oxidation have also been reported[92]. However, most reports implemented some kind of heterojunction or co-catalyst to improve the reaction rate, which is at least several times higher than using CABB alone. This section discusses CABB used for hydrogen generation, CO_2 reduction, dye degradation, as well as other photocatalytic applications.

2.3.1. Hydrogen generation

Like other halide perovskites, CABB is unstable in water, and forms BiOBr as well as other impurities[93]. Its morphology also changes completely. To mitigate this issue, HBr splitting is normally conducted. A dynamic equilibrium could be achieved between CABB and Br^- ions from HBr, where Br^- is continuously being oxidised to Br_3^-, and hydrogen is being generated[94]. To prevent excess Br_3^- from building up, H_3PO_2 is also added along with HBr, so Br_3^- could be reduced to Br^-, keeping the HBr splitting reaction going[95].

As an alternative, Chen et al.[78] managed to immerse CABB in water with 30 vol% methanol for photoreaction, by first depositing CABB flakes onto a Ag_3PO_4 nanoflower. Methanol acts as a sacrificial agent in this case, and a hydrogen evolution rate of 819.2 $\mu mol\ h^{-1}\ g^{-1}$ was achieved. The sacrificial agent captures the excess electrons or holes generated from the photocatalytic reaction, so the electron-hole pair would not recombine and stop the reaction. In this case methanol captured the holes. However, the reaction rate decreased with repeated tests. Table 2.1 lists the reported performance on hydrogen production, using CABB and its heterojunction or co-catalyst.

Table 2.1. Reported CABB performance in hydrogen production, in chronological order.

Notes:

1. The 'Washing solvent(s)' in the third column means the extra liquids used that are not mentioned in the second column. The same applies to Tables 2.2-2.4.
2. In the 'CABB synthesis method' column, some synthesis methods are described as 'Dissolving in…', or 'Mixing and heating in…'. The starting reagents for these methods are CsBr, AgBr and $BiBr_3$ unless specified. The same applies to Tables 2.2-2.4.

Sample	CABB synthesis method	Washing solvent(s)	Reaction conditions	Light used	Best activity ($\mu mol\ h^{-1}\ g^{-1}$)	Stability	Year and reference
0.5 wt% Pt/CABB	HBr method	Methanol during Pt doping	100 mg catalyst, 50 mL saturated HBr/H_3PO_2	300 W Xe lamp with 420 nm filter	54.7	4 cycles, around 11 hours in total	2020[74]
2.5 wt% reduced graphene oxide/CABB	HBr method	/	200 mg catalyst, 20 mL CABB-saturated HBr/H_3PO_2 (volume ratio 5:1)	300 W Xe lamp with 420 nm filter	48.9	12 x 10-hour cycles	2020[80]
0.064% $Mo_3S_{13}^{2-}$/CABB	Mixing and heating in HBr/H_3PO_2 (volume ratio 2:3), followed by Xe lamp irradiation	/	0.5 (unit missing, likely in grams) catalyst, 10 mL CABB-saturated HBr/H_3PO_2 (volume ratio 2:3)	300 W Xe lamp, 420 nm filter	2.47	8 x 10-hour cycles	2021[96]
0.47 wt% Nitrogen-doped carbon/CABB	HBr method	/	10 mg catalyst, 10 mL HBr and 2 mL H_3PO_2	300 W Xe lamp with 420 nm filter, 100 mW cm^{-2}	380	6 x 4-hour cycles	2021[59]
12.5% NiCoP nanoparticles/CABB	Mixing and heating in HBr/H_3PO_2 (volume ratio 5:1)	Isopropanol	100 mg catalyst, 24 mL CABB-saturated HBr/H_3PO_2 solution (volume ratio 5:1)	300 W Xe lamp, 420 nm filter	373.16	4 x 4-hour cycles	2022[95]
10% black phosphorus/CABB	HBr method	/	50 mg catalyst, 10 mL CABB-saturated HBr/H_3PO_2 (volume ratio 5:1)	300 W Xe lamp, 420 nm filter	104.6	7 x 3-hour cycles	2022[94]

20% MoS_2/CABB	HBr method	Ethyl acetate and diethyl ether, three times	20 mg catalyst, 5 mL CABB-saturated HBr containing 17 vol% H_3PO_2	Xe lamp, 300 mW cm^{-2}, 420 nm filter	87.5	500 hours	2022[97]
$CuBr_2$ (6.67 mM Cu ions)/CABB	Mixing and heating in HBr/H_3PO_2 (volume ratio 5:1)	/	200 mg CABB, 6.67 mM Cu ions, 20 mL CABB-saturated HBr/H_3PO_2 (volume ratio 5:1)	300 W Xe lamp, 420 nm filter, about 150 mW cm^{-2}	182	50 hours	2022[98]
CABB/Ag_3PO_4 nanoflower	Dissolving in ethanol and precipitating in DMF with n-octylamine	Ethanol and water	20 mg catalyst in 100 mL water with 30% methanol	300 W Xe lamp with 420 nm filter	819.2	Reduced to 633 at the fifth 6-hour cycle	2022[78]
10% g-C_3N_4/CABB	HBr method	Ethanol	50 mg catalyst, 10 mL saturated HBr comprising 20 vol% H_3PO_2	300 W Xe lamp, 420 nm filter	60	14 x 3-hour cycles	2022[99]
WO_3/enriched Br-vacancies CABB, molar ratio 1:2	Modified HBr method to create Br vacancies	/	10 mg catalyst, 15 mL CABB-saturated HBr/H_3PO_2 (volume ratio 5:1)	300 W Xe lamp with 420 nm filter, 100 mW cm^{-2}	364.89	4 x 4-hour cycles, 10.1% decay	2023[100]
g-C_3N_4(NiCoB)/CABB	HBr method	Ethanol, several times	30 mg catalyst, 10 mL CABB-saturated HBr/ H_3PO_2	300 W Xe lamp with 420 nm filter	89.68	5 x 3-hour cycles	2024[101]
5% g-C_3N_4/CABB-NC	Cs-oleate hot injection	Ethanol and chloroform, repeated twice	30 mg catalyst, 15 mL saturated HBr and 3 mL H_3PO_2	Solar simulator, 1 sun, 100 mW cm^{-2}	268	6 x 1-hour cycles	2024[102]

2.3.2. CO_2 reduction

There are more variations in reaction conditions for CO_2 reduction, compared to hydrogen generation as described in Section 2.3.1. In the reactor for CO_2 photoreduction, ethyl acetate is mainly used, and sometimes with addition of other liquids. The reported results are listed in Table 2.2. Ethyl acetate is commonly used because CABB nanocubes remain stable in mildly polar ethyl acetate for 5 days, and CO_2 is highly soluble in it[103]. CH_4 and CO are the main reduction products[84], but when additional water is added to the system, side products such as H_2 are generated[104]. Water is added in some cases to act as a hole scavenger to increase the reaction rate[104]. To initiate the reaction, as illustrated in Figure 2.9, the conduction band needs to meet the energy requirement, where E (CO_2/CO) is -0.52 V vs NHE, and CABB can meet this demand[105].

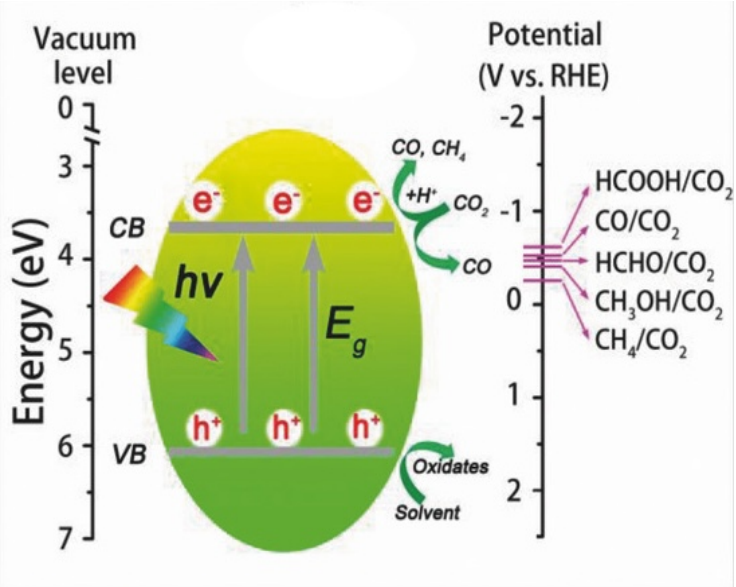

Figure 2.9. Reaction mechanism of photocatalytic CO_2 reduction using CABB, proposed by Zhou et al.[84]. Reproduced with permission. Copyright 2018 Wiley-VCH.

Table 2.2. Reported performance of CABB in CO_2 reduction, in chronological order.

Notes:
1. DMSO = dimethyl sulfoxide, DCM = dichloromethane, rGO = reduced graphene oxide
2. All reactors were filled with CO_2 before light illumination started.

Sample	CABB synthesis method	Washing solvent(s)	Reaction conditions	Light used	Best activity ($\mu mol\ h^{-1}\ g^{-1}$)	Stability	Year and reference
CABB NC	Cs-oleate hot injection	Ethanol and chloroform, repeated twice	15 mg catalyst in 10 mL ethyl acetate	100 W Xe lamp with AM1.5G (a standard solar spectrum) filter	CO: 2.43 CH_4: 1.6	6 hours	2018[84]
CABB-Cu-rGO, about 1 wt% rGO in total, and 5 wt% Cu in Cu-rGO	Ball milling	Isopropanol	50 mg catalyst with 1 mL water slowly injected	300 W Xe lamp with AM1.5G filter, 100 mW cm^{-2}	CO: 1.9 CH_4: 10.7 H_2: 1	3 x 4-hour cycles but activity gradually decreasing	2021[104]
Same as above	Same as above	Same as above	Same as above	300 W Xe lamp with 2 sun intensity	CO: about 6 CH_4: about 12 H_2: about 9	Not mentioned	2021[104]
10% g-C_3N_4/CABB	HBr method, then dissolving in DMSO and precipitating in DCM	/	15 mg catalyst in 4 mL ethyl acetate and 1 mL methanol	Xe lamp with AM1.5G simulated solar light, 150 mW cm^{-2}	CO: around 1.8 CH_4: around 0.2	4 x 3-hour cycles	2021[106]
82% g-C_3N_4/CABB	HBr method, and then dissolving in DMSO and precipitating in DCM	/	15 mg catalyst in 4 mL ethyl acetate and 1 mL methanol	Xe lamp with AM1.5G simulated solar light, 150 mW cm^{-2}	CO: around 0.7 CH_4: around 1.5	Not mentioned	2021[106]
CABB nanoplatelets	Cs-oleate hot injection for nanosheets	Toluene	2 mg catalyst in 10 mL ethyl acetate	405 nm laser diode with 40 mM (as written, could be mW instead) maximum power	CO: about 22 CH_4: about 10	Significant decrease after 1 hour	2021[87]

20% CABB-NC/Ce-UiO-66-H	Cs-oleate hot injection method	/	15 mg catalyst with 50 μL deionised water	300 W Xe lamp	CO: 309.01 CH_4: 0.7	5 x 2-hour cycles	2022[107]
CABB/Sr_2FeNbO_6 (mass ratio 1:2	HBr method, then dissolving in DMSO and precipitating in DCM	Isopropanol	5 mg catalyst in 4.9 mL ethyl acetate and 0.1 mL water	300 W Xe lamp with 420 nm filter at 100 mW cm^{-2}	CO: 50 CH_4: 8.12	4 x 5-hour cycles	2022[81]
8.47% CABB/mesoporous titania framework	Dissolving in DMF and precipitating in isopropanol	/	20 mg catalyst in 30 mL isopropanol	300 W Xe lamp, 70 mW cm^{-2}	CO: 4.2 CH_4: 32.9	5 x 7-hour cycles	2022[108]
CABB/1 wt% bismuthene	LARP method	Ethyl acetate	7 mg catalyst in 35 mL methanol	300 W Xe lamp with AM1.5G filter, 100 mW cm^{-2}	CO: 0.67 CH_4: 1.49 H_2: 0.75	2 x 2-hour cycles. Reduced activity in second run	2022[79]
CABB-NC/$Ti_3C_2T_x$ nanosheets (mass ratio roughly 10:3)	Cs-oleate hot injection	Toluene and ethyl acetate, with small amount of DMF	5 mg catalyst and 20 μL water	150 W Xe lamp with AM1.5G filter, 150 mW cm^{-2}	CO: 11.1 CH_4: 1.3 H_2: 8.9	3 x 5-hour cycles	2022[109]
CABB/amorphous TiO_2 (core-shell)	Dissolving in DMSO and precipitating in isopropanol	/	5 mg catalyst in 10 mL ethyl acetate	450 W Xe lamp at 150 mW cm^{-2}	CO: 5.72 CH_4: 8.46	4 x 4-hour cycles. 9.6% loss in activity	2022[110]
CABB-NS/CTF-1 (covalent triazine framework), mass ratio 9:1	Cs-oleate hot injection for nanosheets	Ethyl acetate	15 mg catalyst in 10 mL ethyl acetate	300 W Xe lamp, 420 nm filter	CO: 30.7 CH_4: 8.6	4 x 4-hour cycles	2022[111]

CABB-NC/Bi_2WO_6 (mass ratio 1:2)	Cs-oleate hot injection	Ethyl acetate	10 mg catalyst in 2 mL ethyl acetate and 0.2 mL isopropanol	300 W Xe lamp with 420 nm filter	CO: 1.9 CH_4: 0.4	3 x 8-hour cycles	2022[105]
CABB-NC@SiO_2 (core-shell)	TMSBr hot injection synthesis	Toluene and methyl acetate	15 mg catalyst with 15 mg 2,2'-bipyridine, 2 μmol of $CoCl_2$, 1.2 mL TEOA, 1.8 mL H_2O and 3.2 mL acetonitrile	300 W Xe lamp with 420 nm filter	CO: 271.76 H_2: 17.93	3 x 5-hour cycles	2023[112]
30 wt% CABB/MCM-48 (a type of molecular sieve)	Dissolving in DMSO and precipitating in isopropanol	/	20 mg catalyst in 10 mL ethyl acetate	300 W Xe lamp with 420 nm filter, 100 mW cm^{-2}	CO: around 30 CH_4: around 5	5 x 4-hour cycles	2023[77]
CABB-NS/Ni-MOF NS (mass ratio 4:6)	Cs-oleate hot injection for nanosheets	Ethyl acetate	15 mg catalyst in 10 mL ethyl acetate	300 W Xe lamp	CO: 58.85 CH_4: 15.43	8 cycles of unspecified time frame	2023[113]
CABB/1 wt% g-C_3N_4	Grinding CsBr, AgBr and $BiBr_3$, then annealing at 260 °C	/	5 mg catalyst in 5 mL isopropanol	250 W Hg vapour lamp	CO: 12.14 CH_4: 8.85	4 x 9-hour cycles. Decrease in activity over each cycle	2023[114]
CABB/MIL-101(Fe)	HBr method, then dissolving in DMSO and precipitating in isopropanol	DMF and ethanol	3 mg catalyst in 4 mL acetonitrile, 2 mL methanol and 100 μL water	300 W Xe lamp	HCOOH: 1375 HCHO: 30	4-hour reaction. Repeated experiments not mentioned	2023[115]

g-C_3N_4@CABB (mass ratio 0.84:1)	Dissolving in DMF and DMSO, then precipitating in toluene	/	Amount of catalyst not mentioned. 99 mL ethyl acetate, 1 mL water, with 10 % volume triethylamine	300 W Xe lamp with 420 nm filter, 80 mW cm^{-2}	CO: 10.3 CH_4: 0.88	Not mentioned	2023[116]
Same as above	Same as above	/	Same as above	365 nm irradiation	CO: 35.71 CH_4: 10.12	Activity decreasing over time	2023[116]
CABB-NC/Bi_2WO_6-NS (mass ratio 1:3)	Cs-oleate hot injection	Ethyl acetate	10 mg catalyst in 98 mL ethyl acetate and 2 mL isopropanol	300 W Xe lamp with AM1.5G filter, 100 mW cm^{-2}	CO: 42.19 CH_4: 0.41	6 x 6-hour cycles. Activity decreasing over time	2023[117]
20% CABB-NC/UiO-66	Cs-oleate hot injection	Hexane	20 mg catalyst in 99 mL ethyl acetate and 1 mL water, with 10% triethylamine	300 W Xe lamp, 420 nm filter, 230 mW cm^{-2}	CO: 13.04 CH_4: 0.12 C_2H_6: 1.27	7 hours	2024[118]
10% CABB-NC/Bi-O vacancy pair Bi_2WO_6	Cs-oleate hot injection	Chloroform, then carbon tetrachloride	30 mg catalyst in 50 mL DI water with 50 μL acetonitrile	300 W Xe lamp with 420 nm filter, 150 mW cm^{-2}	CO: 48.5 CH_4: 7.2 O_2: 23.6	25 hours	2024[119]
Cobalt phthalocyanine tetracarboxylic acid (CoTCPc)@CABB-NS (mass ratio 1:10)	Cs-oleate hot injection for nanosheets	Ethanol	2 mg catalyst with 100 μL H_2O	300 W Xe lamp with 400 nm filter at 100 mW cm^{-2}	CO: 150 O_2: 77	4 x 12-hour cycles	2024[120]

1.46% Rb doped CABB microsphere	Dissolving in DMSO and precipitating in isopropanol	Ethanol	5 mg catalyst with 100 μL DI water	300 W Xe lamp at 150 mW cm^{-2}	CO: 12.7 CH_4: 2.9	5 x 5-hour cycles	2024[121]
CABB/$BiVO_4$, mass ratio 1:2	Modified HBr method with $Bi(NO)_3 \cdot 5H_2O$ replacing $BiBr_3$	Ethanol	5 mg catalyst in 30 mL ethyl acetate with 100 μL DI water	300 W Xe lamp with AM 1.5 G filter	CO: 143.59 CH_4: 8.13	3 x 3-hour cycles	2025[122]

2.3.3. Dye degradation

CABB was also found to be capable of decomposing organic dyes such as Rhodamine B (RhB), Rhodamine 110 (Rh110), methyl orange (MO) and methyl red (MR)[58]. This photocatalytic reaction is generally carried out with the catalyst immersed in ethanol with dye. Ethanol is chosen because CABB in ethanol remains stable during the dye degradation process, and ethanol photo-oxidation byproducts are only present in trace amounts[58].

In degradation studies, a factor called the k value is often calculated to evaluate the activity of the catalyst. The higher the k value is, the higher the photocatalytic performance. This k value is calculated as:

$$\ln\left(\frac{C_t}{C_0}\right) = -kt \tag{2.1}$$

where C_0 is the concentration of the dye just before light irradiation, C_t is the concentration of the dye at the end of the reaction, t is the time taken for photocatalytic dye degradation, and k is the rate constant of this pseudo-first order reaction[93]. Table 2.3 summarises the reported photocatalytic performance of CABB in dye degradation.

Table 2.3. Reported performance of CABB in dye degradation, in chronological order.

Sample	CABB synthesis method	Washing solvent(s)	Reaction conditions	Light used	Best activity (k value in minute^{-1})	Stability	Year and reference
Pt or Au doped CABB NC	HBr method	Ethanol during doping	RhB, Rh110, MR and MO, tested separately. 20 mg catalyst in 10 mL ethanol with dye at 100 mg L^{-1}	Xe lamp, 100 mW cm^{-2}, 420 nm filter	Almost complete RhB degradation within 50 minutes using Pt-CABB. Other dyes took longer	5 x 60 minutes	2019[58]
Water-soaked nano-CABB	Dissolving in DMSO and precipitating in isopropanol with oleic acid	/	Water and ethanol mixture, volume ratio 1:1, with RhB at 10 mg L^{-1}	300 W Xe lamp with 420 nm filter. Ultraviolet light tested separately	Visible light k value: 0.1099, almost complete degradation after 50 minutes. Ultraviolet light k value: 0.1543, almost complete degradation after 40 minutes.	5 x 40-minute cycles. 5% dip at the end	2022[93]
40% CABB-NC/TiO_2	Dissolving in DMSO and precipitating in isopropanol with oleic acid	Ethanol	RhB 10 mg L^{-1}. Catalyst weight and solvent type not mentioned	Xe lamp, 20 mW cm^{-2}, 420 nm filter	98.6% degradation after 40 minutes. k value: 0.1369	5 x 40 minutes	2023[123]
Cationic polyurethane/SiO2/CABB/TiO_2 coating	Dissolving in DMSO and precipitating in isopropanol	/	RhB removal on leather surface.	Visible light	Almost complete degradation within 1 hour	10 cycles. Also survived water spraying and wear tests	2023[75]
CABB-NC/$Ti_3C_2T_x$ nanosheet	TMSBr hot injection	Toluene	20 mg catalyst in 30 mL ethanol with RhB at 30 mg / L	300 W Xe light	Almost complete degradation within 40 minutes. k value: 0.131	3 x 40-minute cycles. Some AgBr formed at the end	2023[124]

WO_3/CABB	Mixing and heating in HBr and water mixture, using $Bi(NO_3)_3 \cdot 5H_2O$ instead of $BiBr_3$	Ethanol	20 mg catalyst in 50 mL ethanol with 20 mg / L dye (MO, RhB or MB)	Visible light	MO: 93.64% within 30 minutes, k value 0.0891 RhB: 100% within 25 minutes, k value 0.1639 MB: 84.65% in 80 minutes, k value 0.0265	5 x 30-minute cycles for MO degradation	2023[125]
20% CABB-NC/UiO-66	Cs-oleate hot injection	Hexane	20 mg catalyst in 50 mL RhB aqueous solution at 20 mg mL^{-1}	75 mW cm^{-2} light	Almost complete degradation after 1 hour, k value: 0.0746	4 x 1.5-hour cycles, 70% efficiency at the end	2024[118]
CABB/BiOBr	Dissolving in DMSO and precipitating in isopropanol	Ethanol	5 mg catalyst in 30 mL RhB ethanol solution at 70 mg L^{-1}	300 W Xe lamp with 420 nm filter	98% removal after 40 minutes	90% performance after five consecutive cycles	2024[126]
CABB-NC	TMSBr hot injection involving the use of octane	Not specified	RhB and MO. 20 mg catalyst in 100 mL ethanol, dye at 20 mg L^{-1}	300 W Xe lamp with 420 nm filter	RhB: 97% in 10 minutes, k value 0.3473 MO: 90% in 30 minutes, k value 0.08659	Not mentioned	2025[127]

2.3.4. Other applications

Other applications briefly described in this section include tetracycline hydrochloride (TC-HCl) degradation, 2-mercaptobenzothiazole (MBT) degradation, NO degradation, toluene oxidation, benzyl alcohol oxidation, as well as ofloxacin and meloxicam antibiotics degradation. The reported results are listed in Table 2.4. Some of these reactions are similar to dye degradation and from which a k value (in $minute^{-1}$) can also be calculated.

Table 2.4. Reported performance of CABB in other applications, in chronological order.

Note: EDTA is ethylenediaminetetraacetic acid disodium salt.

Sample	CABB synthesis method	Washing solvent(s)	Reaction type and conditions	Light used	Best activity (μmol h^{-1} g^{-1} unless specified)	Stability	Year and reference
CABB-NC	Cs-oleate hot injection	Ethanol and chloroform, repeated twice	NO degradation. Dried dispersed 200 mg catalyst in reactor with NO at 500 ppb	150 W tungsten lamp, 420 nm filter	97% NO removal within 30 minutes	4 x 30 minutes	2021[90]
8.47% CABB/mesoporous titania framework	Dissolving in DMSO and precipitating in isopropanol	/	MBT degradation. 10 mg catalyst in 50 mL isopropanol with 10 ppm MBT.	300 W Xe lamp with 420 nm filter	95.5% degradation within 14 minutes, k value 0.0756	5 cycles	2022[108]
CABB/Ag_3PO_4 nanoflower	Dissolving in ethanol and precipitating in DMF with n-octylamine	Ethanol and water	TC-HCl degradation. 20 mg catalyst in 100 mL water with TC-HCl at 20 mg / L.	300 W Xe lamp with 420 nm filter	92.43% degraded within 60 minutes. k value 0.0931	Slightly reduced to 89.3% at the fifth cycle	2022[78]
CABB-NC/black TiO_2 sphere (mass ratio 1:19)	TMSBr hot injection	Hexane	Benzyl alcohol to benzaldehyde. 10 mg catalyst in 5 mL of cyclohexane and 0.1 mmol benzyl alcohol solution, N_2 atmosphere	300 W Xe lamp with AM1.5 G filter	75% conversion and 99% selectivity over 8 hours	3 x 8-hour cycles	2023[92]
20 wt% Sb-substituted CABB/g-C_3N_4 (molar ratio of Sb:Bi = 0.125)	Hydrothermal method	Ethanol	Toluene oxidation. 10 mg catalyst in 2 mL acetonitrile with 70 μL toluene. O_2 atmosphere	500 W Hg (Xe) lamp with 420 nm filter	Benzaldehyde: 1088, selectivity 96%	3 x 4-hour cycles	2023[91]

CABB/ultrathin carbon nitride sheet (mass ratio 16:3)	HBr method, then dissolving in DMSO and precipitating in isopropanol	Isopropanol and ethanol	Toluene oxidation. 10 mg catalyst in 5 mL toluene and 100 mL Na_2SO_4	300 W Xe lamp at 300 mW cm^{-2}	Benzaldehyde: 2260 Benzyl alcohol: 370	5 x 2-hour cycles, slight decrease at the end	2023[128]
CABB with Cs vacancies	Modified HBr method, using $Bi(NO_3)_3 \cdot 5H_2O$ instead of $BiBr_3$. Water and EDTA also added	Ethanol	TC-HCl degradation. 20 mg catalyst in 80 mL ethanol solution with TC-HCl at 50 mg / L	300 W Xe lamp with 420 nm filter at 100 mW cm^{-2}	81.8% degradation within 90 minutes, k value 0.01598	4 x 2-hour cycles. Significant change in structure and decrease in activity from 3rd cycle.	2023[129]
WO_3/CABB	Mixing and heating in HBr and water mixture, using $Bi(NO_3)_3 \cdot 5H_2O$ instead of $BiBr_3$	Ethanol	TC-HCl degradation. 20 mg catalyst in 50 mL ethanol with 20 mg / L TC-HCl	Visible light	63.7% in 80 minutes, k value 0.0139	Not mentioned	2023[125]
CABB-NC	TMSBr hot injection including use of octane	Not specified	TC-HCl degradation. 20 mg catalyst in 100 mL ethanol, TC-HCl at 20 mg L^{-1}	300 W Xe lamp with 420 nm filter	TC-HCl: 60% in 30 minutes, k value 0.03348	9% decrease after 3 x 1-hour cycles	2025[127]
5 wt% oxygen deficient WO_{3-x}/CABB	Dissolving in DMF and precipitating in toluene	/	Toluene oxidation. 5 mg catalyst in 4 mL CH_3CN and 1 mL toluene. Purged with O_2	400-800 nm visible light	Benzaldehyde: 9020 Benzyl alcohol: 1560	6 x 1-hour cycles	2025[130]
30 wt% CABB/W-doped $BiVO_4$	Mixing and heating $BiBr_3$, AgBr and $CsBr_3$ in EDTA, water and HBr.	Ethanol	Ofloxacin (OFX) degradation. 30 mg catalyst in 100 mL OFX solution at 20 mg / L	300 W Xe lamp with 420 nm filter	93.20% degradation efficiency within 40 minutes, k value 0.061	4 x 40-minute cycles	2025[131]

Same as above	Same as above	Same as above	Meloxicam (MEL) degradation. 10 mg catalyst in 100 mL MEL solution at 20 mg / L	Same as above	92.73% degradation efficiency within 40 minutes, k value 0.064	Same as above	2025[131]

2.4. Strategies to improve activity

2.4.1. Washing and surface ligand control

The use of oleic acid and oleylamine, especially in the hot injection route, introduces surface ligands on the surface of the CABB particles. Achieving a balance of the number of ligands can critically affect the performance of CABB as photocatalysts. Xiao et al.[132] noted that when the concentration of surface ligand was at 58.3 mM, their sample achieved the best photocatalytic performance. In general, washing the sample only once gave the best results[132]. Their research was on lead-based $CsPbBr_3$, but the findings could also apply to CABB. They noted that if $CsPbBr_3$ nanocubes were washed with hexane and ethyl acetate more than once, then most of the octadecene, oleic acid and oleylamine that remained on the cubic surfaces were washed away. Excess washing would leave fewer ligands on the surface, and the limited number of ligands would not offer adequate protection from the hostile reaction environment, leading to quicker breakdown of the material. This is undesirable as the samples washed more than once were not as stable in the photocatalytic reaction, and performed worse than those only washed once. Samples washed only once remained stable after 160 hours of reaction, compared to ≤23 hours of stability for samples with multiple washes. The authors argued that even though surface ligands hinder charge transfer during the photocatalytic reaction, their number will decrease during the photocatalytic reaction. In addition, inadequate amounts of the

surface ligands would not offer protection to the perovskite structure, so it is more likely to degrade during photocatalysis. They also observed that the cubes grew larger the more they were washed, and the authors suggested that the surface ligands help to control the cubic size. The cubes with fewer surface ligands were more likely to partially dissolve, fuse and agglomerate, which leads to an increase in average size.

Zhou et al.[84] and Wu et al.[90] removed the ligands from CABB nanocubes using an ethanol and chloroform mixture. The removal of ligands was confirmed using FTIR, where specific peaks can be used as indicators, as shown in Figure 2.10. The band at 1642 cm^{-1} corresponds to asymmetric bending of N-H, the band at 1466 cm^{-1} matches the O-C-O asymmetric stretching mode, and the peaks across the region 2840-2960 cm^{-1} are linked to the symmetric and asymmetric stretching vibrations of CH_2 and CH_3 groups[90]. After washing these peaks became diminished, signifying the removal of ligands. However, even though there were not any notable changes in XRD patterns, the nanocubes aggregated and showed a general increase in size in TEM images. The authors explained that this was because of the dissolution and recrystallisation behaviour of CABB nanocubes[84,90]. Washed nanocubes performed a lot better than as-synthesised materials in both cases, but the stability tests were only conducted for up to six hours[84]. For industrial applications longer testing times are needed.

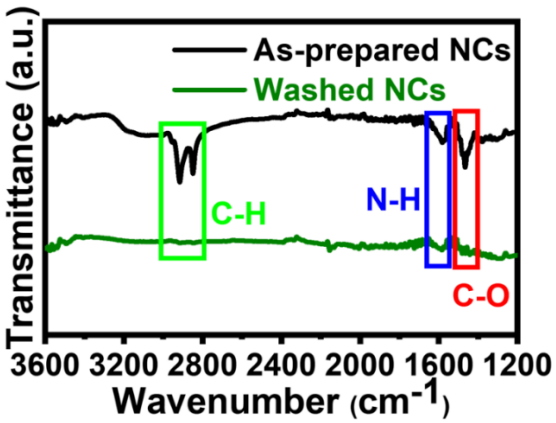

Figure 2.10. FTIR spectrum showing that surface ligands can be washed away. Reproduced with permission from reference[90]. Copyright 2021 Elsevier Inc.

2.4.2. Heterojunctions

Most reports discussed in Section 2.3 adopted some form of heterojunction to boost the catalytic performance of CABB, as well as to improve the stability of the catalyst. A heterojunction is formed between two semiconductors with different band structures. Its main advantage is to minimise unwanted electron-hole recombination, so a lot more of these electron-hole pairs can participate in the photocatalytic reaction[133]. Heterojunctions commonly used include type-I, type-II, Z-scheme and S-scheme. The basic principles and some examples of these heterojunctions are discussed in this section.

2.4.2.1. Type-I heterojunctions

In a type-I heterojunction, the conduction band (CB) of a semiconductor photocatalyst, PC1, is higher than that of the other photocatalyst PC2, while the valence band (VB) of PC1 is lower than that of PC2. Upon illumination, electrons and holes generated at both photocatalysts migrate and accumulate on CB and VB of PC2 for redox reactions, as shown in Figure 2.11.

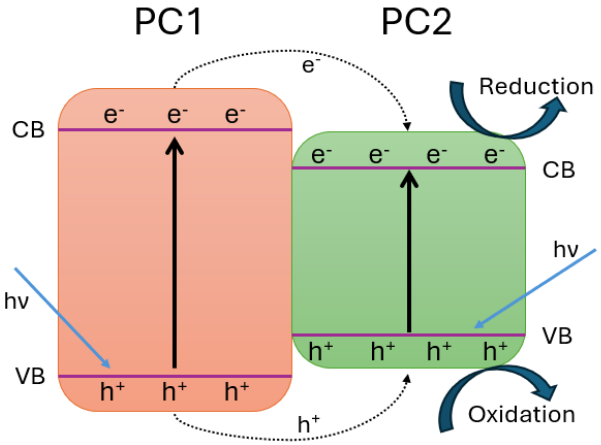

Figure 2.11. Schematic diagram of the working mechanism of a type-I heterojunction in a photoreaction.

Zhang et al.[97] produced a type-I heterojunction by combining CABB and MoS_2. CABB was synthesised using the HBr method, and MoS_2 was synthesised separately. CABB and MoS_2

were then mixed in HBr/H_3PO_2 solution, heated and cooled several times for the dissolution-recrystallisation process. Figure 2.12 (a) shows the XRD data of the heterojunction and its constituents. SEM images in Figure 2.12 (b, c) show that MoS_2 flakes adhered to the surface of bulk CABB. For the photocatalytic hydrogen generation in HBr/H_3PO_2 solution, 20% MoS_2/CABB had the best performance, at 87.5 μmol h^{-1} g^{-1}, compared to CABB at 4.3 μmol h^{-1} g^{-1}, and 9% Pt/CABB at 25.5 μmol h^{-1} g^{-1}. The catalyst remained stable after 500 hours of reaction. Steady-state PL emission spectra in Figure 2.12 (d) revealed that the heterojunction showed a quenched peak, indicating effective charge-carrier separation. Tauc plots and Mott-Schottky plots were also used to determine the bandgaps, and the heterojunction type was found to be type-I. The band structure is depicted in Figure 2.12 (e).

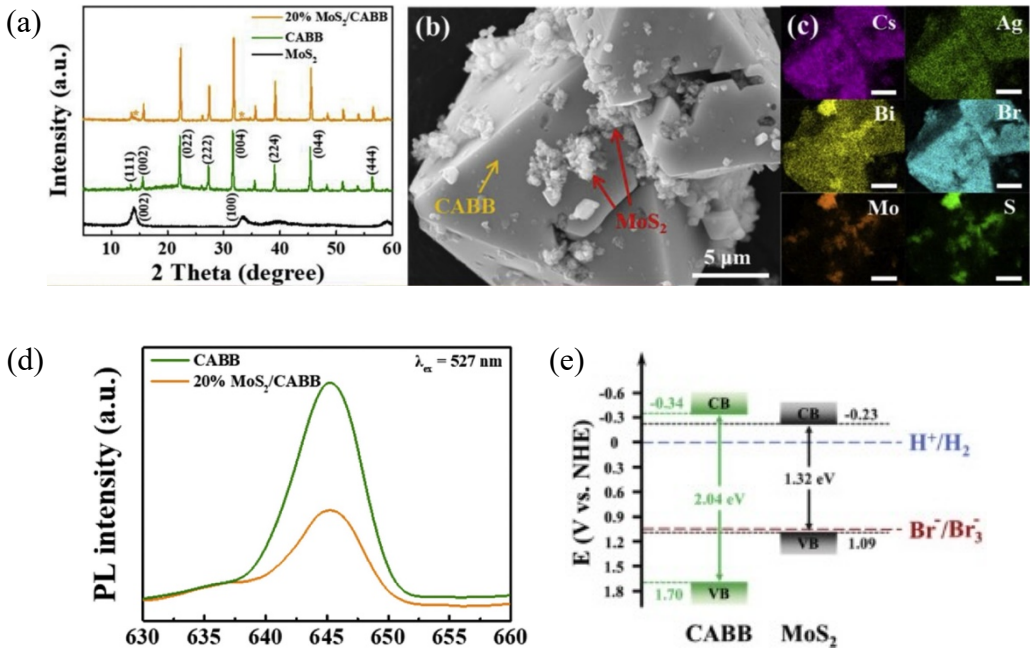

Figure 2.12. (a) XRD data of a MoS_2/CABB heterojunction. (b) SEM image and (c) EDX maps of MoS_2/CABB. Scale bar is 5 μm. (d) PL intensity spectrum of CABB and MoS_2/CABB heterojunction. (e) Bandgap diagram of the MoS_2/CABB heterojunction. Reproduced with permission from reference[97]. Copyright 2022 Hydrogen Energy Publications LLC.

2.4.2.2. Type-II heterojunctions

Considering two photocatalysts PC1 and PC2 again, for a type-II heterojunction, both the CB and VB of PC1 are higher than those of PC2. When exposed to light, both photocatalysts generate electrons and holes. The electrons at CB of PC1 travel to the CB of PC2, while holes at the VB of PC2 migrate to the VB of PC1, as shown in Figure 2.13.

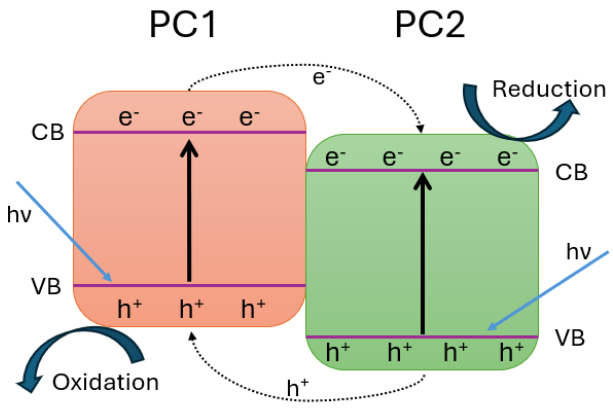

Figure 2.13. Schematic diagram showing how a type-II heterojunction works as a photocatalyst.

Song et al.[94] created a type-II heterojunction using black phosphorous (BP) and CABB. The authors synthesised CABB using the HBr method, and BP was prepared separately. These two materials were combined using a self-assembly method, where CABB and BP were mixed in HBr solution, aided by ultrasonication. As shown in Figure 2.14 (a, b), the shifts in binding energies for Bi 4f and P 2p after BP and CABB were mixed indicated that strong electron coupling exist between these two materials. In the photocatalytic hydrogen generation reaction, 10% BP/CABB yielded the best reaction rate of 104.6 μmol h^{-1} g^{-1} in HBr/H_3PO_2 solution, while CABB alone had a reaction rate of 17.7 μmol h^{-1} g^{-1}, and the activity for BP alone was negligible. The heterojunction was stable after 7 cycles of 3-hour reactions. By calculating the bandgaps of CABB and BP using Tauc plots and valence band spectra, the BP/CABB heterojunction was found to be a type-II heterojunction. Figure 2.14 (c) illustrates the band structure of the heterojunction.

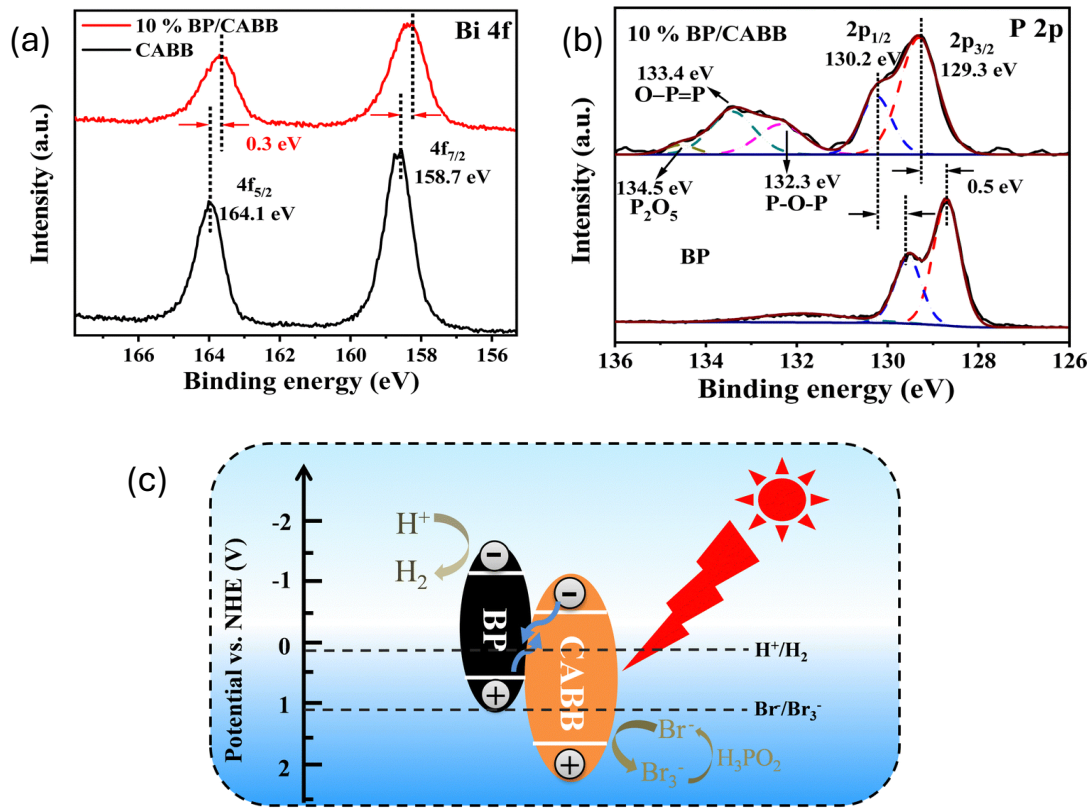

Figure 2.14. (a) X-ray photoelectron spectroscopy (XPS) spectra of Bi 4f from 10% BP/CABB and CABB. (b) XPS spectra of P 2p from 10% BP/CABB and BP. (c) Illustration of how BP and CABB form a type-II heterojunction. Reproduced with permission from reference[94]. Copyright 2022 Royal Society of Chemistry.

2.4.2.3. S-scheme and Z-scheme heterojunctions

The working mechanism of an S-scheme heterojunction in photocatalysis is explained in Figure 2.15. For two photocatalysts; a reduction photocatalyst (RP) and an oxidation photocatalyst (OP), the RP has higher VB and CB than those of OP. When the RP and OP are combined, three contributing factors, the built-in electric field directed from RP to OP, band bending, and attraction caused by Coulomb force, drive the electrons from CB of OP to VB of RP and recombine with holes in this region[105]. This leaves electrons at CB of RP for reduction, and holes at VB of OP for oxidation. It has been suggested that in-situ XPS with light irradiation could be used to obtain direct evidence for such a formation[134].

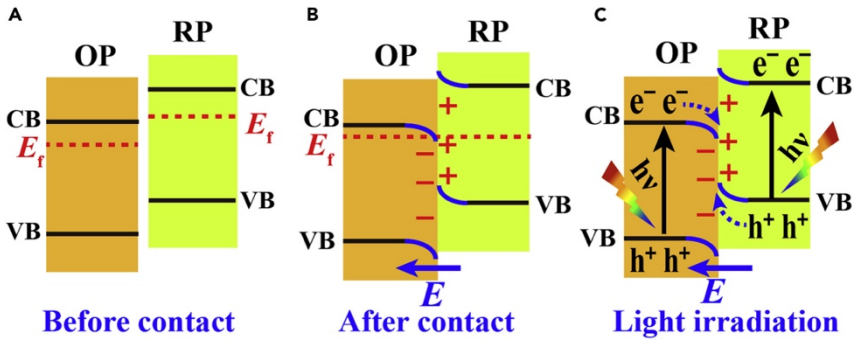

Figure 2.15. Schematic diagram showing how an S-scheme heterojunction works in photocatalysis. Reproduced with permission from reference[135]. Copyright 2020 Elsevier Inc.

Wang et al.[105] used Bi_2WO_6 as the OP (CB -0.4 V, VB 2.4 V, both vs. NHE) and CABB-NC as RP (CB -0.65 V, VB 1.6 V, both vs. NHE) to create an S-scheme heterojunction. The heterojunction was synthesised by simple mixing of two materials with ultrasound. The shift in Bi peaks detected using XPS, shown in Figure 2.16 (a), indicated strong electronic interaction between the two materials. The TEM image in Figure 2.16 (b) shows how the CABB nanoparticles incorporated with Bi_2WO_6. In terms of its photocatalytic performance over CO_2 reduction, the activity of heterojunction was 15.4 μmol g^{-1} CO and 3.2 μmol g^{-1} CH_4 produced over 8 hours, which were better than the constituents (5.4 μmol g^{-1} CO and 2.3 μmol g^{-1} CH_4 for CABB-NC, and only 2.3 μmol g^{-1} CH_4 for Bi_2WO_6 over 8 hours). The heterojunction remained stable after three 8-hour reaction cycles.

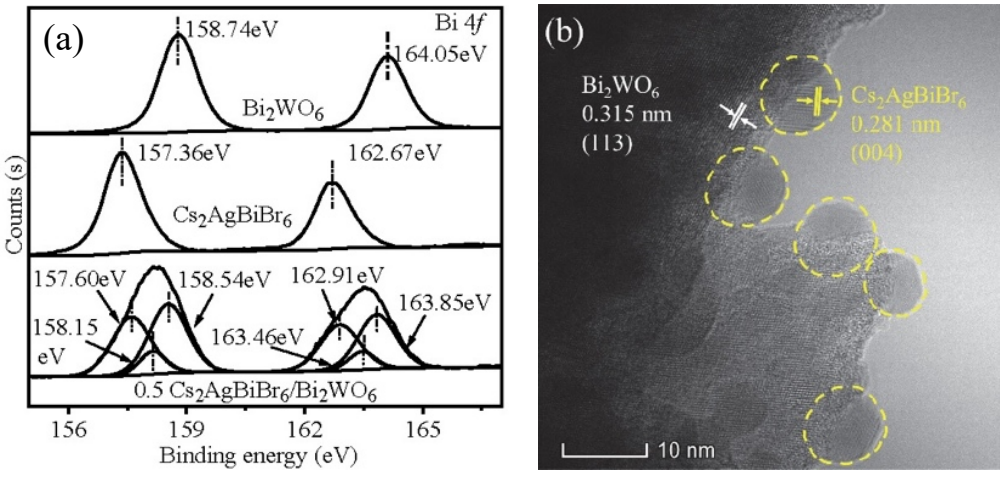

Figure 2.16. (a) Bi 4f XPS spectrum of Bi_2WO_6, CABB-NC and the CABB-NC/Bi_2WO_6 heterojunction. (b) TEM image of the heterojunction. Reproduced with permission from reference[105]. Copyright 2022 Dalian Institute of Chemical Physics, the Chinese Academy of Sciences.

There are reports that their CABB composites form direct Z-scheme heterojunctions. Wang et al.[106] claimed that their CABB with 82% g-C_3N_4 composite was a type of Z-scheme heterojunction. Wu et al.[117] also reported a CABB/Bi_2WO_6 combination as a Z-scheme heterojunction for CO_2 reduction. As shown in Figure 2.17, these direct Z-scheme heterojunctions typically lack mediator(s) that accept and/or donate electrons (denoted as A and D respectively), compared to traditional Z-scheme heterojunctions[135]. In theory, for a direct Z-scheme heterojunction, when two semiconductors are joined, their fermi levels (E_f) come to an equilibrium[136]. However, this proposed mechanism lacks direct experimental evidence[134,136]. It can therefore be argued that these Z-scheme heterojunctions without a mediator are essentially the same as S-scheme heterojunctions.

Significant research on CABB adopted g-C_3N_4 in order to create heterojunctions and boost reaction rate[99,102,106,116], and Zhao et al.[137] have provided a review on how to determine if the charge transfer system belongs to a type-II or S-scheme.

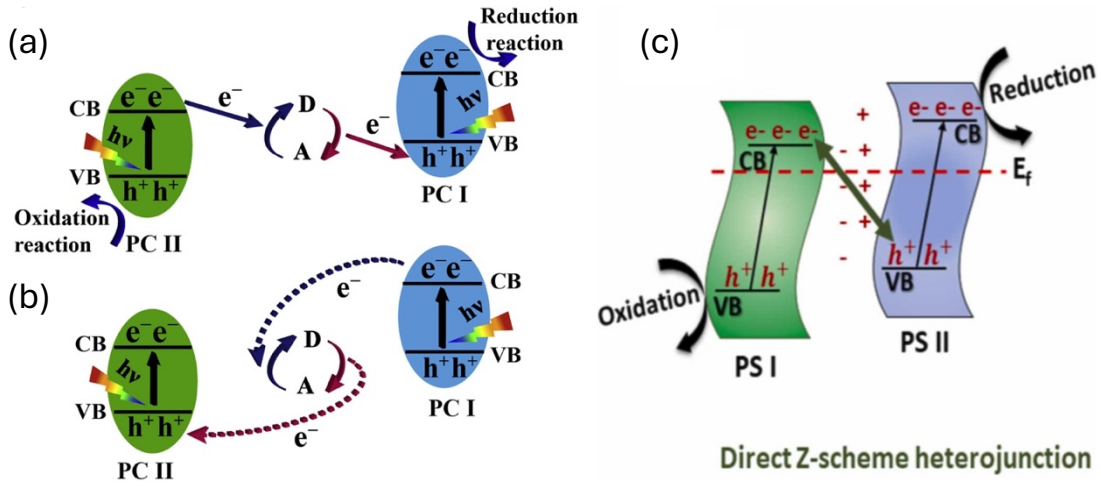

Figure 2.17. Schematic diagrams showing (a) the working mechanism of a traditional Z-scheme heterojunction, and (b) the undesired situation of a Z-scheme heterojunction. Reproduced with permission from reference[135]. Copyright 2020 Elsevier Inc. (c) Schematic presentation illustrating the working mechanism of a direct Z-scheme heterojunction. Reproduced with permission from reference[136]. Copyright 2024 Elsevier B.V.

2.4.3. Elemental doping/substitution

Efforts have been made to reduce the bandgap of CABB, and hence to improve its catalytic performance. DFT calculations indicate that A-site doping or substitution does not affect the band structure of CABB[71], and its conduction band minimum and valence band maximum are mostly determined by Bi-p and Ag-d states respectively[61]. In this way, B-site doping or substitution would be more effective in altering the bandgap of CABB.

Li and colleagues[91] have synthesised Sb-doped CABB (denoted as CASBB), where the amount of doped Sb was 12.5 mol%. $Cs_3Sb_2Br_9$ would form if the doping amount was more than 15 mol%. CASBB exhibited a reduced bandgap (2.07 eV) compared to CABB (2.21 eV), as shown in Figure 2.18. Its charge transfer dynamics also changed, and CASBB showed a longer charge carrier effective lifetime than CABB (3.25 ns to 0.54 ns). The authors incorporated CASBB with g-C_3N_4 to create a type-II heterojunction, and used this in photocatalytic toluene oxidation. A conversion rate of 468 μmol h^{-1} g^{-1} was achieved.

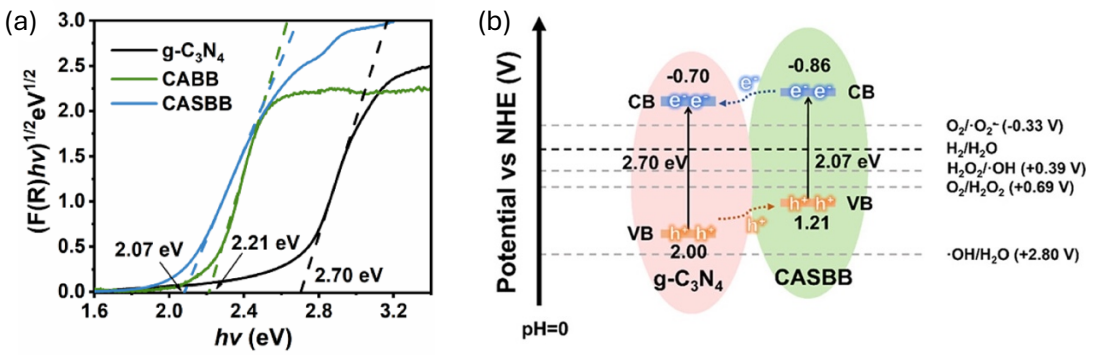

Figure 2.18. (a) Bandgap profiles of CASBB, CABB and g-C_3N_4. (b) Illustration showing how g-C_3N_4 and CASBB form a type-II heterojunction. Reproduced with permission from reference[91]. Copyright 2023 American Chemical Society.

2.4.4. Introducing defects into the structure

Deliberately adding more defects into the CABB structure can improve its activity as a photocatalyst. Lv and colleagues[100] created Br defects within the CABB structure, and the new structure is denoted as V_{Br}-CABB. It was synthesised by modifying the HBr method,

where AgBr was replaced by Ag_2CO_3, and $BiBr_3$ replaced by $(BiO)_2CO_3$. TEM images and XPS proved that Br vacancies were created, as shown in Figure 2.19. In terms of photocatalytic hydrogen generation activity in HBr/H_3PO_2 solution, V_{Br}-CABB had a production rate of 74.44 μmol h^{-1} g^{-1}, which was better than that of CABB. The authors also made an S-scheme heterojunction by joining V_{Br}-CABB and WO_3 nanorods, which boosted the hydrogen production rate to 364.89 μmol h^{-1} g^{-1}.

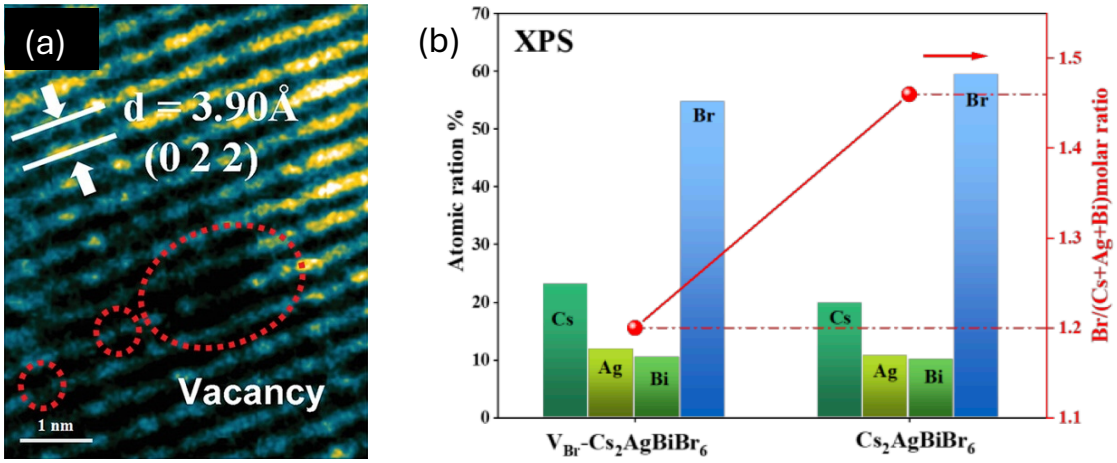

Figure 2.19. (a) Cryo-TEM image showing Br vacancies presented in V_{Br}-CABB. (b) Atomic ratio of four elements Cs, Ag, Bi, Br as determined by XPS, and the molar ratio of Br to the other three elements combined. Reproduced with permission from reference[100]. Copyright 2023 Wiley-VCH.

Zhang et al.[129] created CABB with substantial Cs vacancies, using a chelating agent ethylenediaminetetraacetic acid disodium salt (EDTA). A modified HBr method was used first, where $BiBr_3$ was replaced by $Bi(NO_3)_3 \cdot 5H_2O$, and EDTA was added into the reactor. The mixture was heated to 85°C and held for 1 hour, and the reaction lid was removed for a certain amount of time for evaporation (0-30 minutes), before heating was stopped. Subsequently, ethanol was added for precipitation. Samples that underwent 30 minutes of evaporation (denoted as CABB-30 for standard CABB, and CABB-ET-30 for CABB with Cs vacancies) had the best performance, so they were further studied. Table 2.5 provides information on atomic percentage of each element measured by XPS.

Table 2.5. Chemical compositions of CABB-30 and CABB-ET-30 as measured by XPS[129].

Sample	Cs (at%)	Ag (at%)	Bi (at%)	Br (at%)
CABB-30	18.92	6.64	7.54	49.97
CABB-ET-30	15.77	6.74	7.85	55.53

For the TC photo-degradation reaction, CABB-ET-30 achieved 81.8% degradation in 90 minutes, while CABB-30 could only attain 56.4% degradation within the same timeframe. The authors found that CABB-ET-30 generated more electrons and holes at CB and VB respectively, as demonstrated by increased photocurrent and decreased electrochemical impedance shown in Figure 2.20. This composition also had the strongest reduction capacity among the samples made, with E_{CB} = -1.53 V vs. NHE at pH = 7.

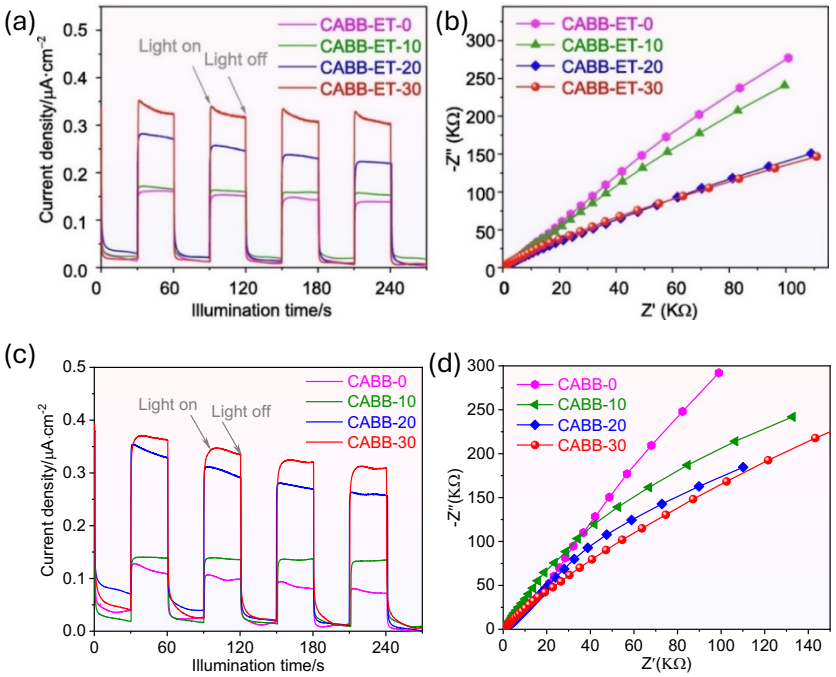

Figure 2.20. (a) Transient current response, and (b) electrochemical impedance spectroscopy (EIS) Nyquist plot under simulated sunlight, of different Cs-vacancies CABB samples. (c) Transient current response, and (d) EIS Nyquist plot under simulated sunlight, of different CABB samples. Reproduced with permission from reference[129]. Copyright 2023 Elsevier B.V.

2.4.5. Adjusting light intensity

The light source used in most reports is a 300 W Xe lamp at around 100 mW cm^{-2}, although the effect of varying light intensity had not been systematically studied. Tailor et al.[138] examined the performance of CABB on CO_2 photoreduction, using light intensities from 100 to 1000 W m^{-2}. They found that even though CH_4 production rate was the highest at 1000 W m^{-2} (= 100 mW cm^{-2}), once the production rate was divided by light intensity on a normalised scale, at lower intensities the effect became more significant, as shown in Figure 2.21. Overall, the production rate of CH_4 was proportional to $I^{0.56}$, where I is the light intensity. This means that higher light intensity did not lead to higher efficiency, albeit higher reaction rate was obtained. The authors argued that the surface trap states promote the CO_2 photoreduction reaction, but the number of traps states are limited. When the light intensity increases, more carriers are excited by photons, and they begin to fill the trap states. When all trap states are filled, excess carriers would go through undesirable electron-hole recombination. Therefore, the ratio of carriers at the CABB surface for CO_2 reduction to the total number of carriers generated was higher at lower light intensities.

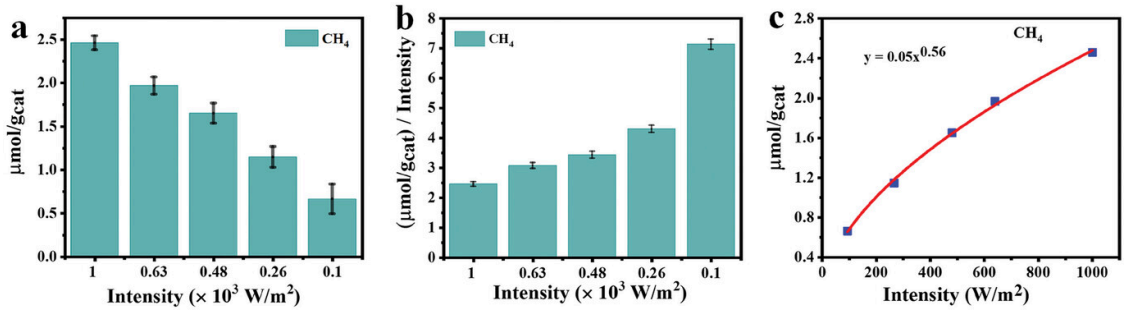

Figure 2.21. (a) CH_4 production rate across a range of light intensities. (b) CH_4 production rate divided by light intensity as y-axis, against the light intensity as x-axis. (c) CH_4 production rate is roughly proportional to $I^{0.56}$, where I is the light intensity. Reproduced with permission from reference[138]. Copyright 2024 Wiley-VCH.

2.5. Methods to improve stability

Research discussed in previous sections has focussed on enhancing the photoreaction activity for CABB. This section reviews methods to improve the stability of CABB in photocatalytic reactions.

2.5.1. Dynamic equilibrium

As noted in Section 2.3.1, immersing CABB in HBr solution is commonly used for photocatalytic hydrogen generation, where the Br^- ions from $Cs_2AgBiBr_6$ and the Br^- ions from HBr form a dynamic equilibrium between CABB and the solution[80,97]. The stability of this type of reaction system is generally good, as shown in Table 2.1. Other parts of this section discuss reaction systems without the presence of HBr, for alternative approaches to improve stability.

2.5.2. Attachment to the surface of larger structures

In some studies, affixing CABB to larger particles made the structure more stable and last longer in reaction[87,107,111]. One of the reasons is that while being fixed in place, the CABB particles are prevented from aggregation during the reactions. As an example, in the CO_2 photocatalytic reaction, the activity of CABB-NS (nanosheets) was drastically reduced after one hour[87]. When CABB-NS were attached to CTF-1 (a type of covalent triazine framework), its stability improved to at least 16 hours of reaction time, and the reaction activity also increased[111]. One contributing factor could be that fixing the CABB in place prevented the CABB-NS from aggregating during the reaction, as seen in Figure 2.22.

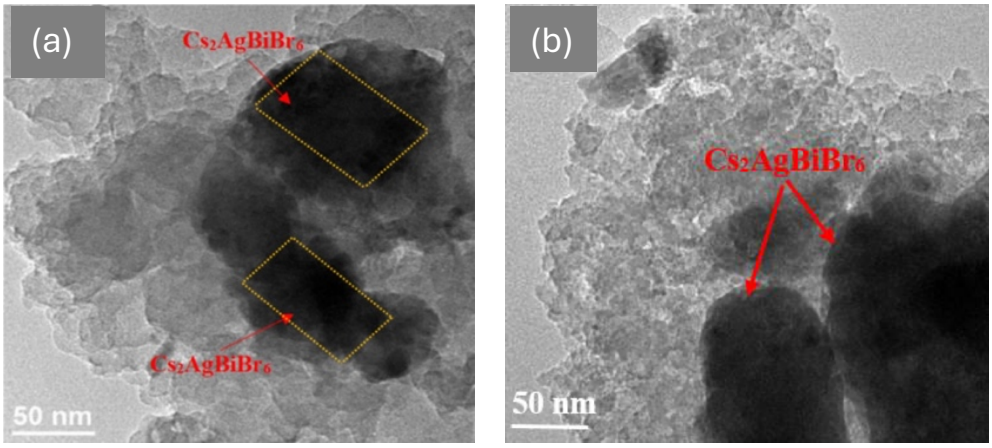

Figure 2.22. TEM images of CABB-NS/CTF-1 (a) before and (b) after reaction. Reproduced with permission from reference[111]. Copyright 2022 American Chemical Society.

Ding et al.[107] anchored CABB-NC (nanocubes) onto a type of UiO-66 named Ce-UiO-66-H, as shown in Figure 2.23 (a). UiO-66 is a three-dimensional metal-organic framework consisting of clusters of one zirconium metal centre, each connected to twelve benzene-1,4-dicarboxylic linkers[139]. The product yield only dipped slightly after a few cycles of the photocatalytic CO_2 reduction reaction, while for Ce-UiO-66-H and CABB each on its own, the photocatalytic performance declined more rapidly, as shown in Figure 2.23 (b).

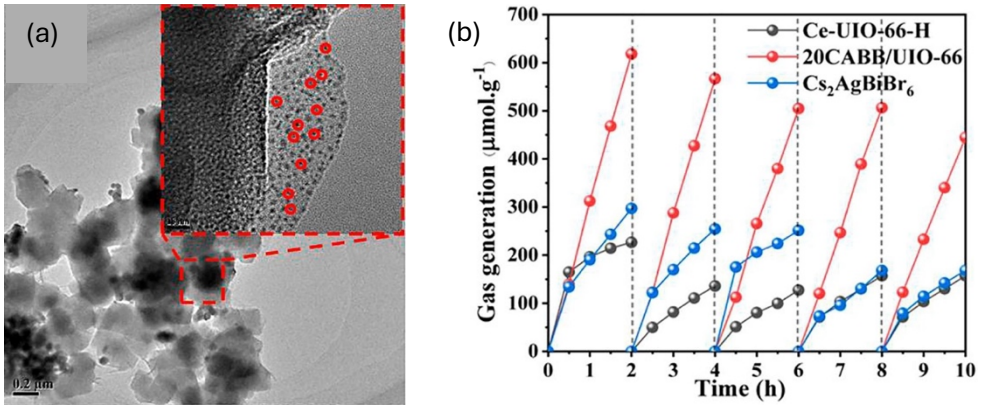

Figure 2.23. (a) TEM image of CABB-NC/Ce-UiO-66-H. Some CABB-NC particles are circled in red. (b) Amount of gas generated in the CO_2 photoreduction reaction over a few cycles, for CABB-NC, Ce-UiO-66-H and CABB-NC/Ce-UiO-66-H. Reproduced with permission from reference[107]. Copyright 2022 Elsevier B.V.

2.5.3. Deposition within porous materials

2.5.3.1. Porous frameworks

Growing CABB within a porous framework has been shown to be effective on improving its stability. Sun et al.[108] have grown CABB and $Cs_3Bi_2Br_9$ (CBB) in a mesoporous titania framework (M-Ti), as shown in Figure 2.24. The CABB and M-Ti composite was denoted as CABB@M-Ti. When the amount of CABB added was 8.47%, the activity of the composite was maximised. Theoretical and practical tests revealed that when the composite was formed, not only the stability was increased, an S-scheme heterojunction was also formed. The electric field between the perovskites and the framework also encouraged more efficient charge transfer for the CO_2 photoreduction reaction. In addition, the porous substrate prevented the CABB from aggregating. For the photocatalytic CO_2 reduction reaction, the CH_4 production rate was 151 μmol g^{-1} over 5 hours for 8.47% CABB@M-Ti, which was significantly higher than that of CABB (3.74 μmol g^{-1} over 5 hours) and M-Ti alone (48.3 μmol g^{-1} over 5 hours). After five cycles of reaction, the activity of 8.47% CABB@M-Ti barely changed, demonstrating superior stability of the structure.

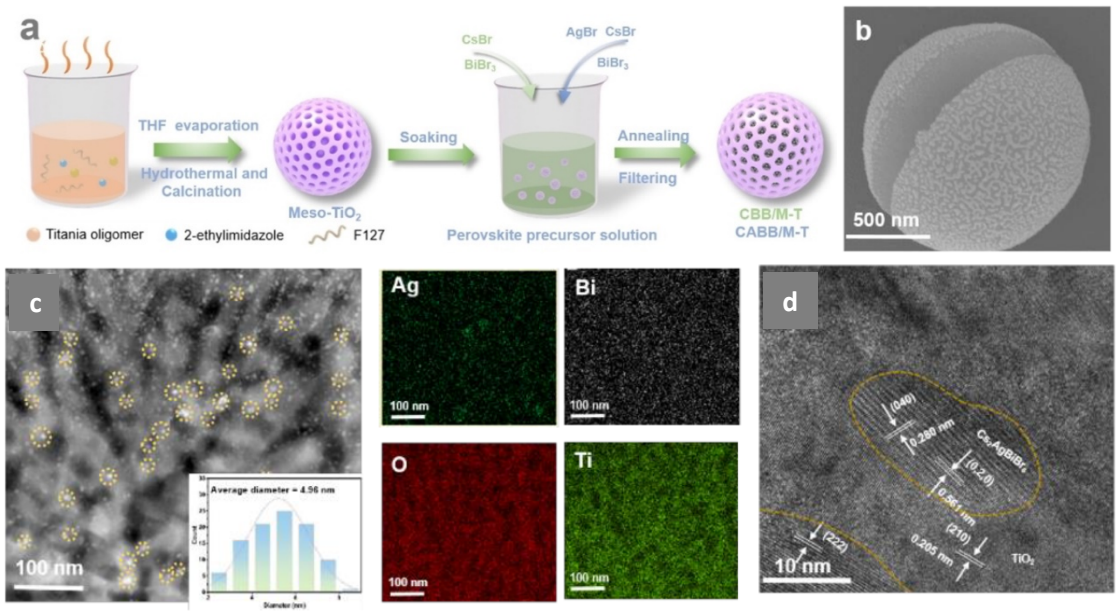

Figure 2.24. (a) Illustrative diagram showing the synthesis of CABB@M-Ti and CBB@M-Ti. (b) SEM image of 8.47% CABB@M-Ti. (c) TEM-EDX data of 8.47% CABB@M-Ti and (d) TEM image of 8.47% CABB@M-Ti. Specimens underwent focused ion beam treatment to obtain data shown in (c) and (d). Reproduced with permission from reference[108]. Copyright 2022 Wiley-VCH.

2.5.3.2. Core-shell structures

Using suitable shells to encapsulate CABB nanocubes can improve the stability of the catalyst as well as the reaction rate in harsh reaction conditions. Liu et al.[112] used mesoporous SiO_2 as the shell, and successfully synthesised CABB-NC@SiO_2 in a core-shell structure. The SiO_2 shell offered sufficient protection, while not fully covering the CABB core to stop carrier transfer. In this synthesis, mesoporous silica microspheres were made first, and then added during the CABB hot injection synthesis process. The TEM-EDX data of the product core-shell structure are shown in Figure 2.25.

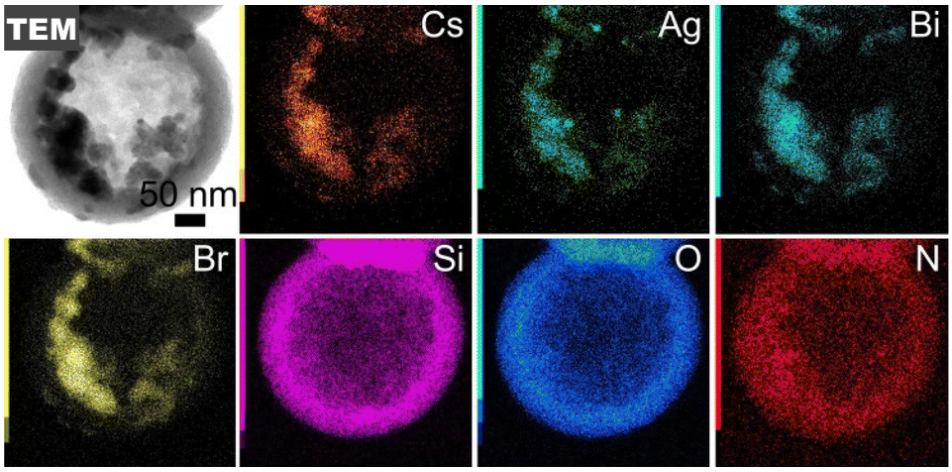

Figure 2.25. TEM-EDX data of CABB-NC@SiO_2. Reproduced with permission from reference[112]. Copyright 2023 Royal Society of Chemistry.

Compared to native CABB-NC, CABB-NC@SiO_2 showed superior stability in strong polar solvents and better activity[112]. XRD data of CABB-NC@SiO_2 showed minimal changes after immersion in water, while CABB-NC underwent significant changes, with lots of impurity peaks appeared, as displayed in Figure 2.26 (a). The photoluminescence (PL) intensity of CABB@SiO_2 dropped slower than that of CABB-NC when placed in different solvents or under light, as shown in Figure 2.26 (b-f). In terms of CO_2 photocatalytic reduction, CABB-NC@SiO_2 yielded more products for each cycle, and lasted longer in repeated tests, as shown in Figure 2.26 (g, h).

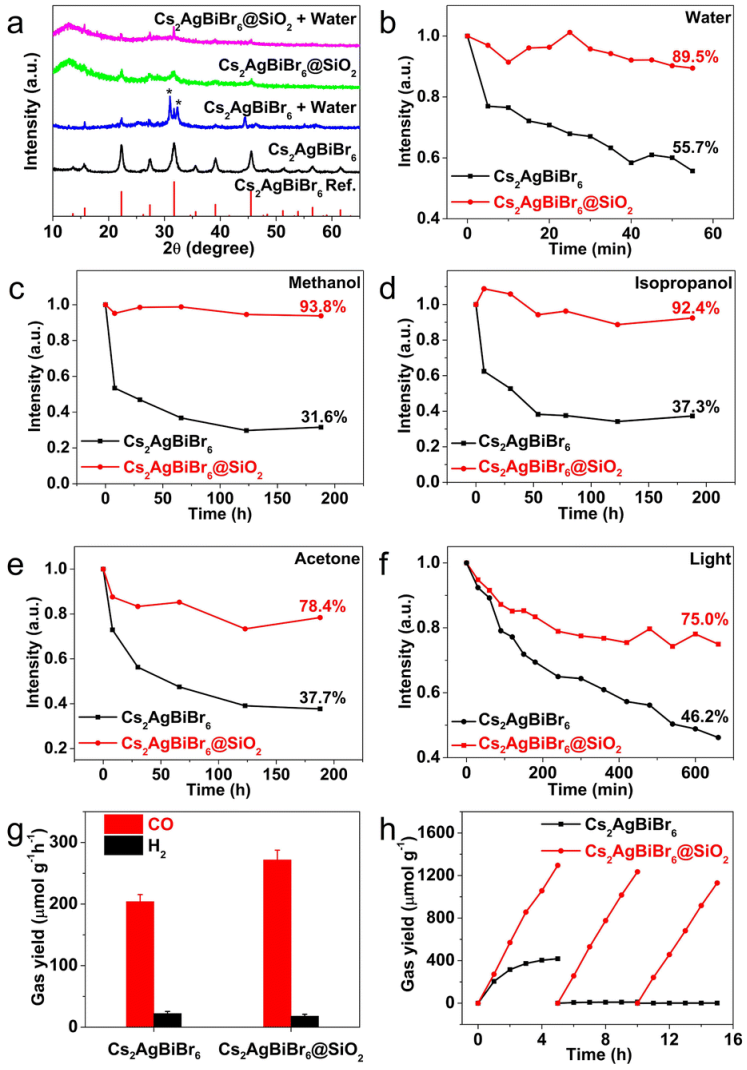

Figure 2.26. (a) XRD of CABB-NC and CABB-NC@SiO_2 before and after immersion in water. (b-e) PL intensity of CABB-NC and CABB-NC@SiO_2 in different solvents. (f) PL intensity of CABB-NC and CABB-NC@SiO_2 under light illumination. (g) Activity and (h) stability of CABB-NC and CABB-NC@SiO_2 in photocatalytic CO_2 reduction reaction. Reproduced with permission from reference[112]. Copyright 2023 Royal Society of Chemistry.

2.6. Research progress of other photocatalysts

A lot of review articles have provided insights into the photocatalytic performances of other halide perovskites[140–142]. According to these reviews and the research reports discussed in Section 2.3, CABB with its heterojunctions or co-catalysts are comparable if not better than lead-containing halide perovskites in a lot of cases. However, considering all types of photocatalysts available, halide perovskites may not be the best option in certain

applications. Some of the prominent photocatalysts that do not contain halide perovskites are discussed in this section.

2.6.1. Hydrogen generation

Catalysts based on perovskite oxide $SrTiO_3$ have achieved very high hydrogen production rates. Takata et al.[143] synthesised $SrTiO_3$:Al with 0.1 wt% Rh, 0.05 wt% Cr_2O_3 and 0.05 wt% CoOOH incorporated. The highest activity was around 3.6 mmol h^{-1} for hydrogen production, and in the meantime around 1.8 mmol h^{-1} for oxygen production. However, this system only operated best when the wavelength of the light source was between 350 nm and 360 nm. When the wavelength was at 370 nm or longer, the efficiency was greatly reduced. Based on this $SrTiO_3$:Al catalyst, Nishiyama et al.[144] created reactors that are similar to solar cells, and conducted experiments under natural sunlight, using 100 m^2 of panels for water splitting. The water splitting rate was around 0.11 mmol h^{-1} cm^{-2}. The authors admitted that $SrTiO_3$:Al mainly absorbs UV light only, and the rest of the energy brought by sunlight was not fully utilised.

2.6.2. CO_2 reduction

The research on photocatalytic CO_2 reduction remains at an early stage of practical development, mostly because of the low energy conversion rate and low product selectivity[145]. Typical photocatalysts used in CO_2 reduction include materials based on metal-organic framework (MOF)[146], covalent-organic framework (COF)[147], Cu_2O[148] and ZnO[149]. The results among different research articles can be difficult to compare, since the reaction conditions such as light source, pressure, type and amount of liquid added, and sacrificial agent used are often different. Different photoreaction conditions can lead to different products, and product separation is another significant challenge. In this way, a standard procedure in conducting CO_2 photoreduction experiments is needed, as proposed by Fang et al.[145].

2.6.3. Pollutant degradation

Wastewater treatment has emerged as the most promising application of photocatalytic pollutant degradation[150,151], and TiO_2-based photocatalysts is arguably the closest to large-scale implementation. TiO_2 is non-toxic, plentiful, stable in water and the production cost is low[151]. In the meantime, it can treat almost every type of wastewater such as textile, petroleum, pharmaceutical and pesticidal[152]. In some systems the pollutant could be completely removed via photocatalytic reaction[153], and even if only a portion of the pollutant is removed, subsequent water treatment using conventional methods can be made easier because of the lower concentration of the pollutant.

The limitations of TiO_2 makes it unable to work on its own. TiO_2 has the problem of weak visible light absorption, so doping is employed to increase its absorption range[154]; its tendency to aggregate and difficulty in recovering the catalyst require the remedy of a substrate[153]. Nevertheless, TiO_2-based photocatalysts have shown potential for industrial applications in wastewater treatment.

2.7. Evaluating output via turnover frequency

Nearly all articles discussed in this chapter evaluated the photocatalytic performance in either $\mu mol\ h^{-1}\ g^{-1}$ for product generation reactions, or k-values for degradation reactions. An alternative approach to assess the activity of the photocatalyst is proposed here, which is turnover frequency (TOF). This is an established concept in other fields of catalysis[155], but rarely seen in reports on photocatalysis.

TOF gauges the performance of the catalyst in terms of reacted molecules per active site on the surface of the catalyst[155]. Using TOF can reduce the effect brought by factors such as the different amounts of catalyst used in the reaction system. It can replace both μmol

h^{-1} g^{-1} and the k-value, as both product generation and degradation involve molecules reacted at the active sites on the catalyst. Quantifying such a process validates the effectiveness of the catalyst.

To work out the value of TOF, the photoreaction mechanism needs to be established, so the active sites can be determined to allow subsequent calculations. The details on how the calculations are performed to convert the reaction rate in μmol h^{-1} g^{-1} to TOF in s^{-1} are provided in Section 3.8.3.

2.8. Conclusions

This chapter has discussed the structures and synthesis routes, applications, and methods to increase activity as well as stability of $Cs_2AgBiBr_6$. CABB is a versatile material in terms of its applications in photocatalysis. It can be synthesised in different sizes and shapes for different needs, and forming heterojunctions and/or using co-catalysts can greatly boost its activity. Some of the photocatalysts that are not halide perovskites have also been discussed, and an alternative approach to evaluate photoreaction output using turnover frequency has been proposed. Other methods to increasing the stability of CABB, especially in nanocube and nanosheet form, could be further explored, as commercial products require hundreds or thousands of hours of consistent output from a given reaction. The reaction mechanisms for different photocatalytic reactions could also be further investigated for a clearer understanding of how the photocatalysts work.

Chapter 3 Experimental methods

Contents

3.1. Synthesis of PEA_2SnBr_4 and MoS_2 heterojunctions 57
3.2. Synthesis of $Cs_2AgBiBr_6$ 57
3.2.1. Synthesis of bulk samples 57
3.2.2. Synthesis of nanocubes via hot injection 58
3.2.3. Synthesis of nanosheets via hot injection 58
3.2.4. Synthesis of bulk and nano CABB at room temperature 59
3.3. Photocatalytic reactions 60
3.3.1. The photocatalytic water splitting reaction 60
3.3.2. Reactions in liquid methanol 61
3.3.3. Reactions with methanol vapour 62
3.4. X-ray diffraction (XRD) 62
3.5. UV-visible spectroscopy (UV-vis) 64
3.5.1. Theory 64
3.5.2. Bandgap calculations using powder UV-vis 66
3.5.3. Formaldehyde quantification using liquid UV-vis 66
3.6. Fourier transform infrared spectroscopy (FTIR) 68
3.7. X-ray photoelectron spectroscopy (XPS) 70
3.8. Gas chromatography (GC) and quantification of hydrogen 74
3.8.1. Principles of gas chromatography 74
3.8.2. Hydrogen quantification process 77
3.8.3. Turnover frequency calculations 78
3.9. Zeta potential and surface charge 79
3.10. (Time-resolved) photoluminescence 81
3.11. Electron microscopy and sample preparations 83
3.11.1. (Scanning) transmission electron microscopy 83
3.11.2. Electron fluence calculations 91
3.11.3. Lattice measurements 93
3.11.4. Scanning electron microscopy 95
3.11.5. TEM sample preparations 97
3.11.6. SEM sample preparations 98
3.11.7. EDX data analysis 98

Unless specified, all practical experiments discussed in this chapter were conducted by the author of this thesis.

3.1. Synthesis of PEA_2SnBr_4 and MoS_2 heterojunctions

The synthesis of PEA_2SnBr_4 (PSB) was carried out in a glovebox. In a typical process, 0.1 mmol (20.2 mg) phenethylammonium bromide (PEABr, ≥98%, Sigma-Aldrich) and 0.05 mmol (13.9 mg) $SnBr_2$ (Sigma-Aldrich) were dissolved in 1 mL N,N-Dimethylformamide (99.8%, Sigma-Aldrich). The solution was added to a flask containing 30 mL toluene (99.9%, Sigma-Aldrich) dropwise under vigorous stirring. The mixture was then centrifuged at 5000 rpm for 5 minutes. The precipitate was dried in vacuum oven to obtain crystals of PEA_2SnBr_4.

To synthesise a PSB/MoS_2 heterojunction, an amount of MoS_2 (Sigma-Aldrich) was added to the flask with toluene beforehand, with the rest of the procedure remaining the same. Heterojunctions with MoS_2 mass ratios of 15% and 85% were synthesised.

3.2. Synthesis of $Cs_2AgBiBr_6$

3.2.1. Synthesis of bulk samples

The synthesis method used was based on a previous publication by Slavney et al.[156]. In a typical synthesis process, 449 mg $BiBr_3$ (99%, Thermo Scientific), 188 mg AgBr (99.5%, Thermo Scientific) and 426 mg CsBr (99.9%, Thermo Scientific) were weighed and transferred into a conical flask with magnetic stirring. Subsequently 10 mL HBr (48 wt% in water, Thermo Scientific) was also added to the flask. The flask was then heated to 110 °C in an oil bath, and held for 2 hours while stirring, before cooling naturally to room temperature. Having cooled, the powder was collected by centrifuge at 5000 rpm for 5 minutes, and the supernatant was discarded. The powder was subsequently put into a 60 °C vacuum oven overnight to dry.

Washing of bulk CABB was also studied. Samples washed with ethanol did not show a change in the powder XRD, but degraded rapidly during TEM observation. Bulk CABB

washed with HBr did not exhibit these effects; CABB processed in this way is subsequently denoted as CABB-HBr.

3.2.2. Synthesis of nanocubes via hot injection

$Cs_2AgBiBr_6$ nanocubes were synthesised following the procedure reported by Creutz et al.[73]. Initially, 136 mg caesium acetate (99.9%, Thermo Scientific), 83 mg silver acetate (99%, Fluorochem) and 193 mg bismuth acetate (99.999%, Thermo Scientific) were put into a three-neck flask with a magnetic stirring bar. Subsequently, 10 mL octadecene (90%, Alfa Aesar), 2.8 mL oleic acid (90%, Thermo Scientific) and 0.62 mL oleylamine (70%, Fluorochem) were added into the flask. The mixture was then heated under vacuum to 110 °C and the temperature maintained for 45 minutes. Next, this was heated to 140 °C in argon, and 0.36 mL bromotrimethylsilane (TMSBr) (98%, Thermo Scientific) was quickly injected into the mixture. After 10 seconds, the flask was removed from heating source, and quenched in a water bath.

To obtain a powder sample, the mixture was poured into two centrifuge tubes and centrifuged at 6000 rpm for 30 minutes, and the dark supernatant was discarded. The precipitate was then washed by adding 5 mL toluene into each tube, and centrifuged again at 6000 rpm for 30 minutes. The final precipitate, which contained the desired nanocubes, was dried in a 60°C vacuum oven for at least one hour. Each batch yielded around 300 mg nanocubes and was stable in air for several weeks.

3.2.3. Synthesis of nanosheets via hot injection

Nanosheet synthesis was carried out according to the procedure due to Liu et al.[87]. Cs-oleate was first separately prepared, where 330 mg Cs_2CO_3 (99.9%, Sigma-Aldrich) and 4 mL oleic acid (90%, Thermo Scientific) were added into a three-neck flask with a magnetic stirring bar. The solution was then placed under vacuum and heated to 100 °C, where it was

held for 30 minutes. Afterwards, it was heated to 150 °C in argon and held for one hour, and subsequently cooled naturally to room temperature.

In a separate flask with a magnetic stirrer bar, 45 mg $BiBr_3$ (99%, Thermo Scientific), 34 mg $AgNO_3$ (99%, Fluorochem), 4 mL octadecene (90%, Alfa Aesar), 100 µL HBr (48 wt% in water, Thermo Scientific), 1 mL oleic acid (90%, Thermo Scientific) and 1 mL oleylamine (70%, Fluorochem) were added. Firstly, the mixture was degassed, placed in vacuum, heated to 120 °C, and held for 30 minutes. Secondly, the flask was filled with argon, further heated to 200 °C and kept for 10 minutes. Thirdly, the flask was cooled by removing the heating element. When room temperature was reached, 0.3 mL Cs-oleate from the first flask was injected into the reaction solution, and this was stirred at room temperature for 10 minutes. Following this, the flask was heated to 230 °C and held for 10 minutes. Finally, the flask was quenched to room temperature in a water bath.

To obtain a powder sample, the contents of the final flask were decanted into two centrifuge tubes and centrifuged at 8000 rpm for 5 minutes. The supernatant was discarded, and the precipitate was dispersed in 5 mL hexane and centrifuged again at 8000 rpm for 5 minutes. The precipitate from this process was nanosheets. For storage, hexane was added into the tubes, although the nanosheets were stable if vacuum dried and stored in air. Each batch yielded around 100 mg of nanosheets.

3.2.4. Synthesis of bulk and nano CABB at room temperature

This synthesis method was based on the work reported by Purohit et al.[114]. 0.1 mmol CsBr (21.3 mg), 0.05 mmol AgBr (9.4 mg) and 0.05 mmol $BiBr_3$ (22.4 mg) were dissolved in 2.5 mL dimethyl sulfoxide (≥99.9%, Sigma-Aldrich), and 2 mL of this solution was added to a flask containing 5 mL isopropanol (≥99.5%, Sigma-Aldrich) with 50 µL oleic acid. A bulk sample was obtained by centrifugation at 4000 rpm for 4 minutes. A nanosized sample was prepared by collecting the supernatant from the previous step, followed by centrifugation

at 14000 rpm for 10 minutes. CABB made this way is subsequently denoted as CABB-DMSO bulk or nano respectively.

3.3. Photocatalytic reactions

3.3.1. The photocatalytic water splitting reaction

For photocatalytic water splitting reactions, the reactor used is shown in Figure 3.1, which has a small window to allow light in. Before running a reaction, deionised water, a sacrificial agent triethanolamine (TEOA, ≥99.0%, Sigma-Aldrich), catalyst and a small magnetic bar were added into a quartz vial. The catalyst in water was typically kept at a concentration of 1 g L^{-1} (15 mg catalyst in 15 mL liquid). The quartz vial was then put into the reactor, which was filled with 6 bar of argon.

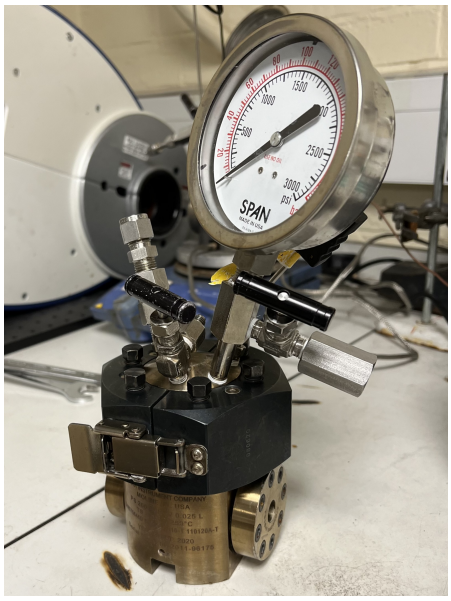

Figure 3.1. Small-window reactor used for photocatalytic reactions.

A 300 W Xe lamp (Sciencetech Inc.) was used as the light source, while the contents were stirred magnetically during the photocatalytic reaction. As seen from Figure 4.3, the samples as catalysts can absorb light across a wide range of wavelengths. The Xe lamp provides a wide spectrum to meet the absorption window of the samples, potentially

maximising their photocatalytic performance. Each reaction lasted for at least two hours. Gas in the reactor after reaction was introduced into a gas chromatograph (Agilent 7890B) for analysis. The gas chromatography system is subsequently denoted as GC.

3.3.2. Reactions in liquid methanol

In a typical experiment, 10 mg of catalyst powder was placed in a vial with 10 mL methanol (≥99.9%, Sigma-Aldrich) and excess NaBr (≥99%, Thermo Scientific). The methanol solution saturated with NaBr had been prepared beforehand, and 360 mg of excess NaBr were added. The excess NaBr was not fully dissolved as the temperature increased during the reaction. This prevented the Br^- ions from escaping the CABB structure, which would otherwise cause a collapse in the halide perovskite structure.

The vial was later placed into the reactor with a window at the top, allowing light input, as shown in Figure 3.2. The reactor was purged with argon for a few minutes to deplete air, and then filled with 2 bar of argon. The reactor was then placed under the light source, irradiated with a 300 W Xe lamp, with the mixture magnetically stirred at around 250 rpm. Normally each test lasted 30 minutes, and the gas in the reactor was analysed by the GC at the end of each run.

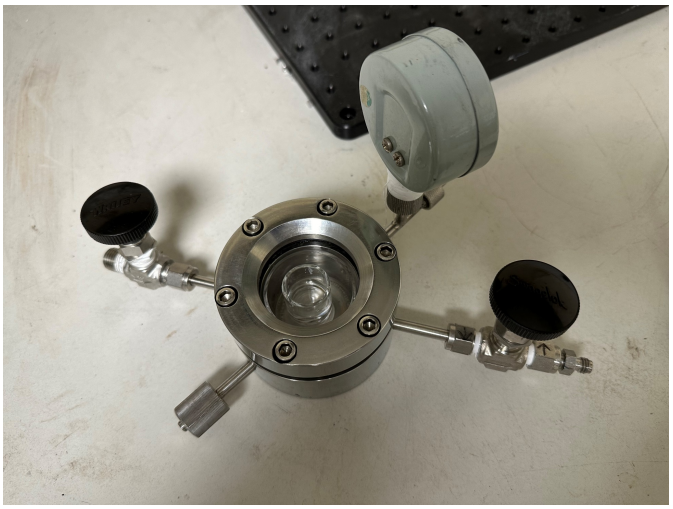

Figure 3.2. The reactor used for methanol photo-oxidation reactions.

3.3.3. Reactions with methanol vapour

The same reactor shown in Figure 3.2 was used for this set of experiments, but another smaller vial was placed into the standard vial in the reactor (see Figure 3.3). This arrangement only allows the catalyst to react with methanol vapour. 4 mg catalyst was added to the small vial, and 4 mL liquid method was added to the large vial. Both vials were then placed inside the reactor, which was purged and filled with 2 bar of argon. The system was then irradiated with a 300 W Xe lamp for typically two hours each run, and the gas product was analysed by the GC.

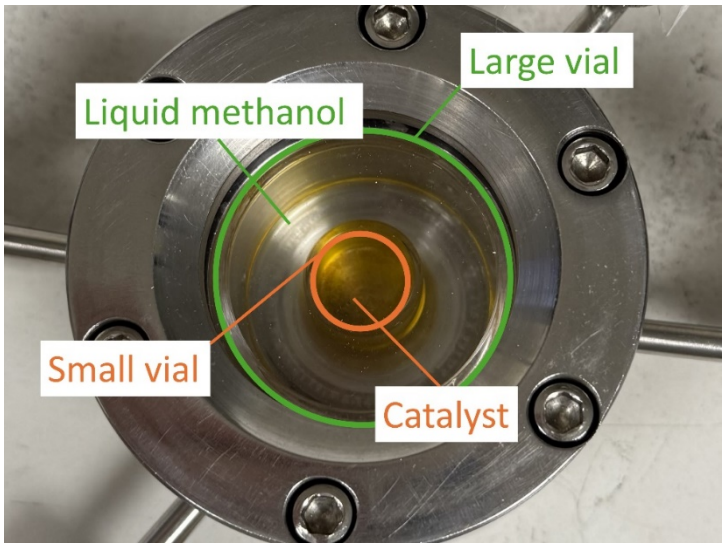

Figure 3.3. An arrangement that allows catalyst to react with gaseous methanol.

3.4. X-ray diffraction (XRD)

X-ray diffraction is a technique commonly used to study crystalline materials, where long-range order at atomic or molecular scale exists. The diffraction pattern is defined by the geometry and structure of the material[157]. It was first discovered and reported by M. Laue, W. Friedrich and P. Knipping in 1912 and further developed by W. H. Bragg and W. L. Bragg[158,159]. Diffraction can be explained using reflection from the crystal planes and Bragg's law, which is Equation (3.1);

$$n\lambda = 2dsin\theta \quad (3.1)$$

where *n* is an integer defining the order of a reflection, λ is the wavelength, *d* is the distance between two neighbouring lattice planes, and θ is the Bragg angle at which a diffraction peak is present[157].

Bragg's law can be visualised using Figure 3.4 below. The path difference between two adjacent planes with a spacing d_{hkl} is equal to:

$$(AB + BC) = 2d_{hkl}sin\theta \tag{3.2}$$

For constructive interference, which is equivalent to a reflection being present, Equation (3.1) is obtained[158].

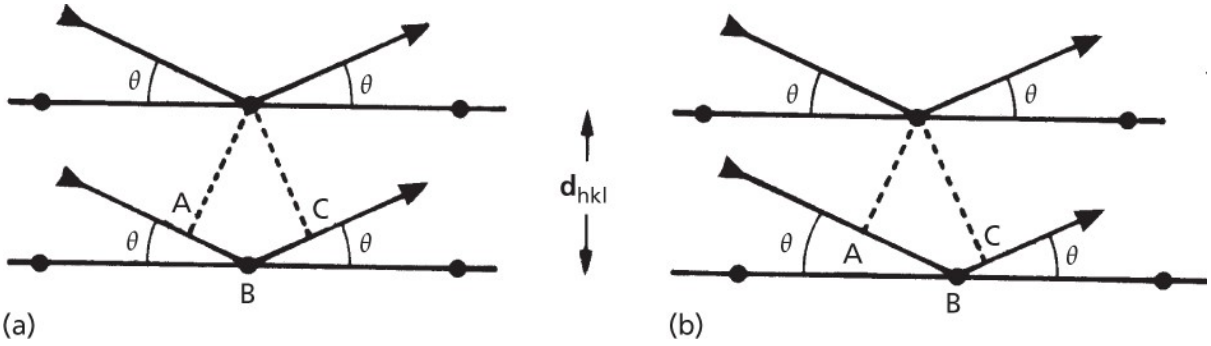

Figure 3.4. (a) Bragg's law applied to a case where the paths AB and BC obey the relationship AB = BC = d_{hkl}sinθ, and (AB + BC) = 2d_{hkl}sinθ. (b) Bragg's law for a general case where AB ≠ BC, and (AB + BC) = 2d_{hkl}sinθ. Image reproduced with permission from reference[158]. Copyright 2015 Christopher Hammond. Published by Oxford University Press.

X-rays are generated in the laboratory from accelerated electrons incident onto a metal plate, from which two classes of X-rays: Bremsstrahlung and a characteristic X-ray spectrum, are generated. The deceleration of electrons creates the Bremsstrahlung (white spectrum). The characteristic X-ray spectrum is produced when the energy of the electron beam is high enough to eject an electron from an inner shell of the metal target, and a second electron from an outer shell of the metal fills the vacancy. When the ejected electron from K shell is replaced by an electron from the 2p orbital (L shell), the radiation generated from this process is the K_α radiation[160]. Similarly, an electron drops down from the 3p orbital (M shell) to the K shell generates K_β radiation. Characteristic X-rays form

sharp peaks above the Bremsstrahlung background and K_α radiation is generally used. Copper K_α (λ = 1.5418 Å) and molybdenum K_α (λ = 0.7107 Å) are two commonly used K_α lines[161]. However, when these K_α lines are produced, weaker K_β lines also appear and need removing. A filter is normally in place that allows the X-ray to pass through, but absorbs the K_β component from the source. The material selected for the filter has one less proton than the metal source, so its absorption K edge sits between the K_α and K_β lines of the metal source[162]. For a copper source, a nickel filter is fitted.

X-ray diffraction data obtained in this thesis were collected from a Bruker Advance Eco, with a Cu source and a LYNXEYE XE-T detector. Typically, a few milligrams of sample powder were sprinkled onto a round glass slide with vacuum grease applied. The glass slide was then placed in a sample holder where some vacuum grease had also been applied, in order to keep the glass slide in place. Next, the sample holder was placed in the diffractometer to obtain diffraction data. Generally, scans started at a 2θ angle of 5° and ended at 80°, over 5956 measurements, with each measurement taking 0.2 seconds. The X-ray generator used had a voltage of 40 kV and a current of 25 mA.

3.5. UV-visible spectroscopy (UV-vis)

3.5.1. Theory

A UV-visible spectrometer typically consists of a light source, two cells for the light to pass, as well as a detector. This set up is called a double (or dual) beam spectrometer. UV-visible spectroscopy normally works in a wavelength range of 200-800 nm. While it is possible to go below 200 nm, the spectra can be affected by absorption of UV light by oxygen[163]. When in operation, the light is split and directed to two cells in parallel, where one cell is the reference, and the other contains the sample. For liquid samples, the reference cell has

solvent only, and the other includes sample dissolved in the solvent. Certain wavelengths in the UV-visible range are absorbed by the sample as a chromophore (where electron transition occurs). This is caused by electron transition from a ground state to a higher excited state[163]. The energy absorbed in this process is fixed due to quantum effects. An atom or molecule has discrete energy levels. If an electron is promoted from the ground state, E_0, to an excited state, E_1, after absorbing a photon, the energy needed is;

$$E_1 - E_0 = h\nu \tag{3.3}$$

where h is the Planck's constant, and v is the frequency of the photon needed. By measuring the amount of light absorbed at each wavelength, a UV-visible spectrum can be obtained.

When the light passes through a sample, its intensity declines exponentially. The absorbance of the sample, A, can be modelled by the Beer-Lambert law as;

$$A = log_{10}\frac{I_0}{I_t} = \varepsilon cl \tag{3.4}$$

where I_0 is the intensity of light transmitted through the reference, I_t is the intensity of light transmitted through the sample cell, ε is the molar absorptivity, c is the concentration of the sample in the solvent, and l is the path length of the light transmitted through the cell[164].

The UV-vis spectrometer used in this project was a Shimadzu UV-2600. Two different attachments were needed for powder and liquid measurements. For powder measurements, a barium sulphite disc was used as the reference. For liquid measurements, solvents were loaded into quartz cuvettes (Thorlabs, Inc.) with a path length of 1 cm.

3.5.2. Bandgap calculations using powder UV-vis

To analyse the bandgap of the sample using UV-vis, the absorbance-wavelength data were processed to generate Tauc plots[165]. A Tauc plot is produced based on Equation (3.5), assuming the absorption coefficient can be interpreted as;

$$(\alpha h\nu)^{\frac{1}{n}} = k(h\nu - E_b) \tag{3.5}$$

where α is the absorption coefficient of the sample, h is Planck's constant, ν is the frequency of the photon, k is a constant, E_b is the bandgap of the material, n = ½ when the material has a direct bandgap, and n = 2 when the material has an indirect bandgap[166]. After plotting $(\alpha h\nu)^{1/n}$ against $h\nu$, the extrapolated intercept between the slope and the flat region before the slope can be regarded as the bandgap of the material[167]. Figure 3.5 gives an example of the Tauc plot.

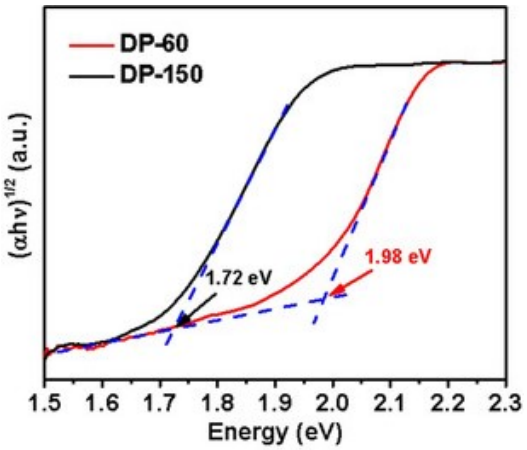

Figure 3.5. Example Tauc plot. The bandgap of the material is the corresponding energy value of the intercept shown in the graph. Reproduced under the Creative Commons CC BY licence from reference[168]. Copyright 2020 The Authors.

3.5.3. Formaldehyde quantification using liquid UV-vis

In the main reaction studied in this project, methanol is oxidised into hydrogen and formaldehyde. Hydrogen can be quantified using a gas chromatography system, while the quantification of formaldehyde is less straightforward. In this work, the detection method was based on the method reported by Yuan et al.[169] and Min et al.[170] with some

modifications. Oxalyldihydrazide was the key reagent for detection and quantification of formaldehyde. Oxalyldihydrazide reacts with aldehyde groups to form hydrazone bonds, which can be detected by UV-vis spectroscopy[170]. These bonds lead to a peak forming around 220 nm in the UV-vis spectra, and the area under the curve can be used to calculate the concentration of formaldehyde in solution. Reactions between oxalyldihydrazide and some organic compounds are shown in Figure 3.6.

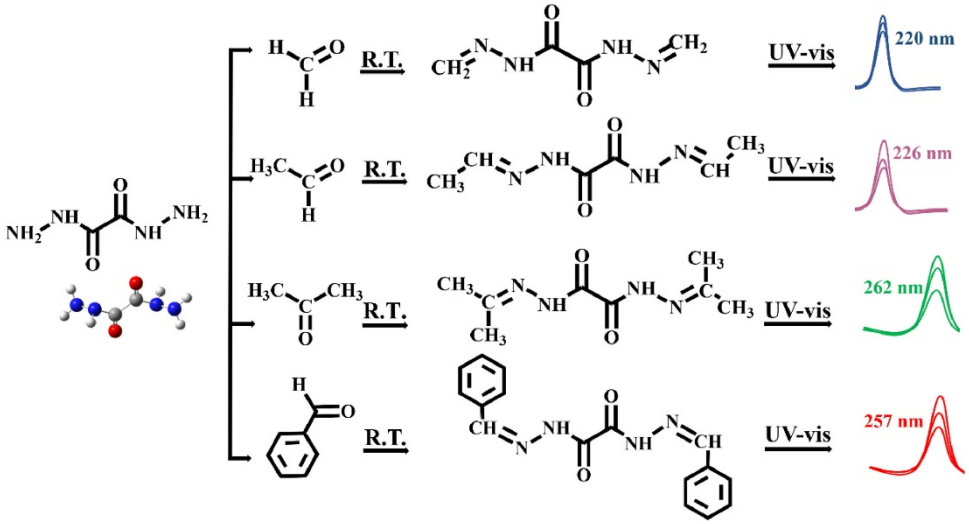

Figure 3.6. Schematic diagram illustrating the reactions between some organic compounds and oxalyldihydrazide for UV-vis analysis. For formaldehyde detection, the top route was used. Reproduced under Creative Commons licence from reference[170]. Copyright 2023 The Authors.

Before quantification, device calibration is needed. Solutions with known concentrations of formaldehyde were prepared by mixing formaldehyde (37 wt%, Thermo Scientific) with methanol (≥99.9%, Sigma-Aldrich) to form solutions with a formaldehyde concentration of 0.1 mM, 0.2 mM, 0.4 mM, 0.8 mM, 1 mM and 10 mM. The formaldehyde-methanol solution is denoted as CHOH. Initially 10 mM CHOH was made where 9 µL of 37 wt% formaldehyde was diluted with 12.5 mL methanol. The 10 mM solution was then diluted to create solutions with lower formaldehyde concentrations.

Separately, oxalyldihydrazide (96%, Fluorochem) was mixed with ultrapure water to create a 0.1 mM standard solution for testing, and this solution is subsequently denoted as ODD.

Initially 10 mM ODD was made by dissolving 17.7 mg oxalyldihydrazide in 15 mL ultrapure water, and then this was further diluted to obtain 0.1 mM ODD; 0.1 mM was found to be the best concentration for ODD[170].

Finally, 2 mL of CHOH at a certain concentration and 2 mL of 0.1 mM ODD were mixed for at least 10 minutes before the mixture was put into the UV-vis spectrometer. This is because the nucleophilic reaction takes about 10 minutes to complete, when it gives the strongest signal[170]. Once the data were processed by creating a plot containing the data sets from different CHOH concentrations, the area under the curve at around 220 nm was found to be proportional to the concentration of formaldehyde. Using this method, the concentration of formaldehyde from an unknown formaldehyde-methanol solution can be worked out.

3.6. Fourier transform infrared spectroscopy (FTIR)

Similar to UV-visible spectroscopy, Fourier transform infrared spectroscopy (FTIR) measures the absorption of light, but in the infrared region. Instead of electron transitions, infrared provides information about the vibrational states of a molecule[163]. Taking a simple two-atom molecule as an example, this can act as a simple oscillator, whose vibration can be promoted to the next vibrational level when irradiated by infrared at a suitable energy[171].

The energy required for the promotion can be calculated using Equation (3.6);

$$E_1 - E_0 = \Delta E = h\bar{\nu}c \qquad (3.6)$$

where E_1 is the excited vibrational state, E_0 is the ground state, h is Planck's constant, $\bar{\nu}$ is the wavenumber of radiation and c is the speed of light[171]. For instance, if the wavenumber required to promote the vibrational level is 3000 cm^{-1}, the energy required is;

$$\Delta E = 6.626 \times 10^{-34}\ \mathrm{J\ s} \times 3000\ cm^{-1} \times 3 \times 10^{10}\ \mathrm{cm\ s^{-1}} \quad (3.7)$$
$$= 5.963 \times 10^{-20}\ \mathrm{J}$$

Infrared spectroscopy can identify molecules and their structures, as well as the environment of functional groups. For example, -C=O groups and -C=O···H-O- give different frequencies[171]. An infrared spectrum can be acquired by passing infrared through a sample and detecting the amount of infrared absorbed at each wavelength, wherein the peaks in the spectrum are linked to the vibrational frequencies of the functional groups in the sample molecule[172].

Most FTIR spectrometers implement a Michelson interferometer, as shown in Figure 3.7.

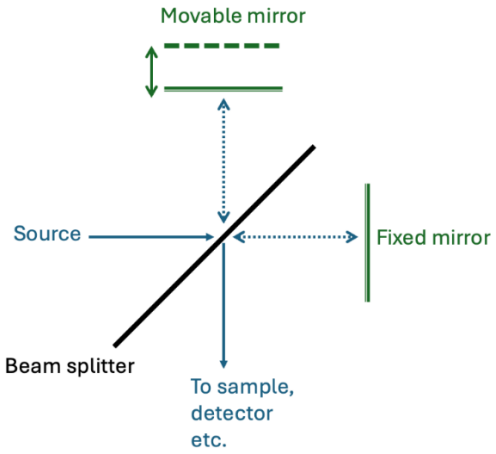

Figure 3.7. Schematic diagram of a Michelson interferometer.

The beam splitter transmits and reflects the incoming beam from the source equally. When the radiation from the source hits the beam splitter, part of the beam is transmitted to a mirror, and the other part is reflected to the other mirror. The beams then reach the mirrors and are reflected. After that they recombine at the beam splitter. The recombined beam consists of an interference pattern, which then passes through the sample and subsequently the detector. An interferogram is thus formed. This contains all information needed to produce a conventional IR spectrum, but it is recorded in the time domain, and a Fourier transform is hence used to convert the spectrum to the frequency domain[171,172].

FTIR data presented in this thesis were collected using a Thermo Scientific Nicolet iS50 FTIR Spectrometer.

3.7. X-ray photoelectron spectroscopy (XPS)

In X-ray photoelectron spectroscopy (XPS), soft X-rays (generally with energy lower than 6 keV) are used to irradiate the sample, where electrons are emitted after full transfer of energy from the X-ray, and the kinetic energy of these electrons is measured[173]. The relationship between the energy of the incident X-ray and the energy of the emitted electron can be expressed as Equation (3.8);

$$h\nu = BE + KE + \Phi_{spec} \tag{3.8}$$

Equation (3.8) shows that the energy of the X-ray ($h\nu$) is equal to the sum of binding energy (*BE*) of the electron, the kinetic energy of the electron emitted (*KE*), and the work function of the spectrometer Φ_{spec}[173]. The interaction can be visualised in Figure 3.8. After ejection of the photoelectron, the hole left in the inner shell leads to either X-ray fluorescence (XRF) or emission of an Auger electron. X-ray fluorescence is not normally detected in XPS. If the Auger electrons interfere with peaks of interest, the effect due to Auger electrons is normally mitigated by switching to another electron source[174]. For example, when a Mg source is used, Ga would produce an Auger peak at 281 eV, which coincides with the peak of C 1s. By switching to an Al source, the Auger peak can be moved to 514 eV, which does not interfere with the main peaks[173].

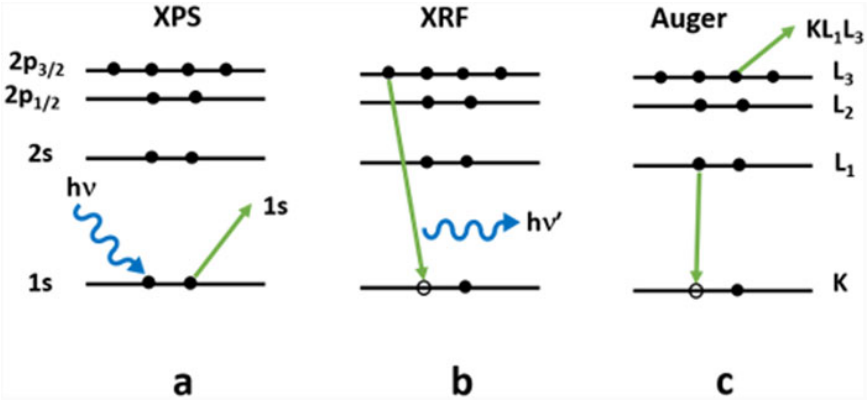

Figure 3.8. Diagrams showing events after X-ray irradiation interacts with the sample. (a) An electron is ejected from the sample as a photoelectron. (b) X-ray fluorescence. (c) Auger electron emission. Figure reproduced with permission from reference[173]. Copyright 2020 AIP Publishing.

XPS is a frequently applied technique for surface analysis[175], which can probe around 10 nm deep from the sample surface[176]. It can identify all elements except hydrogen and helium, due to the different binding energies of the photoelectrons emitted[175]. The peaks in an XPS spectrum are conventionally denoted by the element and the orbital the electron is ejected from, e.g. 'C 1s'. A visual representation of the XPS technique is illustrated in Figure 3.9. Energy spectra, along with a spatial image and depth profile of the sample can be obtained from XPS[177]. However, in the work reported in this thesis only energy spectra are required, so this section does not cover the other modes.

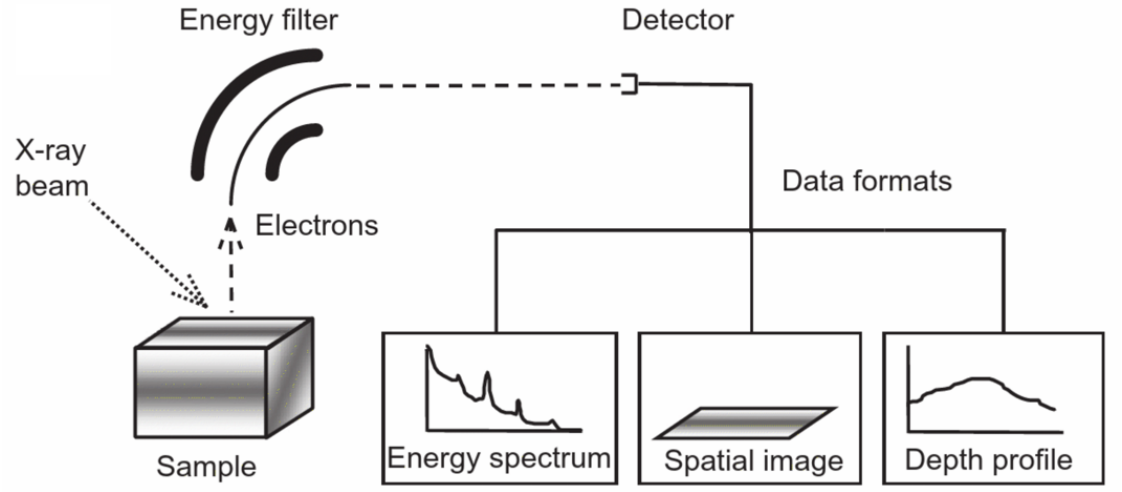

Figure 3.9. The basic mechanism of an XPS instrument. Reproduced with permission from reference[177]. Copyright 2012 John Wiley & Sons, Inc.

In an XPS instrument, ultra-high vacuum (10^{-9}-10^{-10} mbar) is essential to eliminate electrons scattered by air molecules and to prevent accumulation of surface contaminants[173,176]. To generate X-rays, an electron beam impacts a metal target biased as an anode. LaB_6 or W filaments are often used to extract electrons and Mg and/or Al anodes are used as targets[177]. For a monochromated source, Al is the most popular choice, mainly because of the high intensity of Al K_α X-rays and their minimal energy spread[177]. Unwanted Bremsstrahlung and Auger electrons from the anode are also emitted, but with a monochromator in place, they can be removed[173]. The monochromator is normally fitted for the Al source, where a quartz crystal is placed to allow Al K_α radiation to achieve Bragg diffraction criteria, and direct the radiation to the sample, while filtering out other radiations[178]. Figure 3.10 (a) illustrates how the monochromator works.

Since the kinetic energy of the electron is important in XPS to obtain information about the sample, an analyser is used to measure the kinetic energy of the photoelectrons in XPS[176]. The analyser that is fitted in most modern XPS is called the concentric hemispherical analyser (CHA)[177]. The main advantage of a CHA is its fine energy resolution, which is smaller than 0.01 eV. This value is so small that the main limiting factor to the energy resolution of an XPS instrument is the electron source (typically between 0.2 and 0.3 eV)[177]. Figure 3.10 (b) shows the configuration of a CHA, where different potentials are applied to the outer and inner hemisphere. This induces a deflection of the electrons and only those with specific energies can reach the detector[177], and a set of electron extraction lenses are installed before the analyser to determine the collection angle and the area of sample to be assessed[173]. Before entering the analyser, the electron is accelerated or decelerated to a specific energy, which is the pass energy[177]. Lower pass energy leads to better energy resolution, but worse sensitivity[177].

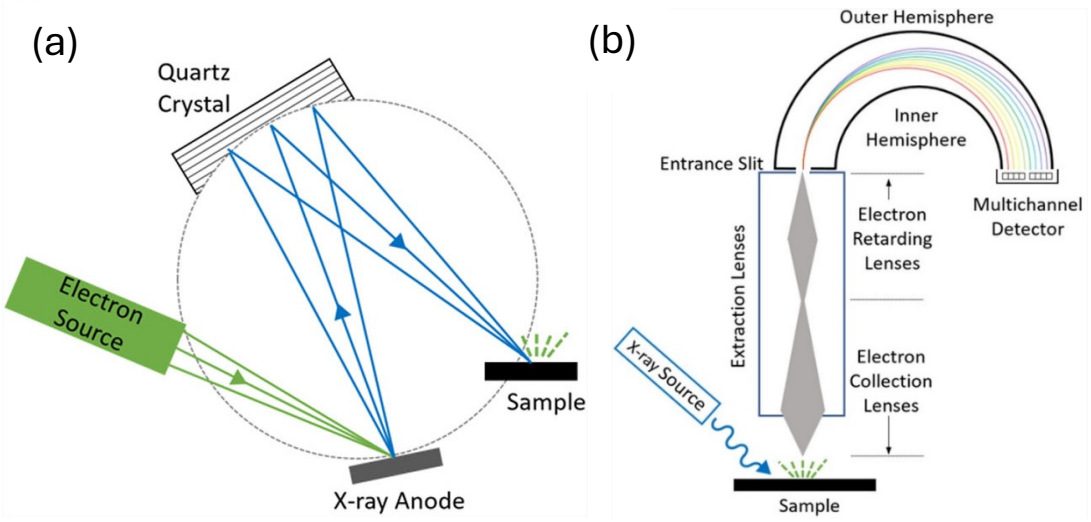

Figure 3.10. Schematic diagrams of (a) working mechanism of a monochromator, and (b) extraction lenses and the concentric hemispherical analyser after emission of photoelectrons from the sample. Reproduced with permission from reference[173]. Copyright 2020 AIP Publishing.

For data collection, both the energy of photoelectrons emitted from the sample and their quantity are important[177]. XPS spectra are normally plotted as intensity against energy, and the intensity is defined by the number of electrons with a specific amount of energy[177]. Multiple factors can affect the binding energy of a specific element. For example, in different environments the binding energy of C 1s in the same molecule can be different, as the binding energy of C 1s in C-C is different from that of C-O. This is due to the difference in electronegativity of the neighbouring atom[173]. Another factor that affects binding energy is the oxidation state of a transition metal. When an atom has already lost one or more electrons, the ion will carry a positive charge, making the remaining electrons harder to be removed. The binding energy will hence be higher[173].

XPS spectra in this thesis were collected by a Thermo Scientific 250Xi, using monochromated Al K_α as the source (energy = 1486.6 eV) working at 150 W with an X-ray spot size of 500 μm, 12.5 kV voltage and a filament current of 16 mA. The pass energy was set at 80 eV.

For in-situ XPS, samples were prepared by adding ca. 20 mg of sample into a 1 mm thick borosilicate glass capillary tube, which was filled with less than 0.1 mL methanol. The amount of methanol added was very low in order to reproduce the reaction with methanol vapour. Next, the tube was cut to 6 cm, with the open end sealed by Araldite glue. This tube was then placed in the XPS instrument, with the Xe lamp turned on for in-situ analysis.

3.8. Gas chromatography (GC) and quantification of hydrogen

3.8.1. Principles of gas chromatography

Chromatography is a technique which separates and analyses the components of a sample, using a stationary phase and a mobile phase[179]. The stationary phase is typically a thin film with large surface area, and the mobile phase is the sample moved by a carrier gas or liquid[180]. In gas chromatography (GC), the sample is carried in gaseous form, and the separation process takes place in the column[179]. Figure 3.11 (a) gives visual aids to chromatography. A mixture comprising components A and B is injected into the column. The area above the line represents the amount of the constituent in the mobile phase, and the area below the line represents the amount of the constituent in the stationary phase. Since component A interacts less with the stationary phase, it flows faster along the column and reaches the detector earlier than component B. On the chromatogram produced at the detector output, the peak corresponding to component A hence appears earlier than the peak corresponding to component B in the time domain[179].

GC possesses advantages that make it a popular technique; each analysis normally takes only minutes; it yields high resolution data, with sensitivity down to parts per billion; only trace amount of sample is needed (in microlitres); and it is reliable and simple to operate[179]. A GC system consists of four major parts; injector, column, detector and data processing units[182]. Figure 3.11 (b) shows how these parts work together for sample analysis.

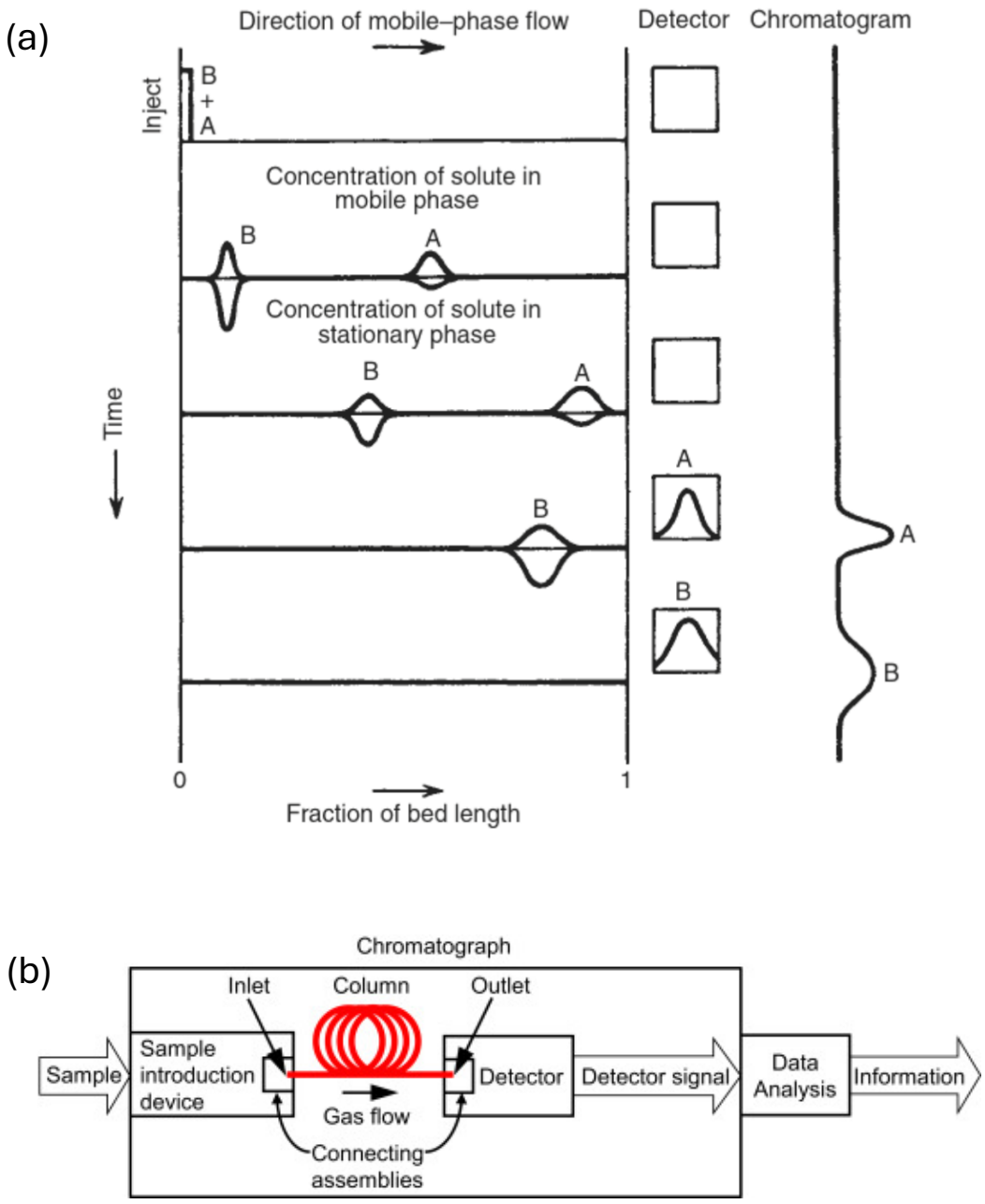

Figure 3.11. (a) The separation of components A and B from a mixed sample in a chromatography column. Reproduced with permission from reference[181]. Copyright 2005 John Wiley & Sons, Inc. (b) Flowchart demonstrating GC analysis. Diagram reproduced with permission from reference[183]. Copyright 2021 Elsevier Inc.

When the sample is introduced into the system, it is subjected to a burst of heat normally at 200-300°C, and then mixed with the carrier gas (Ar, H_2, He or N_2)[182]. This step seems simple but is arguably the most important section in GC analysis[184]. Four types of injectors are commonly used for liquid samples: cold on-column, split, splitless and programmed temperature vaporisation[179,184]. None of these injectors suit all scenarios, so the selection

of the injector should be considered based on the requirements of the user. Table 3.1 provides a guide on choosing an appropriate injector.

Table 3.1. Basic guidelines on selecting a suitable injector based on reference[184]. The list is not exhaustive. For the ratings, the larger the number, the better the injector is for that specific type of sample analysis. "0" is the lowest score while "4" is the highest.

Injector	Cold on-column	Classical split	Classical splitless	Programmed split	Programmed splitless
Type	Non-vaporising	Vaporising	Vaporising	Non-vaporising	Non-vaporising
Concentrated samples	1	3	1	4	1
Diluted samples	4	1	3	1	3
Trace samples	3	0	2	0	2
Volatile compounds	1	3	1	3	1

In terms of gas injection, a manual syringe can be used, but a gas sampling valve gives better performance[179]. A gas sampling valve involves a rotor with etched channels leading to different ports, and through control of the rotor, the channels can be connected or disconnected[184]. Figure 3.12 gives an example of how a 6-port valve injects gas sample into the column. Only at the point of injection will a fraction of the gas sample be mixed with the carrier gas and enter the column.

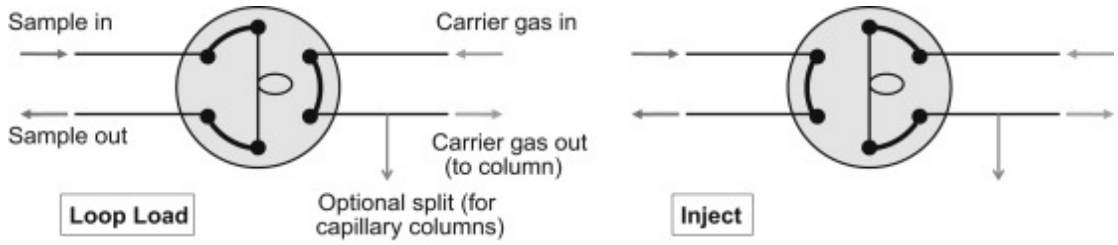

Figure 3.12. Schematic diagram showing the working mechanism of a 6-port valve. Reproduced with permission from reference[184]. Copyright 2012 Elsevier Inc.

While packed columns were commonly used in the early days of GC, they have been almost completely replaced by open tubular capillary columns, especially wall-coated open tubular (WCOT) capillary columns[185]. As the name suggests, packed columns are filled with granular particles coated with the stationary phase, while open tubular columns have the

stationary phase applied along the inner wall of the tubing[180]. Compared with packed columns, open tubular columns offer far superior separation, shorter analysis time, higher sensitivity and lower cost[180]. WCOT capillary columns are typically made of fused silica, with internal diameters ranging from 0.1 mm to 0.53 mm, and their lengths vary from 10 metres to 60 metres[179]. A thin layer of polyimide coating is applied on top of the outer fused silica wall to prevent the column from being corroded or cracked[179].

A variety of detectors can be fitted onto a GC, and among the readily available conventional detectors, flame ionisation detector (FID) and thermal conductivity detector (TCD) are discussed in this section. FID is the most used detector in GC, which can be implemented for organic compounds[186]. When the sample mixed with carrier gas enters FID, it is combusted with a small oxygen-hydrogen flame, creating ions. The ions are collected, which creates a current and produces a signal[186]. Unlike FID, a type of mass flow rate detector that directly evaluates the amount of substance, TCD is a type of concentration detector that assesses the concentration of the substance in the mixture with carrier gas[179]. It is generally used to detect substances where FID is inadequate in, such as for hydrogen[186]. This is because FID uses a flame containing hydrogen. TCD relies on sensing the difference in the thermal conductivity between the pure carrier gas and carrier gas with the sample, and heated filaments in cavities are in place to capture such changes[186]. A TCD typically incorporates a Wheatstone bridge, and introduction of a sample leads to an increase in the resistance in one side of the filaments, creating a voltage which is recorded[179,186]. The minimum detectable quantities for FID are around 50 parts per billion, and for TCD it is about 10 parts per million[179].

3.8.2. Hydrogen quantification process

The amount of hydrogen can be calculated using the ideal gas equation as;

$$PV = nRT \tag{3.9}$$

In Equation (3.9), P is the pressure of gas entering the GC, V is the volume of gas in the reactor, n is the amount of gas in moles, R is the gas constant (8.314 J mol^{-1} K^{-1}), and T is the temperature in Kelvin.

For the reaction system in this project, the pressure of reactor was set at 2 bar, the corresponding volume of gas was measured to be 0.09 L, and the temperature was 297 K. By rearranging Equation (3.9) and substituting these values in, the amount of gas is 0.00739 moles. This is the mixture of gas containing argon and the products, especially hydrogen, from the photocatalytic reaction. By allowing the mixture to flow into the GC for analysis, a peak corresponding to H_2 will appear on the output of the TCD, and the peak area represents the percentage of H_2 in the mixture. The calibration of the GC gives Equation (3.10), revealing the relationship between the area under the peak (y) and the percentage of hydrogen in the gas mixture (x);

$$y = 975.51x \tag{3.10}$$

The area under the curve can now be used to calculate the amount of H_2 in the mixture.

3.8.3. Turnover frequency calculations

From Section 2.3.1, the unit of the photocatalytic hydrogen production rate is typically μmol g^{-1} h^{-1}, which can be further converted to reaction rate per active site on the surface of the catalyst. This is the turnover frequency (TOF), and its unit is s^{-1}.

As an example, the conversion process from μmol g^{-1} h^{-1} to TOF for CABB nanocubes is discussed here. From Figure 4.2 it can be estimated that each nanocube has a 10 nm edge approximately. From Figure 4.14 as well as other high resolution STEM images, the average distance between each active site (Ag or Bi, as discussed in Section 4.2.6) is measured to be 0.597 nm. Assuming that the active sites are exposed on the surface of the cubes, the number of active sites sitting on each edge is 17, and the total number of active sites on each cube, N, is;

$$N = 6n^2 - 12n + 8 \quad (3.11)$$

where n is the number of atoms or active sites on each edge. By substituting in n = 17, the value of N is 1538.

If the reaction rate is 1 μmol g^{-1} h^{-1}, it can be converted to 1.673 x 10^{14} molecules per gram per hour using Avogadro's Number. The density of CABB is 4.9268 g cm^{-3}, estimated from the model provided by McClure et al.[71]. For one gram of the nanocubes, the total volume is hence 2.0297 x 10^{-7} m^3. As the volume of each cube is about 10^{-24} m^{-3}, the number of cubes per gram is 2.0297 x 10^{17}, and thus the number of active sites per gram is 3.122 x 10^{20}. The TOF of the cubes for 1 μmol g^{-1} h^{-1} is 5.359 x 10^{-7} s^{-1}, assuming that the cubes are separated.

Similarly, the bulk form of CABB may be estimated as 3 μm cubes, and the TOF for 1 μmol g^{-1} h^{-1} is 1.469 x 10^{-4} s^{-1}. For CABB nanosheets, they can be estimated as cuboids with two edges being 100 nm x 100 nm, and the thickness 4.8 nm measured by Liu et al.[87]. The TOF for 1 μmol g^{-1} h^{-1} is 6.472 x 10^{-7} s^{-1}.

3.9. Zeta potential and surface charge

Even though surface charge and zeta potential of a particle are two separate properties[187], the surface charge can be assessed based on the value of zeta potential[188]. Zeta potential is defined as the potential of the slipping plane of a moving colloid particle under the influence of an electric field, and Figure 3.13 explains the relevant terms[189]. A particle with positive or negative surface charge attracts ions of opposite charge at its surface, and a layer of tightly bound ions is thus formed, which is called the Stern layer[190]. In another region beyond the Stern layer, the ions are less firmly associated, and this layer is called the diffuse layer[190]. These two regions make up the electrical double layer, EDL[191]. When the charged particle moves under the effect of an electric field, which is called electrophoresis,

a theoretical interface is formed somewhere within the diffuse layer, separating the moving parts and the rest of the dispersant in solution[191]. This interface is called the slipping plane, and the potential at this plane is the zeta potential[189].

Zeta potential data in this thesis were collected using Zetasizer Pro Blue, using a folded capillary zeta cell (Malvern Panalytical). To prepare for suspension, CABB samples were diluted in ethanol, and the concentration was 100 mg / L. Amy Radford kindly carried out the measurements to obtain zeta potential data.

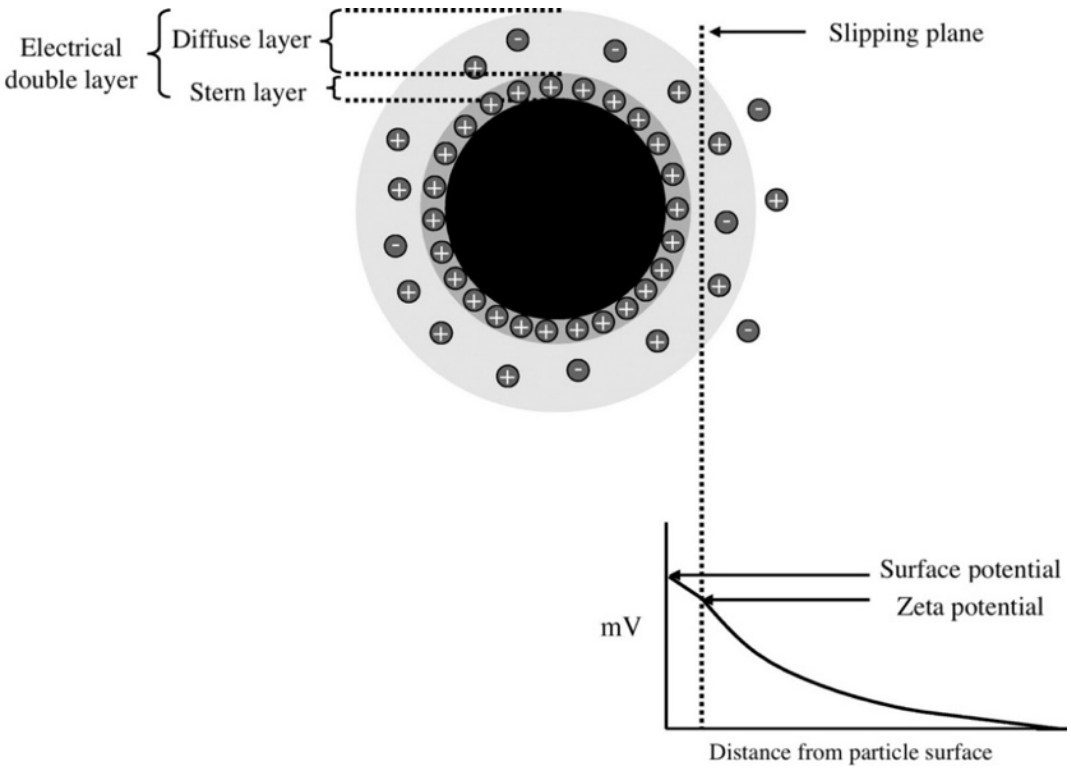

Figure 3.13. Schematic diagram showing the concepts of electrical double layer including stern layer and diffuse layer, as well as slipping plane and zeta potential. Adapted from reference[189] under Creative Commons Attribution License. Copyright 2010 The Royal Society.

3.10. (Time-resolved) photoluminescence

Photoluminescence is the process where a substance absorbs electromagnetic radiation and then emits electromagnetic radiation itself[192]. In the photoluminescent process, when the photon is absorbed by the material, an electron would jump to an excited state. It will eventually fall back to a lower energy state, emitting energy as a photon[193,194]. The photoluminescence spectroscopy (PL) records signals regarding the photons emitted from the sample, which reveal information on its electronic structure.

A typical setup for PL measurements is illustrated in Figure 3.14. In this system, the laser is directed to the sample, and the photoluminescence signal is collected by a spectrometer. Before the signal reaches the spectrometer, it normally goes through a long pass filter to block out the laser[194].

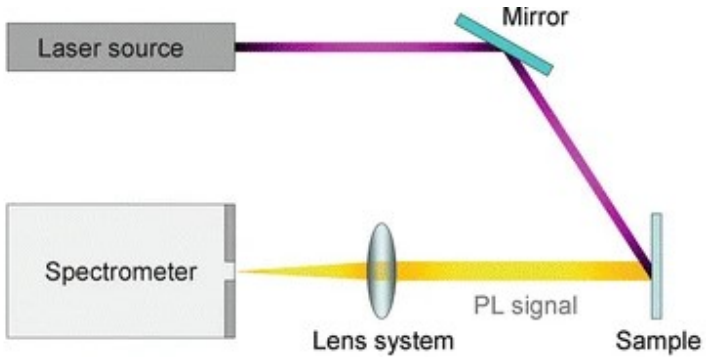

Figure 3.14. Schematic diagram of a typical setup for PL measurements. Reproduced with permission from reference[195]. Copyright 2013 Springer-Verlag Berlin Heidelberg.

To record transient photoluminescence signals, a widely used technique is time-resolved photoluminescence (TRPL), and a diagram of the arrangement is shown in Figure 3.15. A single-photon detector and a time counting device are in place. The laser pulse is directed to the sample, and the first photon emitted by the sample that reaches the detector is recorded. This process is repeated at a frequency in kHz–MHz. Even though only one photon is detected for each laser pulse, this procedure is repeated multiple times, and the data points together resemble a PL decay curve over time elapsed[196].

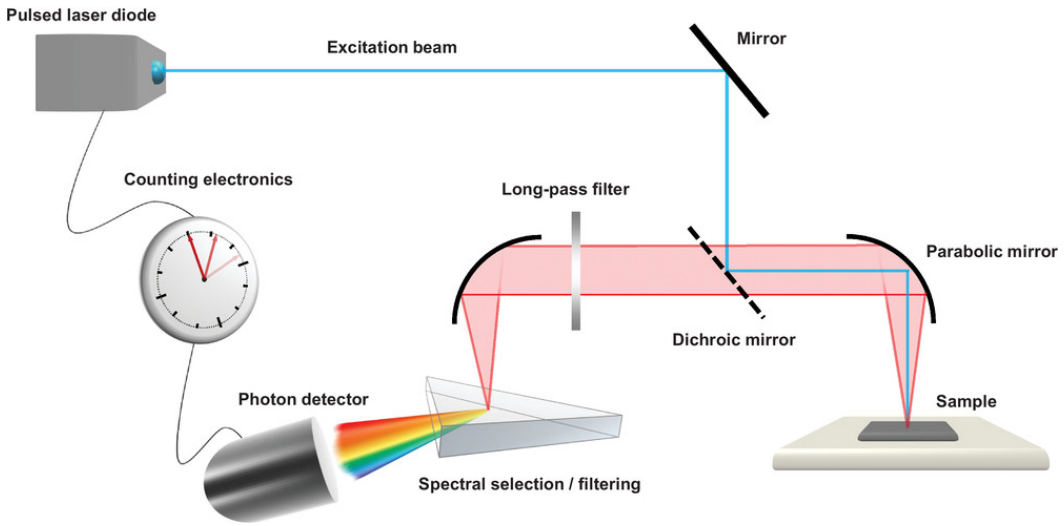

Figure 3.15. Illustration of the components for TRPL measurements. Reproduced from reference[196] under Creative Commons Attribution Licence. Copyright 2020 The Authors.

In this thesis, the photoluminescence spectra and the charge carrier lifetimes of the samples were acquired using a bespoke micro-photoluminescence setup. A frequency-tripled Ti-Sapphire laser was guided onto the sample. The laser has a wavelength of 266 nm, with a pulse duration of 120 fs, and a repetition rate of 76 MHz. Dr Yiyang (Bruce) Li kindly conducted the measurements to acquire PL and TRPL data.

In terms of time-resolved measurements, pulse-picking mode was adopted. The interval between two laser pulses were adjusted to 100 ns, so the excited charge carriers can relax to the ground state completely, before the next pulse reaches the sample. A zero-signal reading signifies the charge carriers have returned to the ground state. The spectrometer, fitted with a monochromator, passes the signal to an avalanche photodiode detector (APD) connected to a time-correlated single-photon counting module. The APD has an instrument resolution of around 50 ps. By fitting the corresponding background-corrected PL spectra with a bi-exponential decay function, the charge carrier lifetime of the sample can be acquired. A least square method was used to verify the errors in the fitting.

3.11. Electron microscopy and sample preparations

3.11.1. (Scanning) transmission electron microscopy

In (scanning) transmission electron microscopy, or (S)TEM, electrons are used to produce high resolution information from the sample. Electrons possess wave-particle duality, and the electron wavelength, λ, can be estimated using de Broglie's relationship as;

$$\lambda = \frac{h}{p} = \frac{h}{\sqrt{2mE_o}} \tag{3.12}$$

where *h* is the Planck's constant, *p* is the momentum of electron, *m* is the mass of electron, and E_o is the kinetic energy of the electron. E_o is equal to eV, where e is the charge of electron, and V is the accelerating voltage.

Considering relativistic effects since the speed of electron approaches the speed of light, Equation (3.12) becomes;

$$\lambda = \frac{1.22643}{\sqrt{V(1 + 0.978476 \times 10^{-6}\, V)}} \tag{3.13}$$

where *V* is in volts and λ is in nanometres[197]. At *V* = 100 kV, λ = 0.00370 nm and at *V* = 200 kV, λ = 0.00251 nm. These values are smaller than the radius of an atom, and even though the optics of electron microscopes are imperfect it is possible to achieve atomic resolution.

Figure 3.16 (a) and (b) show diagrams for TEM and STEM respectively. In a TEM, a condenser aperture is usually placed after the condenser lens to block electrons approaching the sample at large angles[198]. An objective aperture is also located after the objective lens that controls the resolution and contrast of image, by setting a maximum collection angle[199].

The main difference between TEM and STEM is the way they probe the specimen. TEM uses a broad beam that is nearly parallel to the specimen surface, while STEM uses a fine focussed (generally convergent) beam that scans the region of interest position by

position[198]. Most microscopes have now combined both TEM and STEM, and Figure 3.16 (c) shows schematically the arrangement of an integrated (S)TEM. Some of the components are further discussed in this section.

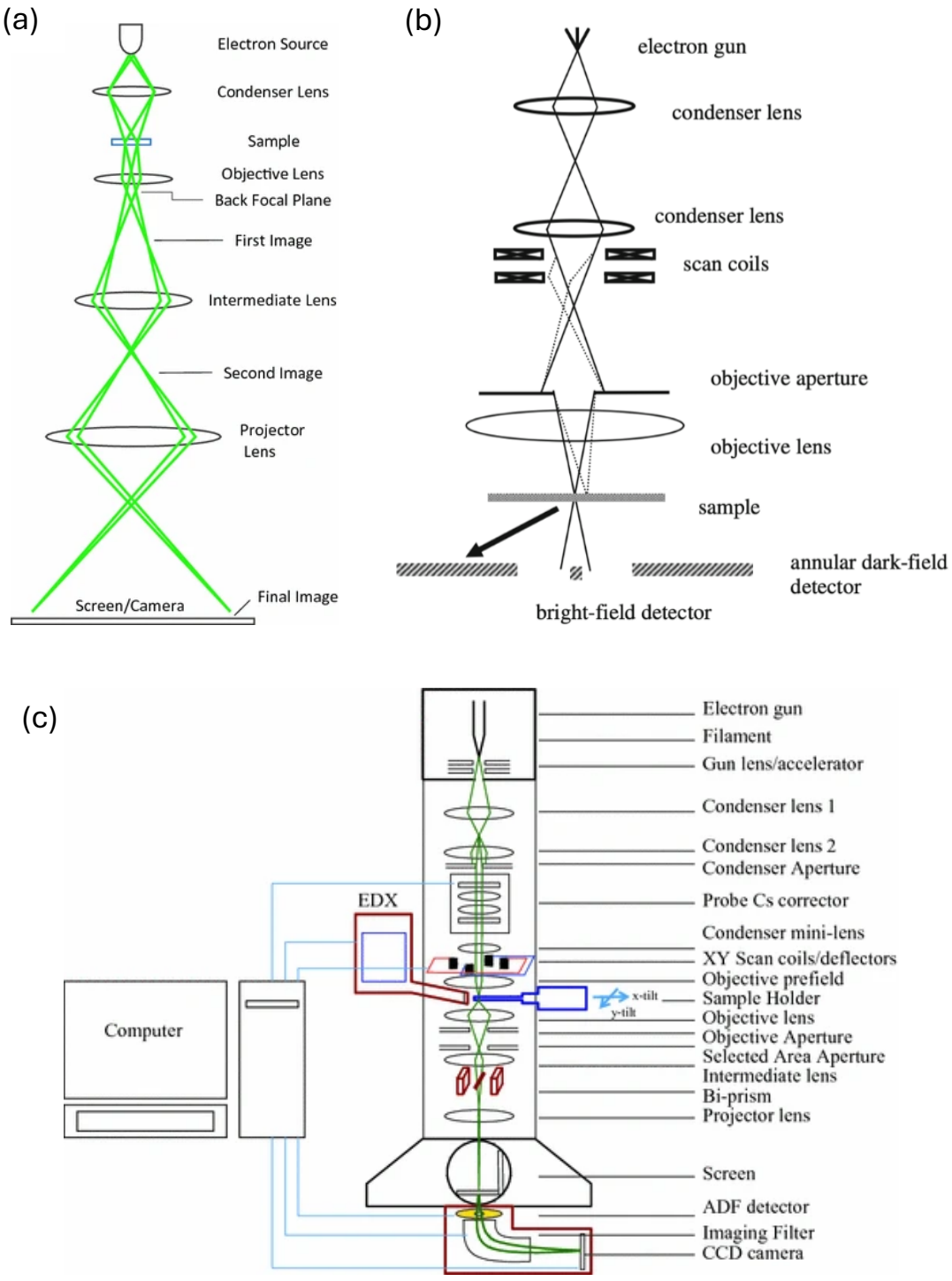

Figure 3.16. Simple ray diagrams of (a) TEM and (b) STEM. (a) Reproduced with permission from reference[197]. Copyright 2017 Springer Science Business Media New York. (b) Reproduced with permission from reference[200]. Copyright 2011 Springer Science Business Media, LLC. (c) Typical setup of a combined (S)TEM. Reproduced with permission from reference[197]. Copyright 2017 Springer Science Business Media New York.

To choose an appropriate electron source, some important parameters need to be considered: source brightness, size, energy spread and stability[197]. Brightness at the source (*B*) is defined by current density (*j*) per unit solid angle of the source ($d\Omega$);

$$B = \frac{j}{d\Omega} = \frac{j}{\pi\alpha^2} \tag{3.14}$$

where α is the divergence semi-angle[201]. Higher brightness means more electrons can be fitted into the electron beam, and hence more information can be obtained from the specimen, while sensitive specimens are more likely to suffer from beam damage[199].

A smaller source size gives better spatial coherency and better quality of electron illumination[197,199]. When perfect spatial coherence is achieved, the electrons are effectively emanating from the same point at the electron source[199]. The spatial coherence can be measured by the fringes created by interference of electrons[199]. The source size for coherent illumination can be defined in terms of distance, *d*;

$$d = \frac{\lambda}{2\alpha} \tag{3.15}$$

where λ is the wavelength of electron, and α is the angle subtended at the specimen from the source[199]. To improve spatial coherence, three methods can be adopted: using an electron source with a smaller source size, such as a field-emission source which is discussed later; inserting an aperture and α can be lowered; decreasing the accelerating voltage to increase λ for a material with large source size[199].

Ideally the electrons should also be temporally coherent, where the frequency of electrons is the same. If the electrons as waves have the same frequency, then they have the same coherence length. The coherence length, λ_c, can be defined as;

$$\lambda_c = \frac{vh}{\Delta E} \tag{3.16}$$

where v is the velocity of electron, h is Planck's constant, and ΔE is the energy spread of the beam[199]. To improve temporal coherence, the energy spread should be kept minimal[199].

There are two main types of emission source available: thermionic and field-emission (FE). In a thermionic source, the electrons are generated by applying heat to the material[197]. The material used for a thermionic source is either tungsten or LaB_6[201]. In a cold field emission gun (CFEG), a Tungsten as source is made into a fine sharp single crystal tip, with two sets of anodes in place to extract and then accelerate the electrons[202]. The CFEG has a lot of advantages, but flashing (applying a current to heat up the tip) is needed to remove the contamination during a session[197]. A Schottky source merges both heat and field emissions[199]. It is made of a tungsten tip coated with zirconia. Table 3.2 gives a list of different parameters for different electron sources.

Table 3.2. Operating parameters for different electron sources used in (S)TEM at 100 keV[199,203].

Electron Source	W filament	LaB_6	Schottky	Cold FEG
Cathode temperature (K)	2500-3000	1400-2000	1800	300
Work function (eV)	4.5	2.7	2.7	4.5
Emission current density (A m^{-2})	$1 \times 10^4 - 3 \times 10^4$	$2 \times 10^5 - 5 \times 10^5$	5×10^6	10^9-10^{10}
Brightness (A m^{-2} sr^{-1})	$1 \times 10^9 - 5 \times 10^9$	$1 \times 10^{10} - 5 \times 10^{10}$	5×10^{12}	10^{13}
Energy spread (eV)	1.5 – 3	1 – 2	0.3 – 0.7	0.2 – 0.7
Vacuum (Pa)	$\leq 10^{-3}$	$\leq 10^{-4}$	$\leq 10^{-6}$	$\leq 10^{-8}$

As already described, the wavelength of electron and hence the ideal resolution of the microscope is less than 0.01 nm, but this is not easily achievable. The two major limiting factors are chromatic and spherical aberrations of the lenses[198,201]. Chromatic aberration (C_c) has an effect when the electron beam is not monochromatic, where electrons with lower energies are deflected more strongly than those with higher energies[202]. Using a CFEG

source can alleviate the issue as it has a small energy width. C_c is also less of an issue before spherical aberration (C_s) is corrected[199]. This is because for Schottky and field emission guns whose energy spread is less than or equal to 0.3 eV, at an operating voltage that is 200 kV or higher, the effects brought by chromatic aberrations are a lot less significant than spherical aberrations[203]. When C_c becomes significant that it needs correcting, electric-magnetic multipole fields can be applied for correction[197,204]. C_s occurs because electrons travelling off axis are bent more strongly by the lens, and the image of a point becomes a disc at the image plane[199]. C_s correctors are commercially available, and an early optical design used a combination of two hexapoles and two round lenses[197].

Electron diffraction patterns can reveal structural and other information regarding the specimen, and diffraction patterns obtained in a TEM mode are discussed here. The diffraction patterns usually consist of spots and/or rings.

To analyse these patterns, Bragg's law is first converted into vector form as;

$$\vec{S} = \vec{K} - \overrightarrow{K_o} = \vec{g} \tag{3.17}$$

where $\vec{S}$ is the scattering vector, which is the difference between the incident wave vector, $\overrightarrow{K_o}$, and the diffracted wave vector, $\vec{K}$, on scattering[197]. This relationship can be visualised using Figure 3.17 (a). In addition, we have;

$$\left|\vec{K}\right| = \left|\overrightarrow{K_o}\right| = \frac{1}{\lambda} \tag{3.18}$$

and;

$$\left|\vec{S}\right| = \frac{2\sin\theta}{\lambda} \tag{3.19}$$

At the Bragg angle, θ_B, combining Equations (3.1), (3.17), (3.19) and let n = 1, we get:

$$|\vec{g}| = \frac{1}{d} \tag{3.20}$$

This is Bragg's law in reciprocal space[199].

A 3D crystal consisting of numerous unit cells becomes a set of points in reciprocal space, with each point corresponding to a certain group of planes in the crystal[199]. Based on the discussion above, we consider a sphere with radius being 1/λ. It cuts through some of the points in the reciprocal lattice, where the Bragg condition is met. The sphere is known as the Ewald sphere[199] as shown in Figure 3.17 (b) in 2D.

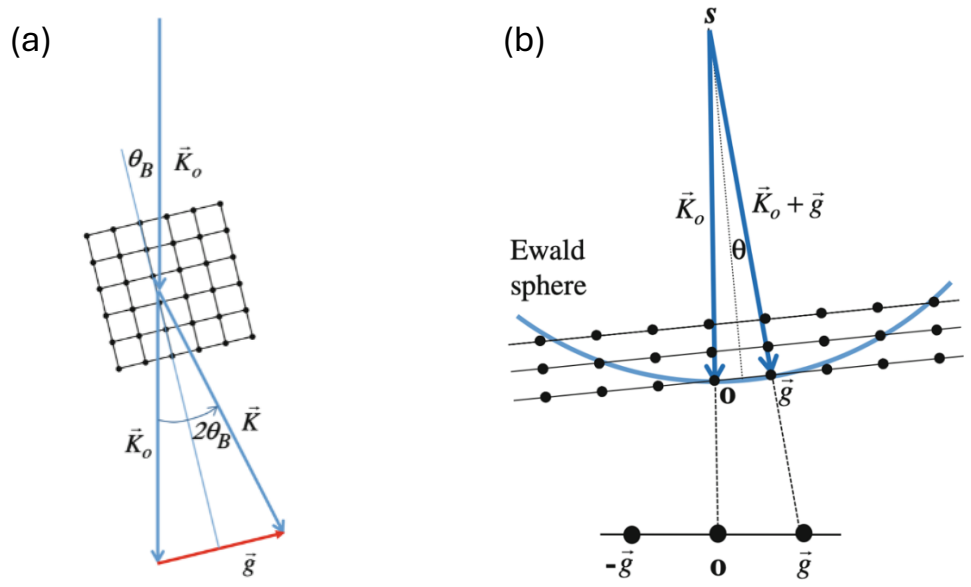

Figure 3.17. (a) Bragg diffraction illustrated in vector form. (b) Construction of an Ewald sphere in a reciprocal lattice. Reproduced with permission from reference[197]. Copyright 2017 Springer Science Business Media New York.

The direction of a zone axis [uvw] is the direction following the intersection of two or more planes[199]. For the reflection of a plane (hkl) to appear on the diffraction pattern, it needs to obey the Weiss zone law;

$$hu + kv + lw = n \tag{3.21}$$

where n is an integer. Each integer represents a planar section in reciprocal space that is normal to the zone axis, and these sections are named Laue zones[197]. When n = 0, this corresponds to the zero-order Laue zone, followed by the first-order Laue zone (FOLZ), second-order Laue zone (SOLZ) and higher order Laue zones (HOLZ) for n = 1, 2,...

respectively[197,199]. The reciprocal lattice points are in practice shaped like a rod, often known as a relrod (reciprocal lattice rod). When the Ewald sphere intersects the relrod, a reflection will appear on the diffraction pattern, even though the Bragg condition is not exactly fulfilled[199]. Relrods originate from the conversion of actual TEM thin foil specimen to reciprocal space, where something that is very large in real space appears very small in reciprocal space. The thin film specimen is virtually infinitely large normal to the direction of electron beam, while being very thin parallel to the beam. The intensity of diffraction can hence be represented as rods in reciprocal space[199]. Figure 3.18 (a) shows an illustration of the relrods within a thin foil crystal. Figure 3.18 (b) gives an example of the effects the relrods can bring, and in this case extra diffraction reflections were created. In addition to the example provided in Figure 3.18 (b), even when the extra reflections were not created, and the Ewald sphere did not cut right through the (020) point, but instead through the relrod from (020), the diffraction reflection representing (020) could still be observed in the diffraction pattern.

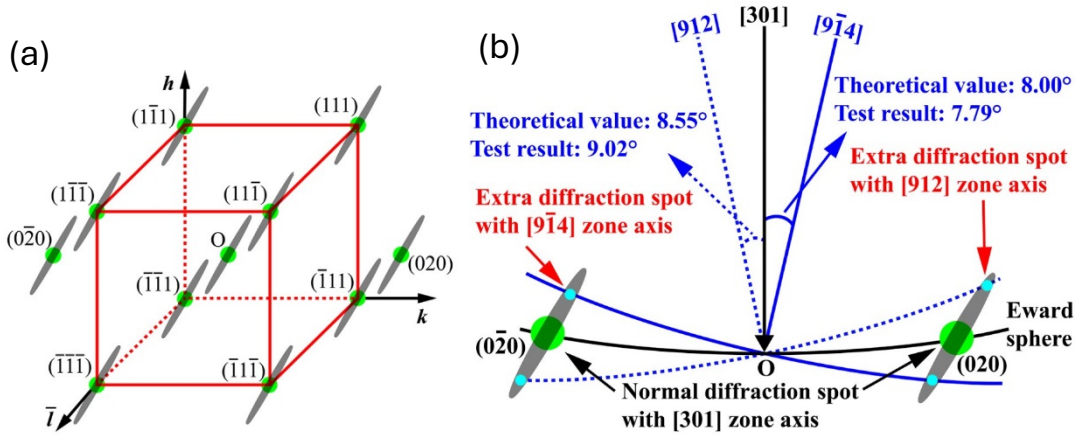

Figure 3.18. (a) The relrods of a thin foil specimen with a face-centred cubic structure. (b) Creation of extra diffraction reflections caused by the relrods. Reproduced with permission from reference[205]. Copyright 2019 IOP Publishing.

To form an image, detectors are placed below the specimen to collect information from the transmitted or scattered electrons. Figure 3.19 shows typical detectors used in STEM. Forward-scattered electrons travelling along the axis are recorded by the bright field (BF)

detector, which gives contrast equivalent to a bright field image in TEM[199,206]. Electrons travelling at small angles (<3°) are recorded by an annular dark field (ADF) detector, and those travelling at higher angles are collected by a high angle annular dark field (HAADF) detector[199]. Both ADF and HAADF detectors are circular discs. All three detectors can be used simultaneously, and adjustments can be made, such as the retraction of BF detector for electron energy loss spectroscopy (EELS) analysis[206].

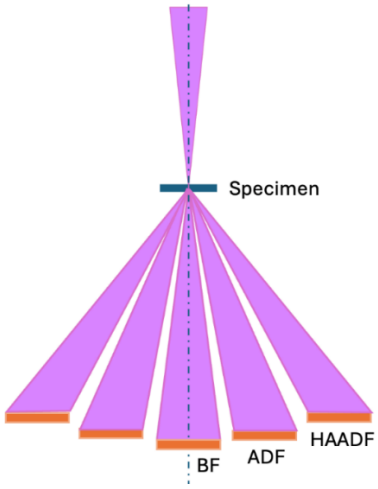

Figure 3.19. Illustration of typical detectors used in STEM.

When the electron beam interacts with the specimen, one type of signal produced is the characteristic X-ray (as previously described in Section 3.4). It can be collected by an energy dispersive X-ray (EDX) detector. Each element has unique X-ray energies, so they can be used to identify the elements present in the specimen.

The electron beam can easily introduce damage and other unwanted effects in the specimen. The structure or chemistry may be changed as a result, so that the TEM specimen is no longer a good representation of the sample[199]. There are three main types of beam damage: radiolysis, knock-on damage (or sputtering), and heating[197]. Radiolysis is a result of inelastic scattering, where ionisation breaks chemical bonds in the specimen and leads to atomic rearrangement[197,199]. Knock-on damage is caused by point defects originating from atomic displacements from the lattice, and it is known as sputtering if

atoms are expelled from the specimen surface[199]. Heating of the illuminated area can also give rise to significant damage. There are various techniques available to reduce these effects, depending on the specimen and the information required. Typical methods include lowering the accelerating voltage, reducing the electron fluence and operating in a cryogenic environment.

In this thesis, TEM images and diffraction patterns were acquired using a JEOL JEM-2100 using a LaB_6 source operating at 200 kV. Bright-field images were taken using a Orius SC200W Bottom Mount camera, and the diffraction patterns were recorded using a Orius SC200D Diffraction camera. STEM data were acquired using a JEOL JEM-ARM200F (with a cold field emission source, and a spherical aberration corrector) at 200 kV. For STEM-HAADF images, the inner collection angle was 72.80 mrad, and the outer collection angle was 235.75 mrad. The convergence angle used was either 22.48 mrad for the 30 µm aperture, or 14.38 mrad for the 20 µm aperture. The STEM-EDX data were collected using a 100 mm^2 Centurion EDX detector. Camera length was kept at 8 cm for all STEM acquisitions.

3.11.2. Electron fluence calculations

3.11.2.1. For TEM

To begin, a Faraday cup was used to measure the current of the electron beam in TEM. Since the sample and Faraday cup could not be inserted at the same time, the magnification and brightness were kept constant. The magnification of the TEM was set at 4000x. The brightness was set to lowest value possible, by turning the brightness knob clockwise to underfocus and fully spread the electron beam. The current readings using different condenser apertures and different spot sizes were also recorded. The 70 µm condenser aperture at Spot 5, which yielded a beam size of 13.3 µm, gave the best quality of diffraction patterns. This is because the electron fluence per second (i.e., electron flux) is low enough that the sample would not degrade instantly, while the changes in intensity

of the reflection over time could be captured. The size of the beam was estimated from images at the edge of the beam, so the area of the circle (i.e. the electron beam) could be calculated. This arrangement was used to calculate the critical electron fluence above which the sample structure is likely to degrade.

Having obtained the beam current, the Faraday cup was removed, and the specimen was inserted into the TEM. The TEM was then switched to diffraction mode, and the stage was moved until a clear diffraction pattern could be seen. As soon as the diffraction pattern was observed, a series of images were taken, and the total time to record each image was also noted. The intensity of the reflections decreased with time. Different reflections were chosen to create plots of reflection intensity against time. The reflections picked for calculations were clearly bright at the beginning of the imaging, and not too close to another reflection for overlapping crystals. The intensity-time relationship could be matched to the following equation;

$$S = Ae^{bt} \tag{3.22}$$

Where *S* is the intensity of a reflection, *A* and *b* are constants, and *t* is the time elapsed. The intensity of the reflections was measured in Gatan DigitalMicrograph, using a suite of software tools developed by David Mitchell called DiffTools[207]. The critical electron fluence was determined to be when $S = \frac{A}{e}$, and hence the corresponding value of *t* could be calculated. The total charge, *Q*, was then calculated using;

$$Q = It \tag{3.23}$$

where *I* is the beam current recorded using the Faraday cup.

Finally, the total number of electrons could be calculated by dividing the number of electrons by the area of the beam, and the critical electron fluence can be calculated in unit of e / $Å^{-2}$.

3.11.2.2. For STEM

The beam current in STEM had been calibrated beforehand, at each aperture and spot size. The relationship between the root of field of view (FOV) on y-axis and magnification on x-axis is as follows;

$$y = 227.61x^{-1.0243} \tag{3.24}$$

The scan area (FOV) is the square of y, so the FOV at each magnification can be calculated. The dwell time at each pixel, t, is a known value. The electron fluence in the image in e / $Å^{-2}$, can be calculated as;

$$Electron\ fluence = \frac{beam\ current \times t \times total\ number\ of\ pixels}{1.602 \times 10^{-19} \times scan\ area} \tag{3.25}$$

3.11.3. Lattice measurements

CABB has a face-centred $Fm\bar{3}m$ structure, and its unit cell is illustrated in Figure 3.20 (a). The unit cell can be regarded as two cubes joined together with one sharing face. At the centre of each cube sits a Cs atom, with an eighth of Ag or Bi occupies each corner of the cube, and a quarter of Br takes up each edge of the cube. A 3D model of CABB was used to compare against the STEM images obtained, and the model of CABB observed along the <100> direction is shown in Figure 3.20 (b). Two unit cells of CABB can be seen from this image. The 3D atomic arrangement of CABB was previously shown in Figure 1.5 (a). The boundary of the structure lies in the (001) plane, which is shown as a red line in Figure 3.20 (b, c). Figure 3.20 (b, c) illustrate that the surface of the CABB structure could terminate at either the plane containing Ag/Bi and Br, or the plane containing Cs and Br only. The plane distance between the Ag/Bi column and the Cs column is 2.818 Å, and the distance between each atom within the same column (e.g. Cs and adjacent Cs, Ag and adjacent Bi) is 5.636 Å for all columns. These two values are both bulk values.

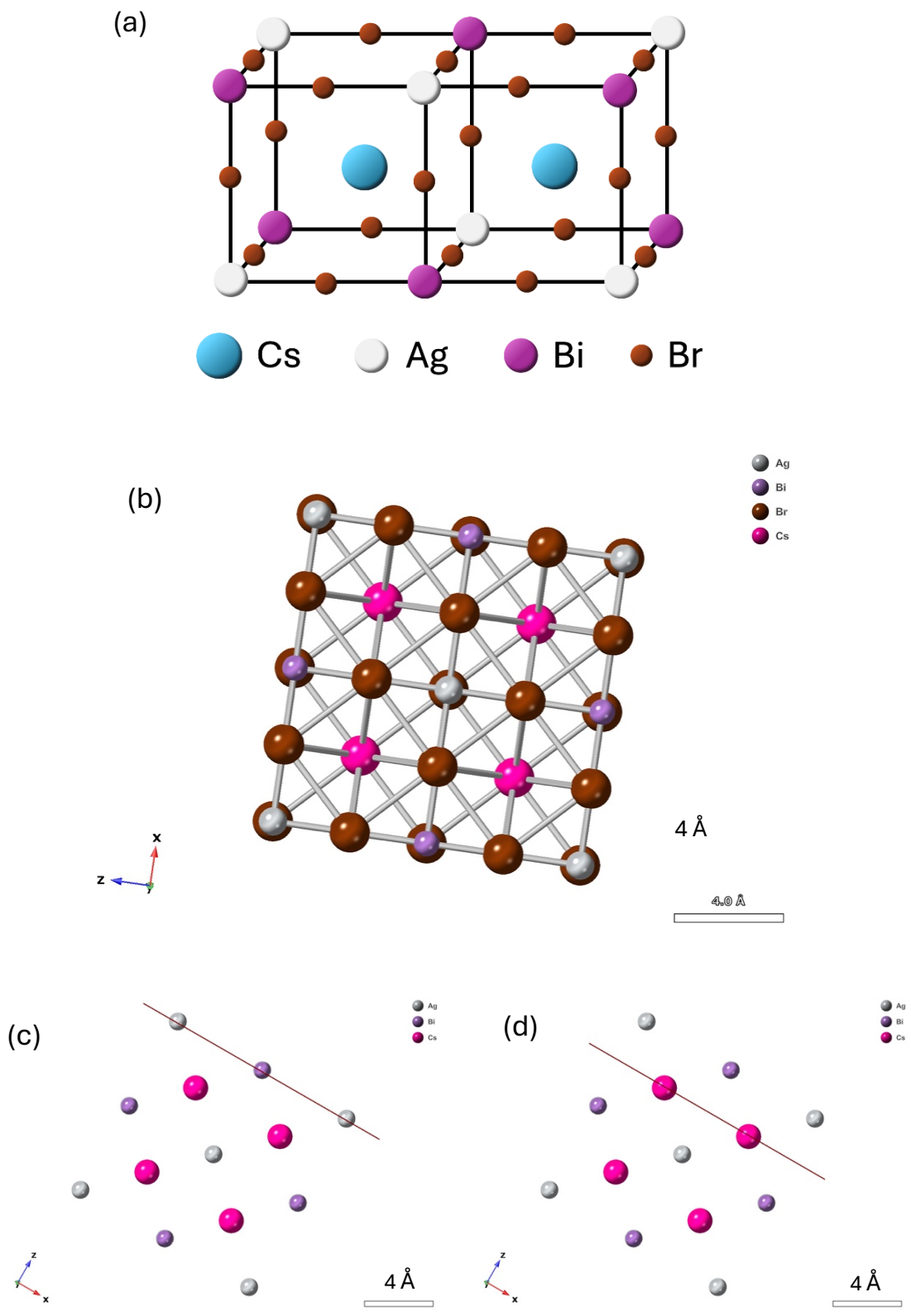

Figure 3.20. (a) Illustration of CABB unit cell, which consists of two cubes. Each Ag and Bi shown only has an eighth of the atom included within either cube, and each Br has a quarter included. (b) A 3D model of the CABB observed along <100>. (c) The (001) plane in red that cuts through Ag and Bi atoms, as well as the Br atoms omitted in the graph. (d) The (001) plane can also cut through Cs and Br atoms.

Atoms close to the surface of the sample particles were studied and the method used for analysis is discussed here. Due to limitations in the resolution of the image, as well as surface contamination and beam damage to the specimens, STEM images containing information regarding atomic arrangements were obtained but not close to a sub-Angstrom level. The images were binned by two, so 2x2 pixels, which are four pixels in total, were merged into one to increase the intensity of the atoms in the image. The background was first calculated by taking line profiles from three different places around the sample particles, and an average was worked out. Subsequently, intensity profiles of the atom arrays containing either Ag/Bi or Cs were taken, where the lines were drawn from the bulk region and terminated at a point outside the particle. The intensities of the line spectra generated were then subtracted by the background value. The distances from one atom to the next along the line was also measured, as the distance between atoms close to the surface may vary from the distance between atoms in the bulk region.

3.11.4. Scanning electron microscopy

A scanning electron microscope (SEM) also uses electrons to study materials. SEM has its own advantages, such as a large depth of focus, which means regions of different heights can be in focus at the same time[208]. Figure 3.21 shows the main components of an SEM. A focussed electron beam is used to probe the sample, and an image is formed by performing a raster scan across the region of interest[209]. The energy of the beam typically ranges from 2 keV to 40 keV[210].

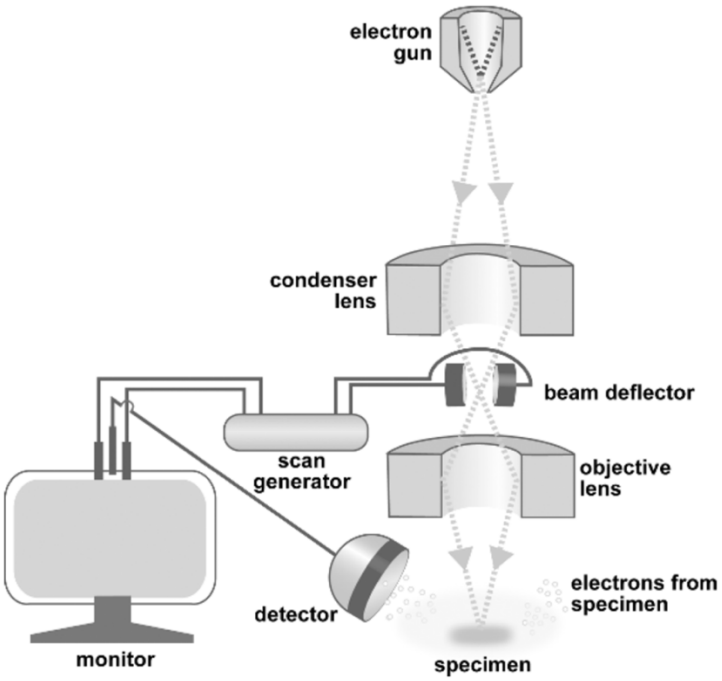

Figure 3.21. The main components of an SEM. Reproduced with permission from reference[209]. Copyright 2012 Cambridge University Press.

The electron gun is very similar to the ones used in TEM, with a thermionic source, cold field emission source or Schottky source[211]. Modern field emission SEM (FESEM) utilised for high resolution imaging have either a CFEG or Schottky source[208].

Multiple signals are produced from the interaction between the electron beam and the sample, and the main signals collected are secondary electrons (SE), back-scattered electrons (BSE) and characteristic X-rays. Figure 3.22 shows how SE and BSE are produced from electron-specimen interaction. Secondary electrons are the product of inelastic scattering, where the incident electron transfers some of its kinetic energy and ejects an electron from the atom[211]. This type of electron has low energy (< 50 eV) and is used for routine imaging[208]. Back-scattered electrons arise from elastic scattering, where the incident electron with an energy of 5-20 keV is deflected at a large angle because of the positively charged nucleus[211]. Heavier atoms are more likely to produce BSE, but if the energy of incident electron is too high, the positive nuclear charge may have little effect[211]. The principles of SEM-EDX are the same as those of (S)TEM-EDX.

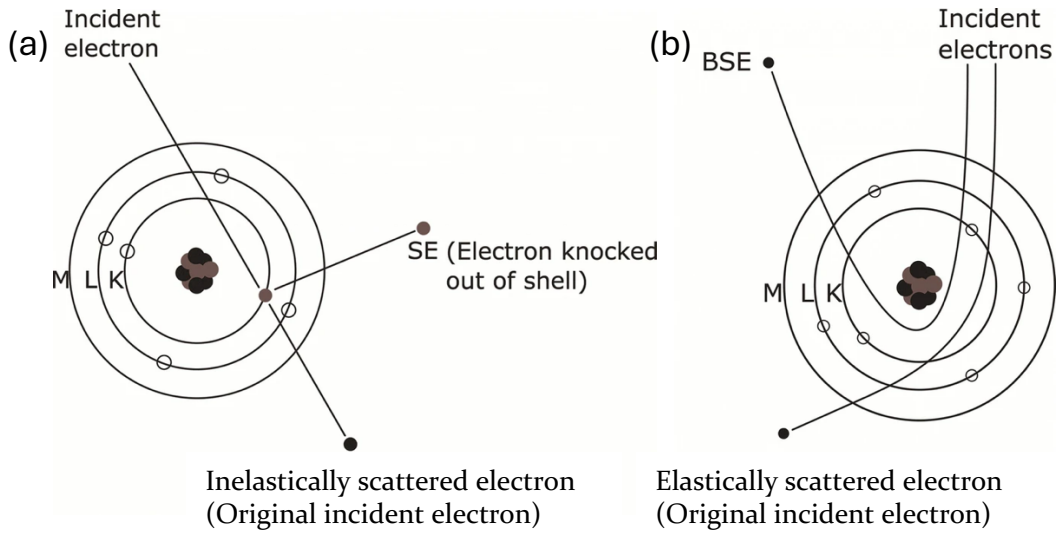

Figure 3.22. The formation process of (a) SE and (b) BSE. Reproduced with permission from reference[211]. Copyright 2018 Springer Nature Switzerland AG.

SEM-EDX data in this research project were obtained using a Carl Zeiss Merlin FEG SEM, fitted with an Oxford Instrument Ultim Max 100 EDX detector.

3.11.5. TEM sample preparations

Unless the sample was as-synthesised CABB nanocubes or nanosheets, where the TEM specimen was prepared directly from a dispersion at the end of the synthesis process, all other TEM specimens were prepared from dry solid powders.

Multiple types of dispersion media were tested to disperse the sample powder, and the ones frequently used were methyl acetate, hexane and toluene. Methyl acetate has the lowest toxicity among the three, but CABB powder did not disperse as well as for the other two options. Ethyl acetate changed the XRD pattern of bulk CABB. Alcohols were not suitable liquids for dispersion; for example, bulk CABB washed by ethanol suffered from instant structural damage once exposed to the electron beam. For PEA_2SnBr_4 (PSB), toluene was used to disperse the powder to prepare TEM specimens.

To achieve a good dispersion, 1 mL dispersion medium was added for every 1 mg sample into a vial. The vial was then usually sonicated for a few minutes, and a few droplets of the

dispersion were deposited onto a 200-mesh or 300-mesh copper grid, or a 200-mesh gold grid (all from Agar Scientific). Micropipettes were used to ensure a homogeneous dispersion, and each drop was around 20 µL. A piece of filter paper was placed underneath the grid when loading the sample, in order to absorb excess liquid.

Sometimes not enough sample particles were added to the grid, and when operating the (S)TEM a lot of time was spent finding suitable particles. To prevent this from happening, a rule of thumb of adding enough sample particles is that the filter paper begins to show the colour of the dispersion at the point where the dispersion is dropped.

3.11.6. SEM sample preparations

For SEM, the sample dispersion was prepared first, and the procedure used was the same as that for TEM samples. The difference is that for SEM samples, the suspension was transferred dropwise onto a copper tape, instead of a TEM grid, and 1 mL or larger plastic pipettes were used. When dried, the copper tape was attached to a SEM stub.

3.11.7. EDX data analysis

EDX data were collected from both SEM and STEM, and most were recorded in Aztec format, which could be loaded directly using the Aztec software developed by Oxford Instruments. To perform elemental quantification, deconvolution can be done in Aztec. This means the effects of common interfering elements, such as Cu and C, can be minimised when performing quantification limiting to the elements of interest. In this thesis, Cs, Ag, Bi and Br are the main elements of interest. EDX data stored in other formats were loaded and analysed in HyperSpy, and elemental quantification was performed based on the guide on the HyperSpy website[212,213]. The k-factor method (proposed by Cliff and Lorimer[214]) was used in both Aztec and HyperSpy to work out the atomic percentage of each element. Map sum spectra were used for each dataset. Point and line spectra reconstruction were attempted, but the number of counts were inadequate for such reconstruction.

Chapter 4 $Cs_2AgBiBr_6$ as a photocatalyst in methanol oxidation

Contents

4.1. Introduction 99
4.2. Results and discussion 101
4.2.1. Characterisation of as-synthesised bulk CABB and nanocubes 101
4.2.2. Photocatalytic performance in liquid methanol with NaBr 105
4.2.3. Photocatalytic performance with methanol vapour 107
4.2.4. Fast Fourier Transform and nanoparticle surface study 120
4.2.5. Formaldehyde detection 124
4.2.6. Mechanistic analysis 125
4.3. Conclusions 133

4.1. Introduction

Hydrogen is a potential source of clean energy, but its storage and transport remain key issues. Methanol is a good storage vessel for hydrogen, as each molecule contains four hydrogen atoms. Industrially, methanol can be decomposed into H_2, CO and/or CO_2, using methods including the water ballast process and Formox process, but high temperature and pressure are required[216,217]. Alternatively, under milder conditions such as room temperature photo-oxidation, methanol can be split into hydrogen and formaldehyde with a suitable catalyst. Here, CABB has been studied as a lead-free halide perovskite photocatalyst.

CABB can be made by a variety of routes, and the morphology of the resulting product differs when the synthesis conditions are different. Three types of CABB were synthesised and are discussed in this chapter; bulk CABB, CABB nanocubes and CABB nanosheets.

Bulk CABB was simple to synthesise using HBr and heating, with a high yield for each batch. It also possesses good ambient stability, as it can be stored in air for weeks without significant changes. Bulk CABB synthesised using this route is denoted as CABB-HBr, since HBr is the main solvent in the synthesis procedure. Synthesis of nanosized CABB required the use of a Schlenk line, as the workflow need switching between vacuum and inert gas environments. The products are typically in cubic shape (denoted as CABB-NC) or sheet-like (denoted as 2D-CABB). The atomic structures of the nanosized samples are easier to study and should also provide more active sites for photocatalytic reaction.

When immersed in methanol directly, CABB degrades even before the application of light to initiate the reaction. Different methods were proposed and tested in order to prevent the halide perovskite structure from breaking down, and reaction with gaseous methanol was found to be the most effective way. This reaction system using lead-based halide perovskites as catalysts has been studied [132,218], but no studies on less toxic lead-free halide perovskites have been reported. This chapter hence investigates the reaction system using lead-free CABB as the photocatalyst.

Ideally, the catalyst would remain unchanged throughout, but some morphological changes were observed when the reaction was running for extended times, visible using electron microscopy (EM). In summary, this chapter focusses on synthesis, photocatalytic tests and characterisation of $Cs_2AgBiBr_6$ (CABB) in bulk and nano form.

4.2. Results and discussion

4.2.1. Characterisation of as-synthesised bulk CABB and nanocubes

XRD data from the as-synthesised bulk CABB (denoted as CABB-HBr) are shown in Figure 4.1 (a). The XRD reflections matched the CABB peaks generated from simulation using CrystalDiffract, and the model was provided by McClure et al.[71]. Details regarding the production of CABB nanocubes (denoted as CABB-NC) were discussed in Section 3.2.2. From visual observation, the CABB-NC powder looked similar to CABB-HBr, its bulk form counterpart. Figure 4.1 (b) shows the XRD plot of CABB-NC, whose peaks matched those from the simulation. The SEM image shown in Figure 4.2 (a) reveals that the particle size for CABB-HBr was typically a few micrometres. The TEM image in Figure 4.2 (b) shows the shape of the CABB-NC cubes. The STEM-HAADF image in Figure 4.2 (c) makes the structure of CABB-NC visible.

In terms of CABB-HBr, the UV-vis data in Figure 4.3 (a) shows that it strongly absorbed light in the range of 200 nm to 550 nm. This suggests CABB-HBr could be used as a type of photocatalyst. Having converted the UV-vis data to a Tauc plot, the bandgap was estimated to be around 2.12 eV, as shown in Figure 4.3 (b). As for CABB-NC, the powder UV-vis absorbance spectrum in Figure 4.3 (c) revealed that the nanocubes exhibited light absorption from 200 nm up to around 700 nm, which falls in the visible light range and is broader than the absorption range of CABB-HBr. From the Tauc plot in Figure 4.3 (d), the bandgap of the CABB-NC is at 2.21 eV. This bandgap value is slightly larger than the bandgap of CABB-HBr, due to the quantum confinement effect[84]. Quantum confinement effect is common for semiconductor materials with particle sizes smaller than 100 nm, normally the same order of magnitude as the excited electron-hole pair Bohr radius[219,220]. These nanoparticles have electronic energy states that are similar to atoms, which are

discrete; while for bulk particles their energy states form continuous bands, which leads to smaller bandgaps[220].

To prepare specimens for (S)TEM imaging, ethanol is not a suitable solvent for dispersing or washing CABB-HBr, as specimens washed with ethanol degraded rapidly under the electron beam. Figure A1 in Appendix presents four TEM images that reflect the change in structure, when the ethanol-washed CABB-HBr specimen was exposed to the electron beam. Methyl acetate was found to be a suitable medium to disperse CABB-HBr and prepare (S)TEM specimens. CABB-HBr prepared using methyl acetate was more stable under the beam, but the particles were too thick to extract useful information, as shown in Figure A2. SEM was hence used for microscopic analysis on CABB-HBr. Neither washing with ethanol or methyl acetate altered the XRD pattern of CABB-HBr.

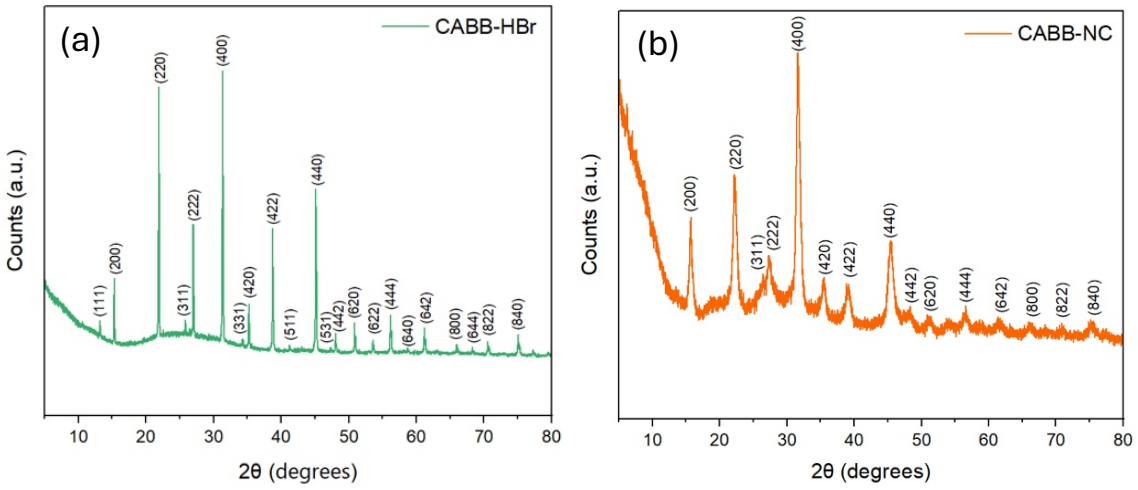

Figure 4.1. XRD spectra of (a) as-synthesised CABB-HBr, and (b) as-synthesised CABB-NC.

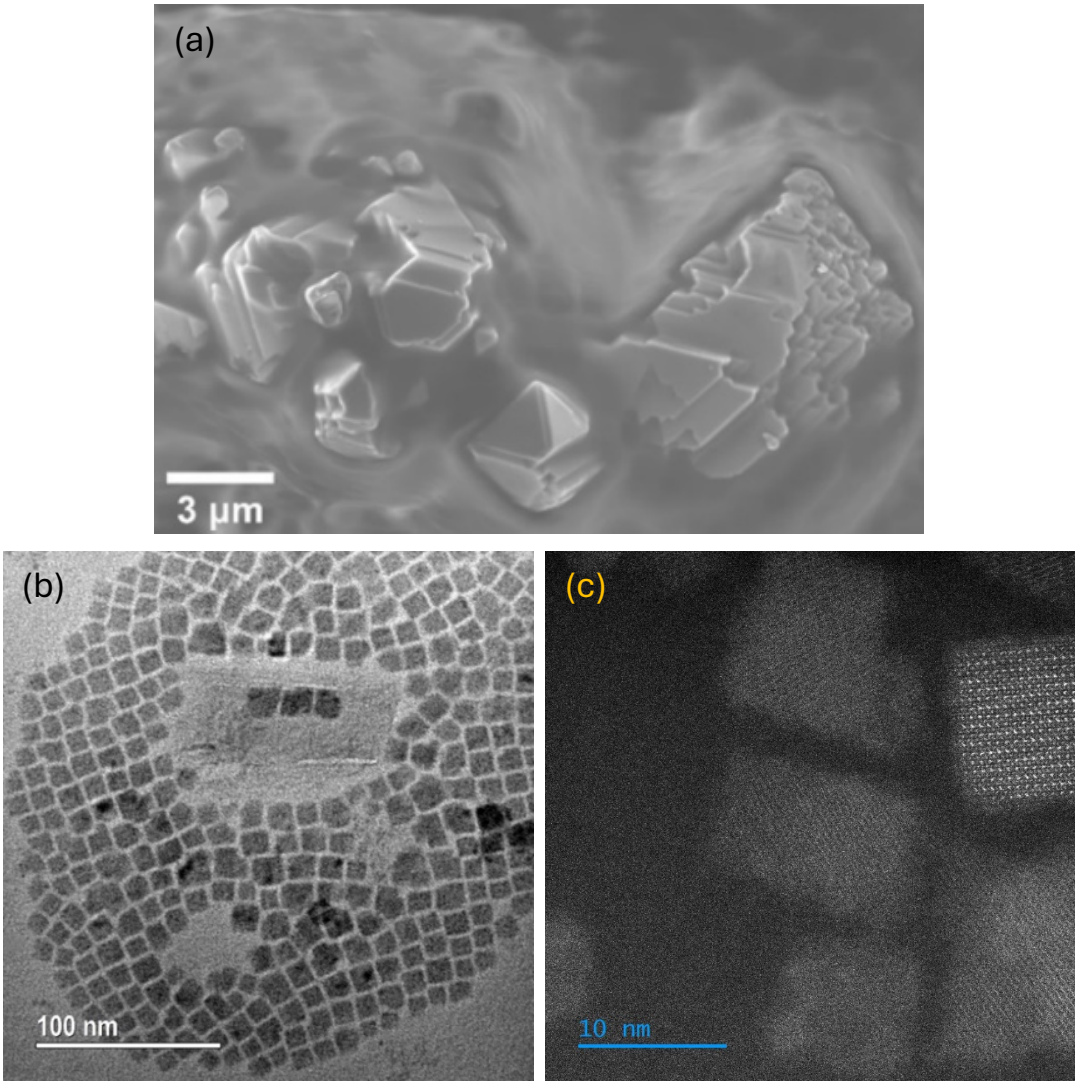

Figure 4.2. (a) SEM image of CABB-HBr. The image was taken using 5 kV, 600 pA, 10 mm working distance and an SE2 detector. (b) TEM image of CABB-NC showing the cubic shape of the particles. (c) STEM-HAADF image revealing the atomic structure of CABB-NC. The TEM image was taken using 40000x magnification, 56 nA probe current and an exposure time of 0.5 s. The STEM-HAADF image was taken with a beam current of 5.6 pA, 14.38 mrad convergence angle, 1024 x 1024 pixels, and 6 µs dwell time per pixel; the pixel size was 0.35 Å x 0.35 Å and the electron fluence was 1.7 x 10^3 e $Å^{-2}$.

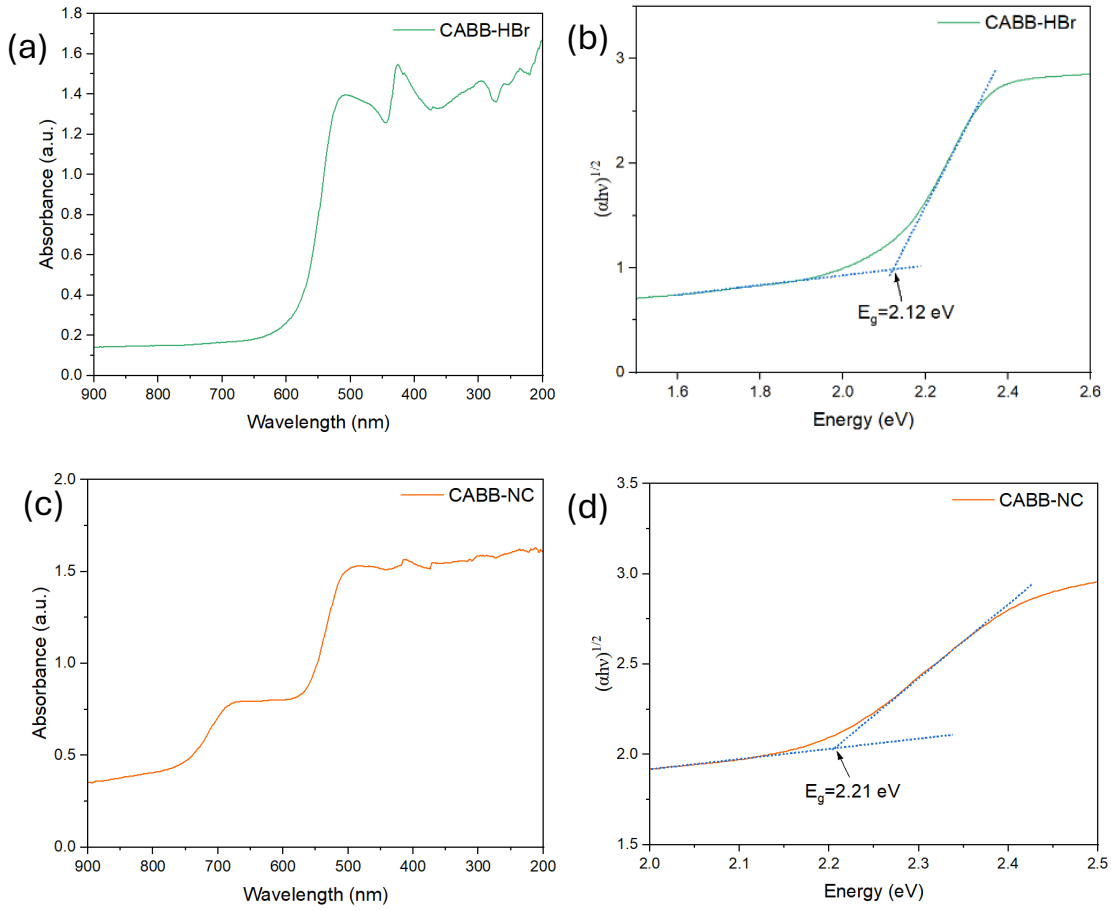

Figure 4.3. (a) Powder UV-vis absorption spectrum of CABB-HBr showing good absorbance in the range of 200 nm to 550 nm. (b) Tauc plot calculated from the UV-vis data of CABB-HBr, with its bandgap found to be 2.12 eV. (c) UV-vis absorbance spectrum of CABB-NC showing good absorption from 200 nm to 700 nm. (d) Tauc plot of CABB-NC derived from the UV-vis spectrum, and from the plot the bandgap of CABB-NC was found to be 2.21 eV.

4.2.2. Photocatalytic performance in liquid methanol with NaBr

Without protection, CABB rapidly decomposes in methanol. The XRD plot in Figure A3 shows that CABB degrades into AgBr and $Cs_3Bi_2Br_9$ when mixed with methanol. A method to protect the perovskite structure was hence needed. Initial ideas were taken from the literature, where a HBr/H_3PO_2 mixture is often used for photocatalytic H_2 production to keep the catalyst stable after many hours of reaction[80,94]. In this work, it may also be possible to retain the structure of CABB by adding excess Br^-, for equilibration of Br^- ions in CABB and in the environment to prevent CABB from breaking down. This was discussed in Sections 2.3.1 and 2.5.1. After testing methanol saturated with NH_4Br, CsBr, KBr and NaBr it was found that NaBr achieved the best protection for CABB-HBr during the photocatalytic reaction. XRD data in Figure 4.4 (a) show that the structure did not undergo significant changes during the photoreaction. The extra peaks were attributed to trace amounts of NaBr. Notably, the CABB powder retained its orange colour throughout. The H_2 production rates under such conditions are shown in Figure 4.4 (b). The turnover frequency for CABB-HBr in this photoreaction is 0.0113 s^{-1}, and the calculation process was discussed in Section 3.8.3. The hydrogen generation rate when the CABB was added showed improvements, compared to the reaction mixture with methanol and NaBr only. This shows that CABB played a role as a catalyst to increase the reaction rate of methanol photo-oxidation reaction.

Although NaBr provided protection to CABB-HBr, it did not work for CABB-NC particles. The STEM-HAADF images of CABB-NC after photoreaction in methanol with excess NaBr are shown in Figure A4. The particles have lost their cubic shapes, and agglomeration has taken place during the reaction. The hydrogen production rate of this system was 76 μmol g^{-1} h^{-1}, which was not superior to CABB-HBr in methanol with excess NaBr. This is likely to result from the damage to the structure which lowered the catalytic performance.

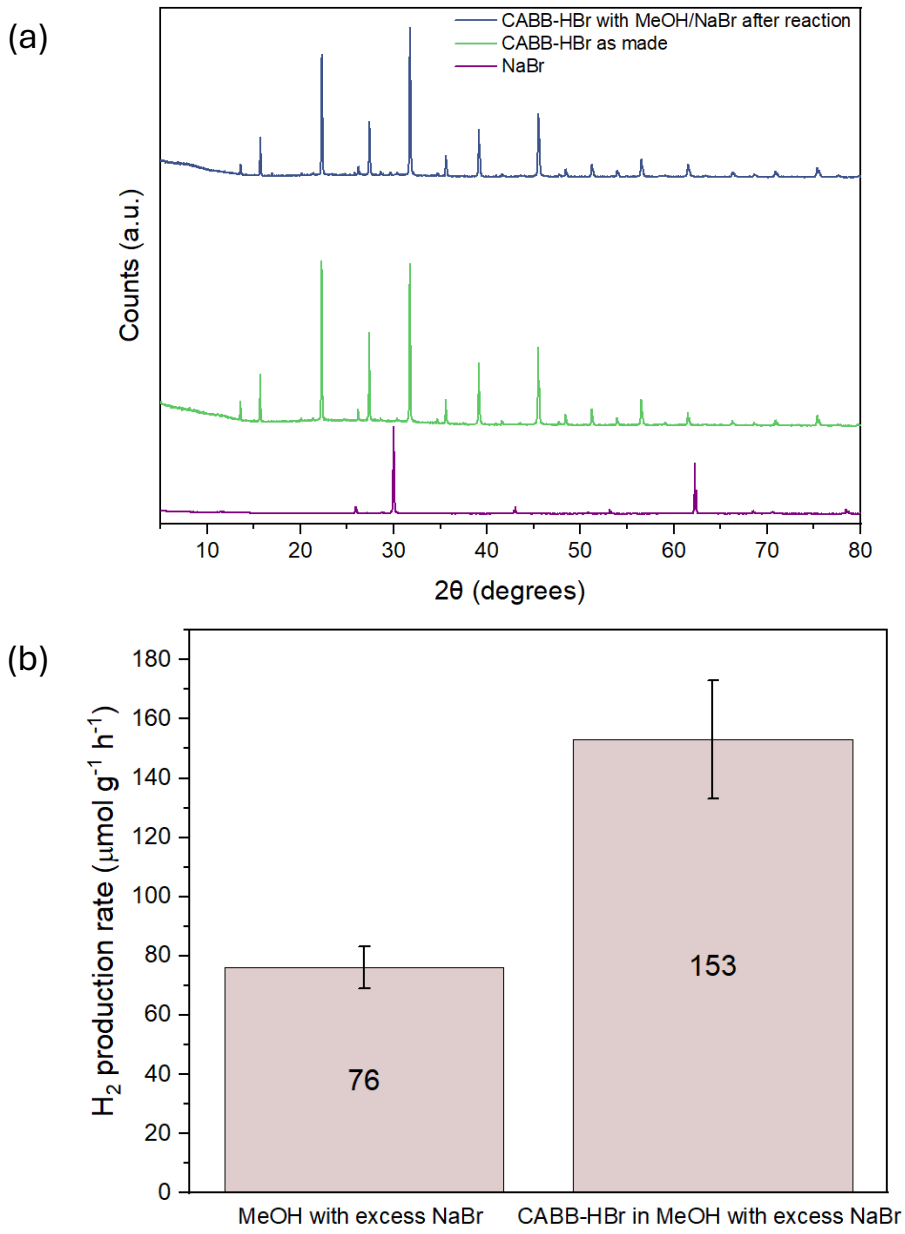

Figure 4.4. (a) XRD plots of NaBr, as-made CABB-HBr, and CABB-HBr after photoreaction in methanol (denoted as MeOH) with excess NaBr. Trace amounts of NaBr was mixed with the CABB-HBr sample at the end of the photoreaction. (b) Hydrogen production rates from photoreactions of methanol with excess NaBr, and CABB-HBr in methanol with excess NaBr. Addition of CABB-HBr into the reaction system clearly showed a boost in reaction rate.

Excess NaBr was added because the temperature in the reactor increased during the reaction, which increased the solubility to Br^- ions and shifted the dynamic equilibrium between Br^- ions in CABB and Br^- ions in methanol provided by NaBr. Unless extra NaBr was added into methanol, Br^- would be taken from the CABB, which leads to the collapse of the halide perovskite structure. Another drawback of this method is that a lot of NaBr precipitated during the reaction and stuck to the wall of reactor, instead of redissolving in methanol. When too much NaBr was lost from the methanol, the dynamic equilibrium would be broken. Overall, extra NaBr needs to be added constantly to maintain the dynamic equilibrium and the reaction.

4.2.3. Photocatalytic performance with methanol vapour

Photoreaction with methanol vapour was found to be a mild yet effective reaction system for CABB. This reaction does not induce significant damage to the CABB structure, whether in bulk or nano form, and NaBr is not required. The experimental arrangement was discussed in Section 3.3.3, with vials separating the catalyst and liquid methanol by which only methanol vapour would be in contact and react with the catalyst. To disperse the CABB-NC sample, some hexane was added into the small vial with the catalyst, and the contents were stirred until dry. A layer of CABB-NC would form on the inside wall of the small vial. This step spreads the nanocubes within the small vial.

When the photoreaction time was two hours for each run, the hydrogen production rates were higher for both bulk and nano CABB, compared to one-hour reactions. For CABB-HBr, this is likely to be because initially some HBr was not completely removed from the surface of the CABB-HBr, and it acted as an obstacle to the photoreaction. When the reaction time exceeded one hour, the remaining HBr was removed from the CABB-HBr surface, and the reaction rate increased. For CABB-NC, the partial removal of remnant organic ligands

introduced by the oleic acid and oleylamine is thought to be responsible for the increased reaction rate[132]. The one-hour photoreactions are discussed in Section A2 in Appendix.

The photoreaction rates for bulk and nano CABB are shown in Figure 4.5 (a, b) and Table 4.1, where the reaction systems were tested for up to 12 hours. For every two hours, the reaction was stopped so the gas mixture in the reactor could be transferred into a gas chromatography system (GC) for H_2 quantification. Methanol and argon were then refilled before starting the reaction for another two hours.

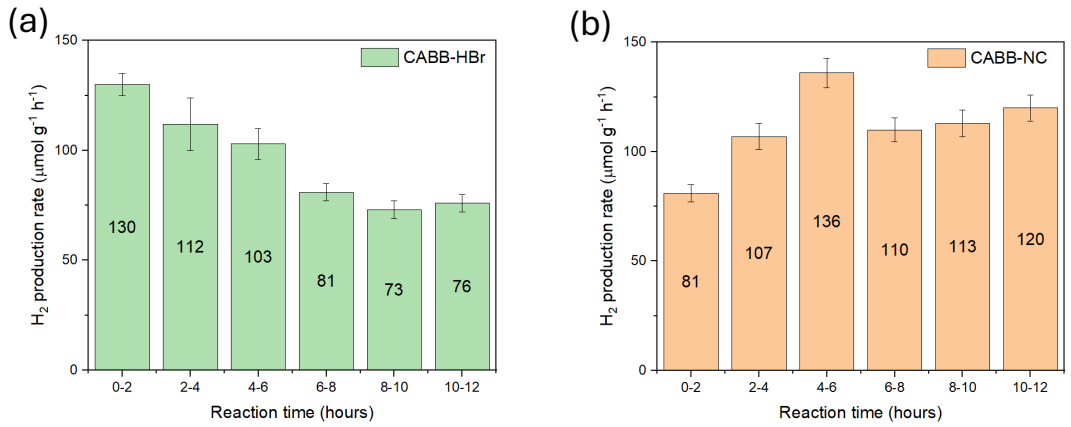

Figure 4.5. Hydrogen production rates of the photoreaction with methanol vapour, using (a) CABB-HBr and (b) CABB-NC as the catalyst. The activity of CABB-HBr showed a decreasing trend with longer reaction time. The activity of CABB-NC showed an increasing trend but with a dip at around six hours of reaction time.

Table 4.1. TOF of the photoreaction with methanol vapour, using CABB-HBr or CABB-NC as the catalyst. The unit of TOF is s^{-1}.

Reaction time	CABB-HBr	CABB-NC
0-2h	1.26×10^{-2}	1.98×10^{-5}
2-4h	9.99×10^{-3}	3.38×10^{-5}
4-6h	8.67×10^{-3}	4.93×10^{-5}
6-8h	5.44×10^{-3}	3.54×10^{-5}
8-10h	4.26×10^{-3}	3.70×10^{-5}
10-12h	4.70×10^{-3}	4.07×10^{-5}

Some trends are evident from Figure 4.5 and Table 4.1. For CABB-HBr, the reaction rate decreased over time. For CABB-NC, its performance steadily improved over time, but a dip occurred after six hours of reaction. The possible reasons for these trends are discussed later in this section. CABB-NC seems to be the better catalyst for photoreactions that last

longer, but in terms of TOF the cubes are few hundred times lower than the TOF of bulk sample, meaning their full potential was not achieved during the reaction. This is likely to result from the aggregation of CABB-NC throughout the synthesis and reaction process, forming clusters and blocking a lot of potential active sites for the photoreaction. The vial used for the photoreaction could also be too small to fully spread the nanocubes to be one layer thick. At the end of the reaction, the sample turned dark brown, but when the reactor was opened and the system exposed to air, the sample powder returned to bright orange. It has been proposed that the lack of oxygen in the reaction system affects the colour of the sample[17]. Adding extra amount of catalyst did not lead to an increase in the amount of hydrogen produced, due to the limitations of the size of the vial and reactor. Additional experiments were performed to prove that the reactions were photocatalytic. No hydrogen was detected after leaving the reaction system in the dark for several hours. However, in contrast for the reaction with methanol only, i.e., not adding any catalyst, the average hydrogen production rate is equivalent to 44 μmol g^{-1} h^{-1}. When CABB was added to the system, the hydrogen production rates increased, showing that CABB was able to act as a photocatalyst to increase the reaction rate.

XRD plots of CABB-HBr and CABB-NC before and after photoreaction with gaseous methanol are shown in Figure 4.6 (a) and (b), respectively. Samples that went through ten hours of reaction are denoted with “10h”. The crystal structures of CABB halide perovskite were generally not altered during the photoreaction. In Figure 4.6 (b), two extra peaks marked with “*” for CABB-NC after reaction can be attributed to a $BiBr_3$ impurity[90], which means a small fraction of CABB-NC may have decomposed during the reaction.

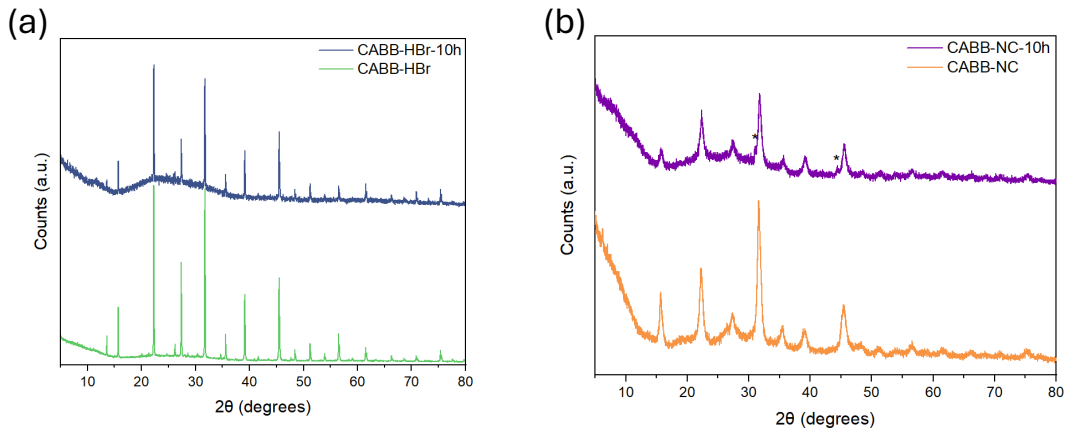

Figure 4.6. XRD data of (a) CABB-HBr and (b) CABB-NC before and after the photoreactions with methanol vapour. The new peaks marked with * can be attributed to a $BiBr_3$ impurity.

Even though XRD showed that the sample did not undergo significant changes during the reaction, electron microscopy (EM) was used to further examine the sample for longer reaction times. At the end of each two-hour reaction, a trace amount of sample was extracted for investigation using EM. SEM images of CABB-HBr after reaction are shown Figure 4.7. At a first glance, the CABB-HBr after two hours of reaction, as shown in Figure 4.7 (a), seems to undergo little change compared with the as-synthesised CABB-HBr shown in Figure 4.2 (a). However, as the reaction time increased, the surface of the bulk particles became rougher. Closer inspection of CABB-HBr-6h in Figure 4.7 (b) revealed that the surface of the particles was no longer as smooth as the surface of CABB-HBr before reaction, and pits and crevices were visible. The uneven surface was also obvious in CABB-HBr-12h, as shown in Figure 4.7 (c). The surface of sample at this point seems to be etched, which may have been formed during the photocatalytic reaction with methanol. With the decreasing trend in hydrogen production rate for CABB-HBr as the reaction went longer, these features shown in Figure 4.7 (b, c) were unlikely to be beneficial to increasing the activity of the reaction, but instead reduced the reaction rate over time.

The SEM-EDX spectrum and maps of CABB-HBr-12h are displayed in Figure A7. All four elements, Cs, Ag, Bi and Br, which make up CABB-HBr, could all be detected after 12 hours of photoreaction. The information obtained from EDX data, coupled with the XRD pattern in

Figure 4.6 (a) indicated that the CABB structure was intact, and it was the changes at the surface of the CABB-HBr particles observed using SEM that led to a change in reaction rate. Quantification was performed to analyse the changes in atomic ratios among the four elements Cs, Ag, Bi, Br. CABB-HBr before and after the photoreaction was examined, and the results are presented in Table 4.2. The method used to obtain these results is discussed in Section 3.11.7. From Table 4.2, the atomic percentage of Ag and Bi decreased for CABB-HBr-12h, which could explain the decline in the reaction rate over time. Ag and Bi at the surface of the CABB catalyst are likely to play an important role in the photocatalytic process, and fewer Ag and Bi sites available were linked to a reduction in the reaction rate.

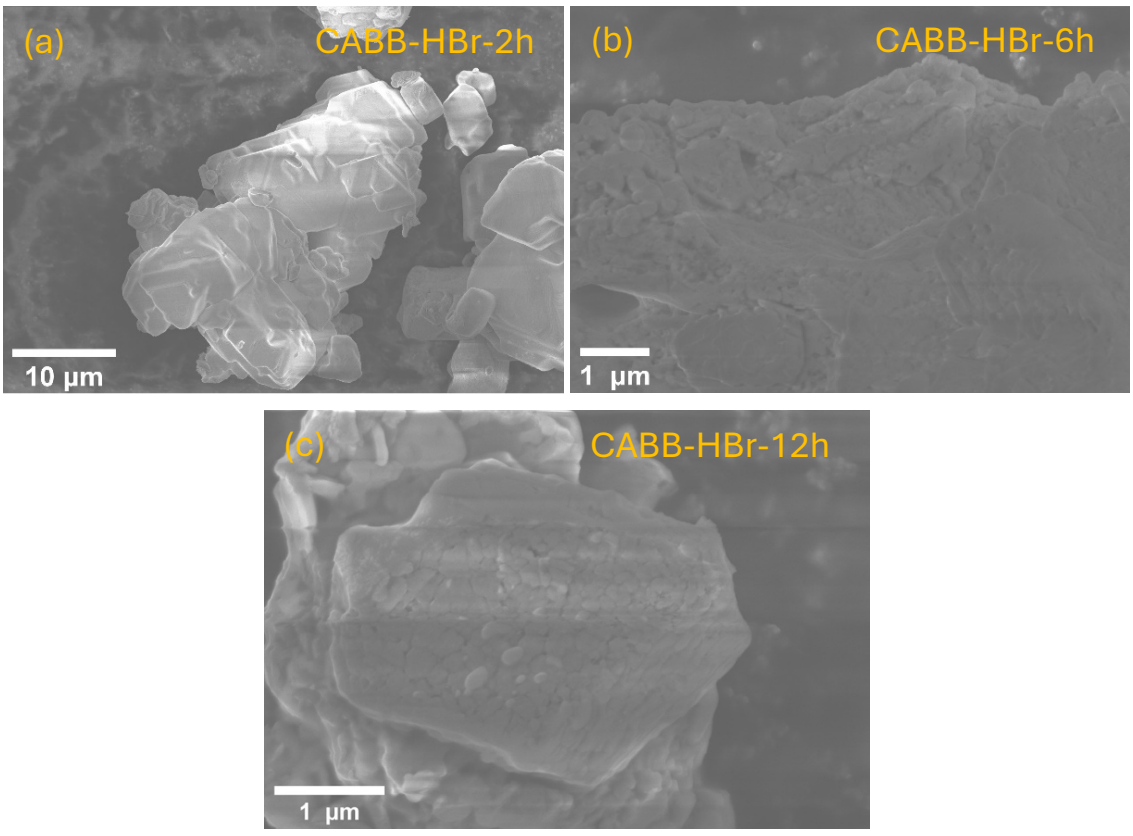

Figure 4.7. SEM images of CABB-HBr after (a) two hours, (b) six hours and (c) 12 hours of photoreaction. Some pits and crevices seem to have formed on the surface of CABB-HBr. The surface of the particles became rougher with longer reaction times. All images were taken with an SE2 detector. Images (a, b) were taken using 5 kV, 80 pA and 14 mm working distance. Image (c) was taken using 5 kV, 500 pA and 14 mm working distance.

Table 4.2. SEM-EDX quantification results for CABB-HBr samples before and after the photoreaction with methanol vapour.

Sample	Cs atomic %	Ag atomic %	Bi atomic %	Br atomic %
CABB-HBr	0.50	5.19	7.89	86.42
CABB-HBr-12h	0.52	3.40	6.13	89.95

As described in Section 3.2.2, the synthesis of CABB-NC involved the use of oleic acid and oleylamine, which left ligands on the surface of the nanocubes[84]. Ethanol was found to be an effective detergent to wash the surface ligands away at the end of the synthesis process, and FTIR was used to validate that most of the ligands were washed off. From the FTIR spectra shown in Figure 4.8 (a), the peaks indicating the presence of ligands were evident before washing with ethanol. These peaks are due to C-H bonds, N-H bonds and O-C-O bonds. After the washing process, the intensities of these peaks were greatly reduced (see the peaks highlighted with rectangles in the plot), indicating the successful removal of most of the ligands. The XRD data of the washed CABB nanocubes (denoted as CABB-NC-EtOH), compared with unwashed CABB-NC, are shown in Figure 4.8 (b). The $BiBr_3$ impurity peaks marked with "*" were again detected, which means a small fraction of CABB could have been decomposed during the washing process. The STEM-HAADF image in Figure 4.8 (c) revealed that the nanocubes maintained their cubic shape after washing. In terms of the catalytic activity of CABB-NC-EtOH in the methanol photo-oxidation reaction, the results are shown as a plot in Figure 4.8 (d), as well as Table 4.3. The hydrogen production rates were significantly higher than those of unwashed CABB-NC, and the TOF also improved. Both CABB-NC and CABB-NC-EtOH showed a dip in reaction rate when the total reaction time was 6-8 hours. The reason for it is discussed subsequently. Figure 4.8 (e) compares the XRD patterns of CABB-NC-EtOH before reaction and after ten hours of reaction. The broad peak at around 20°-40° indicates the presence of microstrain[221]. Commercially available 25 nm TiO_2 particles (P25) was also tested, and its average reaction rate was 71 μmol g^{-1} h^{-1}. This shows that CABB-NC-EtOH had better performance over P25 in the methanol photo-oxidation reaction with gaseous methanol.

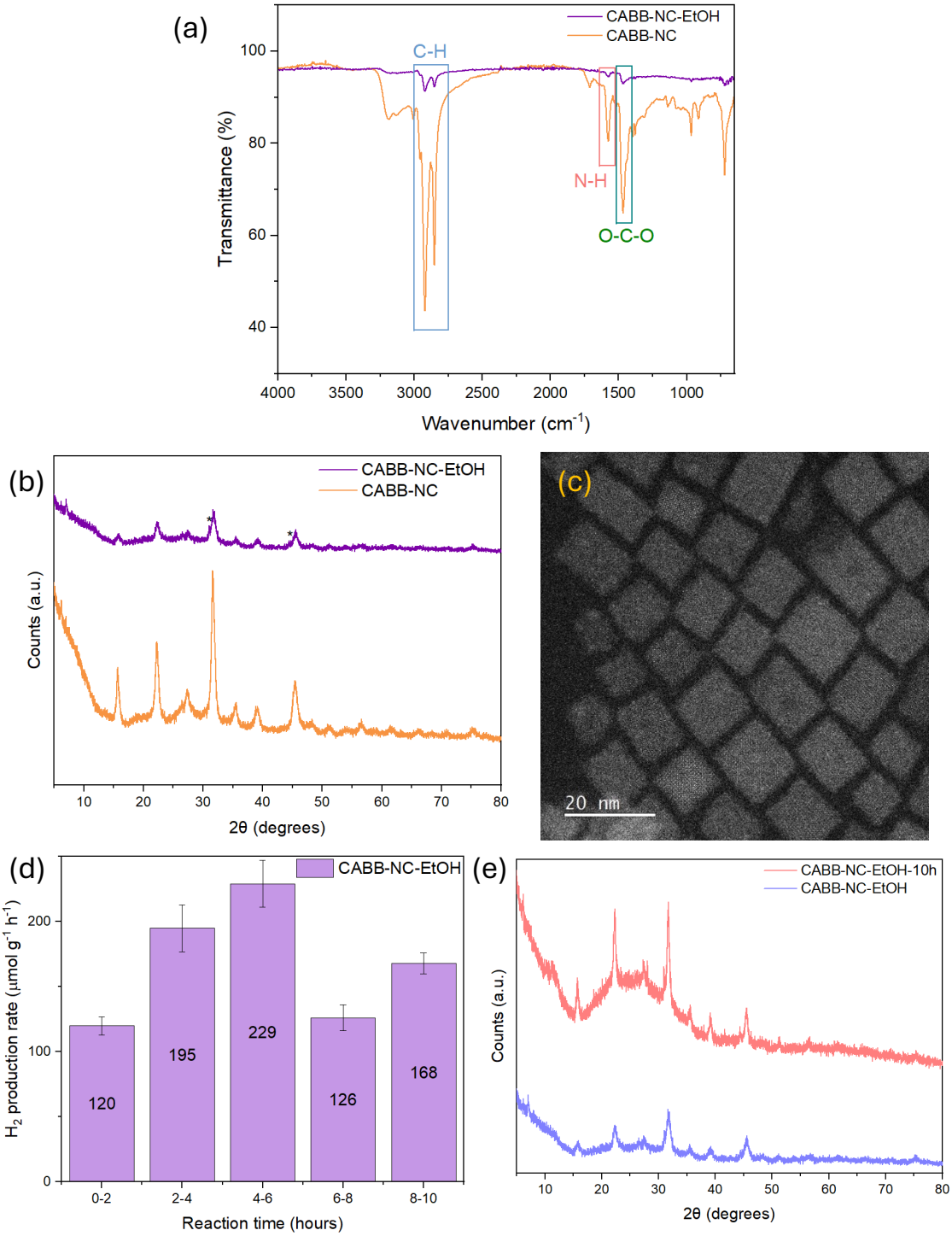

Figure 4.8. (a) FTIR spectra of CABB-NC synthesised without washing (orange), and the nanocubes washed with ethanol (purple). The intensity of peaks associated to the surface ligands were greatly reduced after washing with ethanol, which means that most of the ligands were removed during the washing process. (b) XRD plot comparing the diffraction patterns of unwashed CABB-NC and washed CABB-NC-EtOH. The peaks marked with "*" can be attributed to a $BiBr_3$ impurity. (c) STEM-HAADF image of CABB-NC-EtOH. This shows that the nanocubes were preserved during the washing process. The STEM-HAADF image were taken with a beam current of 5.6 pA, 14.38 mrad convergence angle, 1024 x 1024 pixels, and 6 µs dwell time per pixel; the pixel size was 0.83 Å x 0.83 Å and the electron fluence was 304 e $Å^{-2}$. (d) Hydrogen generation rates using CABB-NC-EtOH as the catalyst in the methanol photo-oxidation reaction. (e) Comparison in XRD pattern between CABB-NC-EtOH and CABB-NC-EtOH after 10 hours of photoreaction. The peaks due to CABB-NC-EtOH were retained after 10 hours of reaction.

Table 4.3. Reaction rates converted to TOF for CABB-NC-EtOH in methanol photo-oxidation reaction.

Reaction time	0-2h	2-4h	4-6h	6-8h	8-10h
TOF (s^{-1})	4.07×10^{-5}	8.09×10^{-5}	9.91×10^{-5}	4.39×10^{-5}	6.65×10^{-5}

STEM-EDX of the CABB-NC-EtOH sample before and after the photoreaction was studied, and the results are presented in Table 4.4. From the STEM-EDX results, the atomic percentages of Cs and Ag both showed decreasing trends, and the proportion of Bi stayed at the same level, while the percentage of Br increased. This could be due to erosion at the sample surface during the photoreaction, which led to the loss of Cs and Ag, while Bi and Br were more likely to remain within the perovskite structure. STEM images and EDX analysis of CABB-NC after the photoreaction are discussed in Section A3, from Figure A8 to Figure A10. STEM-EDX maps and spectrum of CABB-NC-EtOH-10h are shown in Figure A11.

The STEM-HAADF images of CABB-NC-EtOH after two to six hours of photoreaction are shown in Figure 4.9. To prepare TEM specimens for samples after the photoreaction, a miniscule amount of sample was taken from the vial and then dispersed in hexane to create a suspension. Droplets of suspension were then deposited onto the TEM grid as discussed in Section 3.11.5. In Figure 4.9 (a), the cubes did not seem to undergo significant changes during the first two hours of reaction. Subsequently after four hours of reaction, as shown in Figure 4.9 (b, c), some cubes aggregated while others remain separated. When the reaction time reached six hours, Figure 4.9 (d) shows that some sheets began to appear. This is similar to the phenomenon observed in CABB-NC after reaction, which is shown in Figure A8. STEM-HAADF images of CABB-NC-EtOH after eight and ten hours of reaction are shown in Figure 4.10. After eight hours of reaction, as shown in Figure 4.10 (a), the sheets could still be seen. However, thick agglomerates also formed, which are the particles that appear white in Figure 4.10 (b). When the reaction time reached ten hours, the sheets became larger in size, and they are easily discernible in Figure 4.10 (c-e). Not all large sheets took the shape of a rectangle, as seen in Figure 4.10 (c), where a large sheet appeared to be in an octagon.

Evaluating the information collected, the dip in the reaction rate when the reaction time was six to eight hours could be attributed to the aggregation of cubes. The aggregation became severe during these hours, causing the number of active sites to be lowered. However, going beyond this time, more sheets were formed, providing more contact area for the photoreaction to take place. This hence drove the photoreaction rate up at eight to ten hours of reaction time.

Some bright regions of haze could be observed in Figure 4.9 (c) and Figure 4.10 (b, d). Such haze only existed locally, and separated cubes could still be observed in other regions within the same TEM specimen, as shown in Figure 4.9 (b) and Figure 4.10 (a, c). By adjusting the brightness and contrast of the detector, the haze was revealed to be a number of nanocubes tightly packed together, instead of one large particle. In this way, the existence of such haze did not affect the size distribution analysis discussed subsequently.

Table 4.4. STEM-EDX quantification results of CABB-NC-EtOH before and after the photoreaction with methanol vapour. The results presented are the average values and standard deviations, calculated from the quantification results over at least two different sites.

Sample	Cs atomic %	Ag atomic %	Bi atomic %	Br atomic %
CABB-NC-EtOH	28.1 (±1.9)	16.3 (±0.7)	9.6 (±0.9)	46.0 (±1.9)
CABB-NC-EtOH-2h	28.7 (±1.7)	15.8 (±0.9)	9.6 (±2.8)	45.9 (±1.4)
CABB-NC-EtOH-4h	24.1 (±1.7)	14.1 (±0.5)	9.6 (±0.4)	52.2 (±1.8)
CABB-NC-EtOH-6h	22.8 (±2.8)	12.2 (±1.8)	10.1 (±0.5)	54.9 (±3.2)
CABB-NC-EtOH-8h	25.6 (±1.5)	11.2 (±0.6)	10.2 (±0.7)	53.0 (±0.2)
CABB-NC-EtOH-10h	25.2 (±0.4)	10.9 (±1.1)	9.3 (±0.2)	54.6 (±0.8)

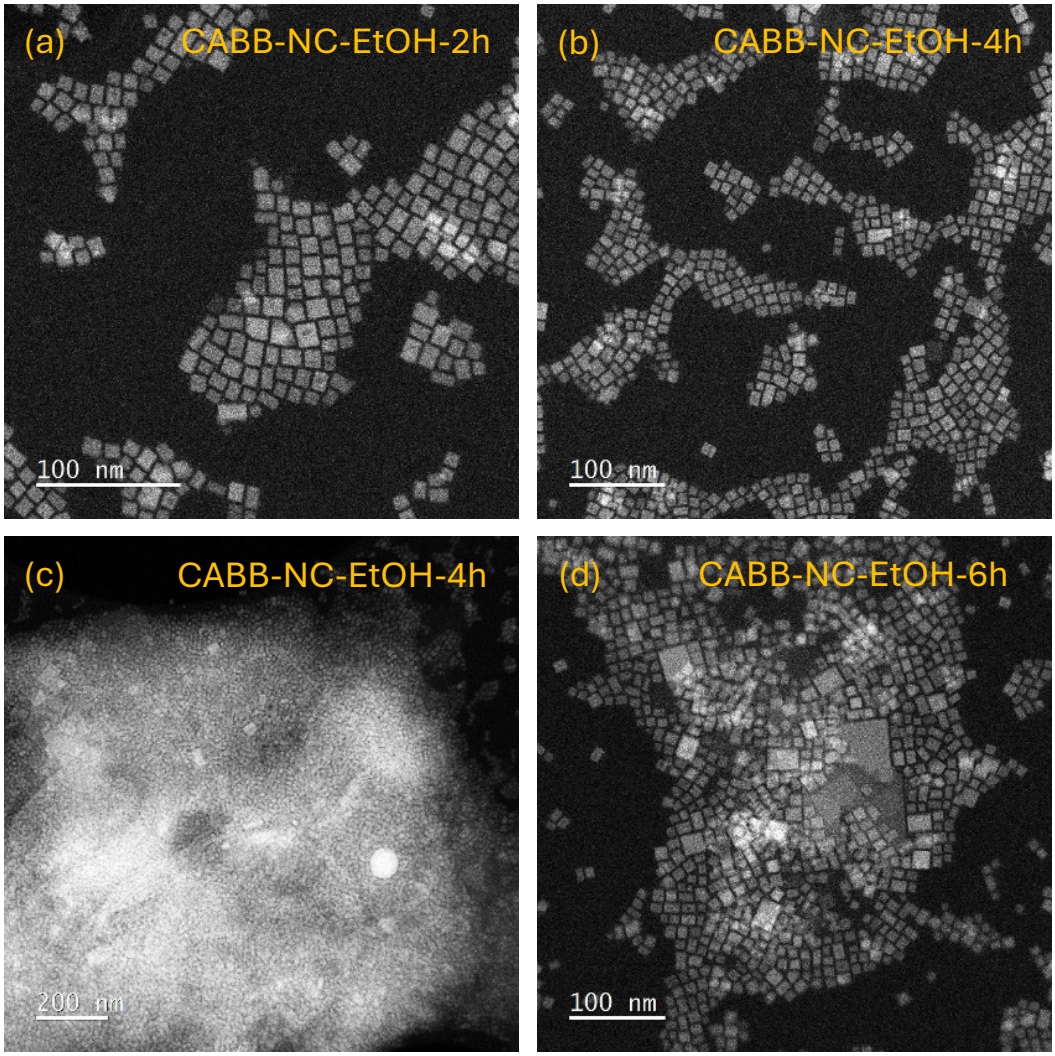

Figure 4.9. STEM-HAADF images of CABB-NC-EtOH after photoreaction, with a total reaction time of (a) two hours, (b, c) four hours and (d) six hours. After four hours of reaction the cubes aggregated at some regions. After six hours of reaction the nanosheets emerged. The STEM-HAADF images were taken using 5.6 pA beam current, 14.38 mrad convergence angle, 1024 x 1024 pixels, and 6 µs dwell time per pixel; for image (a) the pixel size was 3.5 Å x 3.5 Å and the electron fluence was 17 e $Å^{-2}$; for images (b, d) the pixel size was 5.2 Å x 5.2 Å and the electron fluence was 7.8 e $Å^{-2}$; for image (c) the pixel size was 14 Å x 14 Å and the electron fluence was 1.1 e $Å^{-2}$.

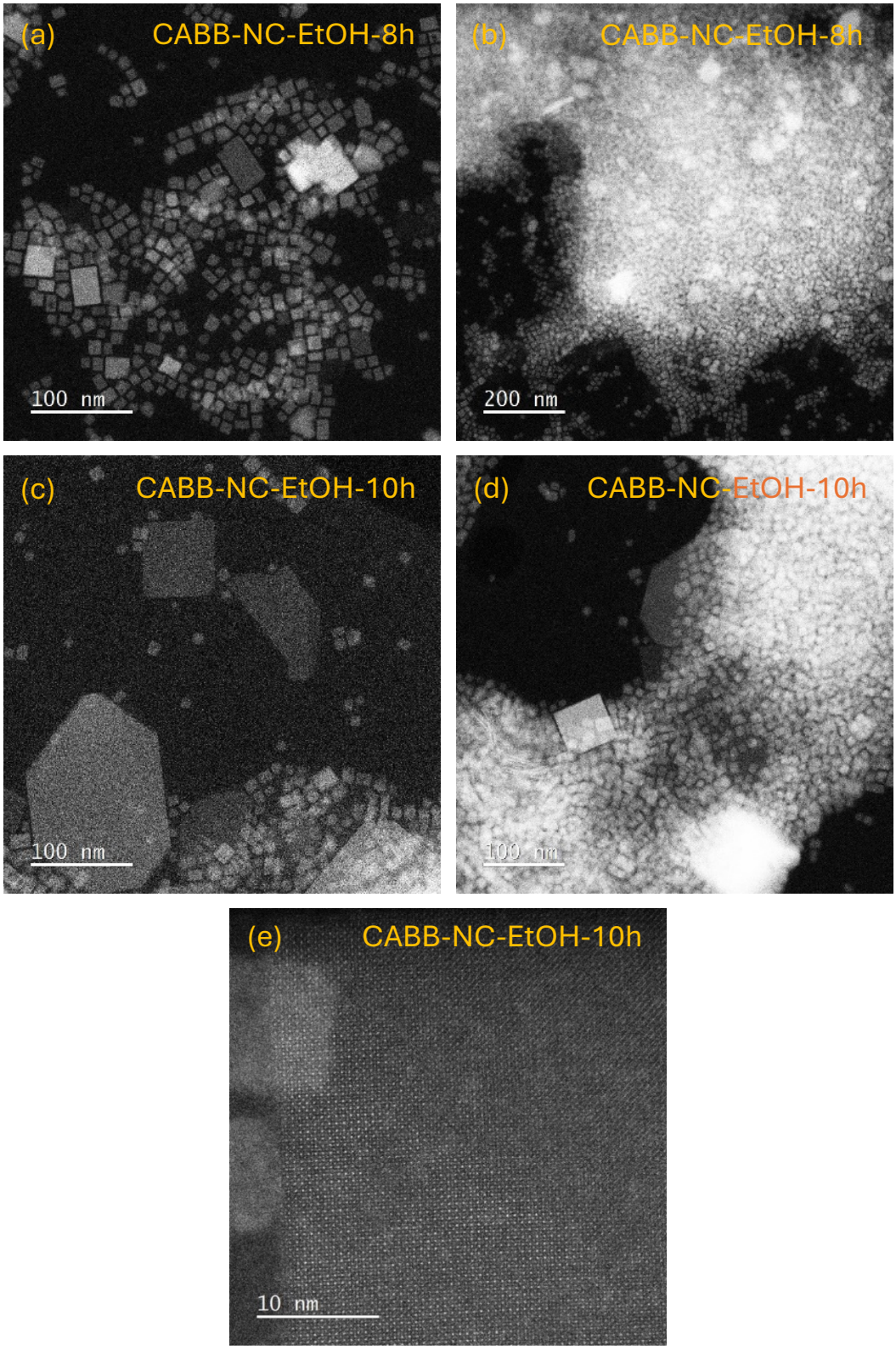

Figure 4.10. STEM-HAADF images of CABB-NC-EtOH after photoreaction, with a total reaction time of (a, b) eight hours and (c-e) ten hours. Both the agglomeration effect and formation of sheets could be seen. The STEM-HAADF images were taken using 5.6 pA beam current, 14.38 mrad convergence angle, 1024 x 1024 pixels, and 6 µs dwell time per pixel; for images (a, c) the pixel size was 4.2 Å x 4.2 Å and the electron fluence was 12 e $Å^{-2}$; for image (b) the pixel size was 10 Å x 10 Å and the electron fluence was 2.1 e $Å^{-2}$; for image (d) the pixel size was 5.2 Å x 5.2 Å and the electron fluence was 7.8 e $Å^{-2}$; for image (e) the pixel size was 0.35 Å x 0.35 Å and the electron fluence was 1.7 x 10^3 e $Å^{-2}$.

The size distribution of the specimen was tracked as the reaction progressed. ImageJ[222] was used for particle size analysis. The results are shown in Figure 4.11. The average size of the particles, mu, and the standard variation, sigma, are given.

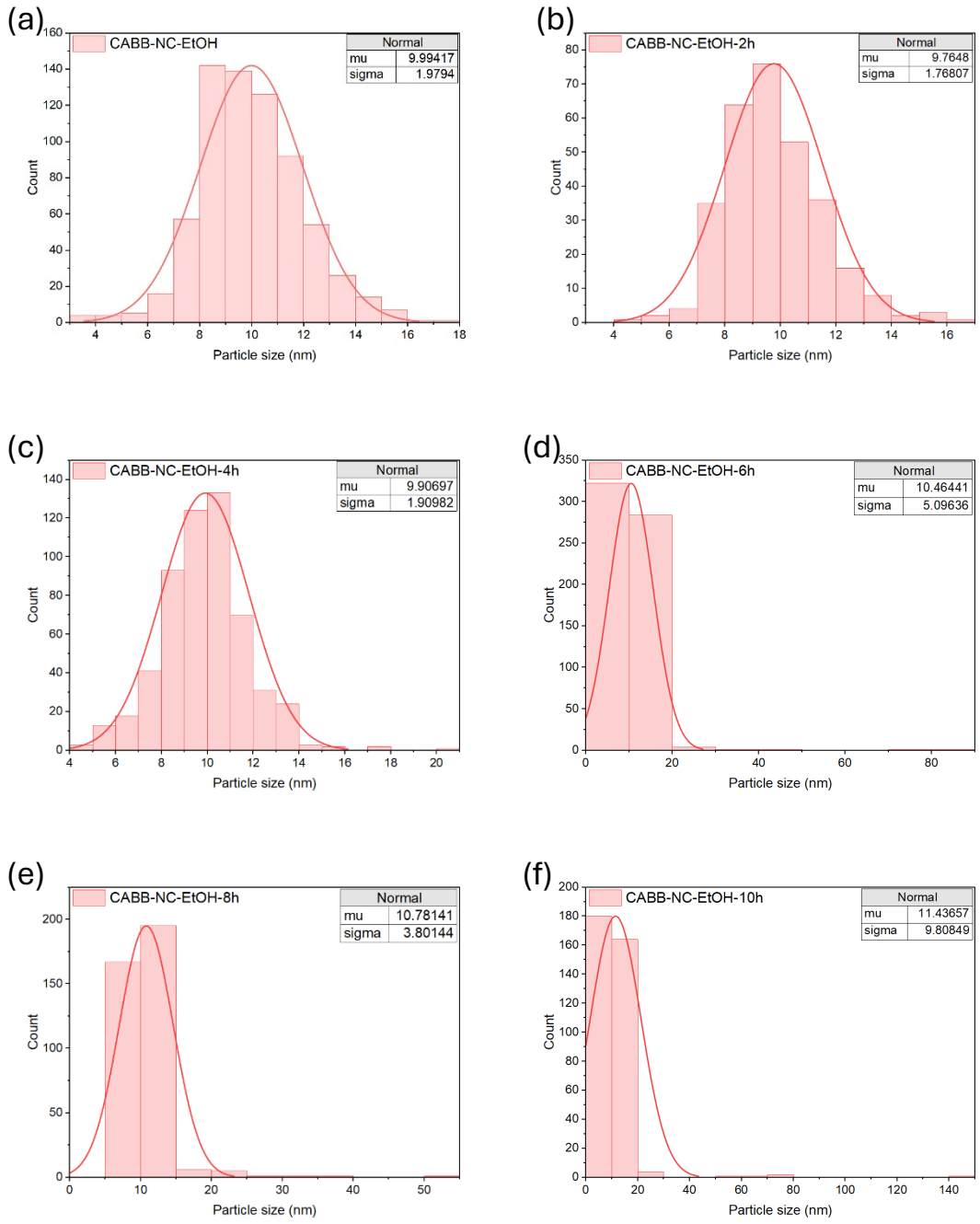

Figure 4.11. Size distribution plots of (a) CABB-NC-EtOH, (b) CABB-NC-EtOH after two hours of reaction, (c) CABB-NC-EtOH after four hours of reaction, (d) CABB-NC-EtOH after six hours of reaction, (e) CABB-NC-EtOH after eight hours of reaction and (f) CABB-NC-EtOH after ten hours of reaction. The average particle size increased as the photoreaction progressed. Sheets several times larger than cubes appeared after six hours of reaction, which greatly skewed the results.

From the data obtained in Figure 4.11, throughout the reaction process, the average size of the cubes was around 10 nm. However, as the reaction time became longer, larger sheets were formed, which skewed the size distribution analysis. To analyse the change in size for most cubes, whilst the sheets were being formed, plots excluding the cubes and sheets with a size of more than 20 nm were created, as presented in Figure 4.12.

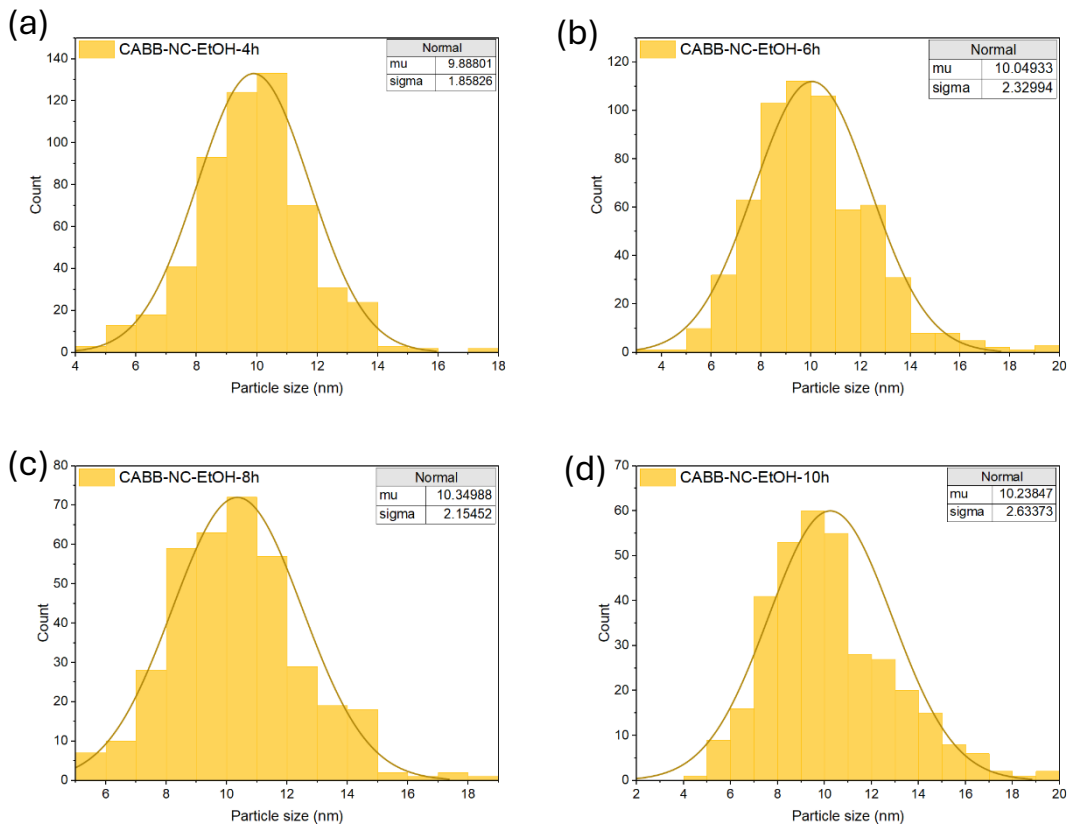

Figure 4.12. Size distribution plots excluding particles larger than 20 nm, for (a) CABB-NC-EtOH after four hours of reaction, (b) CABB-NC-EtOH after six hours of reaction, (c) CABB-NC-EtOH after eight hours of reaction and (d) CABB-NC-EtOH after ten hours of reaction. Even with the large sheets excluded, the average size of the particles increased during the reaction.

Combining the results from Figure 4.11 and Figure 4.12, even with large particles excluded, the size distribution of the cubes still exhibited an increasing trend with longer reaction time. Taking the formation of large sheets into account, after six hours of reaction, the average size of the CABB-NC-EtOH particles increased by 0.5 nm, and another two hours of reaction led to a further 0.3 nm growth. The increase in size became more significant between 8-10 hours of reaction, where the average particle size grew by 0.7 nm. Excluding the large

sheets, the remaining nanocubes still showed an increase in size by around 0.3 nm, after ten hours of reaction.

CABB nanosheets (denoted as 2D-CABB) were also synthesised, tested for photoreaction with methanol, and characterised. The results are discussed in Section A4, as its performance was no better than CABB-HBr or CABB-NC. In addition, attempts to create heterojunctions using CABB-HBr and CABB-NC were discussed in Section A5.

4.2.4. Fast Fourier Transform and nanoparticle surface study

Fast Fourier Transform (FFT) was implemented to analyse the high-resolution STEM images of CABB-NC-EtOH to extract structural information of the samples. The ideal structure of CABB is a cube[71], so theoretically the diffraction patterns or FFT patterns from the family of crystallographic directions <100> are equivalent. The crystallographic direction [010] was used to label the reflection spots. As an example, the FFT pattern of CABB-NC-EtOH is shown in Figure 4.13 (a). The red square shown in Figure 4.13 (b) indicates where the FFT data were acquired from. The FFT patterns of CABB-NC-EtOH after reaction and 2D-CABB are shown in Figure A16 and Figure A17. The distance in reciprocal space (1/d) between (000) and (400) grew as the reaction time increased, signifying a gradual reduction in the lattice spacing. This phenomenon can be associated to the formation of nanosheets during the photoreaction, and can be attributed to the microstrain that exists within the nanosheet structure[221]. To support this theory, FFT data were also extracted from STEM images of 2D-CABB as shown in Figure A17 (c, d). The 1/d measured for 2D-CABB was very close to that of CABB-NC-EtOH-10h in Figure A17 (a), which suggests that the nanosheet structure inherently possesses the microstrain. Moreover, the broad peak at around 20°-40°, in the XRD patterns of CABB-NC-EtOH-10h in Figure 4.8 (e) and 2D-CABB in Figure A12 (a), could also indicate the existence of the microstrain. The changes in 1/d and hence the lattice spacing are summarised in Table 4.5. Here a nanosheet is defined as a CABB nanoparticle

whose size exceeds 50 nm laterally. The FFT patterns for CABB-NC-EtOH-10h were obtained from nanosheets formed during the photoreaction, and the FFT patterns for CABB-NC-EtOH, CABB-NC-EtOH-2h, and CABB-NC-EtOH-6h were obtained from nanocubes. The FFT patterns acquired from CABB-NC before and after photoreaction are shown in Figure A18 and Figure A19.

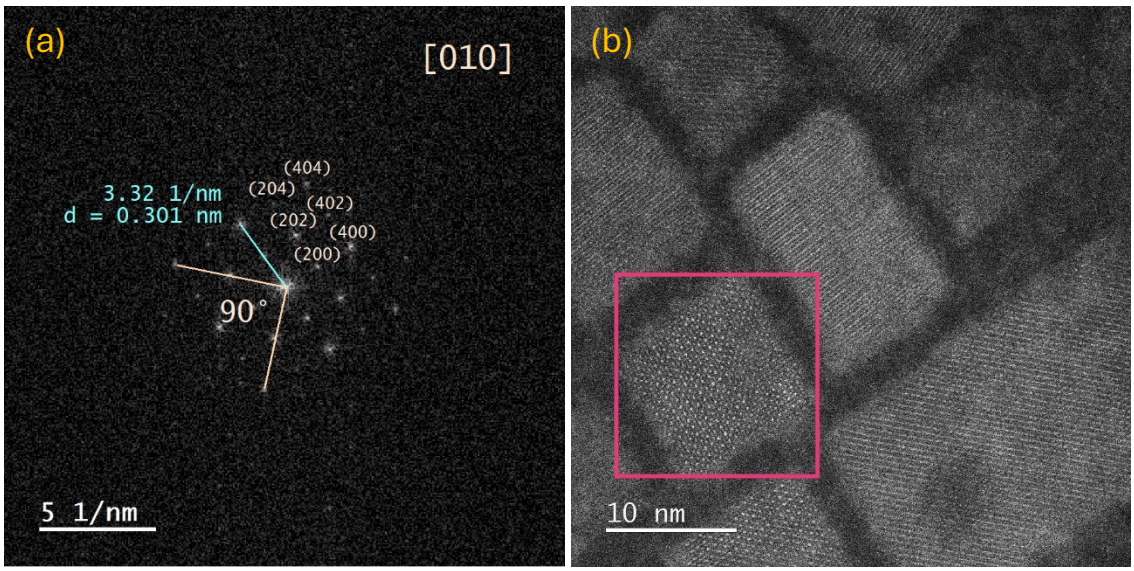

Figure 4.13. (a) FFT pattern of CABB-NC-EtOH. (b) The region where the FFT pattern is obtained from in a STEM image (indicated with a square).

Table 4.5. Measured distance between (000) and (400) from FFT patterns and its corresponding planar distance for CABB-NC-EtOH before and after photoreaction, as well as 2D-CABB. At least two particles were investigated from each sample, and the average values are presented here.

Sample	Distance in 1/nm	Distance in nm
CABB-NC-EtOH	3.27	0.306
CABB-NC-EtOH-2h	3.30	0.303
CABB-NC-EtOH-6h	3.32	0.301
CABB-NC-EtOH-10h	3.41	0.293
2D-CABB	3.42	0.292

The surface of CABB-NC and CABB-NC-EtOH nanoparticles were studied by examining the high-resolution STEM images of these specimens. The method to perform analysis at the edge of the nanoparticles was discussed in Section 3.11.3. Some background-subtracted line profiles of the atomic rows containing either Ag/Bi or Cs from a CABB-NC-EtOH-2h particle are shown in Figure 4.14 as examples. The peaks in the spectra representing the

location of an atom showed a decrease in intensity towards the edge of the particle, and at some places the signal became so weak that it could not be differentiated from the background noise. The distance between each peak for each row of atoms were calculated, and the results in average for CABB-NC-EtOH-2h, CABB-NC-EtOH-6h, CABB-NC-EtOH-10h, CABB-NC and CABB-NC-4h are presented in Table A3 and Table A4. The analysis was performed on nanosheets for CABB-NC-EtOH-10h and the rest was done on nanocubes. No obvious patterns could be observed in terms of any significant changes in the distance between atoms close to the surface of the nanoparticles, compared to the distance between atoms in the bulk region.

However, given that the resolution of the images were limited and the full resolving power of the microscope was not achieved, the observations made so far have been tentative. In addition, due to the lighter weight of Cs atoms than Bi, Cs columns were not as easy to discern as Ag/Bi columns, especially around the surface of the nanoparticles. Even Ag/Bi atoms could be difficult to distinguish near the surface, as the intensity of the spot where the next atom should be was no stronger than background noise, or it could be caused by surface contamination instead. The limited resolution of the STEM images also made the identification of the outmost atoms of the perovskite structures difficult, aggravated by the fact that Br atoms were not visible in the images. The use of high-resolution STEM-EDX may help identifying the outmost atoms of the nanoparticles. As for the relative occupancy of atoms in the perovskite structure, the number should be close to 1. This is because no obvious vacancies could be observed in STEM images for all samples, except around the surface of the nanoparticles, as seen in Figure A16 (b, d) and Figure A18 (b).

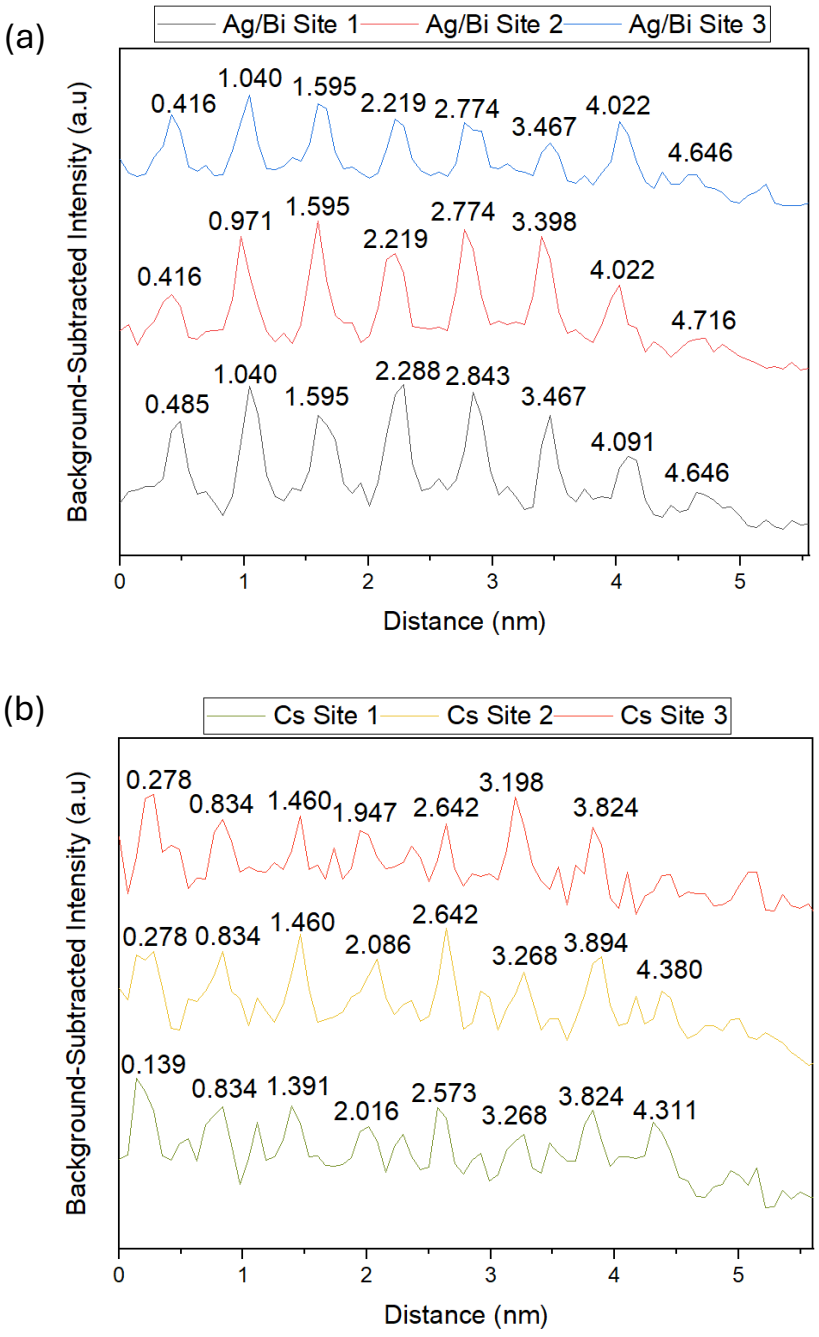

Figure 4.14. (a) Intensity line profiles of three atomic rows containing Ag/Bi from a CABB-NC-EtOH-2h sample particle. (b) Intensity line profiles of three rows containing Cs from a CABB-NC-EtOH-2h sample particle. The line profiles started from the bulk region of the sample particle (at 0 nm) and ended outside the boundary of the particle. The labels indicate the corresponding x-coordinates of the peaks.

4.2.5. Formaldehyde detection

The method used to quantify the amount of formaldehyde produced was described in Section 3.5.3, and the results are presented in this section. Figure 4.15 (a) shows the data collected from UV-vis spectroscopy, using diluted formaldehyde of known concentrations, and the methanol sample with unknown concentration of formaldehyde after reaction with CABB. In the region around 250 nm, as shown in Figure 4.15 (b), the area under the curve was proportional to the concentration of formaldehyde present in the sample liquid. Methanol before reaction can also produce a peak in this region, which can be assessed using liquid UV-vis spectroscopy. As shown in Figure 4.15 (c), the area under the curve for methanol before reaction was calculated, and in subsequent calculations the value of this area was used as a baseline. The area under other curves was subtracted from this value, in order to eliminate the effect of methanol present in the liquid samples for UV-vis measurements. Figure 4.15 (d) shows a linear fit, connecting known formaldehyde concentrations and their corresponding values determined from area under the curve.

As an example, the area under curve for a methanol sample after a photoreaction run was found to be 2.9765, corresponding to 3.56 μmol formaldehyde produced. Separately, from hydrogen GC the amount of H_2 produced was determined to be 3.6 μmol in this photoreaction run, giving a hydrogen to formaldehyde product ratio close to 1:1. Other possible by-products such as CO and CO_2 were not detected in a hydrocarbon GC, and therefore hydrogen and formaldehyde can be assumed to be the sole photoreaction products in the methanol photo-oxidation reaction.

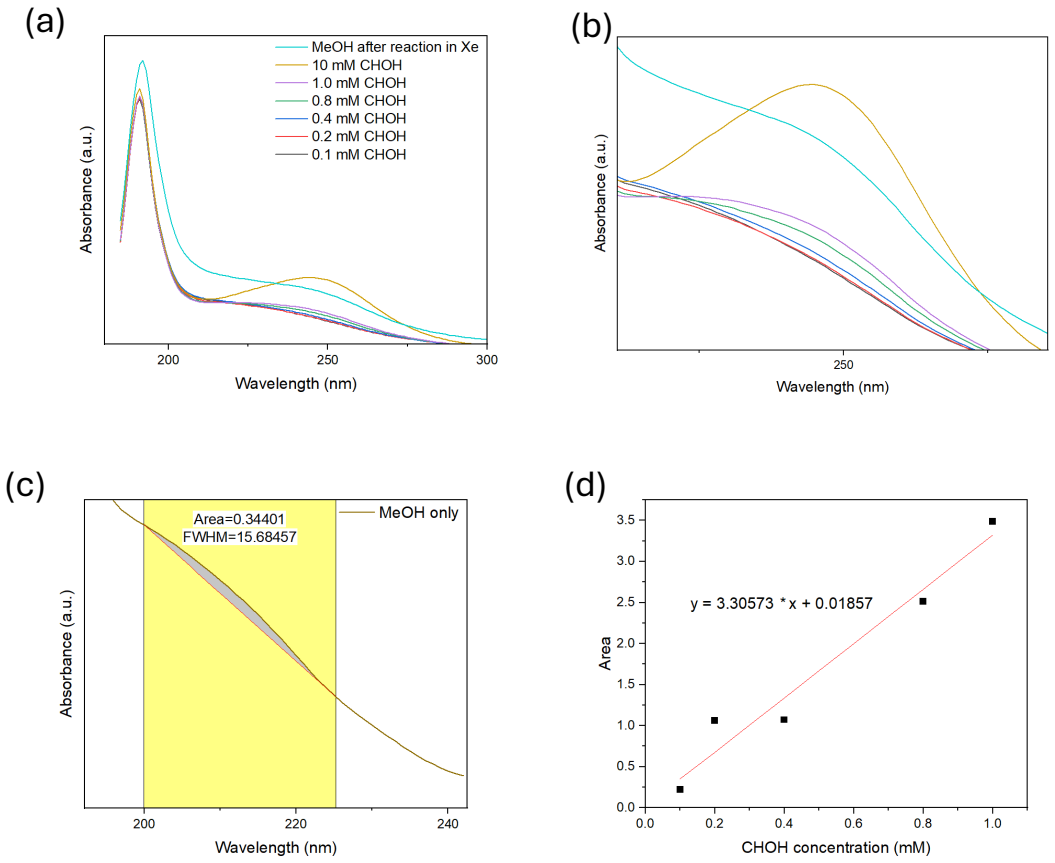

Figure 4.15. (a) Plot of liquid UV-vis data containing diluted formaldehyde with known concentrations, and methanol obtained after a photoreaction run, and (b) an enlarged graph of the region around 250 nm wavelength. (c) An example showing how the area under the curve was calculated, using methanol before reaction as the sample. (d) The linear fit of formaldehyde samples with known concentrations and their corresponding area under curve.

4.2.6. Mechanistic analysis

A series of XPS data were taken for CABB-HBr and CABB-NC-EtOH to investigate the reaction mechanism in methanol photo-oxidation. Figure 4.16 shows the valence spectra of both CABB-HBr and CABB-NC-EtOH. The valence band of CABB-HBr was measured to be 2.18 eV, and that of CABB-NC-EtOH sat at 1.99 eV. The valence band edge can be converted to potential versus normal hydrogen electrode (vs. NHE) as;

$$VB_{(vs.\ NHE)} = \Phi + VB - 4.44\ eV \qquad (4.1)$$

where VB is the valence band measured using XPS and Φ is the work function of the XPS analyser[223]. Φ is 4.20 eV in this case. The valence band vs. NHE of CABB-HBr is hence 1.85 eV, and that of CABB-NC-EtOH is 1.75 eV. Combined with Tauc plots in Figure 4.3 (b) and Figure 4.3 (d), the conduction band of CABB-HBr is at -0.27 eV (vs. NHE), and the conduction band of CABB-NC-EtOH is -0.46 eV (vs. NHE).

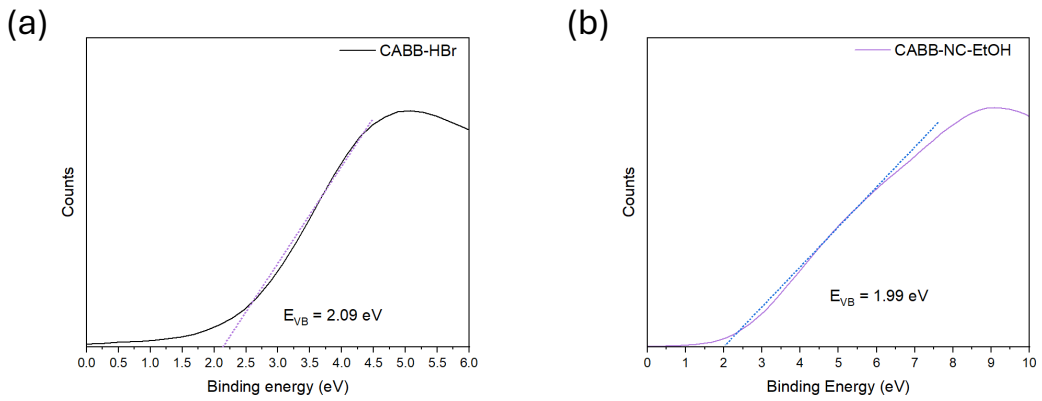

Figure 4.16. XPS valence spectra of (a) CABB-HBr and (b) CABB-NC-EtOH. The valence bands were measured to be 2.09 eV for CABB-HBr and 1.99 eV for CABB-NC-EtOH.

In order to acquire in-situ XPS data, the CABB samples were loaded into a borosilicate capillary tube, with trace amount of methanol. This was used to reproduce the original reaction environment, at the point at which the Xe light was turned on for in-situ XPS measurements. The peak shifts for CABB-HBr are recorded in Table 4.6. When the Xe lamp was turned on, all four elements showed a trend with a slight shift to higher binding energy. Figure 4.17 shows the plots obtained from in-situ XPS analysis on CABB-HBr. All shifts in peaks except for Ag 3d and Bi 4f were smaller than 0.1 eV, signifying that the most significant changes in electron density took place around Ag and Bi in the CABB-HBr sample during the photoreaction. When the binding energy increases, the outer electron density decreases and vice versa[224]. The measurement interval was 0.1 eV between each step, and due to imperfect curve fitting, changes within 0.1 eV may not reflect actual electron density variations. C 1s peaks were also measured and calibrated.

Table 4.6. In-situ XPS peak shifts for CABB-HBr before and after Xe lamp was switched on.

Peaks	First peak (eV)		Second peak (eV)	
	Old position	New position	Old position	New position
Cs 3d	724.48	724.53	738.38	738.43
Ag 3d	367.55	367.67	373.55	373.57
Bi 4f	158.98	159.14	164.28	164.44
Br 3d	68.68	68.77	75.38	75.47

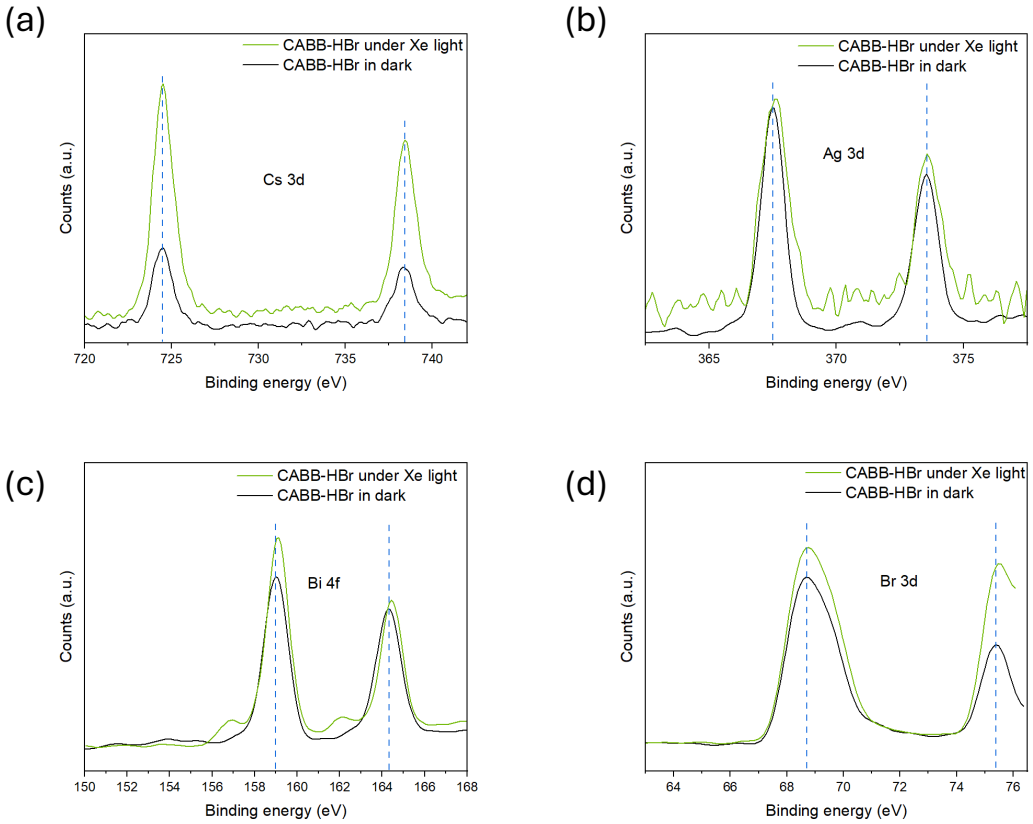

Figure 4.17. In-situ XPS plots of CABB-HBr, in dark and illuminated with Xe light, of (a) Cs 3d, (b) Ag 3d, (c) Bi 4f and (d) Br 3d. When the light was switched on, Ag 3d and Bi 4f peaks exhibited substantial shifts to higher binding energies, and the peaks due to Cs 3d and Br 3d remained at the same energy.

Similarly, in-situ XPS measurements for CABB-NC-EtOH were also conducted, and Table 4.7 records the peak positions of the CABB-NC-EtOH sample without and with illumination from Xe lamp. The Cs 3d peaks barely moved, whereas the Ag 3d and Bi 4f peaks underwent noticeable changes; no changes in Br 3d peaks were observed, as the peaks stayed at the same positions. The plots obtained from the in-situ XPS are shown in Figure 4.18. The in-situ XPS data from CABB-NC-EtOH further proved that Ag and Bi took up a significant role during the methanol photo-oxidation reaction.

Table 4.7. In-situ XPS peak shifts for CABB-NC-EtOH before and after Xe lamp was switched on.

Peaks	First peak (eV)		Second peak (eV)	
	Old position	New position	Old position	New position
Cs 3d	724.48	724.49	738.38	738.39
Ag 3d	367.32	367.53	373.22	373.53
Bi 4f	158.98	159.20	164.38	164.50
Br 3d	68.48	68.48	75.28	75.28

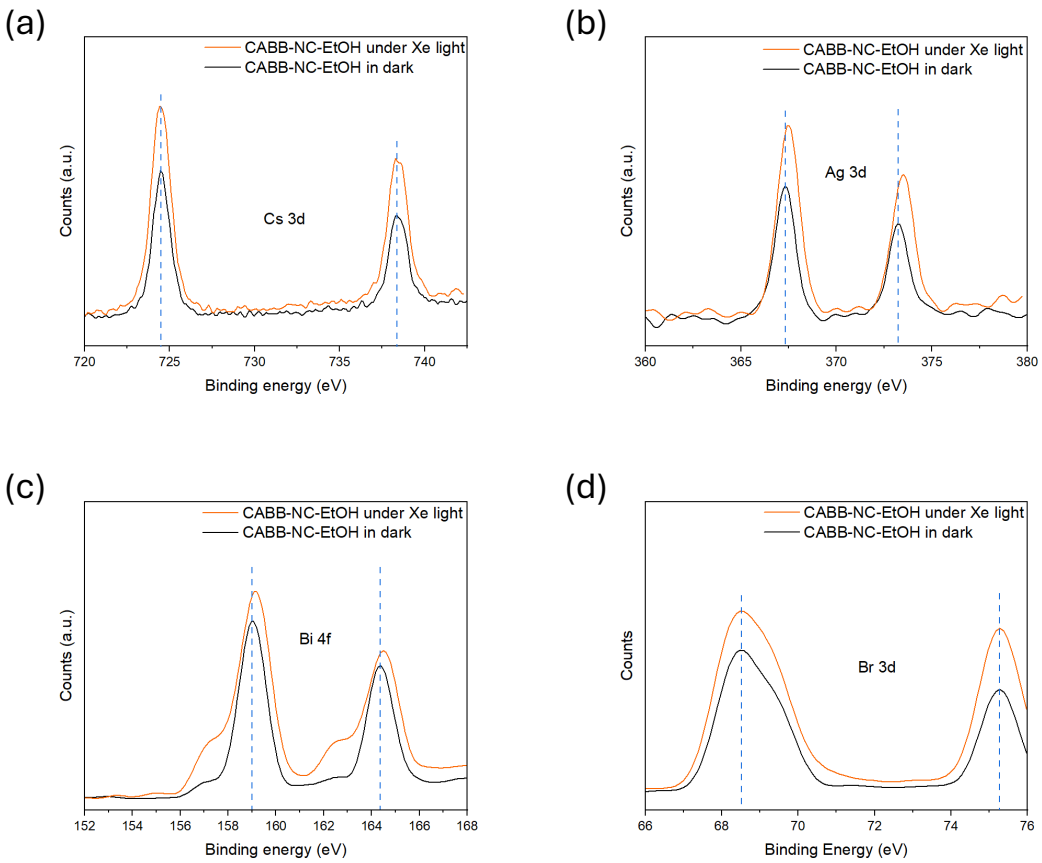

Figure 4.18. In-situ XPS plots of CABB-NC-EtOH, in dark and illuminated with Xe light, of (a) Cs 3d, (b) Ag 3d, (c) Bi 4f and (d) Br 3d. Similar to CABB-HBr, when the light was on, Ag 3d and Bi 4f peaks exhibited substantial shifts to higher binding energies, and the peaks due to Cs 3d and Br 3d remained at the same energies.

Combining the in-situ XPS data and the electron configurations of Ag and Bi, a possible photoreaction mechanism is proposed here. During the photoreaction, the oxidation state of Ag may be constantly changing between +1 and +2, and that of Bi may be constantly moving between +3 and +5. The changes in oxidation states provide the electrons and holes required to split methanol into formaldehyde and hydrogen. This proposed mechanism is

explained in Figure 4.19. The electrons generated from photoexcitation attract the hydrogen from a H-O-R bond and forms a hydrogen free radical, and a C=O double bond is formed in the remaining methanol structure. Carrying an extra electron and being negatively charged, the remaining structure is then attracted towards the holes left in the catalyst, where it becomes formaldehyde. In the meantime, another hydrogen free radical is formed. These two hydrogen free radicals combine, and hydrogen gas is hence produced. Figure 4.20 illustrates how this photocatalytic system works, where the reduction reaction takes place at the conduction band of CABB, and oxidation reaction takes places at the valence band.

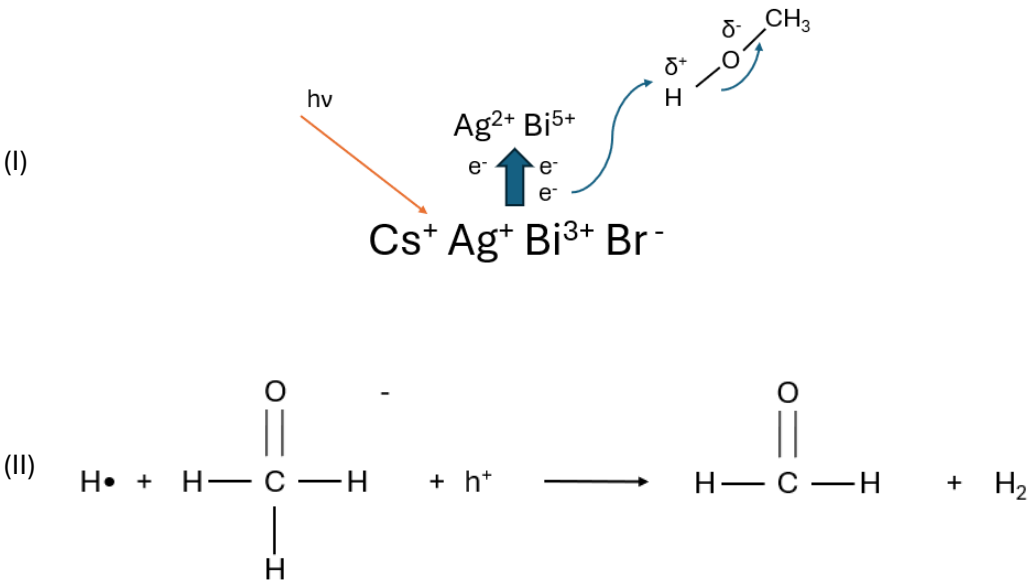

Figure 4.19. Possible reaction pathway of methanol photo-oxidation, where CABB is the photocatalyst.

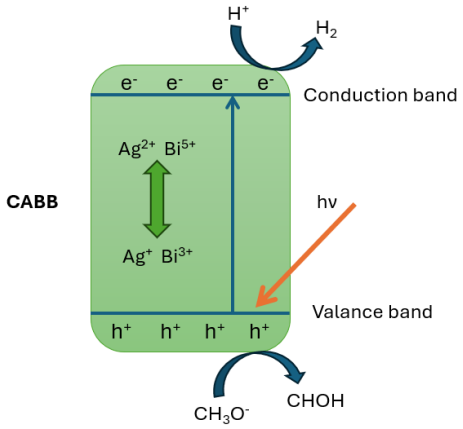

Figure 4.20. Schematic diagram showing the possible reaction mechanism of methanol photo-oxidation using CABB as the catalyst.

Photoluminescence (PL) and time-resolved photoluminescence (TRPL) techniques are frequently used to study the electron-hole recombination kinetics[196]. PL and TRPL data were kindly obtained by Yiyang Li from Inorganic Chemistry Laboratory, University of Oxford, and are shown in Figure 4.21. The PL spectra in Figure 4.21 (a) revealed that the PL emission of CABB-NC-EtOH was quenched, compared with that of CABB-HBr. PL can lead to competitive radiative process which releases photons, and non-radiative process that releases phonons during electron-hole recombination[225]. In addition, the electron-hole pair may remain separated so the charge carriers can participate in the photocatalytic reaction, which is the desired scenario. From Figure 4.21 (a), in terms of CABB-NC-EtOH, the quenched peak means the non-radiative process or the electron-hole pair being separated happened more often than CABB-HBr during the photoreaction, which contributed to higher activity in methanol photo-oxidation. The corresponding wavelengths of the peaks were 644 nm for CABB-HBr, 636 nm for CABB-NC-EtOH and 633 nm for CABB-NC-EtOH-4h. No significant shift was observed for CABB-NC-EtOH-4h.

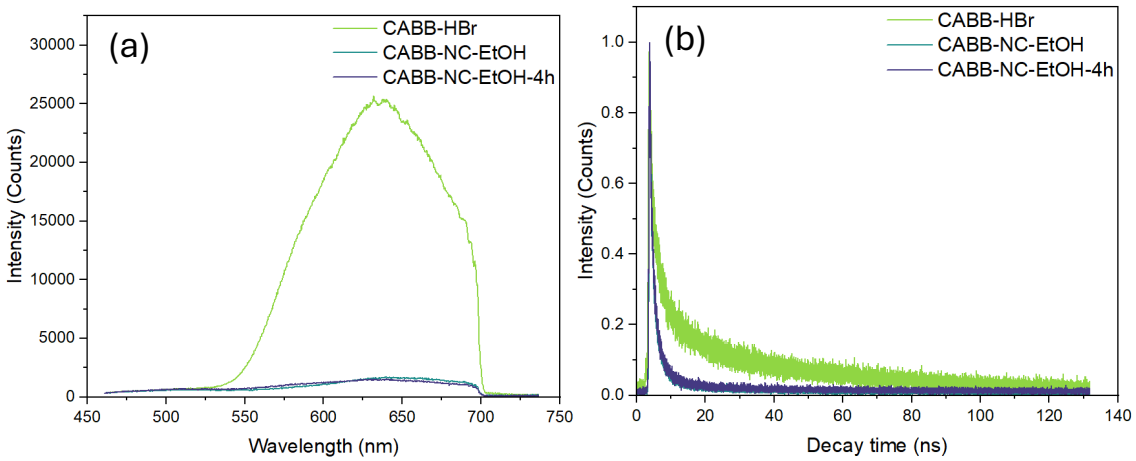

Figure 4.21. (a) PL and (b) TRPL spectra of CABB-HBr, CABB-NC-EtOH and CABB-NC-EtOH-4h. The PL emissions from CABB-NC-EtOH samples were quenched compared to the PL emission from CABB-HBr. In terms of TRPL, CABB-NC-EtOH samples had shorter average lifetimes in the long decay region than CABB-HBr.

To fit the TRPL plots in Figure 4.21 (b), the decays were divided into two segments; a fast exponential decay and a long exponential decay. This can be expressed as;

$$I_{TRPL}(t) = \sum_{1}^{n} A_i e^{-\frac{t}{\tau_i}} \tag{4.2}$$

where I_{TRPL} is the intensity, t is the decay time, A_i is the amplitude of the component i, and τ_i is the lifetime of the component[225]. Since bi-exponential fitting is used here, n takes a value of 2. The segments were created when intensity dropped from 1 to 0.5, and exponential fits to the CABB-HBr and CABB-NC-EtOH TRPL data were performed using the Origin software.

To calculate the average lifetime from the bi-exponential decay, Equation (4.3) is used[226];

$$\tau_{average} = \frac{\sum_i A_i \tau_i}{\sum_i A_i} \tag{4.3}$$

The values of A, τ and hence $\tau_{average}$ obtained are displayed in Table 4.8. In the fast decay region, the lifetime is similar between CABB-HBr and CABB-NC-EtOH. However, in the long decay region, the lifetime of CABB-NC-EtOH is significantly shorter than that of CABB-HBr, resulting in a shorter average lifetime. This means that the photoexcited carriers from CABB-NC-EtOH are quickly used in the non-radiative processes, which include the photoreaction with methanol. As for CABB-HBr, even though its carriers live longer, a lot of which are consumed in the radiative process, and this is unfavourable to photocatalysis.

Table 4.8. Constants of the exponential decay fit from TRPL data.

Sample	A_1	τ_1 (ns)	A_2	τ_2 (ns)	$\tau_{average}$ (ns)
CABB-HBr	0.538	0.661	0.330	15.6	6.34
CABB-NC-EtOH	0.769	0.631	0.533	2.13	1.24

4.3. Conclusions

In this chapter, the synthesis, characterisation and photocatalytic performance of CABB in bulk and nano forms have been reported. The main findings are listed as follows:

- CABB of both forms rapidly decomposed in methanol, while adding excess NaBr only provided protection for CABB-HBr in the photocatalytic reaction with liquid methanol.
- By conducting the photoreaction in methanol vapour, the halide perovskite was prevented from structural breakdown, and long hours of activity were recorded.
- CABB-NC performed better than CABB-HBr in the photoreaction, due to an expanded surface area for reaction, even though the turnover frequency for CABB-NC was lower.
- When CABB-NC had their surface ligands washed away using ethanol, their activity further improved, and the best photocatalytic hydrogen production rate using methanol vapour was 229 μmol g^{-1} h^{-1}.
- STEM-HAADF images of CABB-NC-EtOH before and after photoreaction revealed that nanosheets were formed from nanocubes after around six hours of reaction, and larger sheets were observed with a longer reaction time. The nanosheets helped maintaining the photoreaction rate.
- FFT analysis showed a shorter lattice spacing of nanosheets than that of nanocubes, which may be caused by the microstrain within the nanosheets.
- The surface of the CABB nanoparticles were closely examined. Except for some possible vacancies, the distance between atoms near the surface of nanoparticles did not vary from the distance between atoms in the bulk region.
- In-situ XPS revealed that Ag and Bi played an important role in this photoreaction system. During the reaction, Ag and Bi switched to higher oxidation states after receiving photons, which provided electrons and holes to initiate the methanol oxidation reaction.

Chapter 5 Degradation studies on lead-free halide perovskites in photocatalytic water splitting

Contents

5.1. Introduction 134
5.2. Results and discussion 135
5.2.1. Synthesis and characterisation of PEA_2SnBr_4 and its heterojunctions 135
5.2.2. Reactions of bulk CABB in water 140
5.2.3. CABB nanocubes in water 146
5.2.4. CABB nanosheets in water 150
5.3. Conclusions 154

5.1. Introduction

In this chapter, the application of halide perovskites in water splitting and how they degraded are studied. In addition to $Cs_2AgBiBr_6$ that was extensively discussed in the previous chapter, another type of halide perovskite, phenethylammonium tin bromide PEA_2SnBr_4 (PSB), was also synthesised, tested and characterised.

As discussed in Chapter 1 and Chapter 2, forming heterojunctions could dramatically improve the photocatalytic activity. To date, the only heterojunction reported on PEA_2SnBr_4 was with g-C_3N_4, which greatly increased the hydrogen production rate in water splitting[55]. An alternative option, MoS_2, has already shown its potential in photocatalytic water splitting[227]. MoS_2 in bulk form has a bandgap of 1.23 eV, and in its lower dimension form, i.e., in 2D, the bandgap increases[228,229]. Depending on the dimensions of MoS_2, the heterojunction created with PEA_2SnBr_4 may be either type I or type II.

Little research has been reported on the properties and photocatalytic performance of $Cs_2AgBiBr_6$ in water. Fan et al.[93] reported that water-soaked nanosized CABB formed a

CABB/BiOBr heterojunction, and the activity on Rhodamine B degradation was enhanced. In this chapter, CABB was found to react with water and form BiOBr, and the resulting structure was tested in the water splitting photoreaction and characterised.

5.2. Results and discussion

5.2.1. Synthesis and characterisation of PEA_2SnBr_4 and its heterojunctions

The synthesis process of PSB largely followed the works of Romani et al.[55] and Zhu et al.[54] with some minor modifications described in Section 3.1. The stability of PSB in air and water was tested using XRD, and the results are shown in Figure 5.1 (a). After seven days in air, the XRD data showed almost no change, while some peaks emerged after immersing PSB in deionised water for seven days. This means that a small portion of PSB could react with water, if it stays in water for an extended period of time. PSB was also investigated using SEM, TEM and STEM. Figure 5.1 (b, c) show SEM and TEM images of PSB respectively. It can be seen from Figure 5.1 (b) that the specimen was mostly formed of sheet-like structures, but in this case the sheets were not separated, and a cluster was formed. The thin sheets can be seen more clearly in Figure 5.1 (c). The discrepancy could be due to specimen preparations, where the dispersion for TEM specimen was better separated than the SEM specimen. Figure 5.1 (d, e) are STEM-HAADF images of PSB. A significant problem with PSB is its beam sensitivity. Once the specimen was exposed to the electron beam, significant changes in structure were observed before an image could be recorded. To determine the electron fluence limit for PSB, a series of diffraction patterns were taken to record the decrease in intensity of specific reflections. The details of this process were described in Section 3.11.2.1, and data from one area is shown as an example in Figure 5.2.

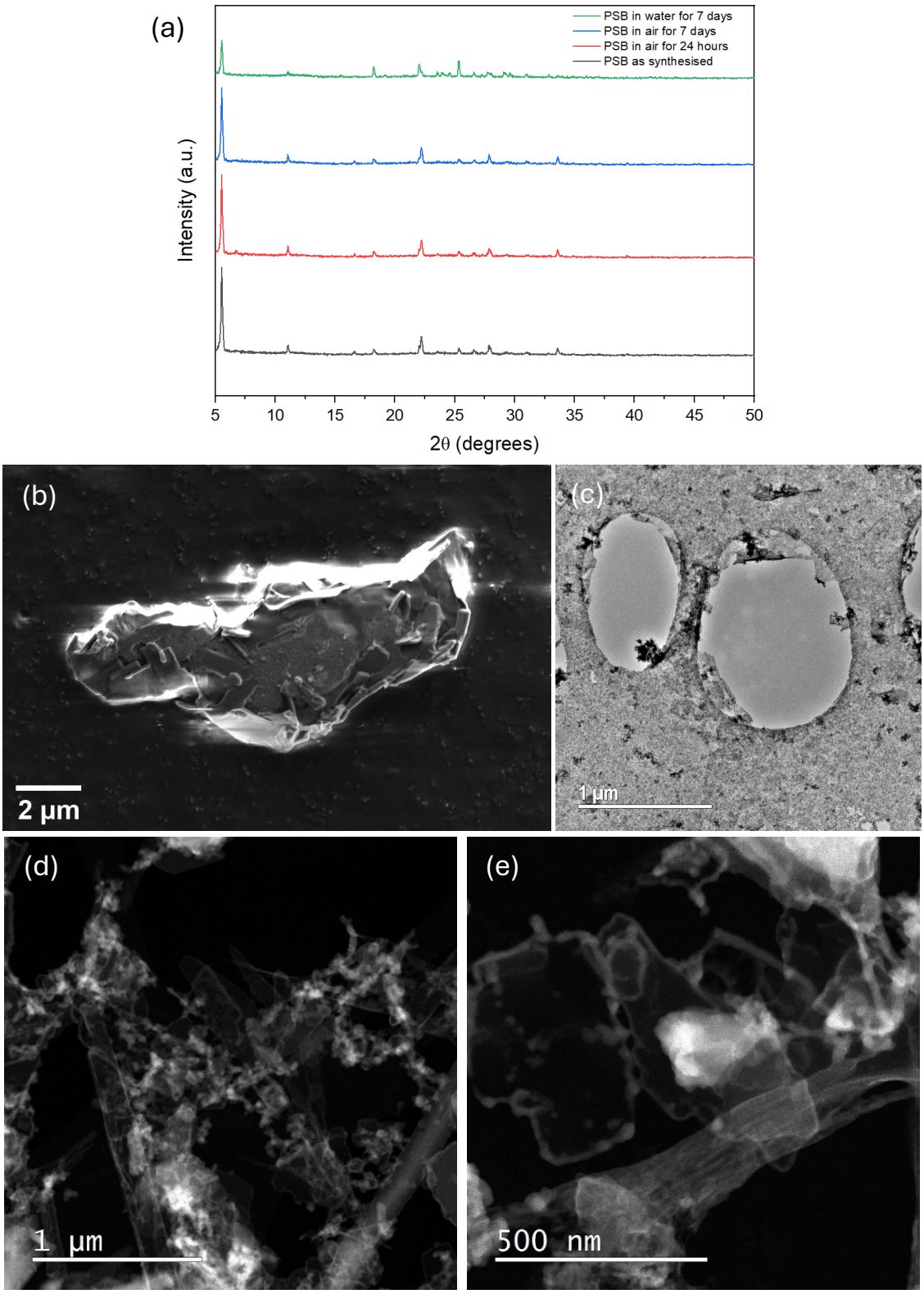

Figure 5.1. (a) XRD data of PSB as synthesised, exposed in air for 24 hours, exposed in air for seven days and immersed in water for seven days. (b) SEM image of PSB. (c) TEM image of PSB. (d, e) STEM-HAADF images of PSB. SEM image (b) was taken using 2 kV voltage, 100 pA current, 5 mm working distance and an SE2 detector. TEM image (c) was taken using 4000x magnification, 56 nA probe current and an exposure time of 0.5 s. STEM-HAADF images (d, e) were taken with a beam current of 28.5 pA, 22.48 mrad convergence angle, 1024 x 1024 pixels, and 12 µs dwell time per pixel. Image (d) had a pixel size of 26 Å x 26 Å and the electron fluence was 3.2 e $Å^{-2}$. Image (e) had a pixel size of 10 Å x 10 Å and the electron fluence was 21 e $Å^{-2}$.

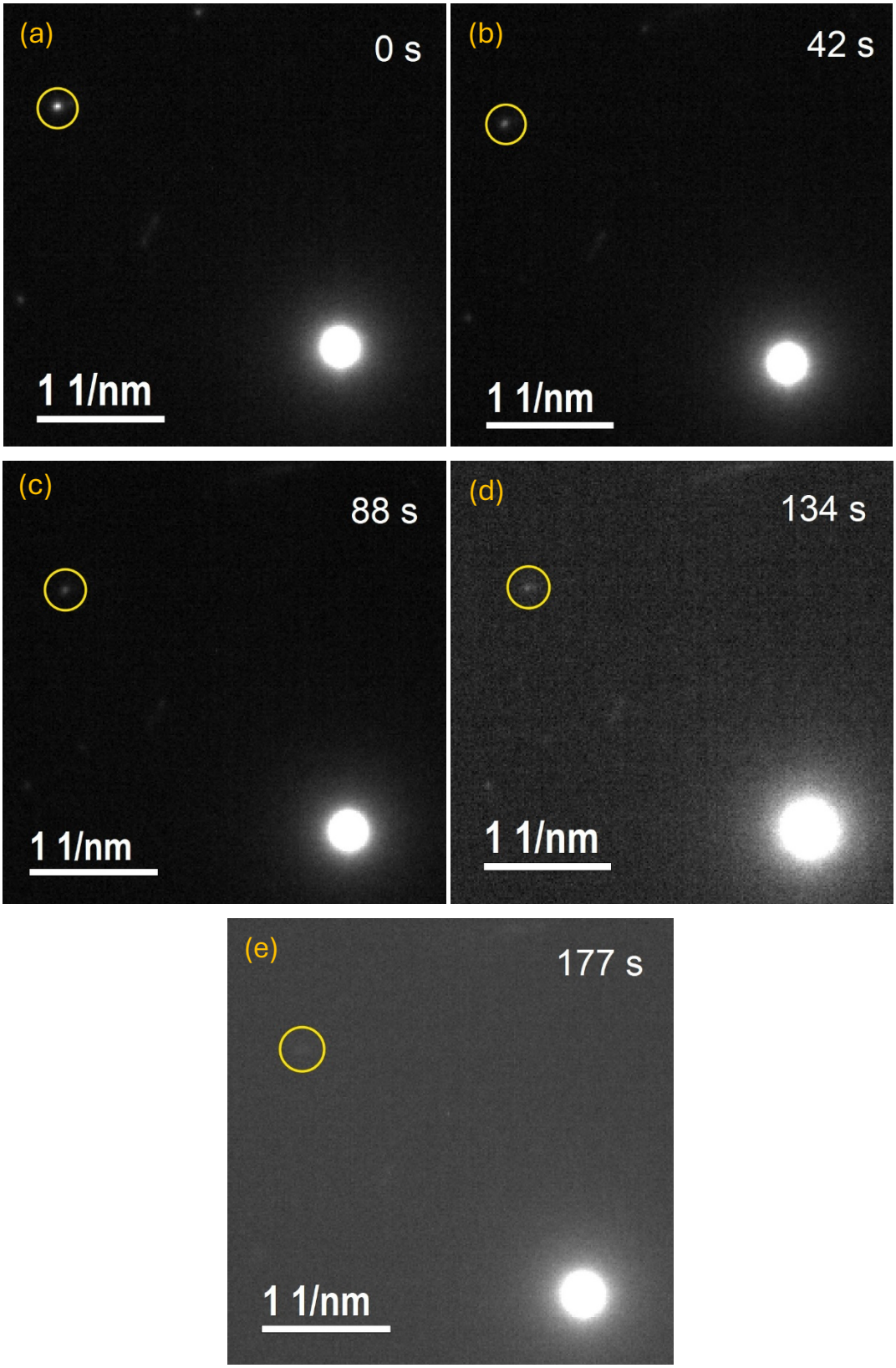

Figure 5.2. (a-e) Diffraction patterns recorded at the same location as a function of elapsed time. The reflection marked with yellow circle was used for intensity measurements. Exposure time for each frame was 0.1 s, and each image was composed of the sum of 10 frames.

Figure 5.2 shows a gradual fading of a specific reflection as a function of time elapsed, and Figure 5.3 (a) plots the reflection intensity, *S*, against time elapsed, *t*. An exponential decay was fitted using Excel, and the equation defining the fit is shown on the graph. When $S = A / e = 357.96 / e = 132$, where *A* is the area of electron beam at the TEM specimen and e is the Euler's number, the corresponding time taken is 143 s. The beam current under such conditions was measured to be 0.16 nA using a Faraday cup. The beam area was estimated from a few images taken at the edge of the beam, and an example is shown in Figure 5.3 (b). Assuming the beam is circular, its area can then be calculated. Several images were taken to work out an average value, and in this case the radius of the beam was 6.654 μm. The critical fluence of PSB was hence found to be 8.0 e / $Å^{-2}$. This means that any conventional (S)TEM imaging methods would certainly cause damage to the specimen.

The UV-vis reflectance spectrum of PSB is shown in Figure 5.3 (c). In the range of 200-700 nm, little light was reflected, corresponding to good absorption in this range. The material is thus likely to be suitable for photocatalytic reactions. To further boost the photocatalytic water splitting activity, MoS_2/PSB heterojunctions with different weight percentage of MoS_2 were synthesised. The XRD data presented in Figure 5.3 (d) shows that MoS_2 mixed well with PSB, and in Figure 5.3 (e) the SEM image shows that the flakes of two materials adhered to each other.

The photocatalytic water splitting ability of PSB and MoS_2/PSB were tested, using the reaction conditions described in Section 3.3.1. TEOA (10 vol%) was added to water as a sacrificial agent to capture the holes generated, and hence to deal with charge carrier recombination problem[57]. 3 wt% Pt was also added as a co-catalyst. Pt has been proved to be an effective additive that can boost the photocatalytic hydrogen generation rate, when combined with another catalyst[230–232]. The reaction activity was evaluated based on the hydrogen evolution reaction (HER) rate, and the results are plotted in Figure 5.3 (f). Reaction

in the dark, reaction with PSB on its own, and reaction with platinum on its own all yielded essentially no H_2 that could be detected by the GC. From the results shown, when MoS_2 took up 15 wt% in the MoS_2/PSB heterojunction, the HER activity was the highest.

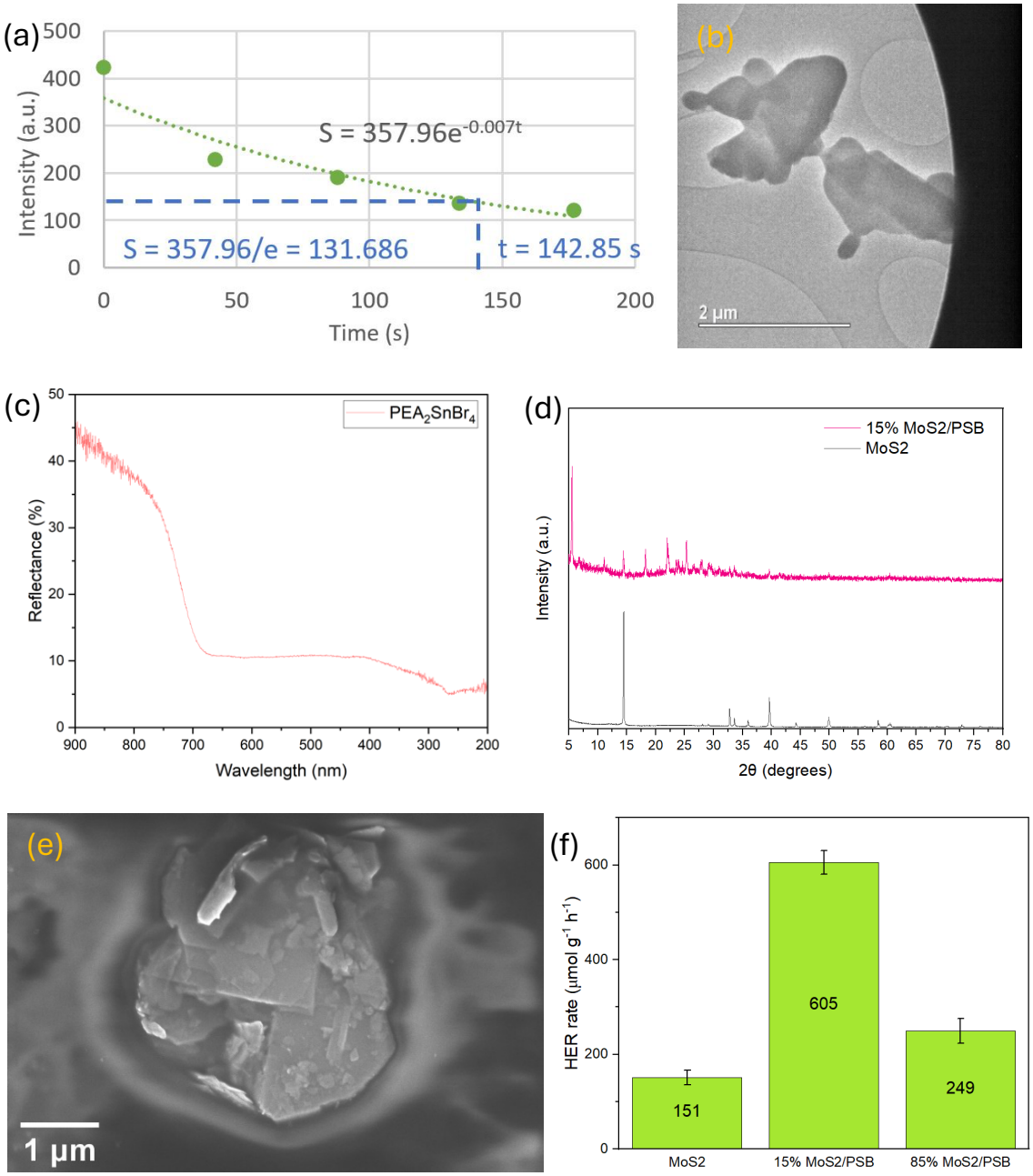

Figure 5.3. (a) Plot of intensity against time with an exponential decay fitting. The corresponding time taken for intensity to drop to A / e (i.e., 357.96 / e) is calculated. (b) TEM image of the edge of the beam, which was used to estimate the beam size. (c) UV-vis reflectance spectrum of PSB. This shows that PSB has good absorption in the range of 200 nm to 700 nm. (d) XRD data of MoS_2 and 15% MoS_2/PSB. (e) SEM image of 15 wt% MoS_2/PSB. SEM image was taken using 3.13 kV voltage, 100 pA current, 6.9 mm working distance and the InLens detector. (f) HER rates of MoS_2, 15% MoS_2/PSB and 85% MoS_2/PSB. When 15 wt% MoS_2 was added to mix with PSB, the MoS_2/PSB system yielded the best performance.

5.2.2. Reactions of bulk CABB in water

Bulk CABB immersed in water and then dried is denoted as CABB-HBr-W, depending on the synthesis method as discussed in Section 3.2.1. When CABB-HBr was immersed in water, the orange powder turned yellow, indicating the formation of BiOBr, whose presence was verified using XRD and EM as shown in Figure 5.4. However, the XRD results in Figure 5.4 (a) showed that apart from BiOBr, a lot of impurities were formed. The SEM image in Figure 5.4 (b) revealed that the material changed its morphology into flakes. This was further proved by the TEM image in Figure 5.4 (c), where the CABB-HBr-W particles appeared as discs. Atomic resolution STEM-HAADF image in Figure 5.4 (d) showed arrays of Bi atoms, as Bi was the heaviest in the composite. TEM diffraction pattern in Figure 5.4 (e) indicated the existence of BiOBr, as it matched the pattern of BiOBr viewed along [001]. These results indicated that when CABB was immersed in water, it reacted with water and yielded BiOBr, which appeared as sheets under electron microscopes. Other substances were also formed during the reaction, as detected by XRD.

Figure 5.5 (a) shows the STEM-EDX spectrum of CABB-HBr-W, with an HAADF image of the acquisition area. STEM-EDX quantification results are shown in Table 5.1, and the atomic ratio was far away from 1:1:1 as expected for BiOBr. Combining with the XRD plot shown in Figure 5.4 (a), the atomic ratio obtained from STEM-EDX was greatly affected by the impurities. The significant proportions occupied by Bi and O could be caused by the large amount of Bi_2O_3 impurity on the surface of the BiOBr particles. Acquiring more EDX data from other sites could support this theory, but the signals from other measurements were too weak to perform quantitative analysis. For photocatalytic water splitting using CABB-HBr-W, the samples were tested under different reaction conditions. All reactions were carried out in water with additives or without. The results are presented in Figure 5.5 (b).

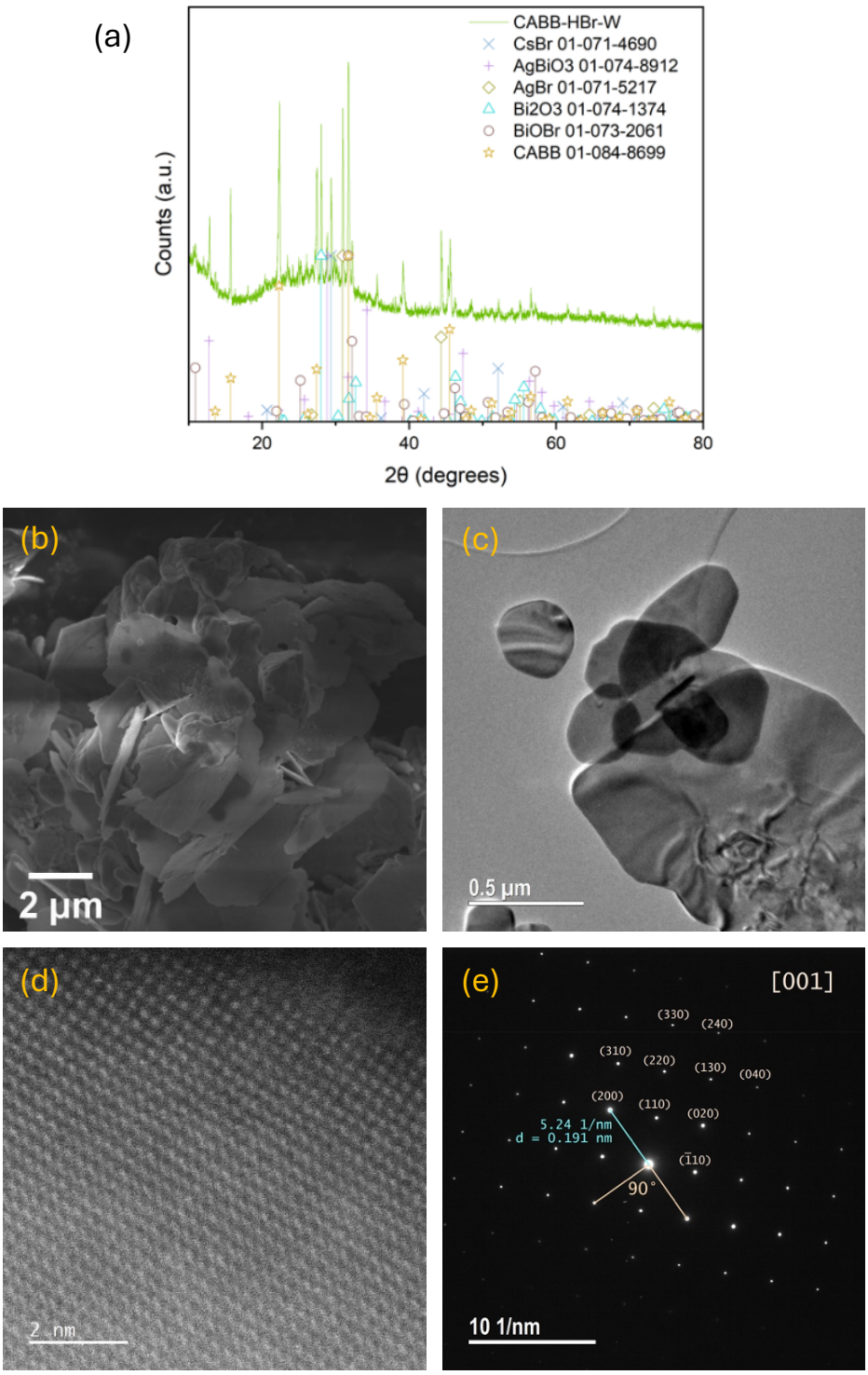

Figure 5.4. (a) XRD data of CABB-HBr-W. Lots of impurities were formed when CABB-HBr was immersed in water. (b) SEM image and (c) TEM image of CABB-HBr-W. (d) High resolution STEM image of CABB-HBr-W. (e) TEM diffraction pattern of CABB-HBr-W, matching the diffraction pattern of BiOBr along [001]. Image (b) was taken using 5 kV voltage, 100 pA current, 7.8 mm working distance and an InLens detector. Image (c) was taken using 56 nA probe current, 6000x magnification and an exposure time of 0.5 s. STEM-HAADF image (d) was taken with a beam current of 5.6 pA, 14.38 mrad convergence angle, 1024 x 1024 pixels, and 6 µs dwell time per pixel; the pixel size was 0.083 Å x 0.083 Å and the electron fluence was calculated to be 3 x 10^4 e $Å^{-2}$. For (e) the beam current was 160 pA; exposure time for each frame was 0.1 s, and the image was the sum of 10 frames.

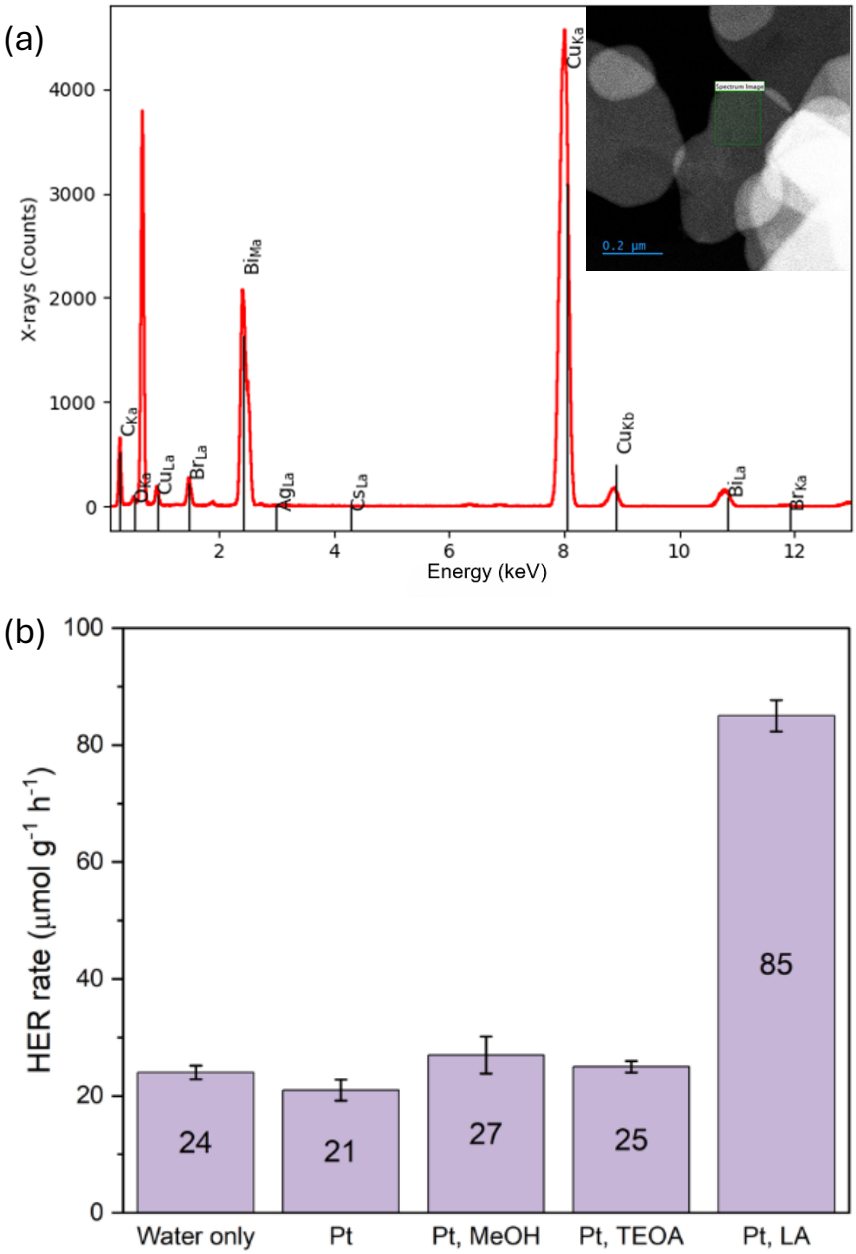

Figure 5.5. (a) STEM-EDX spectrum of CABB-HBr-W, which confirmed that the sheets were BiOBr. The inset indicated the area from which EDX data were collected. The EDX data contained 73 x 85 pixels, and the pixel size was 2 nm x 2 nm; the exposure time for each pixel was 0.2 s; the energy range was 0 – 40.96 keV, and the channel width was 10 eV per channel; the convergence angle was 22.48 mrad, and the beam current was 28.5 pA; the total electron fluence was 9×10^4 e Å^{-2}. The range of 0 – 40.96 keV was initially used in an attempt to capture more signals, but the results showed that no meaningful peaks were detected beyond 12 keV, so the spectrum was cropped to an energy range of 0 – 12.8 keV. (b) HER rates of CABB-HBr-W in water splitting under different conditions. "Pt" means 3 wt% Pt was added. "TEOA" means addition of 10 vol% TEOA, "LA" means addition of 10 vol% lactic acid, and "MeOH" means 10 vol% methanol added. The system gave the best performance when 3 wt% Pt and 10 vol% lactic acid were added.

Table 5.1. STEM-EDX elemental quantification results from the CABB-HBr-W specimen.

Element	Bi	Br	O
Atomic percentage	42.05%	5.42%	52.53%

From the data presented in Figure 5.5 (b), CABB-HBr-W coupled with Pt, and CABB-HBr-W with Pt and methanol/TEOA did not boost the reaction rate, as the results were similar to CABB-HBr-W without any sacrificial agent or co-catalyst added in water. Adding Pt and lactic acid enhanced the activity of the catalyst, so this reaction system was further studied. XRD data and TEM images in Figure 5.6 compare the sample before and after the photoreaction. Changes had occurred before light was introduced into the system, as the CABB peaks became too weak to be detected using XRD in Figure 5.6 (a), and the large particles seen in Figure 5.4 (c) were split into smaller ones as shown in Figure 5.6 (b). The large sheets could no longer be found after lactic acid and Pt were added. This shows that the addition of lactic acid and Pt broke apart the BiOBr layers and reduced the particle size. After the photoreaction, as displayed in Figure 5.6 (c), the XRD peaks due to AgBr, Ag and Bi became prominent, and most BiOBr seemed to have broken down. The combination of lactic acid, Pt and the Xe lamp may have caused the breaking of BiOBr when the sample was immersed in water. In the TEM image shown in Figure 5.6 (d), the small particles observed before the reaction, as seen in Figure 5.6 (b), appeared to have been agglomerated during the reaction. Some large particles were formed again, despite the decomposition of BiOBr. These results suggest that BiOBr could hinder CABB from participating in the water splitting reaction, and only when it was broken down did the activity improve. However, in this process the halide perovskite structure also disintegrated into its constituents.

CABB-HBr-W samples after reaction with TEOA and water, and after reaction with water only were also studied using XRD and SEM. Figure 5.7 (a) showed that TEOA seemed to have destroyed the perovskite structure completely, and most of the peaks could be attributed to $Ag_{99.5}Bi_{0.5}$. Figure 5.7 (b) also revealed a change in morphology of the material. The sample particles became foam-like from flakes. From the XRD data in Figure 5.7 (c), BiOBr was mostly retained after reaction with water and light. The SEM image in Figure 5.7 (d) showed

that the size of the flakes underwent some changes during the reaction, where a lot of smaller particles appeared, compared with the SEM image of the CABB-HBr-W before reaction in Figure 5.4 (b).

CABB synthesised using the DMSO method mentioned in Section 3.2.4 were tested for photocatalytic performance and then characterised. The results are reported in Section A8.

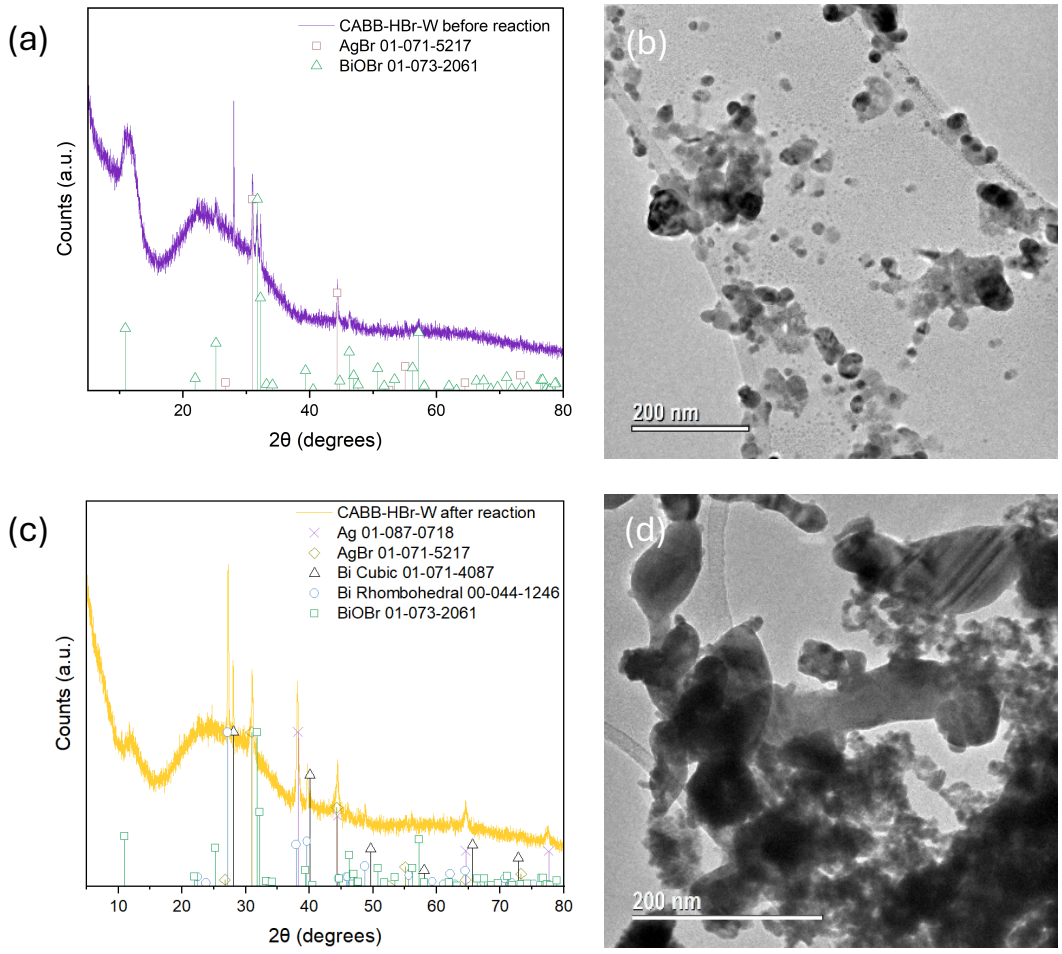

Figure 5.6. (a) XRD plot and (b) TEM image of CABB-HBr-W dispersed in water with lactic acid and Pt before the reaction. (c) XRD plot and (d) TEM image of the same batch of sample reacted in water with lactic acid and Pt after 16 hours of reaction. TEM image (b) was taken using 15000x magnification, 56 nA probe current and an exposure time of 1 s. TEM image (d) was taken using 25000x magnification, 56 nA probe current and an exposure time of 1 s.

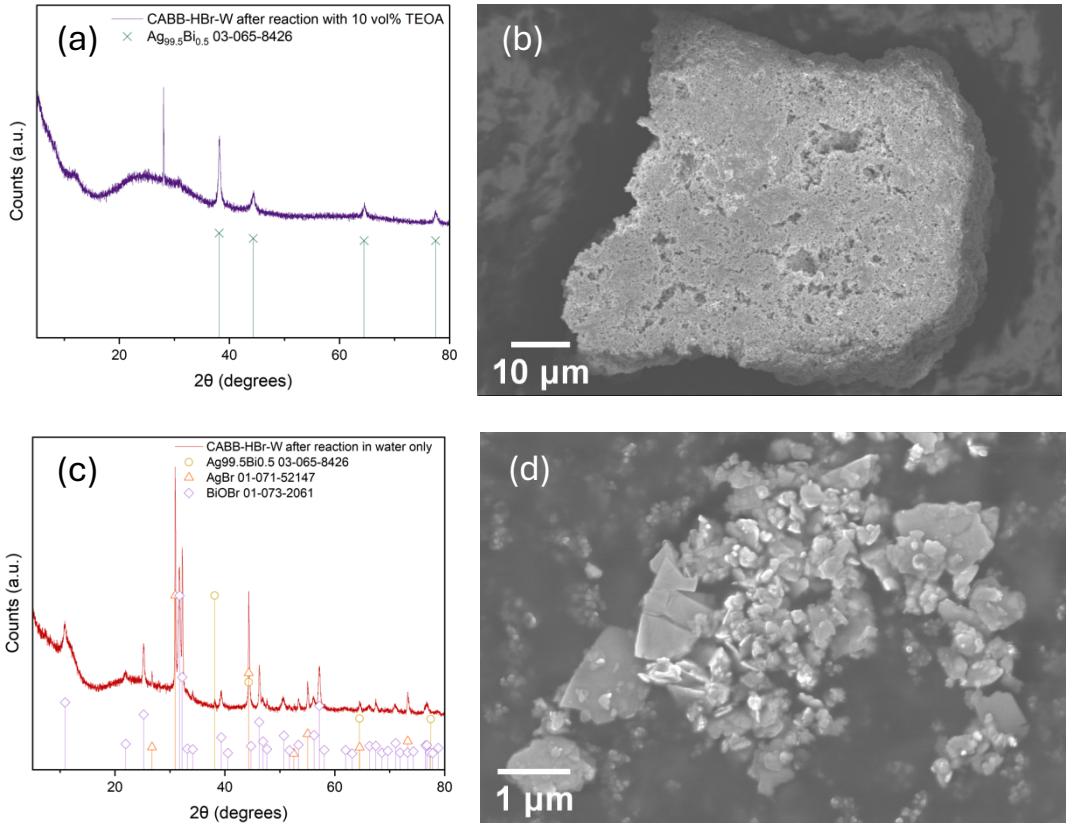

Figure 5.7. (a) XRD plot and (b) SEM image of CABB-HBr-W after photoreaction in water with TEOA. The perovskite structure was severely damaged when mixed with TEOA. (c) XRD plot and (d) SEM image of CABB-HBr-W after photoreaction in water only. Some flakes seem to have shrunk in size during the photoreaction with water. SEM image (b) was taken using 5 kV voltage, 100 pA current, 5.8 mm working distance and an InLens detector. SEM image (d) was taken using 5 kV voltage, 100 pA current, 6.0 mm working distance and an InLens detector.

5.2.3. CABB nanocubes in water

CABB nanocubes (CABB-NC) were also tested by submerging the material in water, followed by characterisation as well as photoreactions. XRD data in Figure 5.8 (a) show that after contact of CABB-NC with water, BiOBr began to form, while a fraction of CABB degraded to AgBr. Figure 5.8 (b) directly compares the XRD data between CABB-NC and CABB-NC-W, with prominent new peaks marked by dashed lines. The peaks at 11°, 24° and 47.4° can be attributed to the formation of BiOBr, and the peak at 44.6° is due to AgBr.

EM data show that the CABB-NC-W particles appear quite different from CABB-HBr-W, as shown in Figure 5.9 (a, b). The cubes changed shape, and a layer likely to be BiOBr was formed, covering the particles. STEM-EDX data with quantification in Figure 5.9 (c, d) reveal that the round particles were likely to consist of at least Ag. Cs could not be detected, which may have detached from the CABB structure and got dissolved when CABB-NC was immersed in water. The atomic ratio of Bi:O:Br is a lot closer to 1:1:1, compared to the quantification results of CABB-HBr-W shown in Table 5.1. However, the existence of the impurity AgBr confirmed by XRD in Figure 5.8 (a) could have interfered with the quantification results, as a higher amount of Br could be detected.

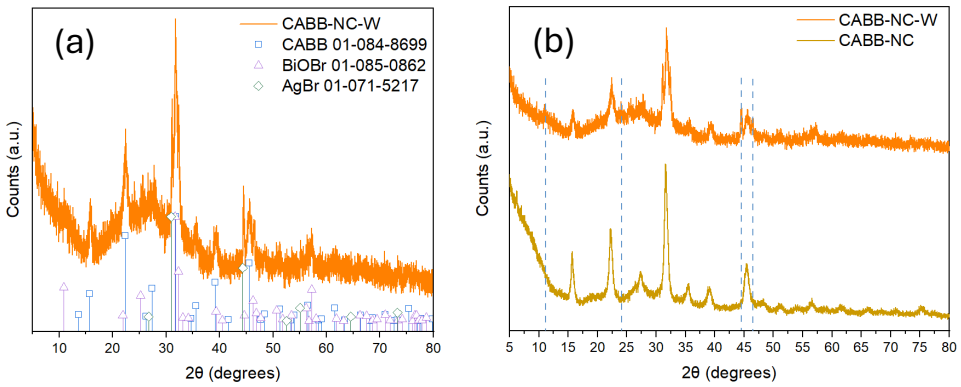

Figure 5.8. (a) XRD data of CABB-NC-W. (b) XRD data comparing CABB-NC and CABB-NC-W. The new peaks are due to BiOBr and AgBr.

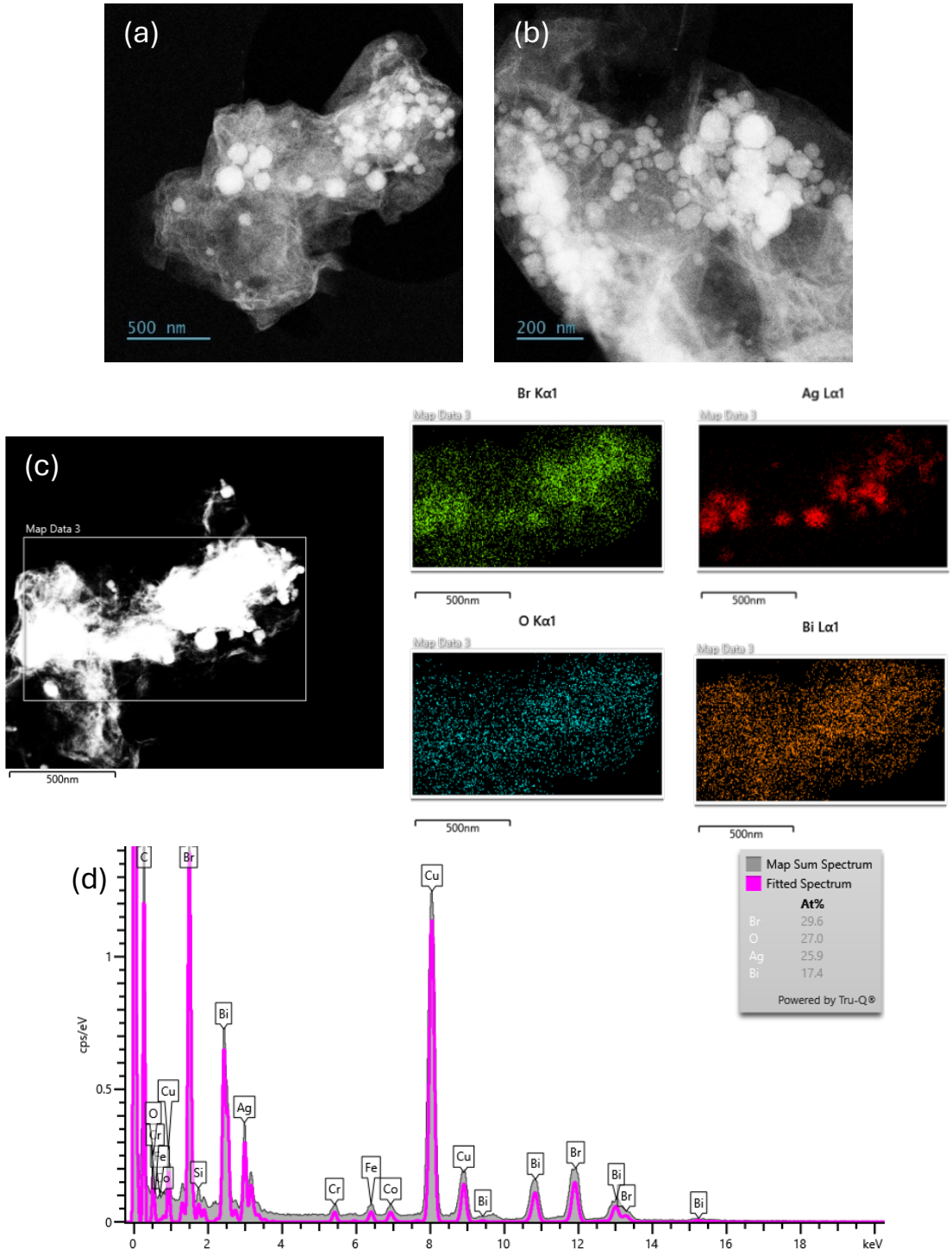

Figure 5.9. (a, b) STEM-HAADF images of CABB-NC-W. (c) STEM-EDX maps of CABB-NC-W. (d) STEM-EDX spectrum with quantification. STEM-HAADF images (a, b) were taken with a beam current of 5.6 pA, 14.38 mrad convergence angle, 1024 x 1024 pixels, and 6 µs dwell time per pixel; for image (a) the pixel size was 21 Å x 21 Å and the electron fluence was 0.5 e $Å^{-2}$; for image (b) the pixel size was 10 Å x 10 Å and the electron fluence was 2 e $Å^{-2}$. The EDX data contained 380 x 220 pixels, and the pixel size was 3.52 nm x 3.52 nm; the dwell time for each pixel was 2.85 ms, and each pixel was scanned for 28 times; the energy range was 0 – 20 keV, and the channel width was 20 eV per channel; the convergence angle was 22.48 mrad, and the beam current was 28.5 pA; the total electron fluence was 1.1 x 10^4 e $Å^{-2}$. Co, Cr and Fe peaks in the EDX spectrum were due to the pole pieces and sample holder in the microscope. The fitted spectrum in purple was calculated by Aztec 6.2 (Oxford Instruments Nanotechnology Tools Limited) automatically, using the deconvolution function discussed in Section 3.11.7. The elements need to be selected manually for the deconvolution.

The photoreactor used in this section and subsequent section, was the reactor with a large window at the top shown in Figure 3.2. This is because the reactor with smaller side window was no longer available. After photoreaction in water, the sample turned black, signifying structural degradation of the sample. The hydrogen production rate of CABB-NC-W in water was 3 μmol g^{-1} h^{-1}. The reaction rate was substantially lower than the performance of CABB-HBr-W in water using the side-window reactor. This is probably because the large window allowed too much light in, and led to severe damage to the halide perovskite structure. Figure 5.10 (a) shows the XRD data of CABB-NC-W after reaction. From the peaks identified, the CABB structure with BiOBr layer was broken down into Bi_2O_3, Ag and Br during the photoreaction. Direct comparison between CABB-NC-W and CABB-NC-W after reaction is shown in Figure 5.10 (b). For CABB-NC-W after reaction, significant changes include a new impurity peak appeared at 6.9°, and a peak due to Bi_2O_3 at 38° emerged; the peaks due to CABB at 15.6°, 35.4° and 39.0° disappeared. This means that the CABB structure may have broken down, and the BiOBr layer was partially degraded into Bi_2O_3. STEM-EDX data with quantification in Figure 5.10 (c, d) show that the particles consist of Ag, Bi, Br and likely O. The STEM-HAADF image shown in Figure 5.10 (e) reveals that the small white particles started to form clusters and lose their spherical shapes, compared to the image of the specimen before reaction in Figure 5.9 (a).

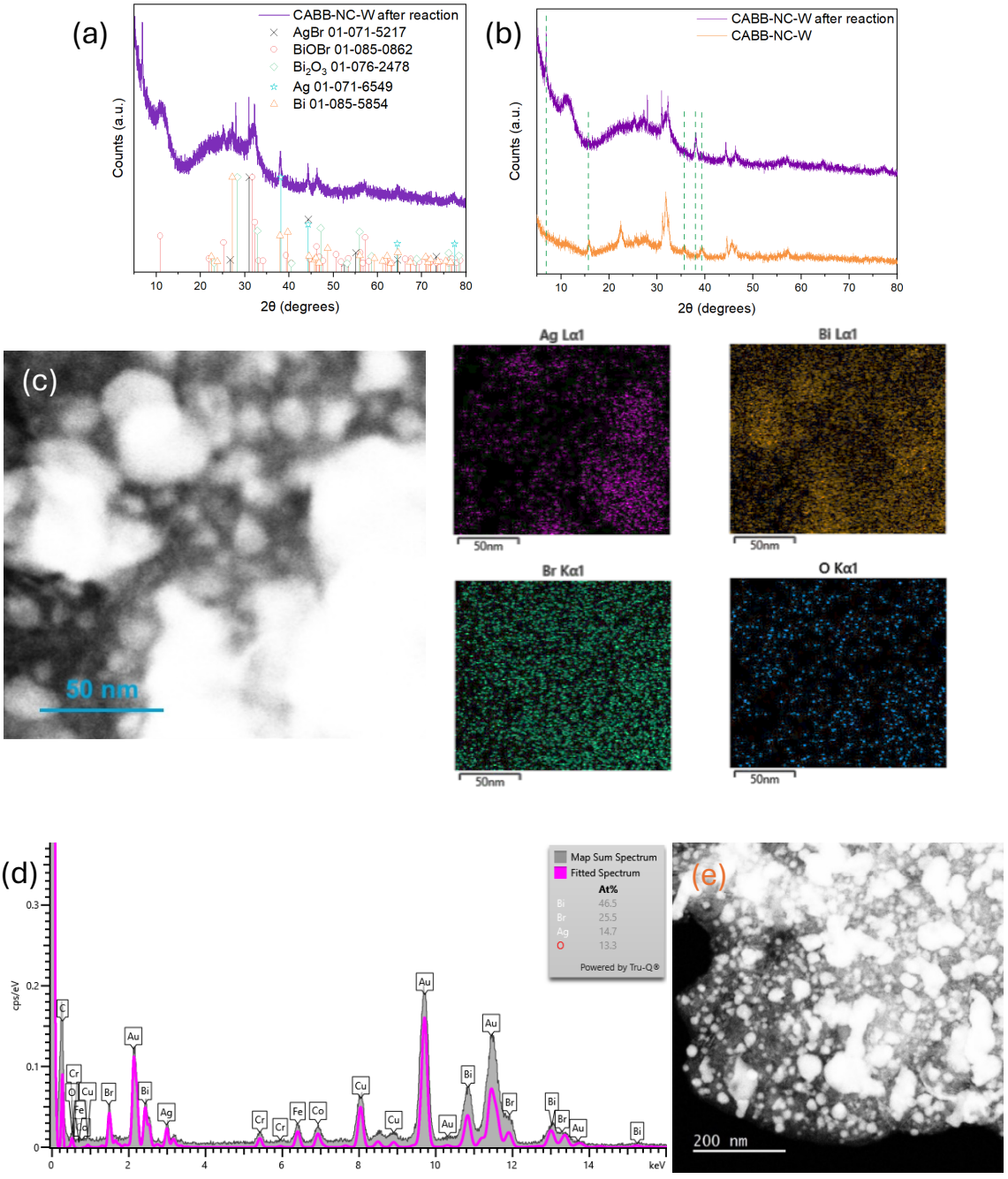

Figure 5.10. (a) XRD data from CABB-NC-W after reaction. The CABB structure may have broken down during the reaction, and lots of impurities were formed. (b) XRD data comparing CABB-NC-W and CABB-NC-W after reaction. (c) STEM-EDX maps of CABB-NC-W after reaction. (d) STEM-EDX spectrum of CABB-NC-W after reaction. (e) STEM-HAADF image of CABB-NC-W after reaction. The EDX data contained 512 x 448 pixels, and the pixel size was 3.5 Å x 3.5 Å; the dwell time for each pixel was 1.99 ms, and each pixel was scanned for 19 times; the energy range was 0 – 20 keV, and the channel width was 10 eV per channel; the convergence angle was 22.48 mrad, and the beam current was 28.5 pA; the total electron fluence was 5.5 x 10^5 e $Å^{-2}$. STEM-HAADF image (e) was taken with a beam current of 12 pA, 14.38 mrad convergence angle, 1024 x 1024 pixels, and 6 µs dwell time per pixel; the pixel size was 7 Å x 7 Å and the electron fluence was 9.2 e $Å^{-2}$.

5.2.4. CABB nanosheets in water

The photoreaction in water using CABB nanosheets (2D-CABB) was also studied. CABB nanosheets immersed in water are denoted as 2D-CABB-W. Similar to CABB-NC, when 2D-CABB came into contact with water, a BiOBr layer was formed, and the perovskite was partially decomposed into $BiBr_3$. This is evidenced by the XRD data of 2D-CABB-W in Figure 5.11 (a). Figure 5.11 (b) compares the XRD patterns between 2D-CABB and 2D-CABB-W, where the new peaks highlighted correspond to $BiBr_3$ at 13.4°, and BiOBr at 32.4°.

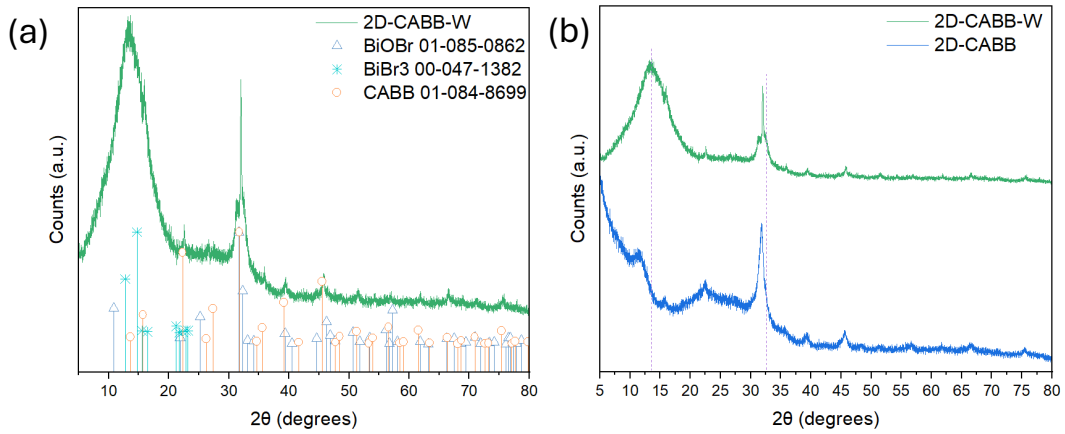

Figure 5.11. (a) XRD data from 2D-CABB-W. Apart from BiOBr, impurity peaks due to $BiBr_3$ could be detected. (b) XRD data comparing 2D-CABB and 2D-CABB-W.

From the STEM-HAADF images and EDX data of the 2D-CABB-W in Figure 5.12, Ag nanoparticles wrapped by a BiOBr layer displayed as haze was observed. In addition, some thin sheets were still present in Figure 5.12 (b), appearing dark grey in the image (not the white particles), but they have round edges instead of sharp ones, compared to the 2D-CABB specimen before water treatment shown in Figure A12. A small amount of Cs was identified, which may be due to a tiny fraction of CABB that did not react with water. Combining the data from XRD and STEM-EDX, the atomic ratio of Br and Bi in Figure 5.12 (d) could be explained based on the presence of BiOBr, $BiBr_3$ and CABB. Ag signal could come from the nanoparticles, while the excessively high amount of O could be caused by some amorphous layers that surrounded the Ag nanoparticles, so the oxides were not detected by XRD except BiOBr.

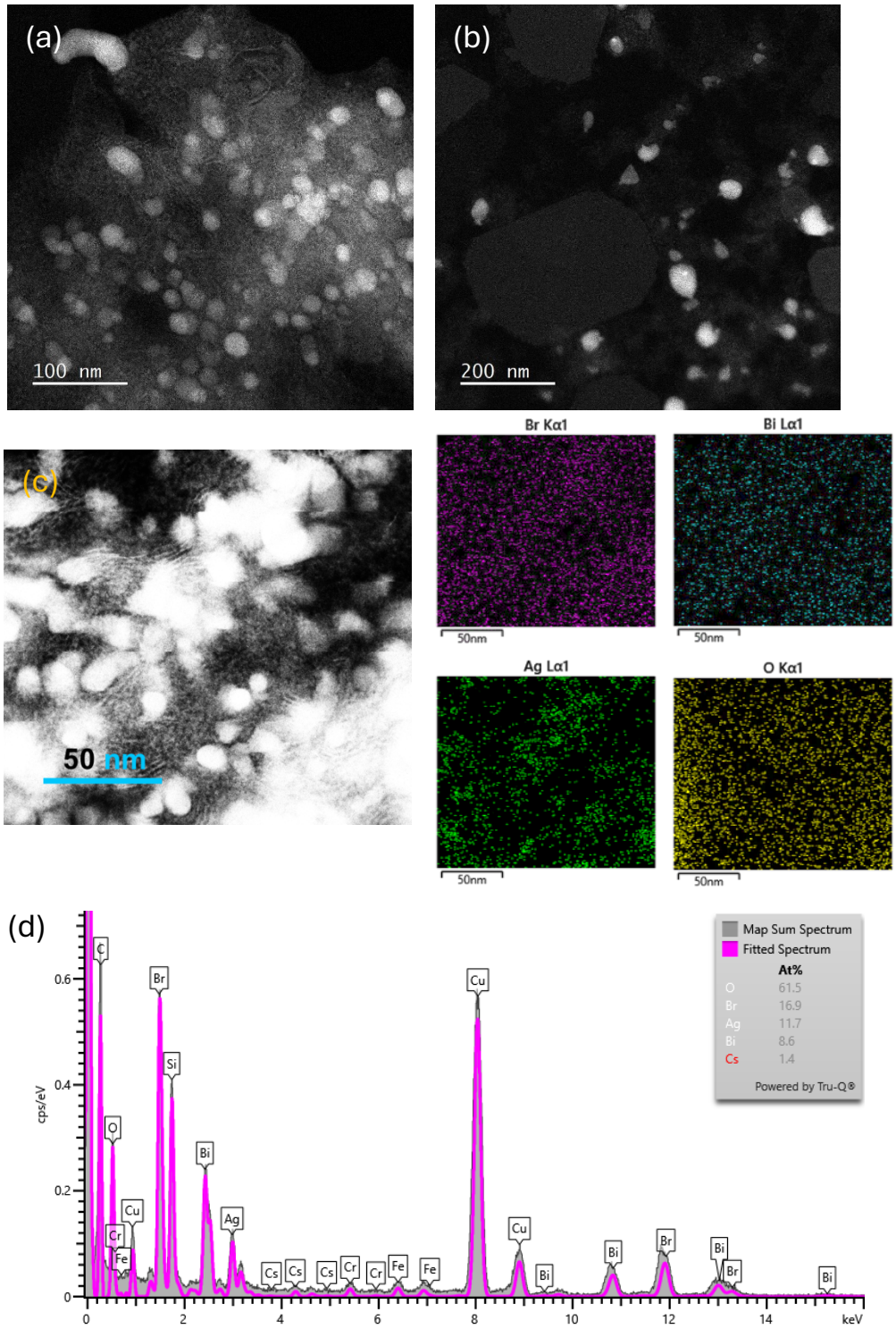

Figure 5.12. (a, b) STEM-HAADF images of 2D-CABB-W. (c) STEM-EDX maps and (d) STEM-EDX spectrum of 2D-CABB-W. The round particles which may be formed of Ag, and may be wrapped by BiOBr could be seen. STEM-HAADF images (a, b) were taken with a beam current of 12 pA, 14.38 mrad convergence angle, 1024 x 1024 pixels, and 6 µs dwell time per pixel; for image (a) the pixel size was 4.2 Å x 4.2 Å and the electron fluence was 25.5 e $Å^{-2}$; for image (b) the pixel size was 8.3 Å x 8.3 Å and the electron fluence was 6.5 e $Å^{-2}$. The EDX data contained 512 x 448 pixels, and the pixel size was 3.5 Å x 3.5 Å; the dwell time for each pixel was 782 µs, and each pixel was scanned for 7 times; the energy range was 0 – 20 keV, and the channel width was 10 eV per channel; the convergence angle was 22.48 mrad, and the beam current was 28.5 pA; the total electron fluence was calculated to be 8 x 10^4 e $Å^{-2}$.

The hydrogen production rate from the photoreaction involving 2D-CABB-W in water was also measured. Without additional co-catalysts or sacrificial agents, the hydrogen production rate was 4 μmol g^{-1} h^{-1}. Again, the reactor with large window could have resulted in additional damage to the structure of the sample. The 2D-CABB-W sample turned brown, suggesting some changes in its structure during the reaction. XRD measurements were carried out for 2D-CABB-W after the reaction, and the results are shown in Figure 5.13 (a). Figure 5.13 (b) compares XRD data between 2D-CABB-W and 2D-CABB-W after photoreaction. The new peak for 2D-CABB-W after reaction at around 28° can be attributed to Bi_2O_3, suggesting that the BiOBr layer suffered damage during the photoreaction. The peaks due to CABB at 22.6°, 32.0°, 35.8°, 39.5° and 45.8° disappeared after reaction. This means that CABB disintegrated during the reaction. STEM-EDX maps and STEM-HAADF image in Figure 5.14 show signs of aggregation for the small particles, which are possibly composed of Ag. Cs signal could no longer be detected after the photoreaction. The atomic ratio among Bi, Br and O in Figure 5.14 (b) matched the XRD peaks of $BiBr_3$ and Bi_2O_3 combined together in Figure 5.13 (a), and the high proportion of Ag could come from the silver nanoparticles. The presence of Ag was not reflected in the XRD is probably because the Ag nanoparticles produced broad and weak peaks which may have been treated as background. They may also be masked by Bi_2O_3 and not in a well-crystallised form.

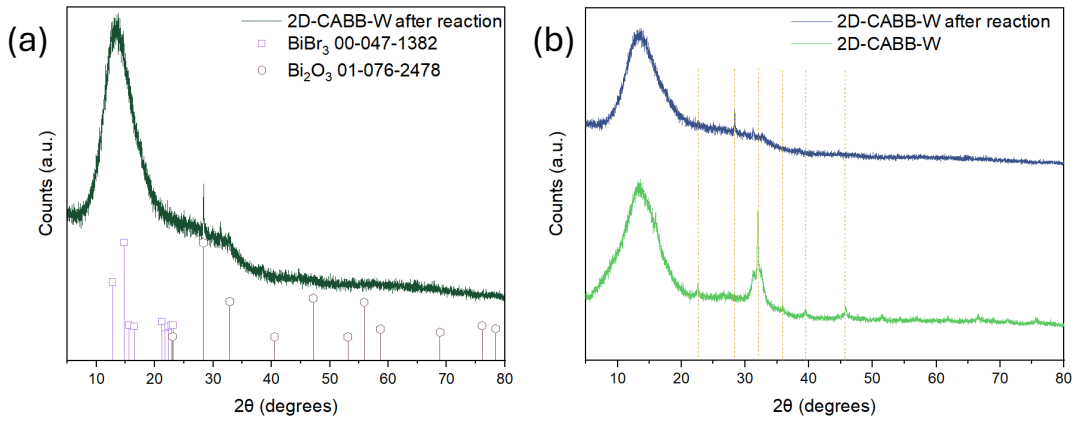

Figure 5.13. (a) XRD data from 2D-CABB-W after reaction. Peaks from CABB could no longer be picked up, suggesting the decomposition of 2D-CABB structure. (b) XRD data comparing 2D-CABB-W and 2D-CABB-W after reaction.

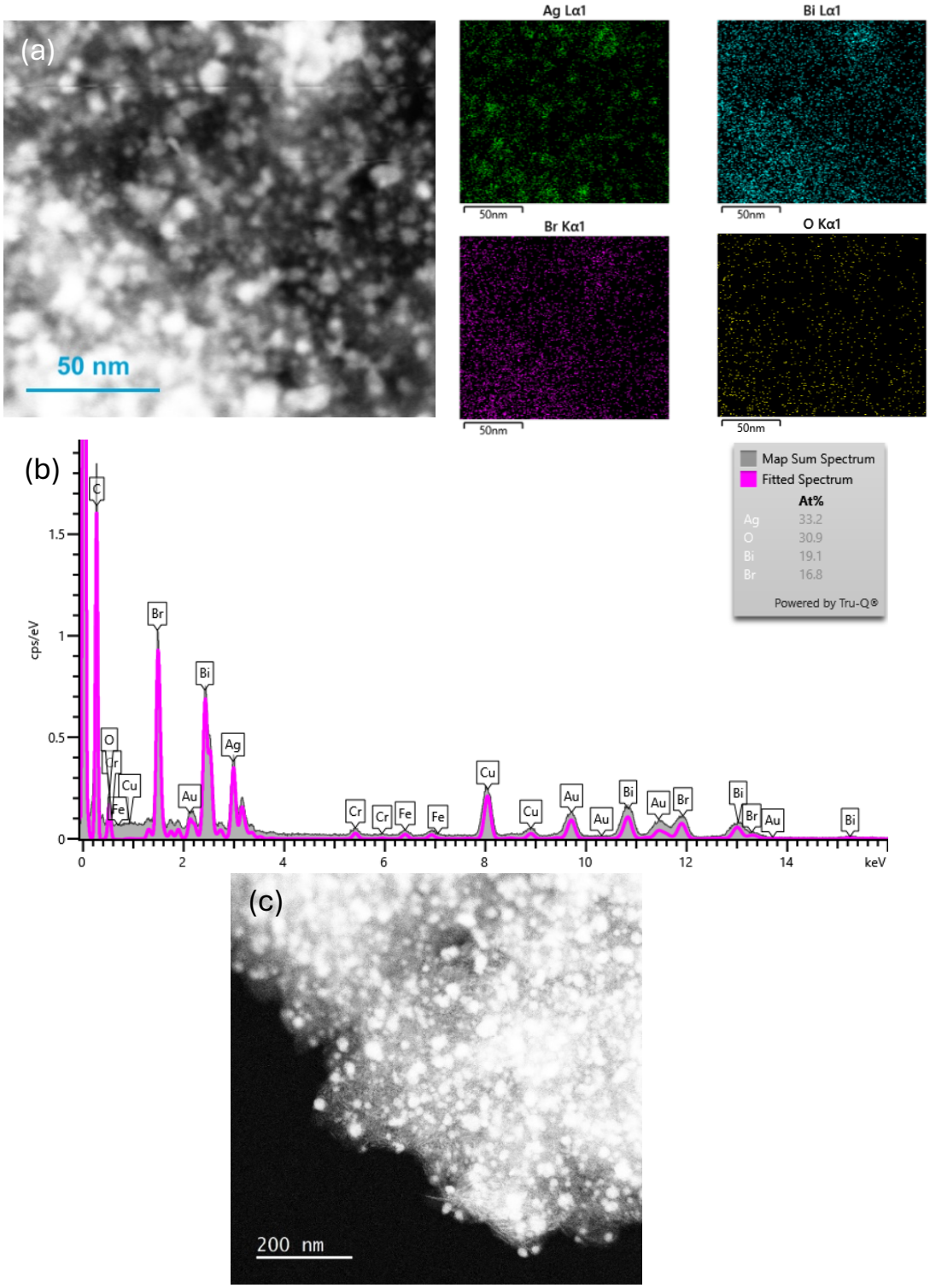

Figure 5.14. (a) STEM-EDX maps of 2D-CABB-W after reaction. (b) STEM-EDX spectrum of 2D-CABB-W after reaction. (c) STEM-HAADF image of 2D-CABB-W after reaction. STEM-HAADF image (c) were taken with a beam current of 12 pA, 14.38 mrad convergence angle, 1024 x 1024 pixels, and 6 µs dwell time per pixel; the pixel size was 8.3 Å x 8.3 Å and the electron fluence was 6.5 e $Å^{-2}$. The EDX data contained 512 x 448 pixels, and the pixel size was 3.5 Å x 3.5 Å; the dwell time for each pixel was 1.2 ms, and each pixel was scanned for 12 times; the energy range was 0 – 20 keV, and the channel width was 10 eV per channel; the convergence angle was 22.48 mrad, and the beam current was 28.5 pA; the total electron fluence was 2.1 x 10^6 e $Å^{-2}$.

5.3. Conclusions

The interaction of PSB and CABB with water, as well as photocatalytic water splitting activities were studied. The main findings are listed as follows:

- Sheets of PSB could be seen using EM. However, the presence of organic cations, coupled with the quasi-2D structure made PSB prone to electron beam damage.
- When PSB was combined with 15 wt% MoS_2 and 3 wt% Pt to form a heterojunction, its photocatalytic water splitting performance was boosted to 605 μmol g^{-1} h^{-1}.
- When bulk CABB was in contact with water, a layer of BiOBr formed on its surface, but impurities also appeared.
- For water splitting photoreaction, the addition of lactic acid as sacrificial agent and Pt as co-catalyst was found to be effective in boosting the reaction rate for bulk CABB. The hydrogen generation rate was 85 μmol g^{-1} h^{-1}.
- When CABB nanocubes and nanosheets were immersed in water, a BiOBr layer was also formed. Silver nanoparticles could be seen possibly situated inside these BiOBr layers. A common impurity was $BiBr_3$.
- CABB nanocubes and nanosheets underwent further changes during the photoreaction in water, where BiOBr degraded into Bi_2O_3. The photoreaction rates for hydrogen generation were 3 μmol g^{-1} h^{-1} using nanocubes in water, and 4 μmol g^{-1} h^{-1} using nanosheets in water.

Chapter 6 Conclusions and future work

6.1. Conclusions

In this thesis, $Cs_2AgBiBr_6$ (CABB) is studied as a photocatalyst in methanol oxidation and water splitting, and PEA_2SnBr_4 (PSB) is studied for photocatalytic water splitting. CABB with different shapes and sizes were synthesised. Bulk size CABB (CABB-HBr), where individual particles were typically a few micrometres large, was the simplest to synthesise. Its activity in methanol photo-oxidation in μmol g^{-1} h^{-1} was lower than the activity of CABB nanocubes (CABB-NC), especially the ones washed with ethanol (CABB-NC-EtOH) that removed surface ligands. This may be because of the difference in surface area exposed for the photocatalytic reaction to take place, and how the electron-hole pair was transferred within the nanomaterial. The peak activity in methanol photo-oxidation was achieved using CABB-NC-EtOH, with a hydrogen production rate of 229 μmol g^{-1} h^{-1}. Data from in-situ XPS showed that Ag and Bi were very active when the Xe lamp was turned on, indicating their important role in photocatalysis of methanol oxidation. For longer photoreaction times with methanol vapour, the surface of CABB-HBr seemed to form pits and crevices, and SEM-EDX quantification showed a decrease in the amount of Ag and Bi. These observations could explain the reduction in reaction rate over time. Both CABB-NC and CABB-NC-EtOH in methanol photo-oxidation showed an increase in reaction rate, then a sharp decrease, before rising again. This can be explained from the agglomeration of nanocubes during the photoreaction which reduced the activity, and then formation of nanosheets that increased active sites, leading to the reaction rate increasing. Analysis of FFT patterns obtained from STEM-HAADF images of CABB-NC-EtOH before and after reaction showed a shorter lattice spacing of nanosheets than that of nanocubes, which may be caused by the microstrain within the nanosheets. Close examinations of the surface of the CABB nanoparticles under

STEM showed that the distance between atoms near the surface did not vary from the distance between atoms in the bulk region, while some atom vacancies could be discerned near the surface of the nanoparticles.

When in contact with water, all forms of CABB produced a BiOBr layer, along with other impurities, from reaction with water without additional light input. At the end of the photoreaction with water, a change in structure could again be observed, with BiOBr and any remaining CABB further degraded. Among the reaction systems tested, the best performing one was CABB-HBr-W in water, along with 3 wt% Pt and 10 vol% lactic acid added. The hydrogen production rate of this system was 85 μmol g^{-1} h^{-1}.

The low critical electron fluence of PSB placed a limit on the amount of information that was obtained from electron microscopy, as any electron fluence over 8.0 e / $Å^{-2}$ could cause significant damage to the specimen. Nevertheless, it performed well in photocatalytic water splitting, when mixed with 15 wt% MoS_2 and 3 wt% Pt to form a heterojunction plus co-catalyst, and aided with a sacrificial agent TEOA. The activity of this system in terms of hydrogen generation was 605 μmol g^{-1} h^{-1}.

6.2. Future work

Several interesting points arising from this research could be further investigated;

1. In-situ (S)TEM studies of CABB in methanol photo-oxidation would be ideal to observe any changes in the morphology of the particles during the reaction. The system needs to be carefully designed to incorporate the CABB specimen, methanol and light. The electron fluence also needs to be recorded to consider possible beam damage.

2. Not enough high-resolution EM data could be obtained in this research to reach a convincing conclusion on the surface termination of the CABB nanoparticles. High-resolution low-dose techniques for STEM imaging and STEM-EDX can be adopted to investigate the surface of CABB nanocubes and nanosheets more minutely. How the perovskite structure terminates at the surface of the nanoparticles could hence be determined.
3. Some attempts on creating heterojunctions using different forms of CABB were made, but none was successful. More strategies could hence be explored. For example, distributing CABB onto a substrate could also help to increase the reaction rate.
4. Due to limitations in the laboratory, the methanol vapour was static. For industrial applications, the reaction system needs to be adapted to allow continuous flow of gaseous methanol. The system could then be optimised for maximum efficiency.
5. The tin-based organic-inorganic halide perovskite PSB degraded rapidly under (S)TEM, and low-dose EM techniques could be used to obtain high resolution images to further investigate its structure at a nano scale.

Appendix Additional experimental results

Contents

A1. Characterisation of CABB-HBr and CABB-NC 158
A2. Photoreactions with methanol vapour 162
A3. STEM-EDX analysis of CABB-NC and CABB-NC-EtOH after photoreactions 165
A4. CABB nanosheets 170
A5. Zeta potential and heterojunctions 174
A6. FFT analysis of CABB-NC-EtOH, 2D-CABB and CABB-NC 176
A7. Surface analysis of CABB nanoparticles 180
A8. CABB-DMSO photoreactions and characterisation 181

A1. Characterisation of CABB-HBr and CABB-NC

Several S/TEM images and an XRD plot are presented in this section. Figure A1 shows how CABB-HBr washed with ethanol could be easily damaged under the electron beam. Figure A2 shows that little information could be obtained from CABB-HBr under STEM due to the thickness of the sample particles. Figure A3 presents an XRD plot which revealed changes that CABB-HBr went through when it was immersed in methanol. STEM images in Figure A4 show the damage in structure after the photoreaction of CABB-NC immersed in liquid methanol with excess NaBr.

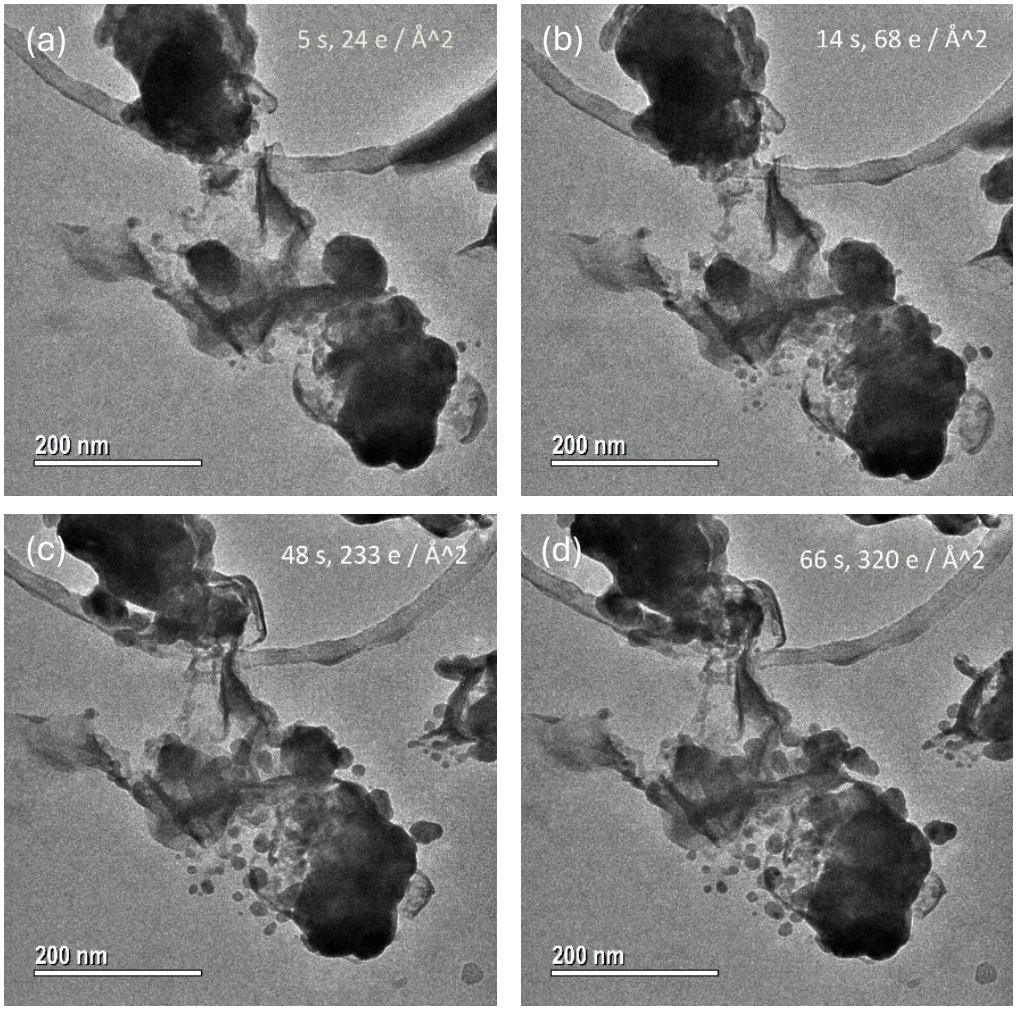

Figure A1. (a-d) TEM images showing degradation of CABB-HBr washed with ethanol under the electron beam. The images were taken using 270 pA probe current, 3.47 μm^2 beam area, and exposure time for each image was 1 s.

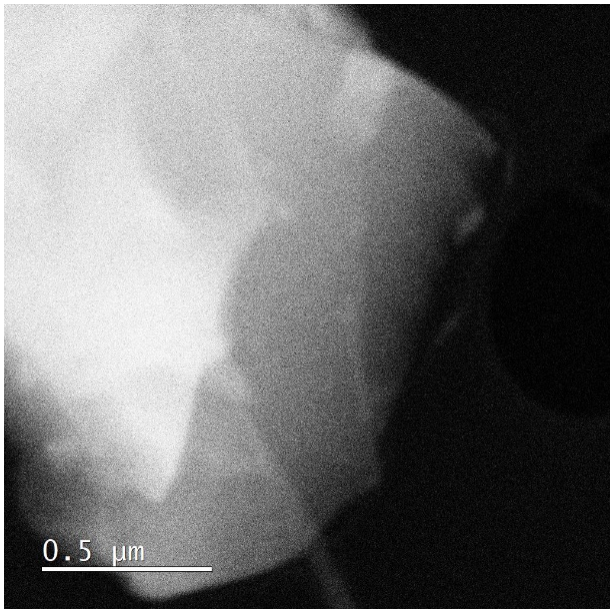

Figure A2. STEM-HAADF image of CABB-HBr prepared using methyl acetate. The image was taken with a probe current of 5.6 pA, a convergence angle of 14.38 mrad, 1024 x 1024 pixels, and 6 µs dwell time per pixel; the pixel size was 1.7 nm x 1.7 nm and the total electron fluence was 0.7 e $Å^{-2}$.

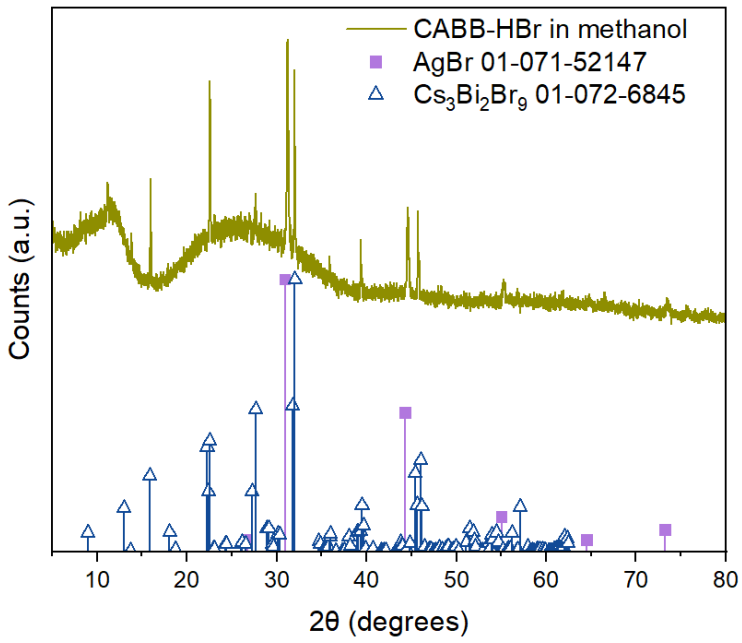

Figure A3. XRD plot of dried CABB-HBr that had been immersed in methanol. CABB-HBr disintegrated into AgBr and $Cs_3Bi_2Br_9$ whilst in methanol.

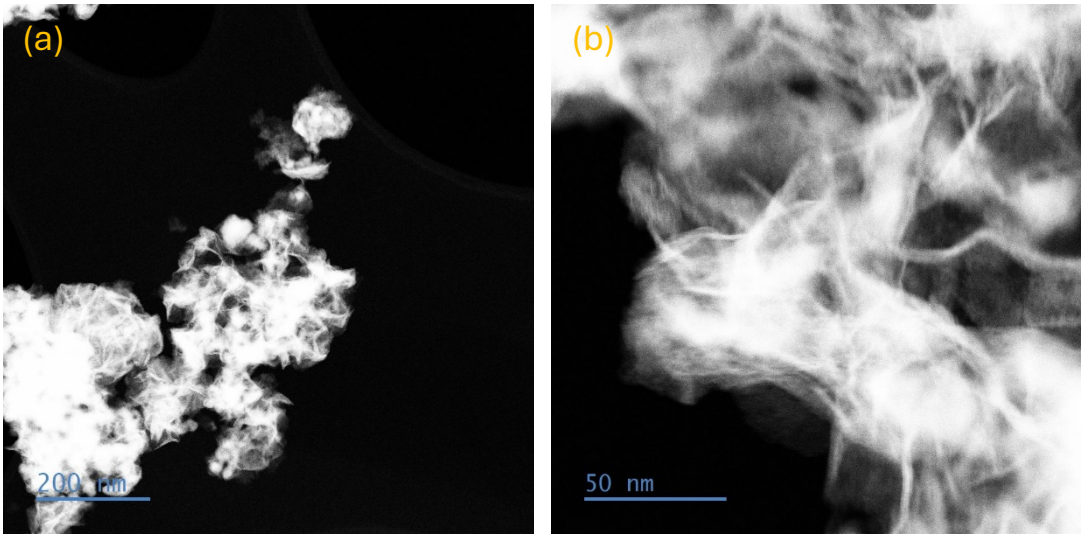

Figure A4. (a, b) STEM-HAADF images of CABB-NC after photoreaction in methanol with excess NaBr. The cubes broke down and aggregated during the reaction even with the addition of NaBr. The images were taken with a beam current of 5.6 pA, 14.38 mrad convergence angle, 1024 x 1024 pixels, and 6 µs dwell time per pixel; for image (a) the pixel size was 9.1 Å x 9.1 Å and the electron fluence was 2.5 e $Å^{-2}$; for image (b) the pixel size was 1.8 Å x 1.8 Å and the electron fluence was 65 e $Å^{-2}$.

A2. Photoreactions with methanol vapour

The hydrogen production rates for CABB-HBr and CABB-NC are shown in Figure A5 and Table A1 for one hour of photoreaction. The results between CABB-HBr and CABB-NC are similar in unit of μmol g^{-1} h^{-1}, but converting to TOF, CABB-NC is a few thousand times less active. The XRD spectra in Figure A6 (a, b) show that both bulk and nano CABB structures were preserved during the reaction, by only allowing contact with methanol vapour. The broad peak at around 12° for CABB-HBr after reaction in Figure A6 (a) was found to be the signal from vacuum grease. In Figure A6 (b), two extra peaks marked with "*" for CABB-NC after reaction are likely to arise from a $BiBr_3$ impurity. The STEM-HAADF images in Figure A6 (c, d) show that the nanocubes retained their shape after the reaction.

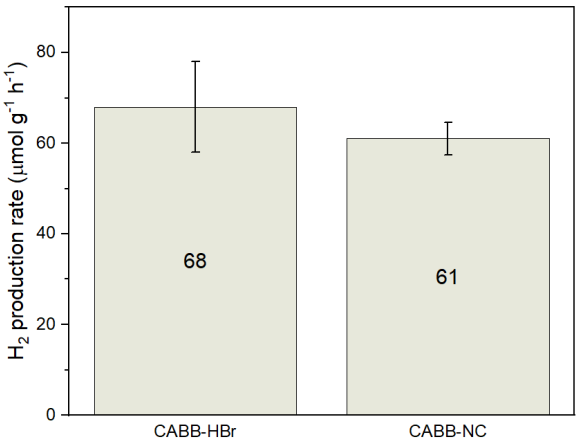

Figure A5. Hydrogen generation rates of CABB-HBr and CABB-NC, from the one-hour methanol photo-oxidation reaction with methanol vapour.

Table A1. Turnover frequency of CABB-HBr and CABB-NC in the one-hour methanol photo-oxidation reaction with methanol vapour.

Sample	CABB-HBr	CABB-NC
Turnover frequency (s^{-1})	3.52×10^{-3}	9.11×10^{-6}

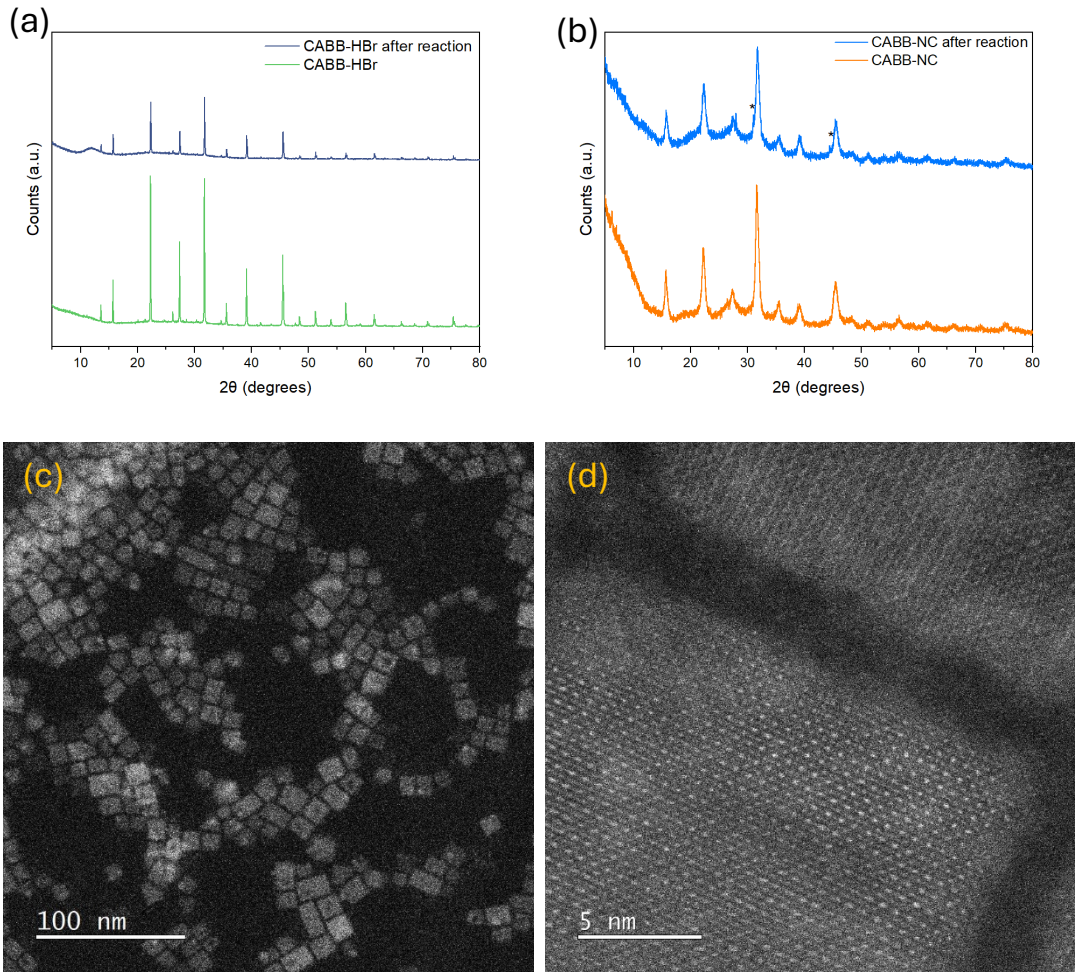

Figure A6. XRD plots comparing (a) CABB-HBr and (b) CABB-NC before and after photoreaction with gaseous methanol. The peaks marked with "*" are due to a $BiBr_3$ impurity. (c, d) STEM-HAADF images of CABB nanocubes after one hour of photoreaction. The images were taken with a beam current of 5.6 pA, 14.38 mrad convergence angle, 1024 x 1024 pixels, and 6 µs dwell time per pixel; for image (c) the pixel size was 3.5 Å x 3.5 Å and the electron fluence was 17 e $Å^{-2}$; for image (d) the pixel size was 0.21 Å x 0.21 Å and the electron fluence was 4.8 x 10^3 e $Å^{-2}$.

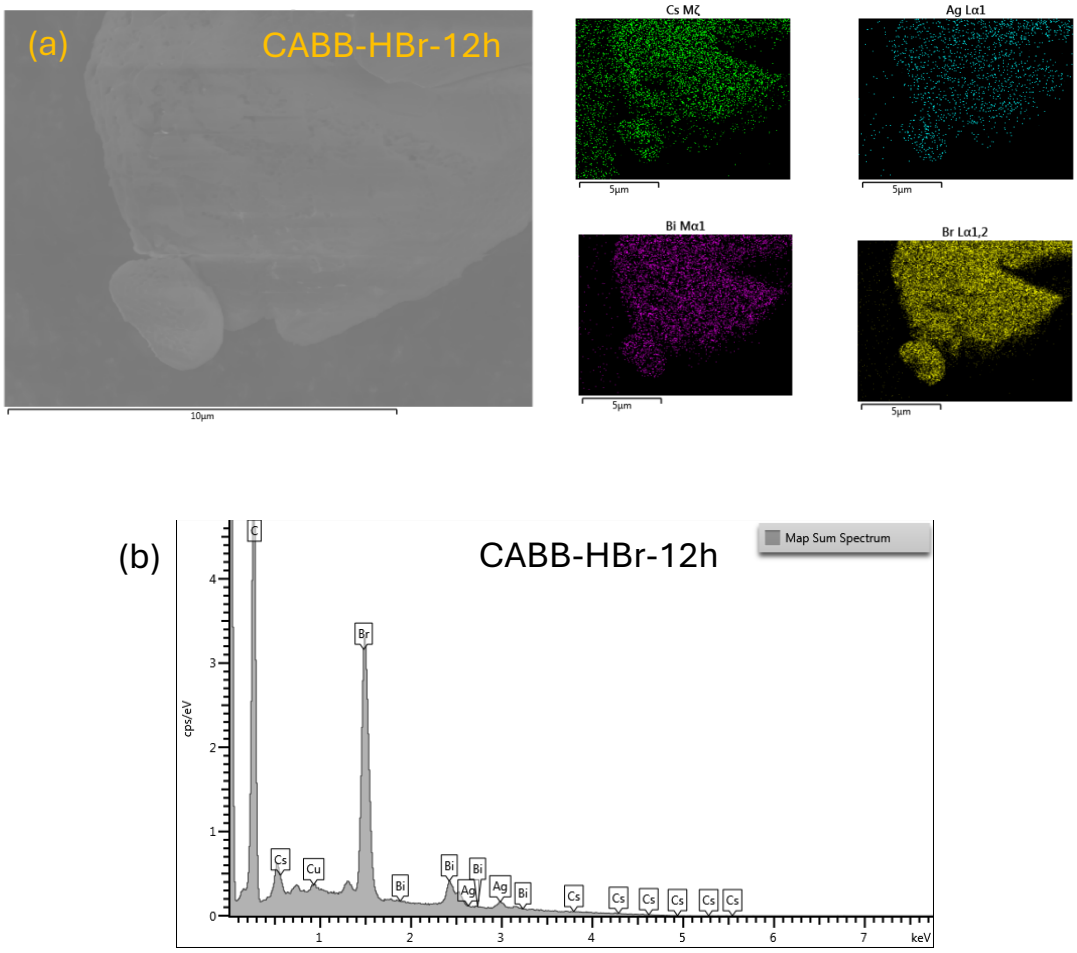

Figure A7. (a) SEM-EDX maps and (b) SEM-EDX spectrum of CABB-HBr after 12 hours of photoreaction, confirming the presence of the elements Cs, Ag, Bi and Br. The EDX data contain 512 x 384 pixels, and the pixel size was 26.6 nm x 26.6 nm; the voltage used was 5 kV, the current was 500 pA, and the working distance was 12.5 mm; the energy range was 0-20 keV, and the energy width per channel was 10 eV; the dwell time per pixel was 1.2 ms, and each pixel was scanned for 12 times; the electron fluence was calculated to be 635 e $Å^{-2}$.

A3. STEM-EDX analysis of CABB-NC and CABB-NC-EtOH after photoreactions

STEM-HAADF images of CABB-NC after two and four hours of reaction are shown in Figure A8. From Figure A8 (a), after two hours of photoreaction with gaseous methanol, some sheets began to appear, possibly produced by merging of a few nanocubes. These sheets were not found in the as-synthesised CABB-NC specimen before reaction. Figure A8 (b) revealed that the halide perovskite structure was retained for the nanocubes two hours into the reaction. Figure A8 (c, d) showed agglomeration of nanocubes after four hours of reaction, and the individual cubes became harder to distinguish as they began to pack together. Figure A9 shows STEM-HAADF images of CABB-NC after 12 hours of reaction. The sheets in Figure A8 (a) are easier to discern in Figure A9 (a, b), as they became larger after a longer reaction time. Figure A9 (c, d) are images of higher magnification investigating the top region in Figure A9 (b). In this region both the nanocubes and sheets were present, where the nanocubes seem to be on top of or underneath the sheet layer. STEM-EDX data shown in Figure A10 were collected from CABB-NC after 12 hours of reaction, and Figure A11 presents STEM-EDX data collected from CABB-NC-EtOH-10h. Signals from all constituent elements of CABB-NC can all be detected.

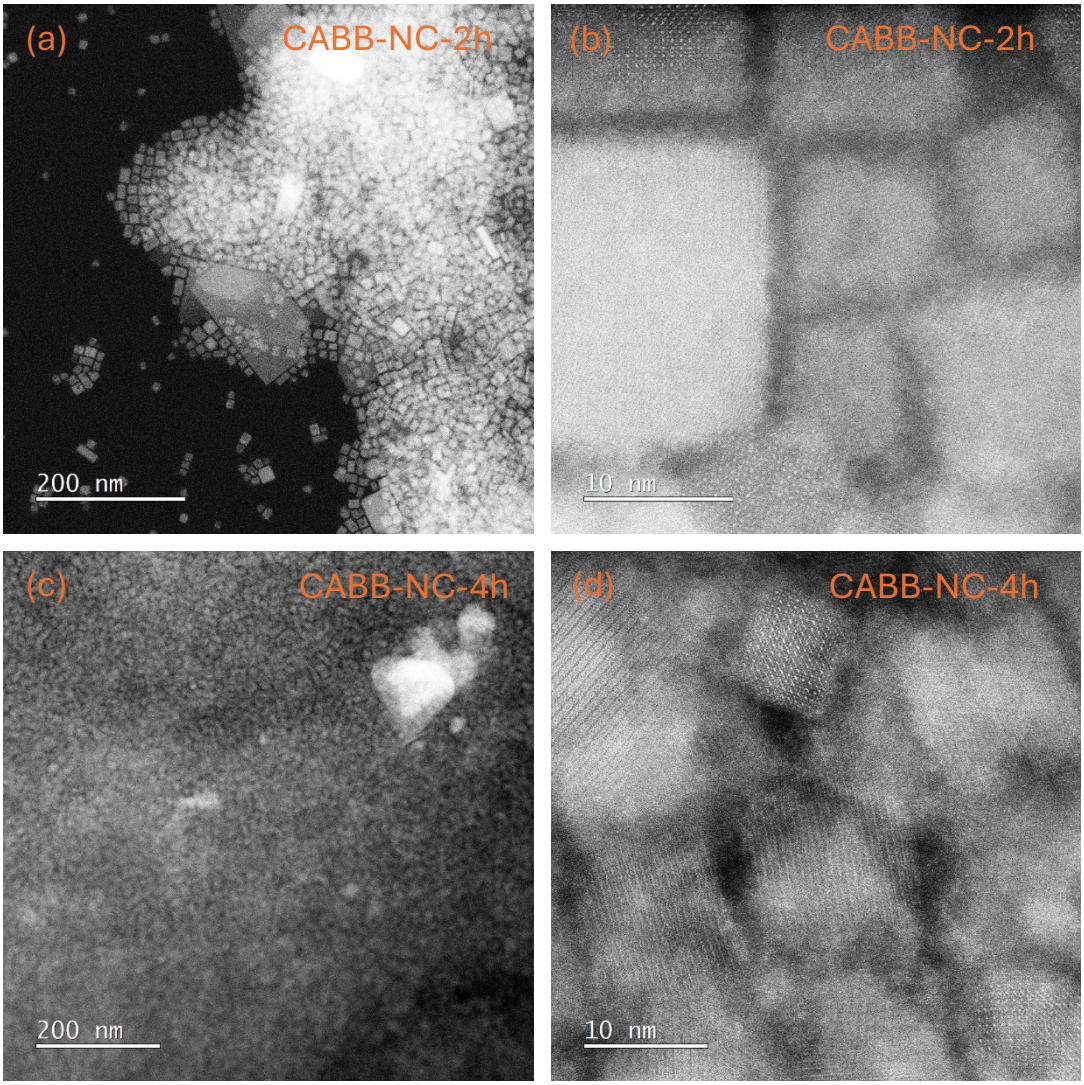

Figure A8. STEM images of CABB-NC after photoreaction with methanol vapour, with a total reaction time of (a, b) two hours, (c, d) four hours. The cubes began to aggregate during the reaction, and formation of sheets was observed. The images were taken with a beam current of 5.6 pA, 14.38 mrad convergence angle, 1024 x 1024 pixels, and 6 µs dwell time per pixel; for image (a) the pixel size was 7 Å x 7 Å and the electron fluence was 4.3 e $Å^{-2}$; for image (b) the pixel size was 0.35 Å x 0.35 Å and the electron fluence was 1.7 x 10^3 e $Å^{-2}$; for image (c) the pixel size was 8.3 Å x 8.3 Å and the electron fluence was 3.0 e $Å^{-2}$; for image (d) the pixel size was 0.42 Å x 0.42 Å and the electron fluence was 1.2 x 10^3 e $Å^{-2}$.

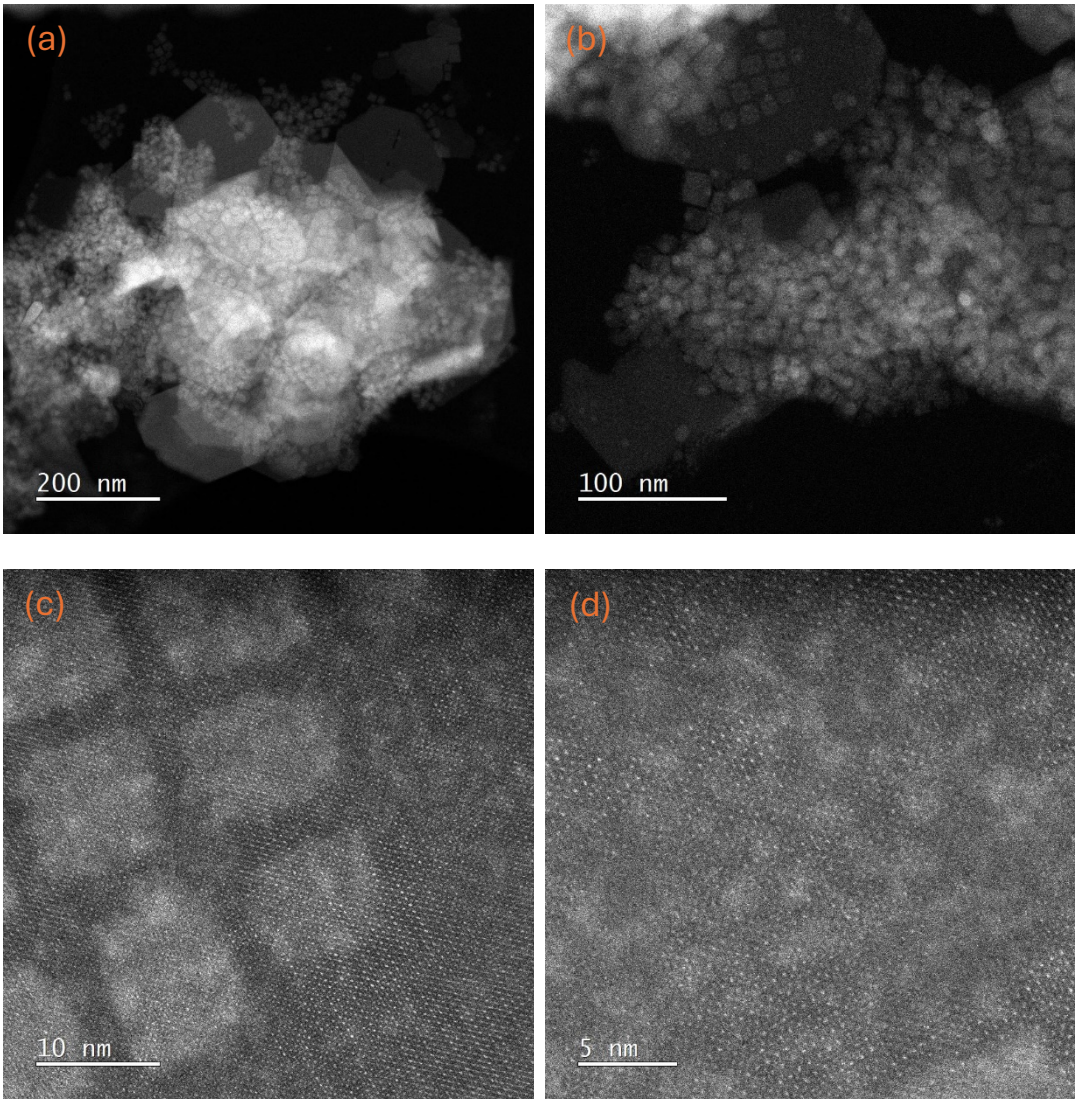

Figure A9. (a-d) STEM images of CABB-NC after 12 hours of photoreaction with methanol vapour. More sheets appeared compared to the specimen after a few hours of reaction, while the nanocubes were still present. Images (c, d) further investigated the top region from image (b), where the nanosheets and nanocubes coexist. The images were taken with a beam current of 5.6 pA, 14.38 mrad convergence angle, 1024 x 1024 pixels, and 6 µs dwell time per pixel; for image (a) the pixel size was 8.3 Å x 8.3 Å and the electron fluence was 3.0 e $Å^{-2}$; for image (b) the pixel size was 3.5 Å x 3.5 Å and the electron fluence was 17 e $Å^{-2}$; for image (c) the pixel size was 0.42 Å x 0.42 Å and the electron fluence was 1.2 x 10^3 e $Å^{-2}$; for image (d) the pixel size was 0.26 Å x 0.26 Å and the electron fluence was 3.1 x 10^3 e $Å^{-2}$.

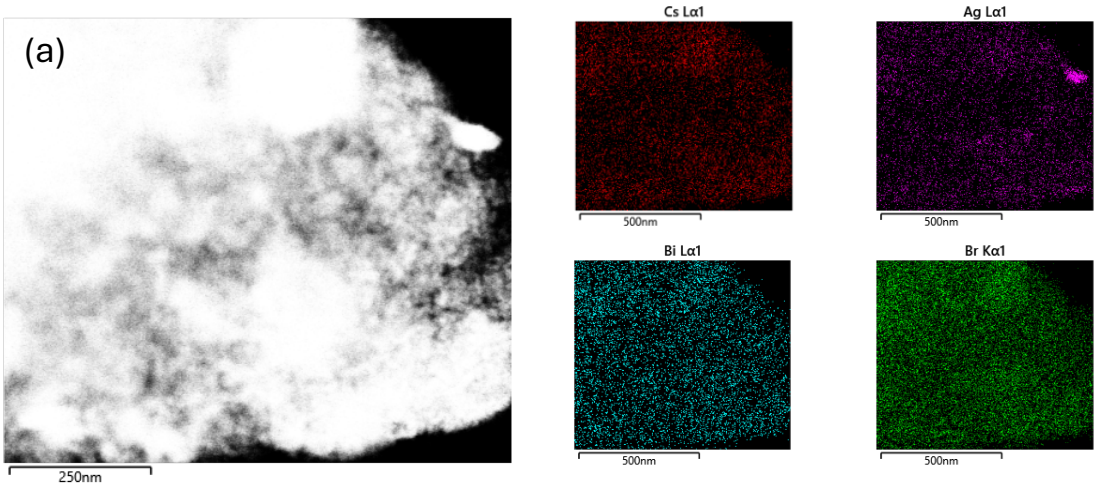

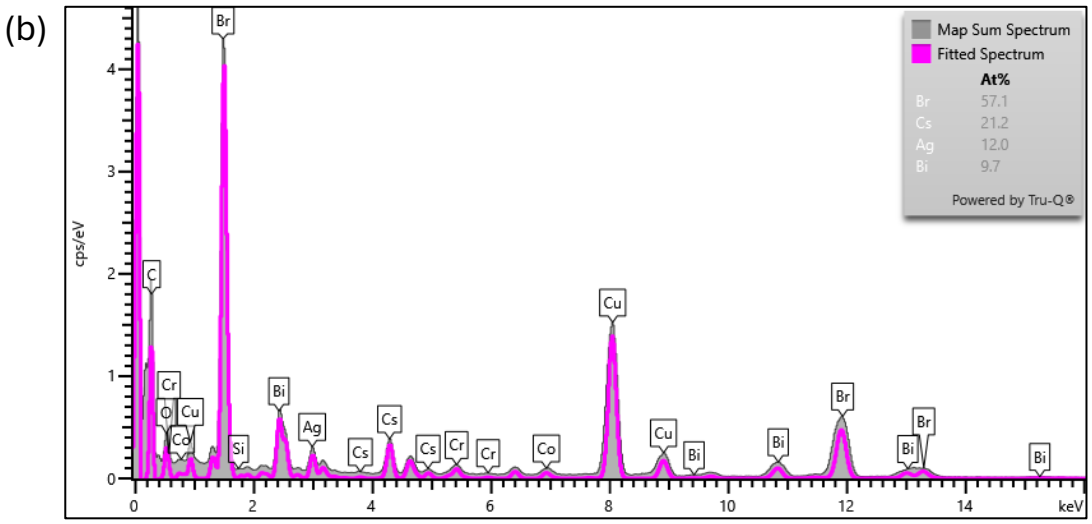

Figure A10. (a) STEM-EDX maps and (b) EDX spectrum of CABB-NC after 12 hours of reaction. All four constituent elements Cs, Ag, Bi and Br were present. The EDX data contained 1024 x 896 pixels, and the pixel size was 0.88 nm x 0.88 nm; the dwell time for each pixel was 1.12 ms, and each pixel was scanned for 11 times; the energy range was 0 – 20 keV, and the channel width was 20 eV per channel; the convergence angle was 22.48 mrad, and the beam current was 28.5 pA; the total electron fluence was 2.8×10^4 e Å^{-2}.

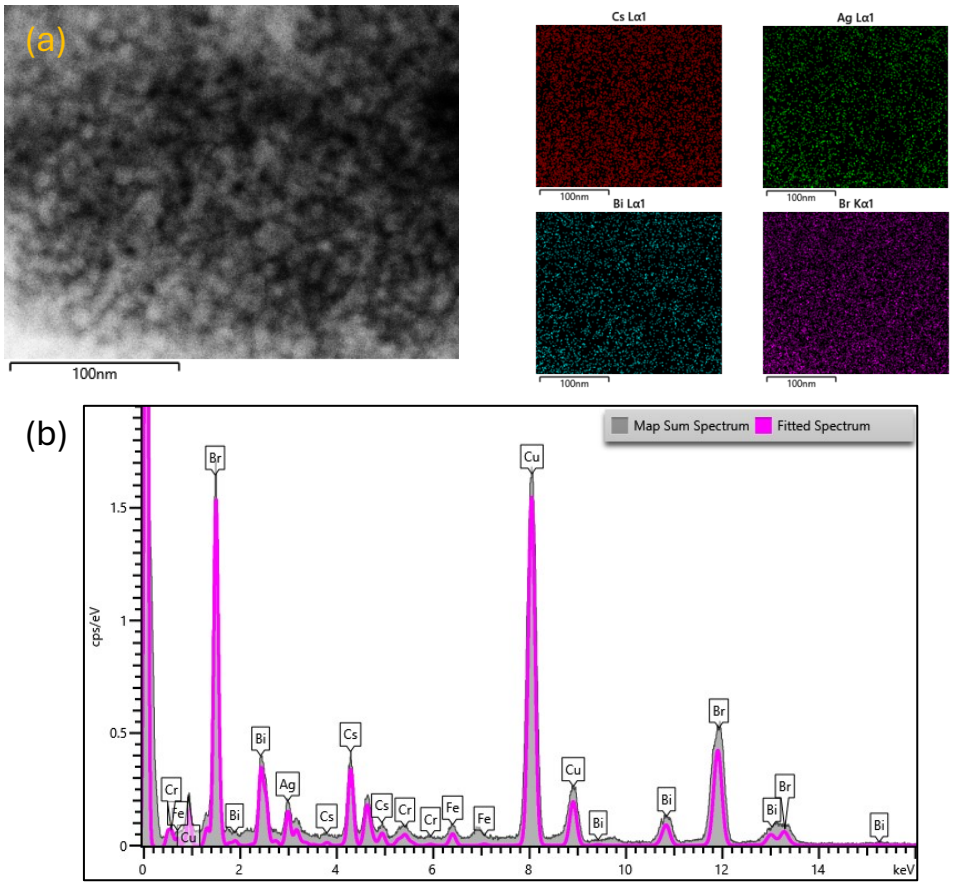

Figure A11. (a) STEM-EDX maps and (b) STEM-EDX spectrum obtained from CABB-NC-EtOH-10h. The EDX data confirmed that all four constituent elements to CABB were present after long hours of reaction. The EDX data contained 512 x 448 pixels, and the pixel size was 5.3 Å x 5.3 Å; the dwell time for each pixel was 631 µs, and each pixel was scanned for six times; the energy range was 0 – 20 keV, and the channel width was 20 eV per channel; the convergence angle was 22.48 mrad, and the beam current was 28.5 pA; the total electron fluence was 2.4×10^4 e Å^{-2}.

A4. CABB nanosheets

The synthesis procedure for CABB nanosheets (2D-CABB) was described in Section 3.2.3. Figure A12 (a) shows the XRD plot of 2D-CABB with a reference of CABB peaks from ICSD database (ICSD 01-084-8699). The peak at around 10° came from the vacuum grease. The TEM image in Figure A12 (b) revealed that the specimen synthesised was mostly made up of thin rectangular sheets. The high-resolution STEM-HAADF image in Figure A12 (c) revealed the atomic arrangements of 2D-CABB. However, during imaging of 2D-CABB, round particles quickly formed under the electron beam, as shown in Figure A12 (d). These particles are likely to be made up of silver[86]. To reduce beam damage to the specimen, the STEM images were taken quickly when operating the microscope. For example, exposure to the electron beam was kept to a minimum while searching for a suitable region for imaging on the specimen.

In the photo-oxidation reaction with liquid methanol and excess NaBr, the reaction system using 2D-CABB had a H_2 generation rate of 74 μmol g^{-1} h^{-1}, which made essentially no contribution to the reaction. The sample underwent significant structural changes during the reaction. As shown in Figure A13 (a, b), the 2D-CABB sheets agglomerated and formed thick particles during the photoreaction. The STEM-EDX data in Figure A13 (c, d) confirmed that these particles were CABB and not NaBr, as a Na peak could not be detected.

The H_2 production rates in methanol photo-oxidation reaction using methanol vapour and 2D-CABB are shown in Figure A14 (a) and Table A2. The low production rates and TOF mean that the catalyst did not achieve its full potential. Combined with information from STEM images in Figure A14 (b, c), agglomeration of the sheets during the reaction would lead to reduction in the number of active sites, causing a decrease in reaction rate. Washing 2D-CABB with ethanol did not improve the activity.

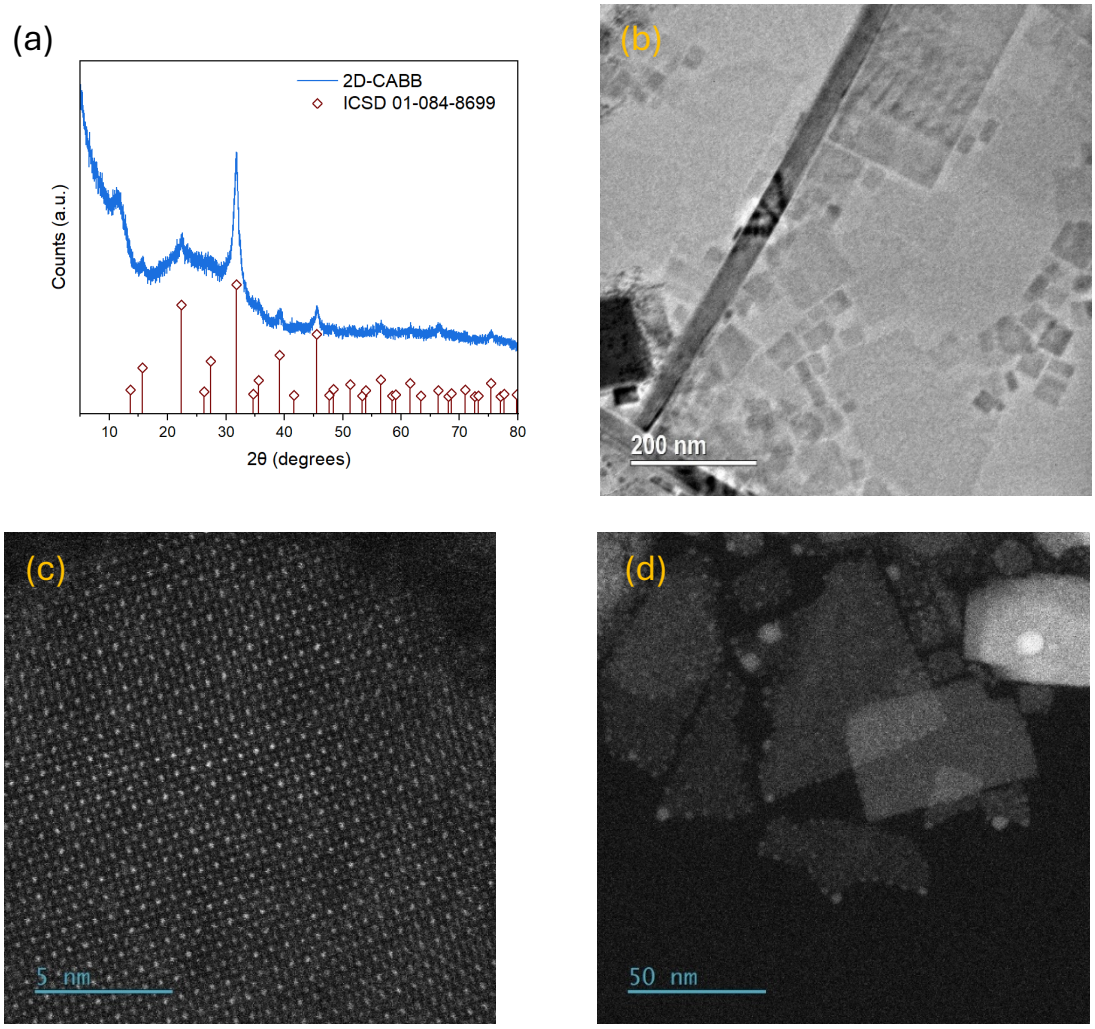

Figure A12. (a) XRD plot of 2D-CABB compared to the reference data ICSD 01-084-8699. (b) TEM image of 2D-CABB, showing the sheet-like structure of the specimen. (c) STEM-HAADF image of 2D-CABB revealing the atomic arrangements of the nanosheets. (d) STEM-HAADF image showing that some round particles quickly formed under the electron beam. TEM image (b) was taken using 15000x magnification, 56 nA probe current and 0.5 s exposure time. STEM-HAADF images (c, d) were taken with a beam current of 4.8 pA, 14.38 mrad convergence angle, 1024 x 1024 pixels, and 6 µs dwell time per pixel; for image (c) the pixel size was 0.17 Å x 0.17 Å and the electron fluence was 6.2 x 10^3 e $Å^{-2}$; for image (d) the pixel size was 1.7 Å x 1.7 Å and the electron fluence was 62 e $Å^{-2}$.

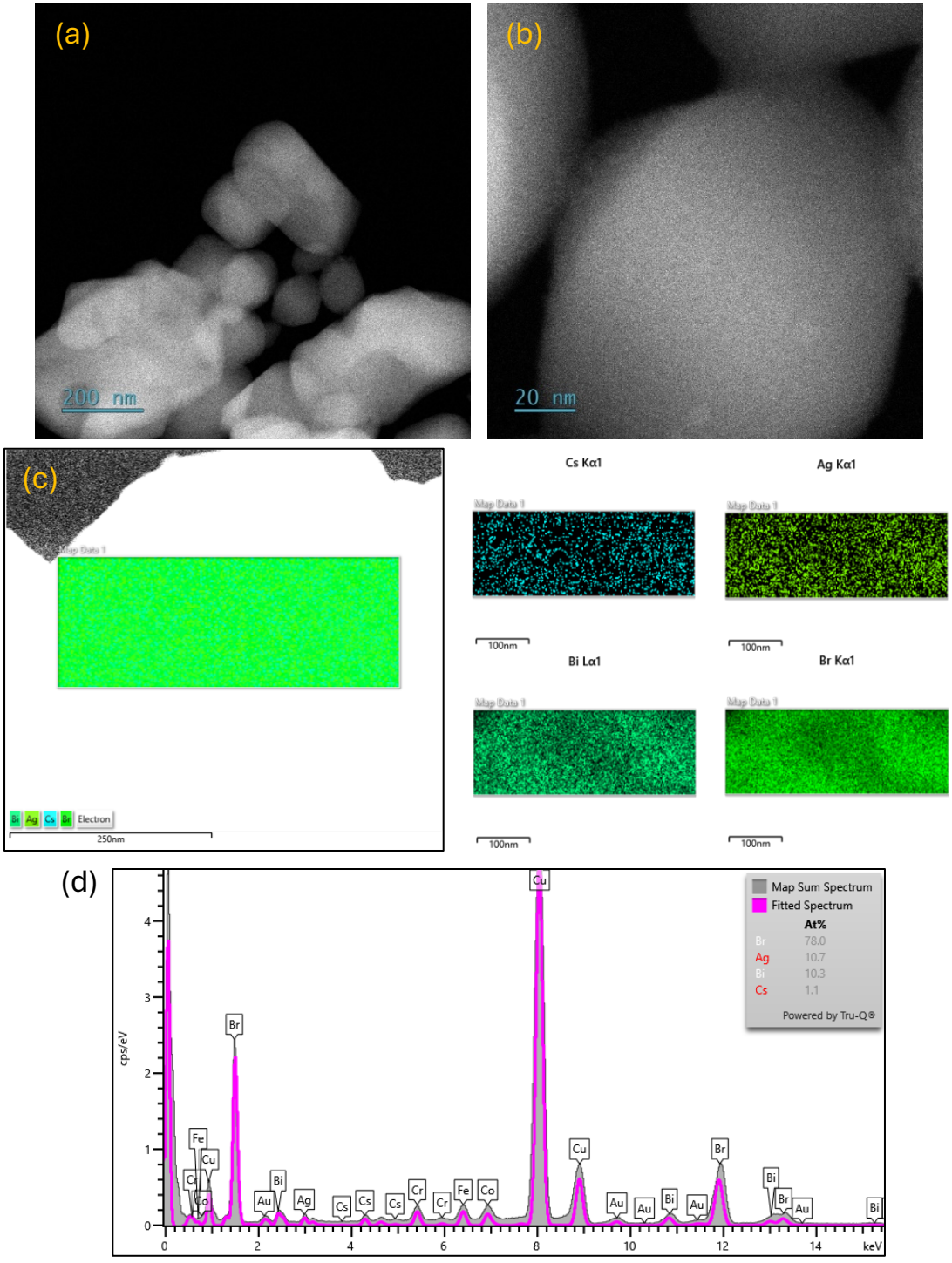

Figure A13. (a, b) STEM-HAADF images of 2D-CABB after photoreaction in liquid methanol with excess NaBr. (c) STEM-EDX maps and (d) EDX spectrum of 2D-CABB after photoreaction. The green box in (c) indicates the region selected for the EDX scan. The STEM-HAADF image appeared white as the particle was very thick. The EDX data proved the thick particles were CABB and not NaBr. Images (a, b) were taken with a beam current of 5.6 pA, 14.38 mrad convergence angle, 1024 x 1024 pixels, and 6 µs dwell time per pixel; the pixel size and electron fluence were (a) 10 Å x 10 Å and 2.1 e $Å^{-2}$, (b) 1.4 Å x 1.4 Å and 107 e $Å^{-2}$ respectively. The EDX data contained 201 x 77 pixels, and the pixel size was 2.1 nm x 2.1 nm; the dwell time for each pixel was 8.42 ms, and each pixel was scanned for 42 times; the energy range was 0 – 40 keV, and the channel width was 20 eV per channel; the convergence angle was 22.48 mrad, and the beam current used for analysis was 28.5 pA; the total electron fluence was 1.4 x 10^5 e $Å^{-2}$.

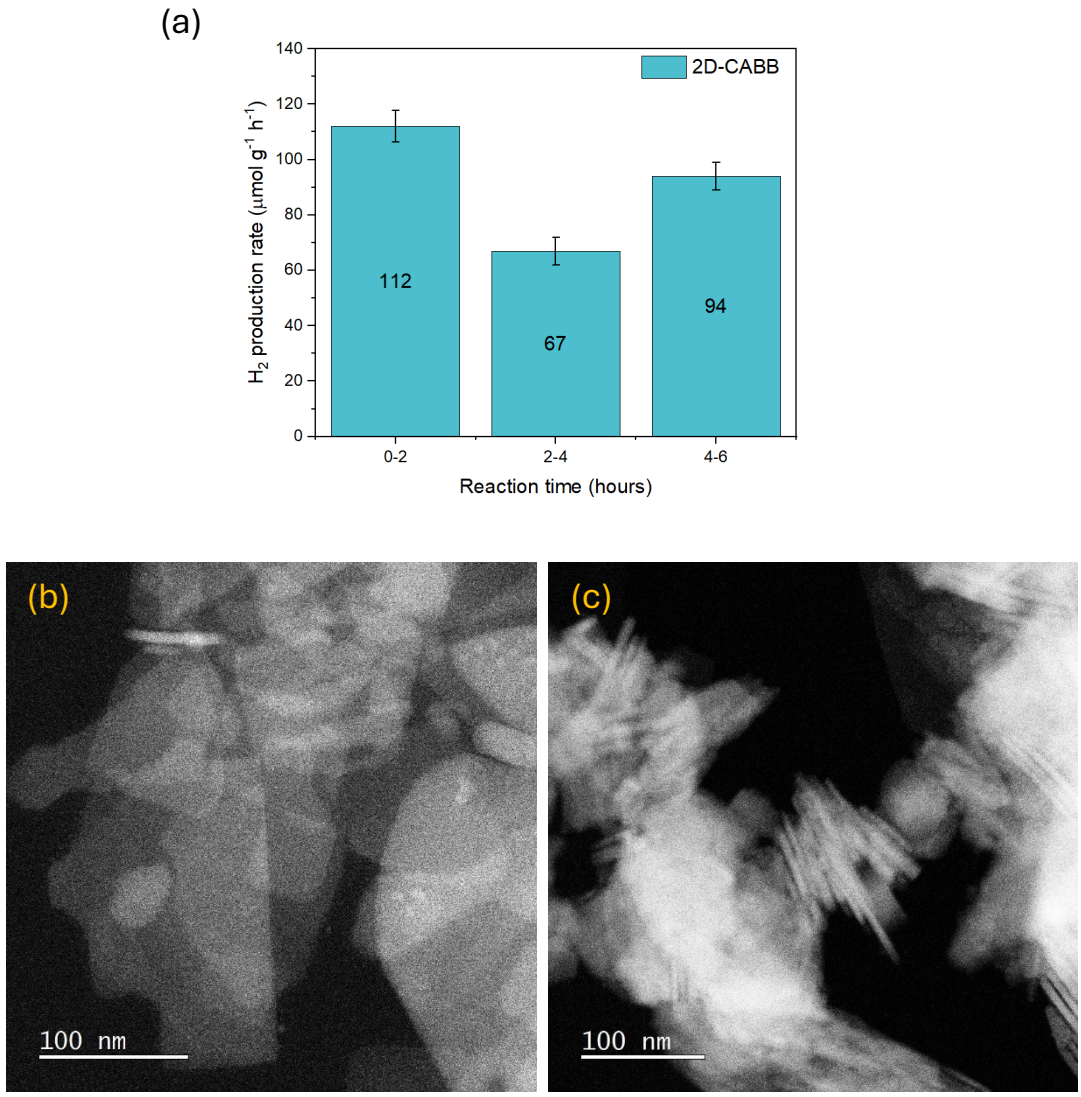

Figure A14. (a) H_2 production rates in methanol photo-oxidation reaction using 2D-CABB and gaseous methanol. Its activity dropped after first two hours and was not as good as CABB-NC overall. (b, c) STEM images of 2D-CABB after reaction. The sheets piled up, which reduced the contact area and could be the main reason for its inferior activity. STEM-HAADF images (b, c) were taken with a beam current of 5.6 pA, 14.38 mrad convergence angle, 1024 x 1024 pixels, and 6 μs dwell time per pixel; for image (b) the pixel size was 3.5 Å x 3.5 Å and the electron fluence was 17 e $Å^{-2}$; for image (c) the pixel size was 4.2 Å x 4.2 Å and the electron fluence was 12 e $Å^{-2}$.

Table A2. Reaction rates in terms of TOF for the methanol photo-oxidation reaction using 2D-CABB and methanol vapour.

Reaction time	0-2h	2-4h	4-6h
TOF (s^{-1})	4.40 x 10^{-5}	1.49 x 10^{-5}	3.24 x 10^{-5}

A5. Zeta potential and heterojunctions

The possibility of forming heterojunctions using CABB and another material was investigated. TiO_2, MoS_2, g-C_3N_4, SiO_2 and silica-alumina were tested. For CABB-HBr, the idea was to attach smaller particles onto the surface of bulk CABB particles; for CABB-NC, core-shell structures and large-area substrates were tested. Since CABB nanocubes are small, they may adhere to larger particles or sheets. Various methods to synthesise heterojunctions were tested, which can be classified into two main categories: adding the second material at the start of the CABB synthesis process, or adding the material at the end of the synthesis process. If the second material was added at the end, where CABB particles had already been formed, CABB would be dispersed in a liquid such as ethanol. The mixture containing CABB and the second material would then be left in sonication and/or stirring for a few hours to allow self-adhesion between CABB and the additive.

TiO_2 was used in three different ways to create heterojunctions. The first route was to add P25 at the start or the end of the synthesis process of CABB-HBr or CABB-NC to try to mix CABB and TiO_2. The second route was to calcine P25 so the particles would aggregate and form a substrate for CABB, and then the calcined P25 was added either at the start or the end of CABB synthesis process. The third route was to synthesise a TiO_2 shell for CABB-NC as the core, following the work by Xu et al.[233].

Other materials were similarly treated. The commercially available bulk form of MoS_2 was tested as the co-catalyst, added either at the start or the end of the CABB synthesis process. Graphitic carbon nitride, g-C_3N_4, which was made by calcinating dicyandiamide in a muffle furnace[106] was also tested. Furthermore, SiO_2 and silica-alumina microbeads were calcined and used as the substrate for CABB separately. Besides, an attempt was made to form a SiO_2 shell for CABB-NC as the core, based on a report by Gao et al.[234].

Unfortunately, none of the samples synthesised as described above showed convincing signs of increased activity in the methanol photo-oxidation reaction. For future materials selection to produce heterojunctions, the surface charge may help to identify the best option. Forming heterojunctions with another material that has an opposite zeta potential (i.e. opposite surface charge) may be optimal, as the materials would adhere to each other due to electrostatic attraction. Amy Radford from Inorganic Chemistry Laboratory, University of Oxford performed zeta potential measurements on CABB-HBr and CABB-NC samples. Grateful acknowledgement also to Charlotte Williams for granting access to the measuring machine. Figure A15 shows the plot obtained, where both CABB-HBr and CABB-NC exhibited negative zeta potentials. For higher likelihood of success, using materials with a positive zeta potential to form a heterojunction with CABB would be preferred.

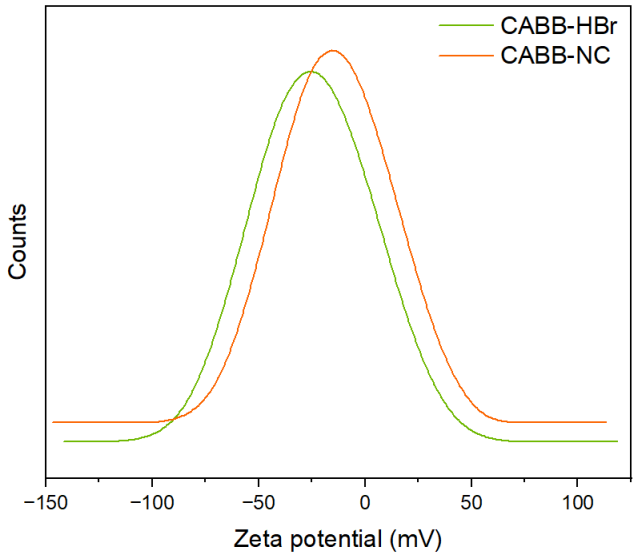

Figure A15. Data plot revealing the zeta potentials of CABB-HBr and CABB-NC. Both bulk and nanocube forms of CABB have negative zeta potentials.

A6. FFT analysis of CABB-NC-EtOH, 2D-CABB and CABB-NC

This section includes the FFT data obtained and analysed, from STEM images of CABB-NC-EtOH, 2D-CABB and CABB-NC specimens. The FFT patterns are labelled and the distance between (000) and (400) is measured to gauge the change in planar spacing within the perovskite structure during the photoreaction.

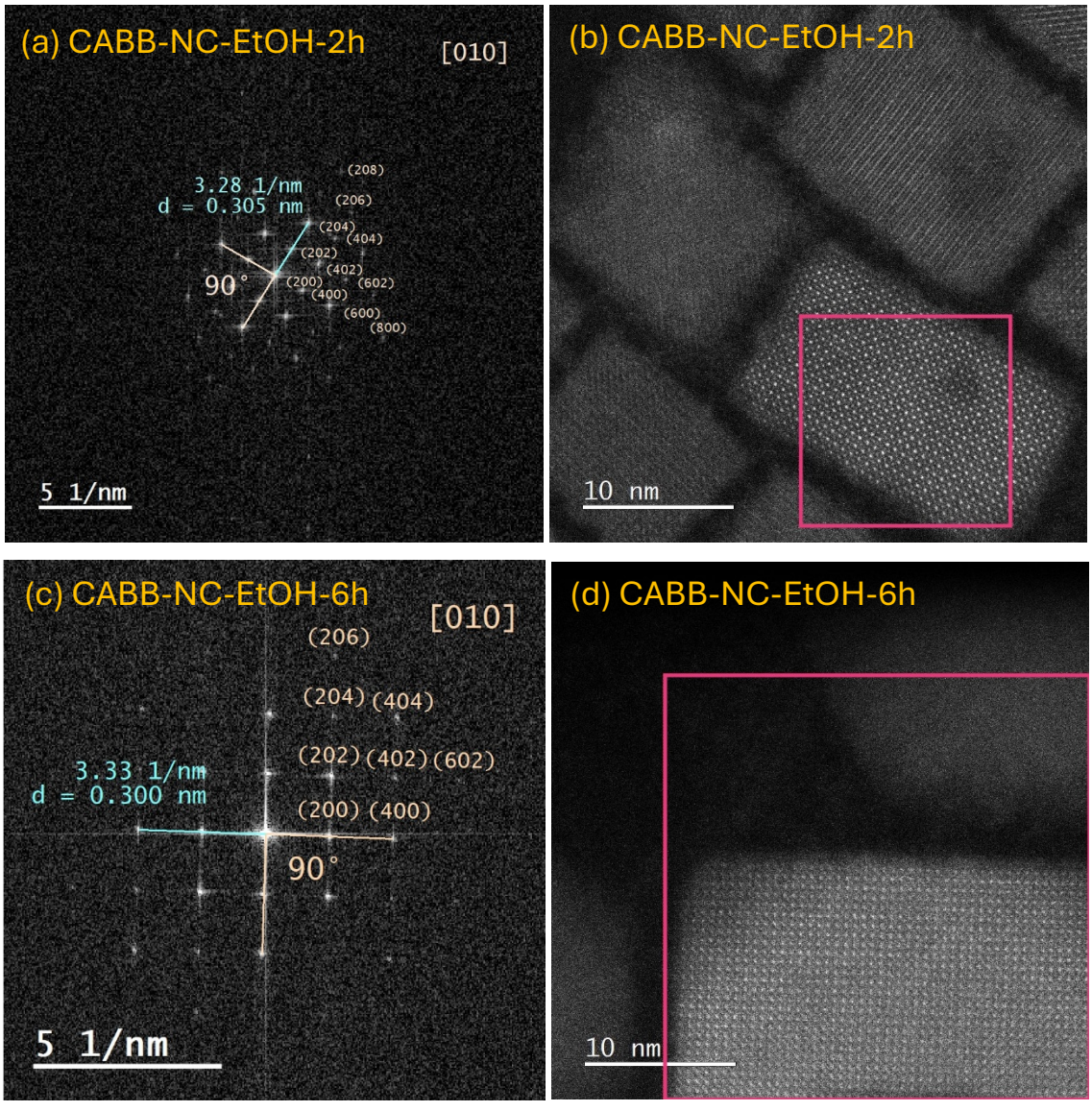

Figure A16. (a) FFT pattern of CABB-NC-EtOH-2h, obtained from the region marked with a square in (b). (c) FFT pattern of CABB-NC-EtOH-6h, obtained from the region marked with a square in (d).

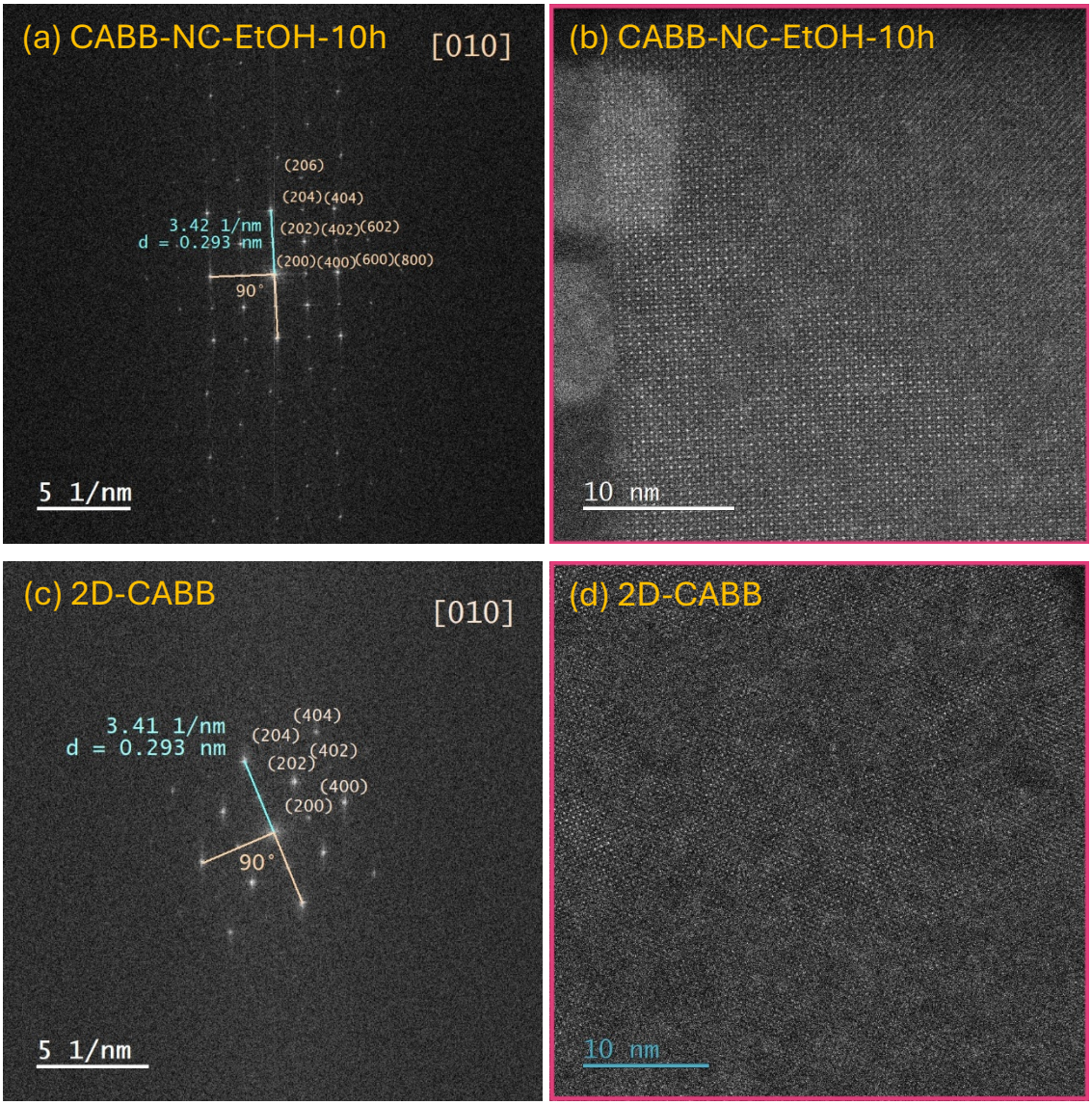

Figure A17. (a) FFT pattern of CABB-NC-EtOH-10h, obtained from the entire region in (b). (c) FFT pattern of 2D-CABB, obtained from the entire region in (d).

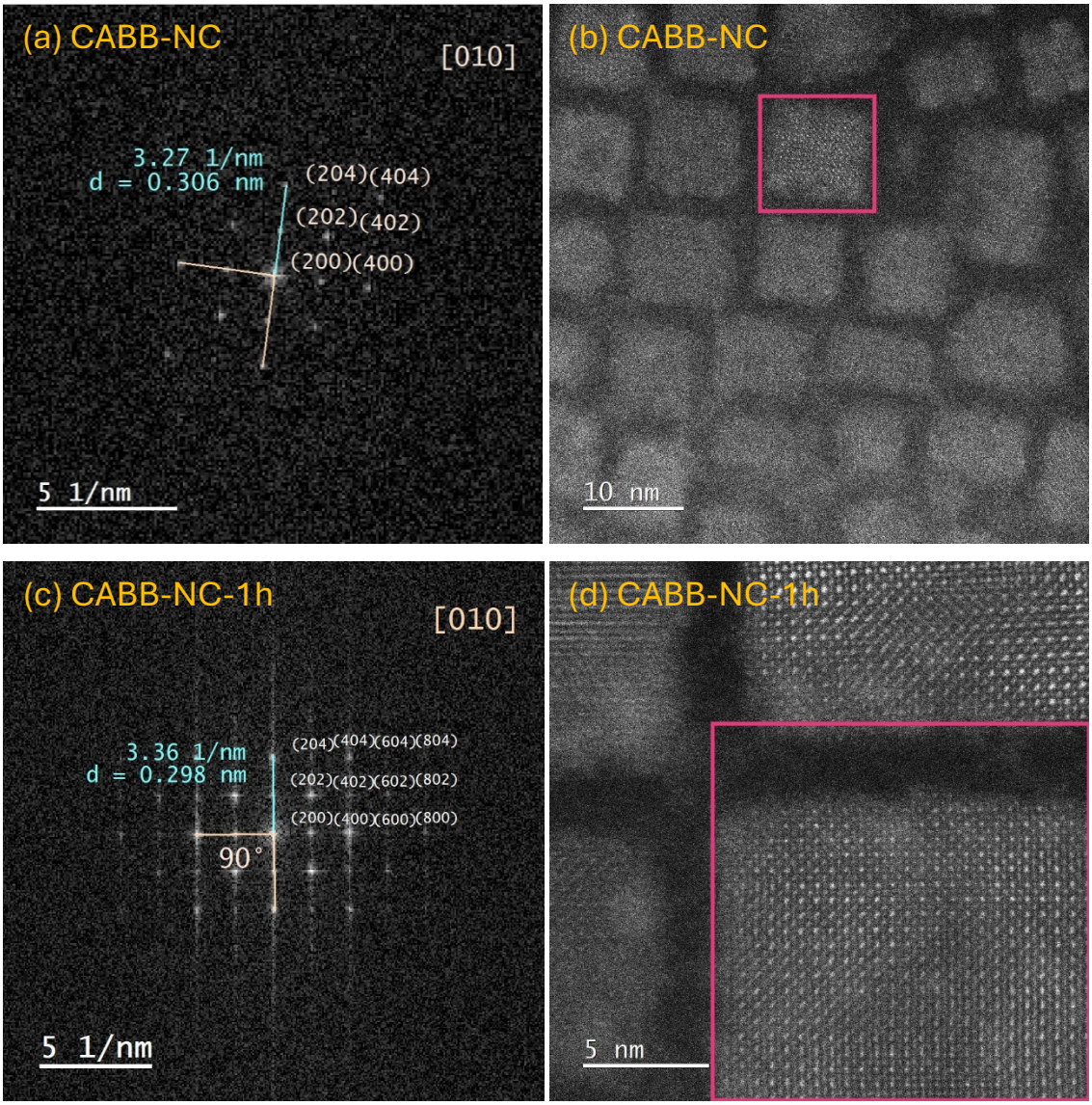

Figure A18. (a) FFT pattern of CABB-NC, obtained from the region marked with a square in (b). (c) FFT pattern of CABB-NC-1h, obtained from the region marked with a square in (d).

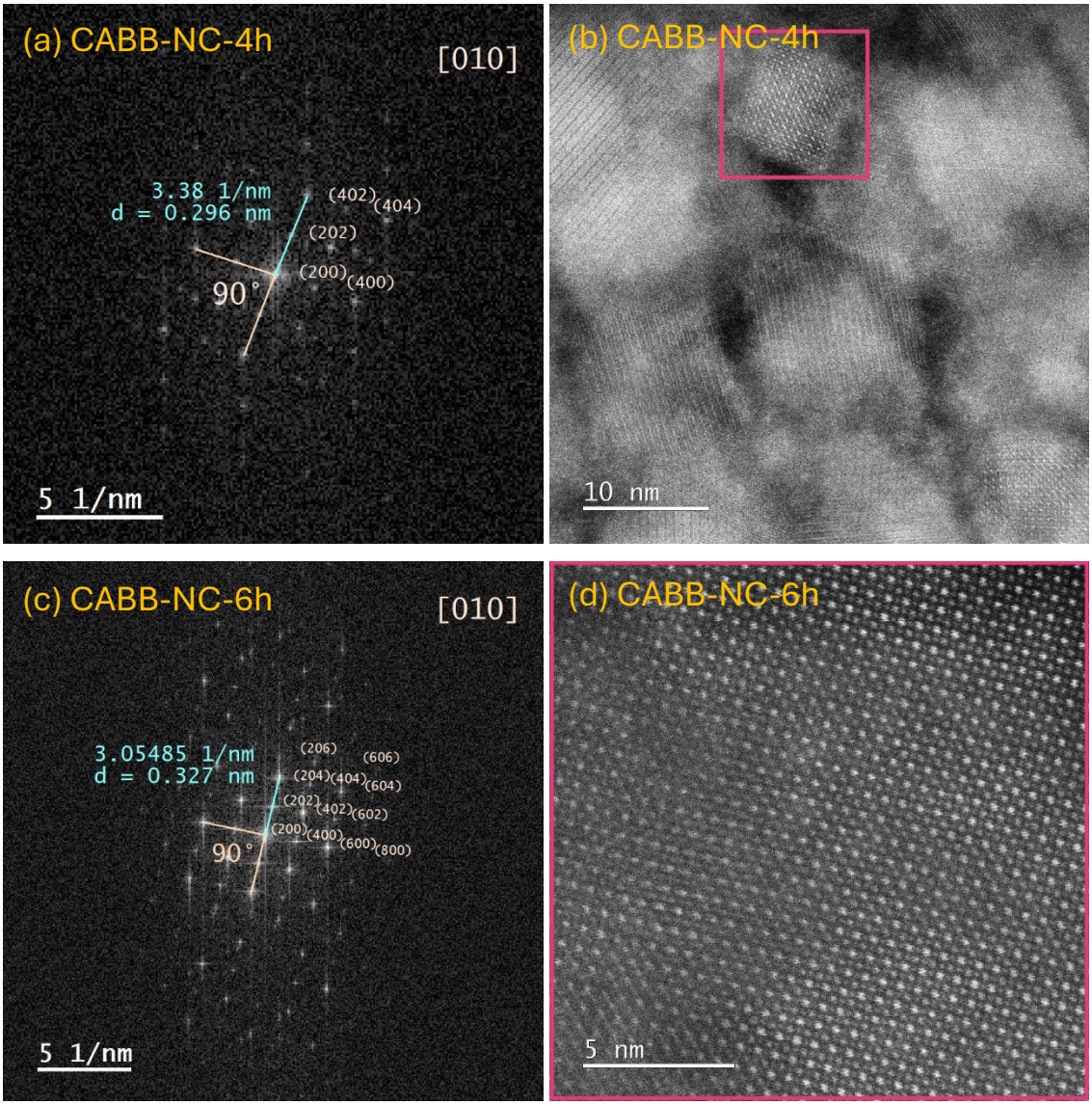

Figure A19. (a) FFT pattern of CABB-NC-4h, obtained from the region marked with a square in (b). (c) FFT pattern of CABB-NC-6h, obtained from the entire region in (d).

A7. Surface analysis of CABB nanoparticles

The calculated results between adjacent atoms along an atomic row containing either Ag/Bi or Cs are presented in this section. In the tables some line profiles drawn along the row was not long enough to cover eight atoms so some boxes were marked with a '/'. Some line spectra along Cs were still noisy after background subtraction, and the peaks representing Cs atoms could not be discerned. In this way, the distance between atoms were not calculated for some samples.

Multiple sites were considered when taking the average values in Table A3 and Table A4, three regions and nine rows each were analysed for Ag/Bi and Cs of CABB-NC-EtOH-2h and CABB-NC-EtOH-6h. Three regions and nine rows were analysed for Ag/Bi of CABB-NC-EtOH-10h and CABB-NC. One region and three rows were analysed for Cs of CABB-NC-EtOH-10h and Ag/Bi of CABB-NC-4h.

Table A3. The average distance between two adjacent atoms in a Ag/Bi column. The units are in nm. The lower the atom number (e.g. Atom 1) the further away the atom is from the edge of the nanoparticle.

Ag/Bi	Atoms 1-2	Atoms 2-3	Atoms 3-4	Atoms 4-5	Atoms 5-6	Atoms 6-7	Atoms 7-8
CABB-NC-EtOH-2h	0.590	0.590	0.616	0.609	0.609	0.601	0.607
CABB-NC-EtOH-6h	0.599	0.615	0.623	0.576	0.592	0.592	0.589
CABB-NC-EtOH-10h	0.573	0.620	0.596	0.558	0.588	0.612	0.557
CABB-NC	0.596	0.611	0.566	0.604	0.573	0.628	/
CABB-NC-4h	0.637	0.581	0.582	0.581	0.582	/	/

Table A4. The average distance between two adjacent atoms in a Cs column. The units are in nm. The lower the atom number the further away the atom is from the edge of the nanoparticle.

Ag/Bi	Atoms 1-2	Atoms 2-3	Atoms 3-4	Atoms 4-5	Atoms 5-6	Atoms 6-7	Atoms 7-8
CABB-NC-EtOH-2h	0.624	0.601	0.586	0.617	0.617	0.593	0.520
CABB-NC-EtOH-6h	0.615	0.607	0.607	0.607	0.569	0.593	0.600
CABB-NC-EtOH-10h	0.602	0.533	0.637	0.568	0.619	0.585	/

A8. CABB-DMSO photoreactions and characterisation

XRD data of CABB-DMSO and CABB-DMSO after immersion in water (denoted as CABB-DMSO-W) are shown in Figure A20 (a) and (b) respectively. CABB synthesised using this method contained some $CsAgBr_2$ impurity, and the specimen suffered from significant beam damage. As shown in Figure A20 (c), (d), significant differences were observed in images from the same area a few seconds apart. After immersion in water, unlike CABB-HBr-W, BiOBr peaks were not present in XRD. This was probably because not as much BiOBr was formed. A TEM image of CABB-DMSO-W is shown in Figure A20 (e). Nanosized CABB-DMSO and CABB-DMSO-W were also studied using TEM. As shown in Figure A20 (f), the shapes of the nanosized CABB-DMSO were irregular. In Figure A20 (g), some thin sheets were also present within nanosized CABB-DMSO-W. The water splitting rate in terms of hydrogen production for bulk CABB-DMSO was found to be 10 μmol g^{-1} h^{-1}, which was lower than that of CABB-HBr.

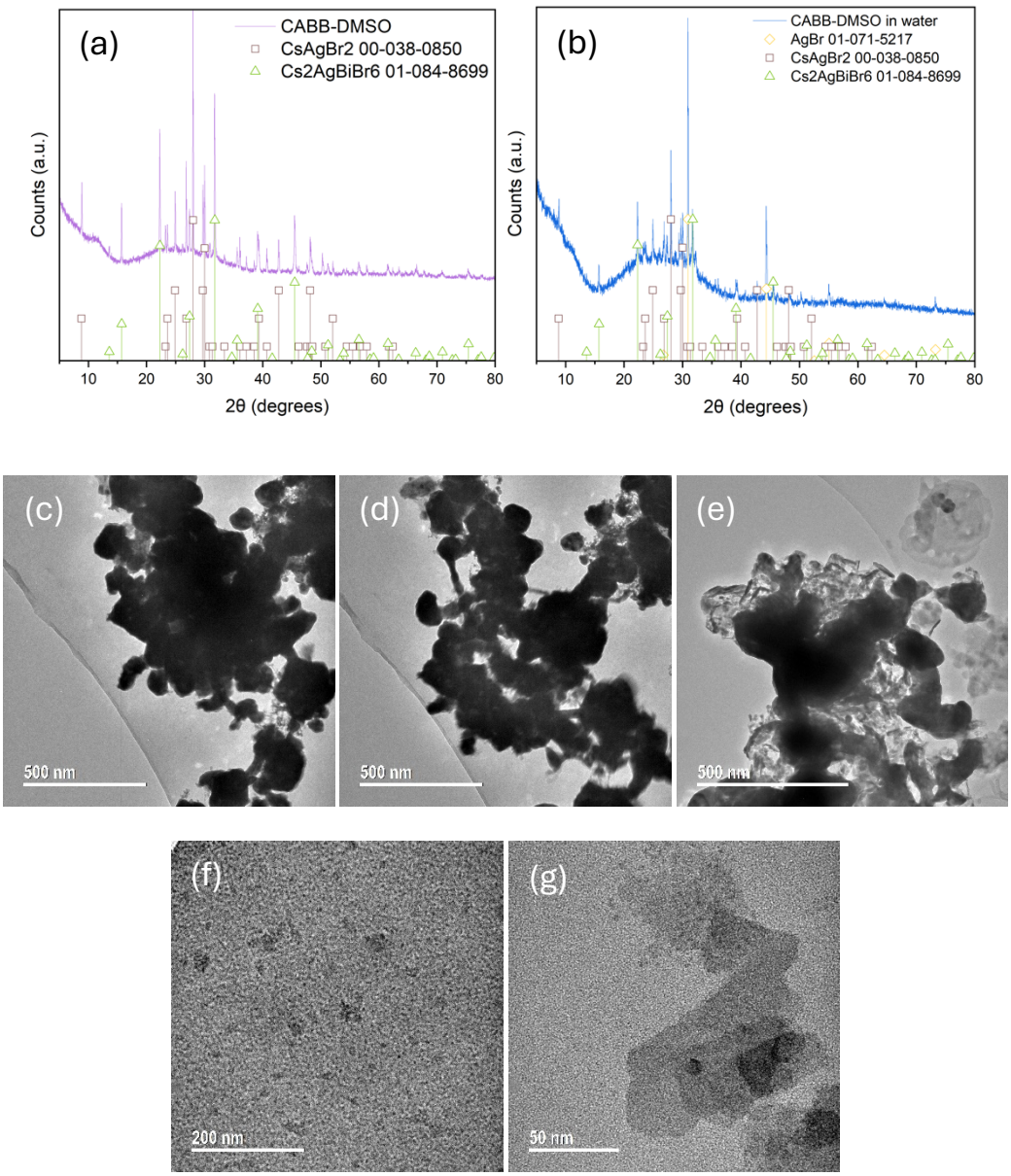

Figure A20. XRD data from (a) bulk CABB-DMSO and (b) bulk CABB-DMSO-W. Peaks due to $CsAgBi_2$ could be detected. TEM images of (c) bulk CABB-DMSO, (d) the same area as the previous image but taken a short time later, (e) bulk CABB-DMSO-W, (f) nanosized CABB-DMSO and (g) nanosized CABB-DMSO-W. The specimens suffered from beam damage easily under TEM, and the nanosized particles had irregular shapes. TEM images (c-g) were taken using 56 nA probe current and 0.5 s exposure time. The magnifications of the TEM images were (c) 8000x, (d) 8000x, (e) 10000x, (f) 20000x and (g) 60000x.

References

1. Ogden, J. M. Hydrogen: The Fuel of the Future? *Phys. Today* **55**, 69–75 (2002).
2. Fujishima, A. & Honda, K. Electrochemical Photolysis of Water at a Semiconductor Electrode. *Nature* **238**, 37–38 (1972).
3. Gong, M. *et al.* Nanoscale nickel oxide/nickel heterostructures for active hydrogen evolution electrocatalysis. *Nat. Commun.* **5**, 4695 (2014).
4. He, Y., Liu, W. & Liu, J. MOF-based/derived catalysts for electrochemical overall water splitting. *J. Colloid Interface Sci.* **661**, 409–435 (2024).
5. Rostrup-Nielsen, J. R. Fuels and Energy for the Future: The Role of Catalysis. *Catalysis Reviews* **46**, 247–270 (2011).
6. Walter, M. G. *et al.* Solar Water Splitting Cells. *Chem. Rev.* **110**, 6446–6473 (2010).
7. Marugán, J., José López-Muñoz, M., Fernández-Ibáñez, P. & Malato, S. Solar Photocatalysis: Fundamentals, Reactors and Applications. in *Photocatalysis: Applications* (eds. Dionysiou, D. D., Li Puma, G., Ye, J., Schneider, J. & Bahnemann, D.) 92–129 (Royal Society of Chemistry, 2016).
8. Yuan, L., Han, C., Yang, M. Q. & Xu, Y. J. Photocatalytic water splitting for solar hydrogen generation: fundamentals and recent advancements. *Int. Rev. Phys. Chem.* **35**, 1–36 (2016).
9. Tasleem, S. & Tahir, M. Current trends in strategies to improve photocatalytic performance of perovskites materials for solar to hydrogen production. *Renewable and Sustainable Energy Reviews* **132**, 110073 (2020).
10. Chen, X., Shen, S., Guo, L. & Mao, S. S. Semiconductor-based photocatalytic hydrogen generation. *Chem. Rev.* **110**, 6503–6570 (2010).
11. Takata, T. *et al.* Photocatalytic water splitting with a quantum efficiency of almost unity. *Nature* **581**, 411–414 (2020).
12. Colón, G. Towards the hydrogen production by photocatalysis. *Appl. Catal. A Gen.* **518**, 48–59 (2016).
13. Dolan, G. A. Methanol Production and Markets: Past, Present, and Future. in *The Toxicology of Methanol* (ed. Clary, J. J.) 1–10 (John Wiley & Sons, Inc., Hoboken, 2013).
14. Dalena, F. *et al.* Methanol Production and Applications: An Overview. in *Methanol: Science and Engineering* (eds. Basile, A. & Dalena, F.) 3–28 (Elsevier, Amsterdam, 2018).
15. Gumber, S. & Gurumoorthy, A. V. P. Methanol Economy Versus Hydrogen Economy. in *Methanol: Science and Engineering* (eds. Basile, A. & Dalena, F.) 661–674 (Elsevier, 2018).
16. Garcia, G., Arriola, E., Chen, W. H. & De Luna, M. D. A comprehensive review of hydrogen production from methanol thermochemical conversion for sustainability. *Energy* **217**, 119384 (2021).
17. Li, Z., Ivanenko, A., Meng, X. & Zhang, Z. Photocatalytic oxidation of methanol to formaldehyde on bismuth-based semiconductors. *J. Hazard. Mater.* **380**, 120822 (2019).
18. Thrane, J., Mentzel, U. V., Thorhauge, M., Høj, M. & Jensen, A. D. A review and experimental revisit of alternative catalysts for selective oxidation of methanol to formaldehyde. *Catalysts* **11**, 1329 (2021).
19. Deitermann, M., Huang, Z., Lechler, S., Merko, M. & Muhler, M. Non-Classical Conversion of Methanol to Formaldehyde. *Chemie Ingenieur Technik* **94**, 1573–1590 (2022).
20. Yang, D. *et al.* All-inorganic cesium lead halide perovskite nanocrystals: synthesis, surface engineering and applications. *J. Mater. Chem. C Mater.* **7**, 757–789 (2019).
21. Nasti, G., Abate, A., Nasti, G. & Abate, A. Tin Halide Perovskite (ASnX3) Solar Cells: A Comprehensive Guide toward the Highest Power Conversion Efficiency. *Adv. Energy Mater.* **10**, 1902467 (2020).
22. Kieslich, G., Sun, S. & Cheetham, A. K. Solid-state principles applied to organic–inorganic perovskites: new tricks for an old dog. *Chem. Sci.* **5**, 4712–4715 (2014).

23. Yao, H. *et al.* Strategies for Improving the Stability of Tin-Based Perovskite (ASnX3) Solar Cells. *Advanced Science* **7**, 1903540 (2020).
24. Zhou, Y. & Zhao, Y. Chemical stability and instability of inorganic halide perovskites. *Energy Environ. Sci.* **12**, 1495–1511 (2019).
25. Sycheva, A. A. R., Falina, I. V. & Berezina, N. P. Sorption and conducting properties of perfluorinated MF-4SC membranes in aqueous solutions containing phenylammonium ions. *Russian Journal of Electrochemistry* **45**, 108–115 (2009).
26. Wooster, W. A. & M, C. K. Crystal Structure and Photoconductivity of Cæsium Plumbohalides. *Nature* **182**, 1436 (1958).
27. Wang, J. *et al.* Two-dimensional lead-free halide perovskite materials and devices. *J. Mater. Chem. A Mater.* **7**, 23563–23576 (2019).
28. Park, N.-G., Snaith, H. J. & Miyasaka, T. Key advances in perovskite solar cells in 2025. *Nature Reviews Clean Technology 2025 2:1* **2**, 6–7 (2026).
29. Wang, G. *et al.* Silicon solar cells with hybrid back contacts. *Nature 2025 647:8089* **647**, 369–374 (2025).
30. Arrigo, A. *et al.* Perovskites based on earth-abundant elements as robust catalysts for photo-driven oxygen production. *Mater. Res. Bull.* **188**, 113437 (2025).
31. Yang, Q. *et al.* Carbon-supported platinum-based electrocatalysts for alkaline hydrogen evolution. *EES Catalysis* **3**, 972–993 (2025).
32. Xu, F. & Weng, B. Photocatalytic hydrogen production: an overview of new advances in structural tuning strategies. *J. Mater. Chem. A Mater.* **11**, 4473–4486 (2023).
33. Temerov, F., Baghdadi, Y., Rattner, E. & Eslava, S. A Review on Halide Perovskite-Based Photocatalysts: Key Factors and Challenges. *ACS Appl. Energy Mater.* **5**, 14605–14637 (2022).
34. Xiao, Z. *et al.* From Lead Halide Perovskites to Lead-Free Metal Halide Perovskites and Perovskite Derivatives. *Advanced Materials* **31**, 1803792 (2019).
35. Kim, G. W. & Petrozza, A. Defect Tolerance and Intolerance in Metal-Halide Perovskites. *Adv. Energy Mater.* **10**, 2001959 (2020).
36. Kang, J. & Wang, L. W. High Defect Tolerance in Lead Halide Perovskite CsPbBr3. *Journal of Physical Chemistry Letters* **8**, 489–493 (2017).
37. Filip, M. R. & Giustino, F. Computational Screening of Homovalent Lead Substitution in Organic-Inorganic Halide Perovskites. *Journal of Physical Chemistry C* **120**, 166–173 (2016).
38. Lin, H. *et al.* The Low-Dimensional Three-Dimensional Tin Halide Perovskite: Film Characterization and Device Performance. *Energies 2020, Vol. 13, Page 2* **13**, 2 (2019).
39. Chatterjee, S. & Pal, A. J. Influence of metal substitution on hybrid halide perovskites: towards lead-free perovskite solar cells. *J. Mater. Chem. A Mater.* **6**, 3793–3823 (2018).
40. Noel, N. K. *et al.* Lead-free organic–inorganic tin halide perovskites for photovoltaic applications. *Energy Environ. Sci.* **7**, 3061–3068 (2014).
41. Ke, W. & Kanatzidis, M. G. Prospects for low-toxicity lead-free perovskite solar cells. *Nat. Commun.* **10**, 965 (2019).
42. Huang, H., Pradhan, B., Hofkens, J., Roeffaers, M. B. J. & Steele, J. A. Solar-Driven Metal Halide Perovskite Photocatalysis: Design, Stability, and Performance. *ACS Energy Lett.* **5**, 1107–1123 (2020).
43. Lin, R. *et al.* Monolithic all-perovskite tandem solar cells with 24.8% efficiency exploiting comproportionation to suppress Sn(ii) oxidation in precursor ink. *Nat. Energy* **4**, 864–873 (2019).
44. Smith, I. C., Hoke, E. T., Solis-Ibarra, D., McGehee, M. D. & Karunadasa, H. I. A Layered Hybrid Perovskite Solar-Cell Absorber with Enhanced Moisture Stability. *Angew. Chem. Int. Ed.* **53**, 11232–11235 (2014).
45. Lin, Y. *et al.* Suppressed Ion Migration in Low-Dimensional Perovskites. *ACS Energy Lett.* **2**, 1571–1572 (2017).
46. Liao, Y. *et al.* Highly Oriented Low-Dimensional Tin Halide Perovskites with Enhanced Stability and Photovoltaic Performance. *J. Am. Chem. Soc.* **139**, 6693–6699 (2017).

47. Ghosh, D. *et al.* Charge carrier dynamics in two-dimensional hybrid perovskites: Dion–Jacobson vs. Ruddlesden–Popper phases. *J. Mater. Chem. A Mater.* **8**, 22009–22022 (2020).
48. Mao, L. *et al.* Hybrid Dion-Jacobson 2D Lead Iodide Perovskites. *J. Am. Chem. Soc.* **140**, 3775–3783 (2018).
49. Cheng, P. *et al.* (C6H5C2H4NH3)2GeI4: A Layered Two-Dimensional Perovskite with Potential for Photovoltaic Applications. *Journal of Physical Chemistry Letters* **8**, 4402–4406 (2017).
50. Pitaro, M. *et al.* Tin Halide Perovskites: From Fundamental Properties to Solar Cells. *Advanced Materials* **34**, 2105844 (2022).
51. Papavassiliou, G. C., Koutselas, J. B. & Lagouvardos, D. J. Preparation and Characterization of (C6H5CH2CH2NH3)2SnI4 and (C6H5CH2CH2NH3)2SnBr4. *Zeitschrift fur Naturforschung - Section B Journal of Chemical Sciences* **48**, 1013–1014 (1993).
52. Hamill, J. C., Schwartz, J. & Loo, Y. L. Influence of Solvent Coordination on Hybrid Organic-Inorganic Perovskite Formation. *ACS Energy Lett.* **3**, 92–97 (2018).
53. Park, S., Choi, S., Kim, S. & Nam, K. T. Metal Halide Perovskites for Solar Fuel Production and Photoreactions. *J. Phys. Chem. Lett.* **12**, 8292–8301 (2021).
54. Zhu, L. *et al.* Synthesis of ultrathin two-dimensional organic–inorganic hybrid perovskite nanosheets for polymer field-effect transistors. *J. Mater. Chem. C Mater.* **6**, 3945–3950 (2018).
55. Romani, L. *et al.* PEA2SnBr4: a water-stable lead-free two-dimensional perovskite and demonstration of its use as a co-catalyst in hydrogen photogeneration and organic-dye degradation. *J. Mater. Chem. C Mater.* **8**, 9189–9194 (2020).
56. Pan, S. *et al.* Halide Perovskite Materials for Photo(Electro)Chemical Applications: Dimensionality, Heterojunction, and Performance. *Adv. Energy Mater.* **12**, 2004002 (2022).
57. Armenise, V., Colella, S., Fracassi, F. & Listorti, A. Lead-Free Metal Halide Perovskites for Hydrogen Evolution from Aqueous Solutions. *Nanomaterials* **11**, 433 (2021).
58. Zhang, Z. *et al.* Stable and Highly Efficient Photocatalysis with Lead-Free Double-Perovskite of Cs2AgBiBr6. *Angew. Chem. Int. Ed.* **58**, 7263–7267 (2019).
59. Jiang, Y. *et al.* In Situ Synthesis of Lead-Free Halide Perovskite Cs2AgBiBr6 Supported on Nitrogen-Doped Carbon for Efficient Hydrogen Evolution in Aqueous HBr Solution. *ACS Appl. Mater. Interfaces* **13**, 10037–10046 (2021).
60. Peng, S. *et al.* Stabilizing Metal Halide Perovskites for Solar Fuel Production: Challenges, Solutions, and Future Prospects. *Advanced Materials* **35**, 2304711 (2023).
61. Yu, W. *et al.* Breaking the bottleneck of lead-free perovskite solar cells through dimensionality modulation. *Chem. Soc. Rev.* **53**, 1769–1788 (2024).
62. Yang, X., Wang, W., Ran, R., Zhou, W. & Shao, Z. Recent Advances in Cs2AgBiBr6-Based Halide Double Perovskites as Lead-Free and Inorganic Light Absorbers for Perovskite Solar Cells. *Energy and Fuels* **34**, 10513–10528 (2020).
63. Huang, J. *et al.* Fundamental understanding in the performance-limiting factors of Cs2AgBiBr6-based perovskite photovoltaics. *Renewable and Sustainable Energy Reviews* **191**, 114187 (2024).
64. Slavney, A. H., Hu, T., Lindenberg, A. M. & Karunadasa, H. I. A Bismuth-Halide Double Perovskite with Long Carrier Recombination Lifetime for Photovoltaic Applications. *J. Am. Chem. Soc.* **138**, 2138–2141 (2016).
65. Du, K.-Z. *et al.* Bandgap Engineering of Lead-Free Double Perovskite Cs2AgBiBr6 through Trivalent Metal Alloying. *Angew. Chem. Int. Ed.* **56**, 8158–8162 (2017).
66. Kar, S. K., Sinha, A. S. K., Bansal, R., Shabani, B. & Harichandan, S. Overview of hydrogen economy in Australia. *Wiley Interdiscip. Rev. Energy Environ.* **12**, e457 (2023).
67. Aslam, S. *et al.* Electrochemical hydrogen production: sustainable hydrogen economy. *Green Chemistry* **25**, 9543–9573 (2023).
68. Le, T. T. *et al.* Fueling the future: A comprehensive review of hydrogen energy systems and their challenges. *Int. J. Hydrogen Energy* **54**, 791–816 (2024).
69. Dillman, K. J. & Heinonen, J. A 'just' hydrogen economy: A normative energy justice assessment of the hydrogen economy. *Renewable and Sustainable Energy Reviews* **167**, 112648 (2022).

70. Boretti, A. & Pollet, B. G. Hydrogen economy: Paving the path to a sustainable, low-carbon future. *Int. J. Hydrogen Energy* **93**, 307–319 (2024).
71. McClure, E. T., Ball, M. R., Windl, W. & Woodward, P. M. Cs2AgBiX6 (X = Br, Cl): New Visible Light Absorbing, Lead-Free Halide Perovskite Semiconductors. *Chemistry of Materials* **28**, 1348–1354 (2016).
72. Wu, C. *et al.* The Dawn of Lead-Free Perovskite Solar Cell: Highly Stable Double Perovskite Cs2AgBiBr6 Film. *Advanced Science* **5**, 1700759 (2018).
73. Creutz, S. E., Crites, E. N., De Siena, M. C. & Gamelin, D. R. Colloidal Nanocrystals of Lead-Free Double-Perovskite (Elpasolite) Semiconductors: Synthesis and Anion Exchange to Access New Materials. *Nano Lett.* **18**, 1118–1123 (2018).
74. Shi, M. *et al.* Understanding the Effect of Crystalline Structural Transformation for Lead-Free Inorganic Halide Perovskites. *Advanced Materials* **32**, 2002137 (2020).
75. Fan, Q. *et al.* Visible light-driven highly efficient self-cleaning coatings crafted on leather surface using double perovskite as the booster. *Appl. Surf. Sci.* **638**, 158108 (2023).
76. Fett, B. *et al.* In Situ Crystallization of the Inorganic Lead-Free Halide Double Perovskite Cs2AgBiBr6 via Spray-Drying. *ACS Appl. Energy Mater.* **6**, 4372–4379 (2023).
77. Zhang, Z. *et al.* Lead-Free Cs2AgBiBr6 Nanocrystals Confined in MCM-48 Mesoporous Molecular Sieve for Efficient Photocatalytic CO2 Reduction. *Solar RRL* **7**, 2300038 (2023).
78. Chen, Z. *et al.* S-scheme Cs2AgBiBr6/Ag3PO4 heterojunction with efficient photocatalysis performance for H2 production and organic pollutant degradation under visible light. *Sep. Purif. Technol.* **295**, 121250 (2022).
79. Sena, M. S. *et al.* Lead-Free Halide Perovskite Cs2AgBiBr6/Bismuthene Composites for Improved CH4 Production in Photocatalytic CO2 Reduction. *ACS Appl. Energy Mater.* https://pubs.acs.org/doi/full/10.1021/acsaem.2c03105 (2022).
80. Wang, T., Yue, D., Li, X. & Zhao, Y. Lead-free double perovskite Cs2AgBiBr6/RGO composite for efficient visible light photocatalytic H2 evolution. *Appl. Catal. B* **268**, 118399 (2020).
81. Mahmoud Idris, A. *et al.* A heterostructure of halide and oxide double perovskites Cs2AgBiBr6/Sr2FeNbO6 for boosting the charge separation toward high efficient photocatalytic CO2 reduction under visible-light irradiation. *Chemical Engineering Journal* **446**, 137197 (2022).
82. Schmidt, L. C. *et al.* Nontemplate synthesis of CH3NH3PbBr3 perovskite nanoparticles. *J. Am. Chem. Soc.* **136**, 850–853 (2014).
83. Protesescu, L. *et al.* Nanocrystals of Cesium Lead Halide Perovskites (CsPbX3, X = Cl, Br, and I): Novel Optoelectronic Materials Showing Bright Emission with Wide Color Gamut. *Nano Lett.* **15**, 3692–3696 (2015).
84. Zhou, L. *et al.* Synthesis and Photocatalytic Application of Stable Lead-Free Cs2AgBiBr6 Perovskite Nanocrystals. *Small* **14**, 1703762 (2018).
85. Zhang, Y., Shah, T., Deepak, F. L. & Korgel, B. A. Surface Science and Colloidal Stability of Double-Perovskite Cs2AgBiBr6 Nanocrystals and Their Superlattices. *Chemistry of Materials* **31**, 7962–7969 (2019).
86. Bekenstein, Y. *et al.* The Making and Breaking of Lead-Free Double Perovskite Nanocrystals of Cesium Silver-Bismuth Halide Compositions. *Nano Lett.* **18**, 3502–3508 (2018).
87. Liu, Z. *et al.* Synthesis of lead-free Cs2AgBix6 (X = Cl, Br, I) double perovskite nanoplatelets and their application in CO2 photocatalytic reduction. *Nano Lett.* **21**, 1620–1627 (2021).
88. Huang, J., Zou, S., Lin, J., Liu, Z. & Qi, M. Ultrathin lead-free double perovskite cesium silver bismuth bromide nanosheets. *Nano Res.* **14**, 4079–4086 (2021).
89. Low, Y. J. *et al.* Synthesis of cesium silver bismuth bromide double perovskite nanoparticles via a microwave-assisted solvothermal method. *Mater. Today Chem.* **29**, 101477 (2023).
90. Wu, D. *et al.* High visible-light photocatalytic performance of stable lead-free Cs2AgBiBr6 double perovskite nanocrystals. *J. Catal.* **397**, 27–35 (2021).
91. Li, X. *et al.* Sb-Substituted Cs2AgBiBr6/g-C3N4 Composite for Photocatalytic C(sp3)-H Bond Activation in Toluene. *Chemistry of Materials* **35**, 3105–3114 (2023).

92. Yu, M. *et al.* Controllable fabrication of a Cs2AgBiBr6 nanocrystal/mesoporous black TiO2 hollow sphere composite for photocatalytic benzyl alcohol oxidation. *J. Mater. Chem. A Mater.* **11**, 4302–4309 (2023).
93. Fan, Q., Wei, S., Ma, J., Zhang, W. & Wen, L. Water-driven boost in the visible light photocatalytic performance of Cs2AgBiBr6 double perovskite nanocrystals. *J. Mater. Chem. A Mater.* **10**, 14923–14932 (2022).
94. Song, K., Gou, J., Wu, L. & Zeng, C. Two-dimensional black phosphorus-modified Cs2AgBiBr6 with efficient charge separation for enhanced visible-light photocatalytic H2 evolution. *J. Mater. Chem. C Mater.* **10**, 15386–15393 (2022).
95. Huang, Q., Guo, Y., Chen, J., Lou, Y. & Zhao, Y. NiCoP modified lead-free double perovskite Cs2AgBiBr6 for efficient photocatalytic hydrogen generation. *New Journal of Chemistry* **46**, 7395–7402 (2022).
96. He, Z. *et al.* Lead-Free Cs2AgBiBr6 Perovskite with Enriched Surface Defects for Efficient Photocatalytic Hydrogen Evolution. *Energy and Fuels* **35**, 15005–15009 (2021).
97. Zhang, Y., Sun, Z., Wang, Z., Zang, Y. & Tao, X. Efficient and long-term photocatalytic H2 evolution stability enabled by Cs2AgBiBr6/MoS2 in aqueous HBr solution. *Int. J. Hydrogen Energy* **47**, 8829–8840 (2022).
98. Wang, T., Li, X., Qin, Z., Wang, T. & Zhao, Y. Activating photocatalytic hydrogen generation on inorganic lead-free Cs2AgBiBr6 perovskite via reversible Cu2+/Cu+ redox couple. *J. Catal.* **413**, 509–516 (2022).
99. Song, K., Gou, J., Yang, L. & Zeng, C. Environmentally Stable Mesoporous g-C3N4 Modified Lead-Free Double Perovskite Cs2AgBiBr6 for Highly Efficient Photocatalytic Hydrogen Evolution. *Catal. Letters* **1**, 1–10 (2022).
100. Lv, H. *et al.* Efficient Charge Transfer and Effective Active Sites in Lead-Free Halide Double Perovskite S-Scheme Heterojunctions for Photocatalytic H2 Evolution. *Small Methods* **7**, 2201365 (2023).
101. Feng, J., Long, Q., Guo, Q., Song, K. & Zeng, C. Highly dispersed NiCoB-modified lead-free double perovskite Cs2AgBiBr6 enhances photocatalytic hydrogen evolution through g-C3N4 assistance. *Surfaces and Interfaces* **46**, 104100 (2024).
102. Vidhya, C., Meera, B., Nair, R. B. & Kurian, S. Enhanced photocatalytic hydrogen evolution through suppressed electron–hole recombination in Cs2AgBiBr6-NC/g-C3N4 nanocomposites. *Catal. Sci. Technol.* **14**, 746–757 (2024).
103. Xu, Y. F. *et al.* A CsPbBr3 Perovskite Quantum Dot/Graphene Oxide Composite for Photocatalytic CO2 Reduction. *J. Am. Chem. Soc.* **139**, 5660–5663 (2017).
104. Kumar, S. *et al.* Mechanochemically synthesized Pb-free halide perovskite-based Cs2AgBiBr6–Cu–RGO nanocomposite for photocatalytic CO2 reduction. *J. Mater. Chem. A Mater.* **9**, 12179–12187 (2021).
105. Wang, J., Cheng, H., Wei, D. & Li, Z. Ultrasonic-assisted fabrication of Cs2AgBiBr6/Bi2WO6 S-scheme heterojunction for photocatalytic CO2 reduction under visible light. *Chinese Journal of Catalysis* **43**, 2606–2614 (2022).
106. Wang, Y. *et al.* Lead-free perovskite Cs2AgBiBr6@g-C3N4 Z-scheme system for improving CH4 production in photocatalytic CO2 reduction. *Appl. Catal. B* **282**, 119570 (2021).
107. Ding, L. *et al.* Embedding Cs2AgBiBr6 QDs into Ce-UiO-66-H to in situ construct a novel bifunctional material for capturing and photocatalytic reduction of CO2. *Chemical Engineering Journal* **446**, 137102 (2022).
108. Sun, Q. M. *et al.* Boosted Inner Surface Charge Transfer in Perovskite Nanodots@Mesoporous Titania Frameworks for Efficient and Selective Photocatalytic CO2 Reduction to Methane. *Angew. Chem. Int. Ed.* **61**, e202200872 (2022).
109. Zhang, Z. *et al.* Self-assembled lead-free double perovskite-MXene heterostructure with efficient charge separation for photocatalytic CO2 reduction. *Appl. Catal. B* **312**, 121358 (2022).
110. Purohit, S. *et al.* Photocatalytic CO2 Reduction Using an Amorphous TiO2-Encapsulated Cs2AgBiBr6 Nanocrystal: Selective Methane Formation. *Energy and Fuels* **36**, 12170–12180 (2022).

111. Zhang, Z., Jiang, Y., Dong, Z., Chu, Y. & Xu, J. 2D/2D Inorganic/Organic Hybrid of Lead-Free Cs2AgBiBr6 Double Perovskite/Covalent Triazine Frameworks with Boosted Charge Separation and Efficient CO2 Photoreduction. *Inorg. Chem.* **61**, 16028–16037 (2022).

112. Liu, J. *et al.* In situ growth of lead-free halide perovskites into SiO2 sub-microcapsules toward water-stable photocatalytic CO2 reduction. *Nanoscale* **15**, 7023–7031 (2023).

113. Jiang, Y., Zhou, R., Zhang, Z., Dong, Z. & Xu, J. Boosted charge transfer and CO2 photoreduction by construction of S-scheme heterojunctions between Cs2AgBiBr6 nanosheets and two-dimensional metal–organic frameworks. *J. Mater. Chem. C Mater.* **11**, 2540–2551 (2023).

114. Purohit, S., Singh, S., Yadav, K. L., Pant, K. K. & Satapathi, S. Enhanced CO2 Reduction with Cs2AgBiBr6-gC3N4 Heterojunction Photocatalysts Prepared by Green Synthesis. *ACS Appl. Energy Mater.* **6**, 5580–5587 (2023).

115. Liu, Z. L., Zhang, M. R., Dong, G. X., Zhang, M. & Lu, T. B. Highly Selective Photosynthesis of Formic Acid by Unifying the Products of CO2 Reduction and Methanol Oxidation. *Solar RRL* **7**, 2300300 (2023).

116. Xiong, W., Dong, Y. & Pan, A. Fabricating a type II heterojunction by growing lead-free perovskite Cs2AgBiBr6in situ on graphite-like g-C3N4 nanosheets for enhanced photocatalytic CO2 reduction. *Nanoscale* **15**, 15619–15625 (2023).

117. Wu, L. *et al.* In-situ assembling 0D/2D Z-scheme heterojunction of Lead-free Cs2AgBiBr6/Bi2WO6 for enhanced photocatalytic CO2 reduction. *J. Colloid Interface Sci.* **629**, 233–242 (2023).

118. Xiong, W. *et al.* Highly stable lead-free perovskite Cs2AgBiBr6/UiO-66 Z-scheme heterostructures with enhanced photocatalytic activity for CO2 photoreduction and organic dyes degradation. *Appl. Surf. Sci.* **644**, 158807 (2024).

119. Wang, H. *et al.* Vacancy pair induced surface chemistry reconstruction of Cs2AgBiBr6/Bi2WO6 heterojunction to enhance photocatalytic CO2 reduction. *Applied Catalysis B: Environment and Energy* **351**, 123956 (2024).

120. Zhao, J. S. *et al.* Directed Electron Delivery from a Pb-Free Halide Perovskite to a Co(II) Molecular Catalyst Boosts CO2 Photoreduction Coupled with Water Oxidation. *Angew. Chem. Int. Ed.* **63**, e202401344 (2024).

121. Chen, Z. *et al.* Rubidium Doped Cs2AgBiBr6 Hierarchical Microsphere for Enhanced Photocatalytic CO2 Reduction. *Small* **20**, 2401202 (2024).

122. Huang, W., Zhu, Q., Li, Z., Zhu, Y. & Shen, J. Construction of S-Scheme Cs2AgBiBr6/BiVO4 Heterojunctions with Fast Charge Transfer Kinetics Toward Promoted Photocatalytic Conversion of CO2. *Small* 2412289 (2025) doi:https://doi.org/10.1002/smll.202412289.

123. Ma, J. *et al.* All-inorganic TiO2/Cs2AgBiBr6 composite as highly efficient photocatalyst under visible light irradiation. *Front. Chem. Sci. Eng.* **17**, 1925–1936 (2023).

124. Cheng, S. *et al.* In-situ growth of Cs2AgBiBr6 perovskite nanocrystals on Ti3C2Tx MXene nanosheets for enhanced photocatalytic activity. *Appl. Surf. Sci.* **621**, 156877 (2023).

125. Huang, X. *et al.* Interfacial chemical bond-modulated Z-scheme Cs2AgBiBr6/WO3 enables stable and highly efficient photocatalysis. *Appl. Surf. Sci.* **637**, 157877 (2023).

126. Qiu, M. *et al.* Water-induced formation of Cs2AgBiBr6/BiOBr heterostructure with enhanced visible-light photocatalytic activity. *Advanced Powder Technology* **35**, 104679 (2024).

127. Wu, J. *et al.* Ultra-small cesium silver bismuth bromide quantum dots fabricated by modified hot-injection method for highly efficient degradation of contaminants in organic solvent. *Journal of Environmental Sciences* **152**, 577–583 (2025).

128. Song, J. *et al.* In situ growth of lead-free perovskite Cs2AgBiBr6 on a flexible ultrathin carbon nitride sheet for highly efficient photocatalytic benzylic C(sp3)–H bond activation. *Chemical Engineering Journal* **453**, 139748 (2023).

129. Zhang, S. *et al.* Surface defect-induced electronic structures of lead-free Cs2AgBiBr6 double-perovskite for efficiently solar-driven photocatalytic performance. *Appl. Surf. Sci.* **609**, 155446 (2023).

130. Chen, T., Qin, T., Sun, H. & Su, C. Oxygen vacancy in lead-free perovskite Cs2AgBiBr6/WO3-X for enhanced photocatalytic C(sp3)-H bond oxidation. *Rare Metals* 1–12 (2025) doi:10.1007/S12598-025-03400-0/FIGURES/4.

131. Liu, Z. *et al.* Fabrication of S-scheme heterojunction consisting of W-doped BiVO4 and biperovskite Cs2AgBiBr6 for photocatalytic degradation of antibiotics. *J. Colloid Interface Sci.* **696**, 137892 (2025).
132. Xiao, M. *et al.* Surface Ligands Stabilized Lead Halide Perovskite Quantum Dot Photocatalyst for Visible Light-Driven Hydrogen Generation. *Adv. Funct. Mater.* **29**, 1905683 (2019).
133. Huang, H. *et al.* Metal Halide Perovskite Based Heterojunction Photocatalysts. *Angewandte Chemie* **134**, e202203261 (2022).
134. Zhang, L., Zhang, J., Yu, H. & Yu, J. Emerging S-Scheme Photocatalyst. *Advanced Materials* **34**, 2107668 (2022).
135. Xu, Q., Zhang, L., Cheng, B., Fan, J. & Yu, J. S-Scheme Heterojunction Photocatalyst. *Chem* **6**, 1543–1559 (2020).
136. Shabbir, A., Sardar, S. & Mumtaz, A. Mechanistic investigations of emerging type-II, Z-scheme and S-scheme heterojunctions for photocatalytic applications – A review. *J. Alloys Compd.* **1003**, 175683 (2024).
137. Zhao, F. *et al.* How to determine whether an electron transfer channel is type-II or S-scheme in g–C3N4–based photocatalysts? A critical review. *Int. J. Hydrogen Energy* **80**, 659–685 (2024).
138. Tailor, N. K. *et al.* Unveiling the Potential of Halide Perovskites for Seasonally Adaptive CO2 Photoreduction under Low Light Conditions. *Adv. Funct. Mater.* 2402894 (2024).
139. Wu, H. *et al.* Unusual and highly tunable missing-linker defects in zirconium metal-organic framework UiO-66 and their important effects on gas adsorption. *J. Am. Chem. Soc.* **135**, 10525–10532 (2013).
140. Singh, S. *et al.* Halide Perovskite Photocatalysts for Clean Fuel Production and Organic Synthesis: Opportunities and Challenges. *Advanced Materials* **37**, 2419603 (2025).
141. Huang, Y., Yu, J., Wu, Z., Li, B. & Li, M. All-inorganic lead halide perovskites for photocatalysis: a review. *RSC Adv.* **14**, 4946–4965 (2024).
142. Tong, H. *et al.* Interface Engineering, Charge Carrier Dynamics, and Solar-Driven Applications of Halide Perovskite/2D Material Heterostructured Photocatalysts. *ACS Appl. Mater. Interfaces* **17**, 23431–23465 (2025).
143. Takata, T. *et al.* Photocatalytic water splitting with a quantum efficiency of almost unity. *Nature 2020 581:7809* **581**, 411–414 (2020).
144. Nishiyama, H. *et al.* Photocatalytic solar hydrogen production from water on a 100-m2 scale. *Nature 2021 598:7880* **598**, 304–307 (2021).
145. Fang, S. *et al.* Photocatalytic CO2 reduction. *Nature Reviews Methods Primers 2023 3:1* **3**, 61- (2023).
146. Stanley, P. M., Ramm, V., Fischer, R. A. & Warnan, J. Analysis of metal–organic framework-based photosynthetic CO2 reduction. *Nature Synthesis 2024 3:3* **3**, 307–318 (2024).
147. Yin, H. Q., Zhang, Z. M. & Lu, T. B. Ordered Integration and Heterogenization of Catalysts and Photosensitizers in Metal-/Covalent-Organic Frameworks for Boosting CO2 Photoreduction. *Acc. Chem. Res.* **56**, 2676–2687 (2023).
148. Li, C. fan, Guo, R. tang, Zhang, Z. rui, Wu, T. & Pan, W. guo. Converting CO2 into Value-Added Products by Cu2O-Based Catalysts: From Photocatalysis, Electrocatalysis to Photoelectrocatalysis. *Small* **19**, 2207875 (2023).
149. Kshirsagar, S. D. *et al.* Emerging ZnO Semiconductors for Photocatalytic CO2 Reduction to Methanol. *Small* **20**, 2407318 (2024).
150. Tawfik, A. *et al.* Solar photo-oxidation of recalcitrant industrial wastewater: a review. *Environmental Chemistry Letters 2022 20:3* **20**, 1839–1862 (2022).
151. Kumari, H. *et al.* A Review on Photocatalysis Used For Wastewater Treatment: Dye Degradation. *Water, Air, & Soil Pollution 2023 234:6* **234**, 349- (2023).
152. Suhan, M. B. K. *et al.* Sustainable pollutant removal and wastewater remediation using TiO2-based nanocomposites: A critical review. *Nano-Structures & Nano-Objects* **36**, 101050 (2023).
153. Chen, D. *et al.* Photocatalytic degradation of organic pollutants using TiO2-based photocatalysts: A review. *J. Clean. Prod.* **268**, 121725 (2020).

154. Nur, A. S. M. *et al.* A review on the development of elemental and codoped TiO2 photocatalysts for enhanced dye degradation under UV–vis irradiation. *Journal of Water Process Engineering* **47**, 102728 (2022).

155. Wachs, I. E. Number of surface sites and turnover frequencies for oxide catalysts. *J. Catal.* **405**, 462–472 (2022).

156. Slavney, A. H., Hu, T., Lindenberg, A. M. & Karunadasa, H. I. A Bismuth-Halide Double Perovskite with Long Carrier Recombination Lifetime for Photovoltaic Applications. *J. Am. Chem. Soc.* **138**, 2138–2141 (2016).

157. Bob B. He. *Two-Dimensional X-Ray Diffraction*. (John Wiley & Sons, Inc., Hoboken, 2009).

158. Hammond, C. *The Basics of Crystallography and Diffraction*. (Oxford University Press, Oxford, 2015).

159. Authier, A. *Dynamical Theory of X-Ray Diffraction*. (Oxford University Press, Oxford, 2003).

160. Stojilovic, N. Using Cu K α1/ K α2 Splitting and a Powder XRD System to Discuss X-ray Generation. *J. Chem. Educ.* **95**, 598–600 (2018).

161. Giacovazzo, C., Monaco, H. L. & Artioli, G. Experimental methods in X-ray and neutron crystallography. in *Fundamentals of Crystallography* (ed. Giacovazzo, C.) 301–416 (Oxford University Press, New York, 2011).

162. Cullity, B. D. & Stock S. R. *Elements of X-Ray Diffraction*. (Pearson Education Limited, Harlow, 2013).

163. Anderson, R. J., Bendell, D. J. & Groundwater, P. W. Ultraviolet–visible (UV-Vis) spectroscopy. in *Organic Spectroscopic Analysis* vol. 22 7–23 (The Royal Society of Chemistry, Cambridge, 2004).

164. Campbell, I. D. Ultraviolet/visible spectroscopy. in *Biophysical Techniques* 161–175 (Oxford University Press, 2012).

165. Tauc, J., Grigorovici, R. & Vancu, A. Optical Properties and Electronic Structure of Amorphous Germanium. *physica status solidi (b)* **15**, 627–637 (1966).

166. Viezbicke, B. D., Patel, S., Davis, B. E. & Birnie, D. P. Evaluation of the Tauc method for optical absorption edge determination: ZnO thin films as a model system. *physica status solidi (b)* **252**, 1700–1710 (2015).

167. Fayaz, M. *et al.* Luminescence and energy transfer mechanism in Ce3+ and Gd3+ ions in bismuth borate glass. *Ceram. Int.* **49**, 24690–24695 (2023).

168. Ji, F. *et al.* Lead-Free Halide Double Perovskite Cs2AgBiBr6 with Decreased Band Gap. *Angewandte Chemie* **132**, 15303–15306 (2020).

169. Yuan, C. *et al.* UV–vis spectroscopic detection of formaldehyde and its analogs: A convenient and sensitive methodology. *J. Hazard. Mater.* **438**, 129457 (2022).

170. Min, Y. *et al.* Highly selective detection of formaldehyde and its analogs in clams based on unique and specific conjugation reactions via ultraviolet-visible absorptions. *Chinese Journal of Analytical Chemistry* **51**, 100287 (2023).

171. Cristy, A. A., Ozaki, Y. & Gregoriou, V. G. Modern Fourier Transform Infrared Spectroscopy. in *Comprehensive Analytical Chemistry* vol. 35 1–356 (Elsevier B.V., 2001).

172. Che Man, Y. B., Syahariza, Z. A. & Rohman, A. Fourier Transform Infrared (FTIR) Spectroscopy: Development, Techniques, and Application in the Analyses of Fats and Oils. in *Fourier Transform Infrared Spectroscopy—Developments, Techniques and Applications* (ed. Rees, O. J.) 1–26 (Nova Science Publishers, Incorporated, 2010).

173. Stevie, F. A. & Donley, C. L. Introduction to x-ray photoelectron spectroscopy. *Journal of Vacuum Science & Technology A: Vacuum, Surfaces, and Films* **38**, (2020).

174. Tougaard, S. Practical guide to the use of backgrounds in quantitative XPS. *Journal of Vacuum Science & Technology A* **39**, (2021).

175. Baer, D. R. *et al.* Practical guides for x-ray photoelectron spectroscopy: First steps in planning, conducting, and reporting XPS measurements. *Journal of Vacuum Science & Technology A: Vacuum, Surfaces, and Films* **37**, (2019).

176. Wren, A. W., Laffir, F. R., Mellot, N. P. & Towler, M. R. X-ray Photoelectron Spectroscopy: Studies from Industrial & Bioactive Glass to Biomaterials. in *X-Ray Photoelectron Spectroscopy* (ed. Wagner, J. M.) 1–30 (Nova Science Publishers, Incorporated, 2010).

177. van der Heide, P. *X-Ray Photoelectron Spectroscopy: An Introduction to Principles and Practices*. (John Wiley & Sons, Incorporated, 2011).

178. Siegbahn, K., Hammond, D., Fellner-Feldegg, H. & Barnett, E. F. Electron spectroscopy with monochromatized x-rays. *Science (1979).* **176**, 245–252 (1972).

179. McNair, H. M., Miller, J. M. & Settle, F. A. *Basic Gas Chromatography*. (John Wiley & Sons, Incorporated, 2019).

180. Jennings, W., Mittlefehldt, E. & Stremple, P. Introduction. in *Analytical Gas Chromatography* 1–29 (Elsevier Inc., 1997). doi:10.1016/B978-012384357-9/50002-7.

181. Miller, J. M. Introduction to Chromatography. in *Chromatography: Concepts and Contrasts* 35–66 (John Wiley & Sons, Inc., 2009).

182. Stashenko, E. & Martínez, J. R. Gas Chromatography-Mass Spectrometry. in *Advances in Gas Chromatography* (ed. Guo, X.) (InTech, 2014).

183. Blumberg, L. M. Theory of gas chromatography. in *Gas Chromatography* 19–97 (Elsevier Inc., 2021).

184. Tipler, A. Sample introduction methods. in *Gas Chromatography* (ed. Poole, C. F.) 217–249 (Elsevier Inc., 2012).

185. Poole, C. F. Column technology: packed columns. in *Gas Chromatography* (ed. Poole, C. F.) 141–163 (Elsevier Inc., 2021).

186. Poole, C. F. Conventional detectors for gas chromatography. in *Gas Chromatography* (ed. Poole, C. F.) 343–369 (Elsevier Inc., 2021).

187. Lunardi, C. N., Gomes, A. J., Rocha, F. S., De Tommaso, J. & Patience, G. S. Experimental methods in chemical engineering: Zeta potential. *Can. J. Chem. Eng.* **99**, 627–639 (2021).

188. Wilson, W. W., Wade, M. M., Holman, S. C. & Champlin, F. R. Status of methods for assessing bacterial cell surface charge properties based on zeta potential measurements. *J. Microbiol. Methods* **43**, 153–164 (2001).

189. Kaszuba, M., Corbett, J., Watson, F. M. N. & Jones, A. High-concentration zeta potential measurements using light-scattering techniques. *Philosophical Transactions of the Royal Society A: Mathematical, Physical and Engineering Sciences* **368**, 4439–4451 (2010).

190. Lowry, G. V. *et al.* Guidance to improve the scientific value of zeta-potential measurements in nanoEHS. *Environ. Sci. Nano* **3**, 953–965 (2016).

191. Bhattacharjee, S. DLS and zeta potential – What they are and what they are not? *Journal of Controlled Release* **235**, 337–351 (2016).

192. Teets, T. S. *Photoluminescence*. (American Chemical Society, Washington, DC, USA, 2021).

193. Yang, K., Venkataraman, M., Wiener, J. & Militky, J. Photoluminescence PCMs and their potential for thermal adaptive textiles. in *Multifunctional Phase Change Materials: Fundamentals, Properties and Applications* (eds. Pielichowska, K. & Pielichowski, K.) 255–277 (Woodhead Publishing, 2023).

194. Chen, R., Li, D., Xiong, Q. & Sun, H. Optical and excitonic properties of crystalline ZNS nanowires. in *UV-VIS and Photoluminescence Spectroscopy for Nanomaterials Characterization* (ed. Kumar Challa) 453–483 (Springer-Verlag Berlin Heidelberg, 2013).

195. Djurišić, A. B., Chen, X. Y., Zapien, J. A., Leung, Y. H. & Ng, A. M. C. Optical Properties of Oxide Nanomaterials. in *UV-VIS and Photoluminescence Spectroscopy for Nanomaterials Characterization* (ed. Kumar, C.) 387–430 (Springer, Berlin, Heidelberg, 2013).

196. Kirchartz, T., Márquez, J. A., Stolterfoht, M. & Unold, T. Photoluminescence-Based Characterization of Halide Perovskites for Photovoltaics. *Adv. Energy Mater.* **10**, 1904134 (2020).

197. Zuo, J. M. & Spence, J. C. H. *Advanced Transmission Electron Microscopy: Imaging and Diffraction in Nanoscience*. *Advanced Transmission Electron Microscopy* (Springer New York, New York, 2017).

198. Goodhew, P. General Introduction to Transmission Electron Microscopy (TEM). in *Aberration-Corrected Analytical Transmission Electron Microscopy* (ed. Brydson, R.) vol. 3 1–20 (John Wiley & Sons, Inc., 2011).

199. Williams, D. B. & Carter, C. B. *Transmission Electron Microscopy: A Textbook for Materials Science*. (Springer New York, 2009).

200. Nellist, P. D. The Principles of STEM Imaging. in *Scanning Transmission Electron Microscopy: Imaging and Analysis* (eds. Pennycook, S. J. & Nellist, P. D.) 91–115 (Springer New York, New York, 2011).

201. Tatlock, G. Introduction to Electron Optics. in *Aberration-Corrected Analytical Transmission Electron Microscopy* (ed. Brydson, R.) vol. 3 21–38 (John Wiley & Sons, Incorporated, 2011).

202. Nellist, P. D. Scanning Transmission Electron Microscopy. in *Springer Handbook of Microscopy* (eds. Hawkes, P. W. & Spence, J. C. H.) 49–99 (Springer Cham, 2019).

203. Reimer, L. & Kohl, H. *Transmission Electron Microscopy: Physics of Image Formation*. (Springer-Verlag, New York, 2008).

204. Hawkes, P. W. & Krivanek, O. L. Aberration correctors, monochromators, spectrometers. in *Springer Handbook of Microscopy* (eds. Hawkes, P. W. & Spence, J. C. H.) 625–675 (Springer Cham, 2019).

205. Cao, W. *et al.* Large relrod extension induced by lattice distortion in high entropy alloy. *Mater. Res. Express* 066558 (2019).

206. Craven, A. Details of STEM. in *Aberration-Corrected Analytical Transmission Electron Microscopy* (ed. Brydson, R.) vol. 3 111–161 (John Wiley & Sons, Incorporated, 2011).

207. Mitchell, D. R. G. DiffTools: Electron diffraction software tools for DigitalMicrograph™. *Microsc. Res. Tech.* **71**, 588–593 (2008).

208. Erdman, N., Bell, D. C. & Reichelt, R. Scanning Electron Microscopy. in *Springer Handbook of Microscopy* (eds. Hawkes, P. W. & Spence, J. C. H.) 229–318 (Springer Cham, 2019).

209. Schatten, H. The role of scanning electron microscopy in cell and molecular biology: SEM basics, past accomplishments, and new frontiers. in *Scanning Electron Microscopy for the Life Sciences: Advances in Microscopy and Microanalysis Series* (ed. Schatten, H.) 1–15 (Cambridge University Press, 2012).

210. Mehta, R. Interactions, Imaging and Spectra in SEM. in *Scanning Electron Microscopy* (ed. Kazmiruk, V.) 17–30 (IntechOpen, 2012).

211. Ul-Hamid, A. *A Beginners' Guide to Scanning Electron Microscopy*. (Springer Cham, 2018).

212. de la Peña, F. *et al.* hyperspy/hyperspy: v2.4.0. Preprint at (2026).

213. de la Pena, F. *et al.* Electron Microscopy (Big and Small) Data Analysis With the Open Source Software Package HyperSpy. *Microscopy and Microanalysis* **23**, 214–215 (2017).

214. Cliff, G. & Lorimer, G. W. The quantitative analysis of thin specimens. *J. Microsc.* **103**, 203–207 (1975).

215. Liu, M. *et al.* Issues and opportunities facing hydrolytic hydrogen production materials. *Chemical Engineering Journal* **461**, 141918 (2023).

216. Wang, H. *et al.* High quantum efficiency of hydrogen production from methanol aqueous solution with PtCu–TiO2 photocatalysts. *Nature Materials 2023 22:5* **22**, 619–626 (2023).

217. Bahmanpour, A. M., Hoadley, A. & Tanksale, A. Critical review and exergy analysis of formaldehyde production processes. *Reviews in Chemical Engineering* **30**, 583–604 (2014).

218. Wu, L. *et al.* Light-Driven Hydrogen Generation from Methanol Vapor Using Halide Perovskite Nanocrystals. *ACS Energy Lett.* **15**, 2978–2985 (2025).

219. Ramalingam, G. *et al.* Quantum Confinement Effect of 2D Nanomaterials. in *Quantum Dots - Fundamental and Applications* (ed. Divsar, F.) (IntechOpen, 2020).

220. Ulbricht, R. *et al.* Loosening quantum confinement: Observation of real conductivity caused by hole polarons in semiconductor nanocrystals smaller than the Bohr radius. *Nano Lett.* **12**, 4937–4942 (2012).

221. Liu, D. *et al.* Strain analysis and engineering in halide perovskite photovoltaics. *Nature Materials 2021 20:10* **20**, 1337–1346 (2021).

222. Schneider, C. A., Rasband, W. S. & Eliceiri, K. W. NIH Image to ImageJ: 25 years of image analysis. *Nature Methods 2012 9:7* **9**, 671–675 (2012).

223. Feng, C. *et al.* Synthesis of Leaf-Vein-Like g-C3N4 with Tunable Band Structures and Charge Transfer Properties for Selective Photocatalytic H2O2 Evolution. *Adv. Funct. Mater.* **30**, 2001922 (2020).

224. Li, Y. *et al.* Revealing electron numbers-binding energy relationships in heterojunctions via in-situ irradiated XPS. *Applied Catalysis B: Environment and Energy* **356**, 124223 (2024).

225. Peán, E. V., Dimitrov, S., De Castro, C. S. & Davies, M. L. Interpreting time-resolved photoluminescence of perovskite materials. *Physical Chemistry Chemical Physics* **22**, 28345–28358 (2020).

226. Ochoa, M., Yang, S. C., Nishiwaki, S., Tiwari, A. N. & Carron, R. Charge Carrier Lifetime Fluctuations and Performance Evaluation of Cu(In,Ga)Se2 Absorbers via Time-Resolved-Photoluminescence Microscopy. *Adv. Energy Mater.* **12**, 2102800 (2022).

227. Chang, K. *et al.* MoS2/graphene cocatalyst for efficient photocatalytic H 2 evolution under visible light irradiation. *ACS Nano* **8**, 7078–7087 (2014).

228. Ho, W., Yu, J. C., Lin, J., Yu, J. & Li, P. Preparation and Photocatalytic Behavior of MoS2 and WS2 Nanocluster Sensitized TiO2. *Langmuir* **20**, 5865–5869 (2004).

229. Kam, K. K. & Parkinson, B. A. Detailed photocurrent spectroscopy of the semiconducting group VIB transition metal dichalcogenides. *Journal of Physical Chemistry* **86**, 463–467 (1982).

230. Escobedo Salas, S., Serrano Rosales, B. & De Lasa, H. Quantum yield with platinum modified TiO2 photocatalyst for hydrogen production. *Appl. Catal. B* **140–141**, 523–536 (2013).

231. Xiao, J.-D. *et al.* Boosting Photocatalytic Hydrogen Production of a Metal–Organic Framework Decorated with Platinum Nanoparticles: The Platinum Location Matters. *Angew. Chem. Int. Ed.* **55**, 9389–9393 (2016).

232. Vamvasakis, I. *et al.* Size Effects of Platinum Nanoparticles in the Photocatalytic Hydrogen Production Over 3D Mesoporous Networks of CdS and Pt Nanojunctions. *Adv. Funct. Mater.* **26**, 8062–8071 (2016).

233. Xu, Y.-F. *et al.* Amorphous-TiO2-Encapsulated CsPbBr3 Nanocrystal Composite Photocatalyst with Enhanced Charge Separation and CO2 Fixation. *Adv. Mater. Interfaces* **5**, 1801015 (2018).

234. Gao, F. *et al.* Highly stable and luminescent silica-coated perovskite quantum dots at nanoscale-particle level via nonpolar solvent synthesis. *Chemical Engineering Journal* **407**, 128001 (2021).